Neutron-neutron correlation in Borromean nucleus ^{11}Li via the (p, pn) reaction

$$\left(\quad {}^{(p,\, pn)} \quad \right)$$

27   12

Abstract

Neutron-neutron correlation in light neutron-rich Borromean nuclei has attracted much attention. In particular, it has long been presumed that the neutron-neutron correlation caused by the *dineutron* (dineutron correlation) is a key ingredient to understand the binding mechanism and the exotic structures of these nuclei.

In the present work, the neutron momentum distribution in ^{11}Li was determined by employing the quasi-free (p, pn) reaction at 246 MeV/nucleon. We employed a new method of kinematically complete measurement, which enabled us to extract the ground-state neutron-neutron correlation as well as to investigate the structure of the ^{9}Li + n subsystem through the momentum measurement and the invariant mass spectroscopy, respectively.

The experiment was performed at the Radioactive Isotope Beam Factory (RIBF) in RIKEN. The MINOS device was used so as to achieve high luminosity. The recoil particle detectors RPD and WINDS, both constructed for this study, were used for the (p, pn) measurement. The SAMURAI spectrometer having a large acceptance contributed to the kinematically complete measurement.

The spectroscopy of the ^{10}Li provided strong constraints on the interaction between a neutron and a ^{9}Li nucleus. The existence of the *s*-wave virtual state and of the *p*-wave resonance was confirmed and their resonance parameters were determined. Moreover, the *d*-wave resonance was newly found at $E_r = 5.52 \pm 0.04$ MeV with a decay width of $\Gamma = 0.72 \pm 0.10$ MeV.

The fraction of each multipole up to *d*-wave was determined from the neutron momentum distribution: $35 \pm 4\%$, $59 \pm 1\%$, and $6 \pm 4\%$ for the two-neutron configurations $(s_{1/2})^2$, $(p_{1/2})^2$, and $(d_{5/2})^2$ or $(d_{3/2})^2$, respectively. This result indicates the dineutron correlation can be weaker than previously reported.

It was suggested experimentally for the first time that the dineutron correlation in ^{11}Li is developed in the surface region. The expectation value of the opening angle between the two neutrons was determined as $\langle \theta_Y^x \rangle = 85 \pm 10$ degrees. It also supports the weaker dineutron correlation than expected from the previous works.

Table of Contents

List of Figures

List of Tables

Chapter 1

Introduction

Atomic nucleus is a finite quantum many-body system consisting of two kinds of fermions, protons and neutrons. Two-particle correlation in nuclei is one of the attractive subjects of nuclear physics; it is closely related to the binding mechanism and the structures of nuclei.

The two-particle correlation in fermionic many-body systems has been successfully described by the Bardeen-Cooper-Schriefer (BCS) theory [1]. In conductive materials, two electrons compose the subsystems called Cooper pairs, which can be regarded as bosonic quasi-particles. At very low temperatures, they can condense in a single low-energy state and reduce the total energy of the system, so that the superconductivity appears. Through the same mechanism, the liquid ^{3}He and the ultra-cold Fermi gas of ^{6}Li exhibit superfluidity [2, 3]. There are several experimental facts suggesting that the structures of open-shell nuclei can also be described by employing the BCS theory [4], such as the energy gap and the odd-even staggering.

The other kind of two-particle correlation, *dineutron correlation* is considered to appear in certain nuclei; it is one of the unique features of nuclei that has not been found so far in other fermionic many-body systems. When the binding strength between two neutrons is comparable to that of the neutron with respect to the nucleus, two neutrons are considered to form a spatially localized pair. In contrast to the BCS-type correlation where many nucleons around the Fermi energy surface constructively contribute to form the pairs, only specific two neutrons contribute to form the pair in the case of the dineutron correlation. The nature of the dineutron correlation is considerably different from that of the BCS-type correlation.

The dineutron correlation was first discussed by Migdal [5] by solving the three-body problem where two interacting light particles exist in a potential well produced by a heavy particle. He showed that under certain circumstances there appears a bound state of the two particles, even in the case when the attraction between the two particles is too weak to form a bound state outside the potential. Such circumstances are realized in certain nuclei. When the single-particle energies of two valence neutrons are close to zero, the interaction between two neutrons becomes important. The loosely-bound nuclei located at the neutron drip line such as ^{11}Li are the best environments to satisfy such conditions.

In analogy with the dineutron correlation in the neutron drip-line nuclei, correlation between two protons, diproton correlation, in the proton-rich nuclei has also been discussed. However, the situation is more complicated in the case of two protons because the repulsive Coulomb interaction takes place. The foundation of the diproton correlation has not yet been fully clarified [6].

1.1   Borromean nucleus ^{11}Li

The dineutron correlation is considered to appear in various nuclei. Shell-model calculation showed that two valence neutrons added to the doubly-magic nucleus ^{208}Pb may form a spatially localized pair. It is also shown that the dineutron correlation appears in medium-heavy neutron-rich nuclei [7, 8] and even in the neutron matter having an infinite number of constituents [9]. Weakly-bound light nuclei such as ^{11}Li and ^{6}He are the best suited systems because the dineutron correlation is considered to play a major role in their binding mechanism [10].

^{11}Li and ^{6}He have the nature of *Borromean* [11]. Borromean nuclei are well described as a three-body system and have no bound subsystem of either two of three constituents. Figure 1.1 schematically shows the Borromean nucleus ^{11}Li composed of ^{9}Li core and two valence neutrons. Although ^{11}Li is bound, its binary subsystems ^{10}Li and ^{2}n are unbound on their own.

<center>^{11}Li: bound ^{10}Li: unbound ^{2}n: unbound</center>
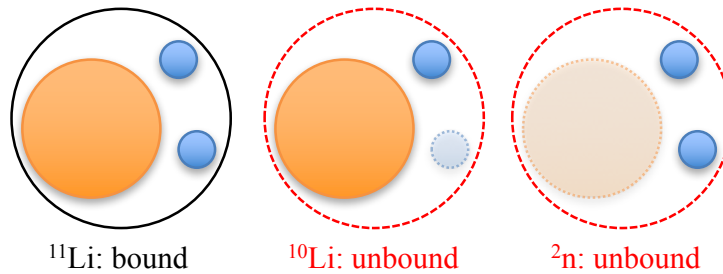
Figure 1.1: Schematic view of the Borromean nucleus ^{11}Li. The orange and the blue circles represent a core and two valence neutrons, respectively. The binary subsystems ^{10}Li and ^{2}n are unbound.

Theoretically, Borromean nuclei have been investigated by the core + n + n three-body models [6, 10, 12–23]. It is because the conventional shell model cannot reproduce the nature of the Borromean nuclei; The n–n interaction in such a loosely-bound system cannot be treated in the mean field approximation. It has been shown that such neutron-neutron correlation in the ground state is characterized as a spatially-localized neutron pair, i.e. dineutron correlation [10, 16–18].

Among the Borromean nuclei shown in Fig. 1.2, ^{11}Li is regarded as a benchmark system. As summarized in Table 1.1, ^{11}Li has the largest root-mean-square (r.m.s.) matter radius, which

		^{9}C	^{10}C	^{11}C	^{12}C	^{13}C	^{14}C	^{15}C	^{16}C	^{17}C	^{18}C	^{19}C	^{20}C		^{22}C
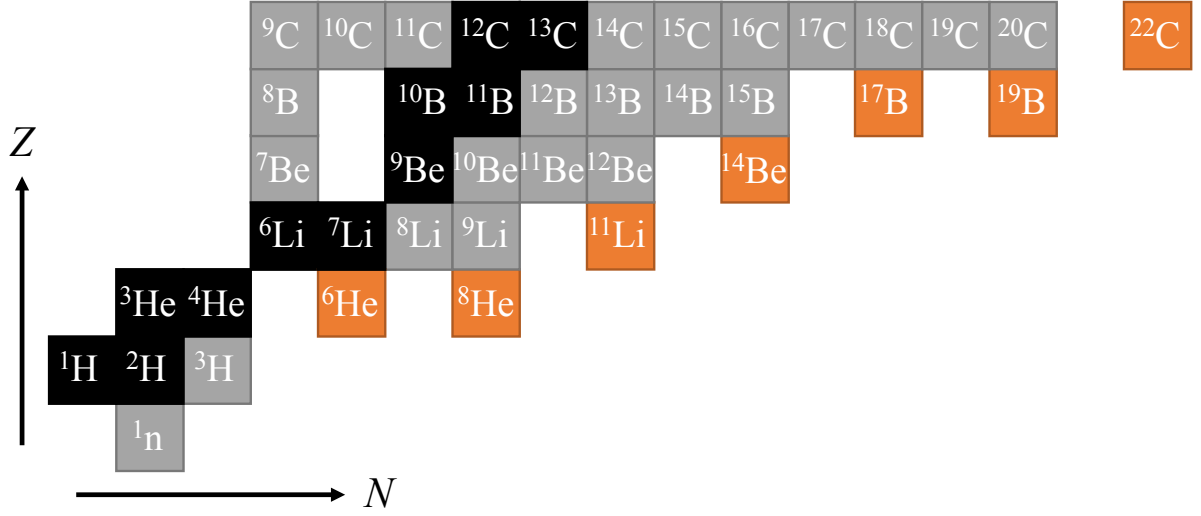
Figure 1.2: Part of the nuclear chart for $Z \leq 6$ nuclei. The horizontal and the vertical axes show the neutron number N and the proton number Z, respectively. The boxes colored by black, gray, and orange represent stable, unstable, and Borromean nuclei, respectively.

is comparable even with those of $A \approx 20$ nuclei by employing the empirical formula of

$$R = r_0 A^{1/3}, \tag{1.1}$$

$$r_0 = 1.2 \text{ fm.} \tag{1.2}$$

The deviation of the r.m.s. matter radius of ^{11}Li from the systematics is also the largest among the Borromean nuclei as listed in Table 1.1. This large r.m.s. matter radius stems from the large neutron halo structure where valence neutrons are expected to be very loosely bound to the core. ^{11}Li may be the nucleus having the smallest two-neutron separation energy S_{2n} among all the nuclei. The small S_{2n} value of ^{11}Li of 369.3 keV also suggests a loosely-bound three-body system. It is known that an admixture of configurations of single-particle orbits with different parities plays a significant role to form the spatial localization [24]. The contributions of s- and p-orbits in ^{11}Li are considered as about 4:5 [25]. The comparable contributions of s- and p-orbits maximize the interference so that the spatial localization of two neutrons can be enhanced. Therefore, the ^{11}Li nucleus is considered as the best system to study the dineutron correlation.

Experimentally, a precise measurement of the nuclear charge radius provided an indirect evidence of the dineutron correlation. The nuclear charge radii of Li isotopes were measured [32, 33] by employing laser spectroscopy techniques [34, 35]. It was found that the r.m.s. charge radii monotonically drops from ^{6}Li (2.51 ± 6 fm) to ^{9}Li (2.22 ± 9 fm), and very rapidly, rises up to ^{11}Li (2.467 ± 37 fm). The rapid increase of the charge radii is considered as the effect of the recoil of the ^{9}Li core in ^{11}Li. Figure 1.3 schematically shows the mechanism of the increase of

Table 1.1: Static properties of Borromean nuclei. The S_{2n} values without citations were retrieved from Ref. [26]. The $\langle r_m^{syst} \rangle$ values were calculated by using Eqs. (1.1) and (1.2).

Nuclide	r.m.s. matter radius $\langle r_m \rangle$ [fm]		Ratio	Two-neutron separation
	systematics $\langle r_m^{syst} \rangle$	measured $\langle r_m^{meas} \rangle$	$\langle r_m^{meas} \rangle / \langle r_m^{syst} \rangle$	energy S_{2n} [keV]
^{6}He	2.18	2.30 ± 0.07 [27]	1.06	975.45 ± 5
^{11}Li	2.67	3.55 ± 0.10 [28]	1.33	369.3 ± 6
^{14}Be	2.89	3.22 ± 0.07 [29]	1.11	1270 ± 130
^{17}B	3.09	2.99 ± 0.09 [30]	0.97	1330 ± 170
^{19}B	3.20	3.11 ± 0.13 [30]	0.97	1100 ± 400
^{22}C	3.36	3.44 ± 0.08 [31]	1.02	400–600 [31]

the charge radii. Due to the spatial localization of two valence neutrons, the ^{9}Li core in ^{11}Li must recoil to the opposite direction from the center of mass of the two neutrons so as to maintain the center of mass system of the whole system. The result supports the existence of the dineutron correlation in ^{11}Li, even though the interpretation strongly depends on nuclear models.
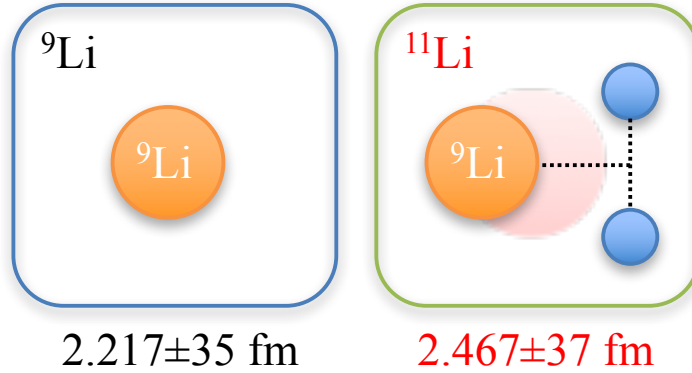
Figure 1.3: Schematic view of spatial configurations of Li isotopes. The orange and the blue circles represent ^{9}Li and neutrons, respectively. The numbers denote the r.m.s. charge radii obtained by employing the laser spectroscopy techniques [33].

1.2 Studies on ^{11}Li through nuclear reactions

With the development of the radioisotope (RI) beam facilities, it has become possible to study the dineutron correlation by using nuclear reactions. It was triggered by the discovery of the neutron halo structure in ^{11}Li through the measurement of the interaction cross section [36, 37]. Since then, the dineutron correlation in ^{11}Li has been investigated through various kinds of physical quantities obtained using nuclear reaction, as listed in Table 1.2.

   In the following subsections, first, an opening angle of two neutrons is introduced as a good measure of dineutron correlation in Sec. 1.2.1. Experimental evidences of the dineutron

Table 1.2: List of physical quantities measured for the study of the ^{11}Li nucleus.

Physical quantity	Reactions
$E1$ transition strength	Coulomb breakup
Neutron momentum	Neutron removal induced by a nuclear target
	Quasi-free neutron knockout

correlation are reviewed: the $B(E1)$ measurement in Sec. 1.2.2, the momentum measurement in Sec. 1.2.3. Finally, the present knowledge is summarized in Sec. 1.2.4.

1.2.1 Opening angle as a measure of dineutron correlation

Employing the three-body model, one can define an opening angle as a measure of the dineutron correlation. Figure 1.4 shows a schematic view of ^{11}Li composed of two valence neutrons and a ^{9}Li core. When the dineutron correlation is developed, the opening angle between two neutrons with respect to the core θ_V^x gets closer to 0 degrees. The smaller opening angle shows the enhancement of the dineutron correlation. It should be noted that the opening angle is 90 degrees when the BCS-type correlation appears or two neutrons have no spatial correlation. There are two conventions of the coordinate, so-called Y and V to represent the three-body system. Depending on the choice of the coordinate system, we call the opening angle θ_Y^x or θ_V^x. The definition of the coordinates is described in Sec. 2.3.
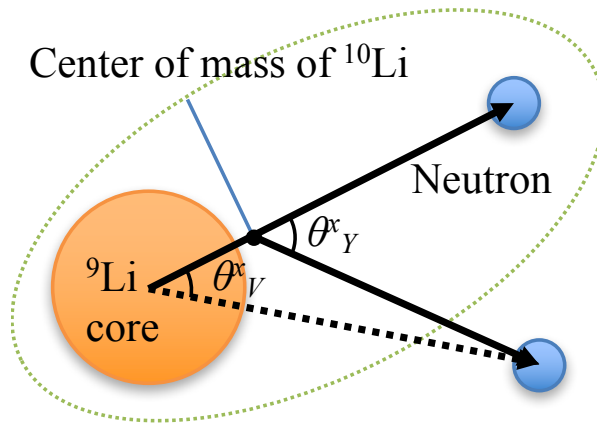
Figure 1.4: Schematic view of the ^{11}Li nucleus by employing the three-body model. The orange and the blue circles represent a ^{9}Li core and two valence neutrons, respectively. Two different definitions of the opening angles θ_Y^x and θ_V^x are shown. See the text for details.

1.2.2 $B(E1)$ measurement

Strong soft electric dipole ($E1$) excitation is a characteristic phenomenon of halo nuclei, where significant $E1$ transition strength $B(E1)$ appears at lower excitation energy. With the help of the

cluster sum rule of the transition strength, this excitation mode has long been used as a tool to investigate the dineutron correlation in the ground state [38, 39].

The Coulomb breakup cross sections have been extensively measured so far for the determination of the $B(E1)$ value [40–54]. In the most recent work at RIKEN [40], the Coulomb breakup cross section of ^{11}Li in the relative energy region of $E_{\text{rel}} \leq 3$ MeV, was obtained with a lead target. The obtained spectrum is shown in the left panel of Fig. 1.5. Strong soft $E1$ excitation was observed at about 0.6 MeV with $B(E1) = 1.42 \pm 0.18$ e^2fm^2. By employing the $E1$ cluster sum rule, the opening angle of the two neutrons in ^{11}Li was determined as $\langle \theta_V^x \rangle = 48^{+14}_{-18}$ degrees. The obtained opening angle was significantly smaller than 90 degrees expected for non-correlated two neutrons. Thus, strong dineutron correlation in ^{11}Li was suggested.
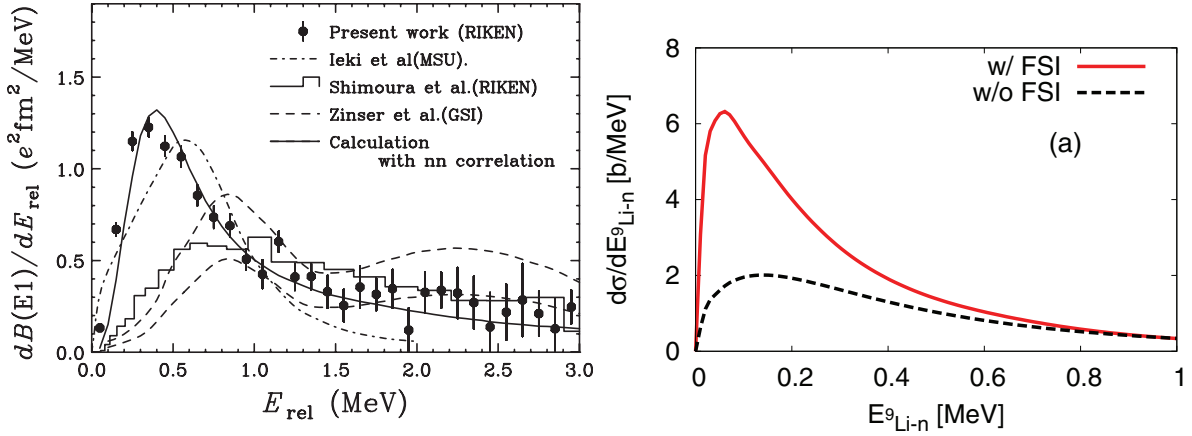
Figure 1.5: (Left) $B(E1)$ distribution from ^{11}Li + Pb at 70 MeV/nucleon. Taken from Ref. [40]. (Right) Calculated cross section of ^{9}Li + n system. The red solid and the black dashed curves show calculated cross sections with the final-state interaction (FSI) and those without the FSI, respectively. Taken from Ref. [23].

However, it has been shown that the measurement has uncertainties in extracting the information on the geometrical configuration of valence neutrons. Recent theoretical study [22, 23] indicated that the low-lying peak in the cross section is governed by final-state interactions (FSIs) and by the sequential decay via the core + n resonance. The right panel of Fig. 1.5 shows the calculated invariant mass spectrum, which is related to the $E1$ strength, with and without the FSIs. The shape of the $E1$ strength distribution is drastically changed with the presence of the FSIs. We note that the total $E1$ strength does not change even with the FSI; the existence of the FSI only affects the shape of the distribution. Experimentally, the total $E1$ cluster sum-rule strength is determined by the extrapolation from the measured strength in the lower energy region, because the experimental acceptance for the $E1$ strength is limited in the higher energy region. In the case of Ref. [40], the Coulomb breakup cross section was measured up to 3 MeV. The drastic change on the shape of the $E1$ strength must impact on the evaluation, resulting in

an unexpected large systematic uncertainty.

The other uncertainties come from the unbound core states. In the cluster sum rule, the core nucleus is assumed to be inert. This assumption is reasonable in the case of ^{6}He because the first excited state of the ^{4}He core is located above 20 MeV. However, it is not the case with ^{11}Li, because the ^{9}Li core can be easily excited; The first excited state is located at 2.7 MeV. Kikuchi *et al.* [23] showed that the sum rule value should be reduced by about 15% due to the ^{9}Li core excitation. By taking account the reduction, the opening angle $\langle\theta_V^x\rangle$ evaluated from the data in Ref. [40] changes from 48^{+14}_{-18} degrees to 65 ± 11 degrees. This drastic change suggests a large model uncertainty or dependence in this method.

Bertulani and Hussein [55] proposed to use a different r.m.s. neutron-neutron distance, which was derived by employing the two-neutron correlation function [56]. They obtained the opening angle of $\langle\theta_V^x\rangle = 66^{+22}_{-18}$ degrees from the data in Ref. [40]. Hagino and Sagawa [57, 58] showed that the effect of Pauli forbidden transitions [59] slightly changes the opening angle as $\langle\theta_V^x\rangle = 65.2^{+11.4}_{-13.0}$ degrees. Although the core excitation was not explicitly taken into account in these analyses, the obtained opening angles unexpectedly agreed with the value discussed above. It implies the theoretical interpretation on the $B(E1)$ measurement via the Coulomb breakup reaction has still not been finalized.

1.2.3 Momentum measurement

The neutron momentum distribution provides the most direct information on the spatial distribution of the valence neutrons [11].

By removing one of the two valence neutrons from ^{11}Li, the remaining system composed of a ^{9}Li core and a neutron immediately decays into two because of the Borromean nature. The momentum vectors of all the particles are measured so that the neutron momentum distribution is reconstructed.

There are two different kinds of probes for this method: a nuclear target such as a carbon and a proton target. These are described in the following subsections.

Neutron removal reaction with nuclear target

A carbon target was used in the neutron momentum measurement conducted at the GSI [60, 61]. In this experiment, the momenta of the removed neutron and of the target were not measured. The contributions of *s*- and *p*-orbits in the ground state were discussed by using the reconstructed angular distributions of the removed neutrons. The opening angle was determined as $\langle\theta_Y^x\rangle = 76.6 \pm 2.1$ degrees. This result supported the dineutron correlation in ^{11}Li. We note that the obtained opening angle is defined in *Y*-coordinates and cannot be directly compared with that defined in *V*-coordinates used in the analysis of $B(E1)$ measurements.

As is the case with the $B(E1)$ measurement, there are difficulties in deducing the opening

angle by employing the carbon-induced neutron removal reaction: the peripherality of the probe and the complexity of the reaction mechanism. These are explained in detail in Sec. 2.2.1.

Neutron knockout reaction with proton target

The proton-induced knockout reaction is more transparent and more simple than the removal reaction using the nuclear target. It is considered as one of the best probe to study the neutron-neutron correlation (Sec. 2.2).

A pioneering experiment was performed at GSI by using a liquid hydrogen target [62–64]. In this experiment, momentum of the knocked-out neutron was not measured. The data were analyzed in a similar way to the Refs. [60, 61]. However, for some unknown reasons, the opening angle distribution was not given.

1.2.4   Summary of knowledge

As described above, there have been extensive studies to search for dineutron correlation in ^{11}Li. From an experimental point of view, most studies supported the existence of the dineutron correlation in ^{11}Li. However, no studies could provide the spatial distribution of two neutrons in ^{11}Li, but only an "integrated" measure of the dineutron correlation. Moreover, the obtained opening angle, the measure of the dineutron correlation, was not consistent between different studies. For the further study, it is inevitable to consider following points which might cause uncertainties in the interpretation of the data.

Effect of the FSI.
  The asymptotic momentum, which is observed experimentally, can be largely changed from that in the ground state by the effect of the FSI [22, 23].

Contributions of components with high angular momentum.
  Catala *et al.* [24] demonstrated that an admixture of configurations of single-particle orbits with different parities plays a significant role to form the spatial localization. In the case of the ^{11}Li, the single-particle orbits with angular momentum of $\ell \geq 2$ is essential to form the dineutron correlation, even though their contributions in the ^{11}Li nucleus are expected to be 10% at most [65].

Core excitation.
  A part of the ^{9}Li core in the ground-state ^{11}Li nucleus is considered to be excited [23, 66]. The core excitation changes the spatial configuration of the two valence neutrons through the Pauli blocking between the excited neutron in the core and the valence neutrons.

1.3 Thesis objectives

The purpose of this thesis is to investigate the spatial distribution of two valence neutrons in ^{11}Li via the quasi-free (p, pn) reaction at 246 MeV/nucleon followed by the neutron emission. We selected the Borromean nucleus ^{11}Li as the target because the dineutron correlation is considered to be strongly developed in this system. We employed the quasi-free (p, pn) reaction followed by the neutron emission because of the simplicity of the reaction mechanism, the minimization of the FSIs, and the transparency. This is the first kinematically complete measurement on ^{11}Li via the quasi-free (p, pn) reaction. The experiment was performed at the Radioactive Isotope Beam Factory (RIBF) in RIKEN, where an intense ^{11}Li beam at intermediate energy and the thick proton target MINOS are available. The dedicated (p, pn) setup was newly constructed and combined with the SAMURAI spectrometer having a large acceptance and a multiple particle detection capability so as to realize the kinematically complete measurement.

The thesis is organized as follows: This chapter has provided a scientific background and motivation of this work. In Chap. 2, we describe the quasi-free (p, pn) reaction followed by the neutron emission, which is the key idea of this study. We then explain the requirements of this experiment. In Chap. 3, we describe the details of the experiment: the experimental facilities, the detectors, and the setup. In Chap. 4, we present the details of the detector calibration and performances. In Chap. 5, we present the details of the data analysis. In Chap. 6, we report the experimental results; we present the invariant mass, the internal momentum, and the opening angle distributions. We compare the results with previous works and theoretical calculations. Finally, in Chap. 7, we conclude this thesis.

The author is one of the spokespersons of the present experiment [67]. He led the collaboration from the planning phase, through the preparation and the beam time, and also in the analysis phase. He developed new method for the study of the neutron-neutron correlation, the quasi-free (p, pn) reaction followed by the neutron emission. He conducted the design and arrangement for all part of the experiment. He designed the supporting frame of the MINOS device for the coupling with the SAMURAI spectrometer. He newly designed two important detector sets, the recoil proton detector RPD and the knocked-out neutron detector array WINDS. He optimized the resolution and the detection efficiency including the geometrical acceptance. He arranged the new configuration of the gamma-ray detector array DALI2 to maximize the acceptance of recoil particle detectors. He designed the secondary beam production; The reduction of triton contaminant in the secondary beam was crucial in the present experiment. He constructed the active collimator ACOL and the beam veto BV so as to stop and to reject the tritons and unwanted beam particles. He rearranged the electronic circuit so as to install new detectors. He newly developed an auxiliary program to control the data acquisition system. Most of the analysis of the experimental data including the Monte-Carlo based simulation were done by the author, except for (i) the time projection chamber (TPC) of the MINOS, (ii) the gamma-ray detector array DALI2, and (iii) the part of the calibration of the neutron detector array NEBULA.

Chapter 2

Experimental approach

In this work, the quasi-free (p, pn) reaction was employed to study the dineutron correlation in the Borromean nucleus ^{11}Li. This chapter describes our idea how we can approach the neutron-neutron correlation, why we selected the quasi-free (p, pn) reaction, and what is required for realizing the experiment; Sec. 2.1 explains our approach to the neutron-neutron correlation. Sec. 2.2 describes the method we employed: the quasi-free (p, pn) reaction followed by the neutron emission. Sec. 2.3 describes the definition of the coordinates used in this work. Finally, Sec. 2.4 lists the requirements for the present experiment.

2.1   Our approach to neutron-neutron correlation

The neutron-neutron correlation can be fully investigated by determining the spatial distributions of two valence neutrons in the ground state. However, it is experimentally difficult to measure the positions of two neutrons in the ground state at the same time because the FSIs take place in the decay process. In this thesis, we approached the spatial distributions of two valence neutrons in ^{11}Li by dividing the problem into two:

- Measurement of the one-neutron ground-state momentum and

- Spectroscopy of the ^{9}Li + n subsystem.

The one-neutron momentum distribution in the ground state provides the most direct information on the spatial distribution of the valence neutron of ^{11}Li [11]. On the other hand, the structure of the ^{9}Li + n subsystem gives information on the interaction between a ^{9}Li nucleus and a neutron, which is essential to describe ^{11}Li, the ^{9}Li + n + n system. By combining all the information (kinematically complete measurement), the spatial distribution of two neutrons are reconstructed as an opening angle distribution without losing the correlation information among them.

11

2.2 The quasi-free (p, pn) reaction followed by the neutron emission

This section describe the quasi-free (p, pn) reaction followed by the neutron emission. This reaction has positive attributes due to the simplicity of the reaction mechanism, the minimization of the FSIs, the capability of the kinematically complete measurement, and the transparency. These are described in the following subsections.

A conceptual diagram of the reaction is shown in Fig. 2.1. One of the valence neutrons is knocked out by the probe proton. Thanks to the quasi-free scattering picture (Sec. 2.2.1), the motion between the knocked-out neutron and the residual can be well separated from that in the residual nucleus, and thus the reaction is hardly affected by the three-body FSI (Sec. 2.2.2). After the occurrence of the quasi-free (p, pn) reaction, the reaction residue immediately decays due to the Borromean nature. Therefore, it is possible to measure momentum vectors of all the constituents at the same time (Sec. 2.2.3). It should be noted that the quasi-free (p, pn) reaction is transparent so that one can probe the whole volume of the nucleus (Sec. 2.2.4).
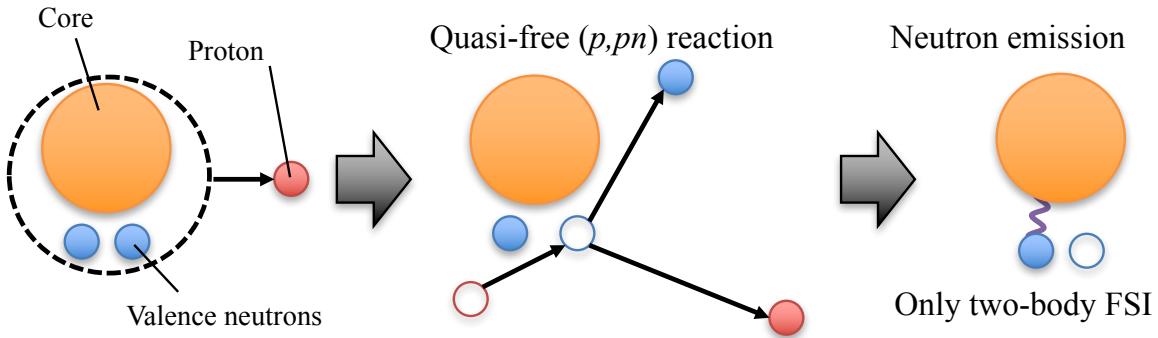
Figure 2.1: Conceptual diagram of the quasi-free (p, pn) reaction followed by the neutron emission. The orange, the blue, and the red circles represent a core nucleus, valence neutrons, and a probe proton, respectively. See the text for details.

2.2.1 Simple reaction mechanism: quasi-free knockout

The measurement of the one-neutron ground-state momentum is one of the most crucial part of this work. One can reliably reconstruct the momentum distribution by employing the quasi-free (p, pn) reaction.

The quasi-free (p, pn) reaction is one of the specific case of the quasi-free knockout reactions. The electron-induced proton knockout $(e, e'p)$ reaction is known as one of the most reliable spectroscopic tool [68]. However, it is hardly applicable to the neutron knockout because neutrons have no electric charge. Therefore, the proton-induced nucleon knockout (p, pN)

reaction, where the nucleon-nucleon interaction takes place, becomes the best tool especially for the study of the neutron single-particle properties [69, 70].

The (p, pN) reaction can be quite simply described. Figure 2.2 shows a schematic view of the (p, pn) reaction in the normal kinematics. The incident proton knocks a neutron out of a target nucleus. Because the mean free path of nucleons in nuclear matter is same order of magnitude as the nuclear radius at the intermediate energy (100–1000 MeV) [71], the reaction is regarded as the quasi-free scattering (QFS) between the incident proton and the knocked-out neutron. Thanks to the simple kinematics, the missing momentum $\boldsymbol{k}$ is obtained owing to the momentum conservation law as

$$\boldsymbol{k} = \boldsymbol{p}'_n + \boldsymbol{p}'_p - \boldsymbol{p}_p. \tag{2.1}$$
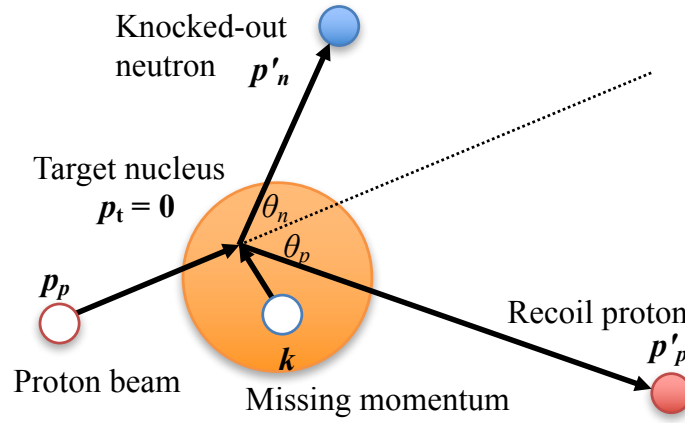
Figure 2.2: Schematic view of the (p, pn) reaction in the normal kinematics in the laboratory frame. The orange, the blue, and the red circles represent a target nucleus, a knocked-out neutron, and a probe proton, respectively. Momentum vectors of corresponding particles are shown by bold italic letters.

The (p, pN) reaction in normal kinematics has been well studied and sophisticated [72] at the Research Center for Nuclear Physics (RCNP), Osaka University. It has been shown that the knockout process is well described within a framework based on the Distorted Wave Impulse Approximation (DWIA) calculation [69]. The spectroscopic factors obtained by the $(p, 2p)$ reaction agree with those determined by the $(e, e'p)$ reaction with typically 20% accuracy. The multipole decomposition analysis is possible to decompose the angular momentum.

QFS condition

The QFS condition guarantees the validity of the QFS picture in the knockout reaction. As described in the previous section, the QFS picture is essential in the (p, pn) reaction. The momentum transfer is a good barometer to confirm the QFS picture. The QFS picture is valid as

far as the momenta of incoming and outgoing nucleons are larger than those of typical nucleons. In the nucleus rest frame, the nucleon has a finite momentum distribution (missing momentum) due to the Fermi motion. The QFS condition can be satisfied by selecting the momentum transfer much larger than the missing momentum. The averaged missing momentum is 1.3 fm^{-1} in the case of well-bound nuclei [73]. Therefore, the momentum transfer of 2–2.5 fm^{-1} is needed. On the other hand, the missing momentum in weakly bound nuclei is much smaller due to large spatial distribution. The averaged missing momentum of ^{11}Li is 0.5 fm^{-1} as we shall see later (Sec. 5.14). In such a case, the momentum transfer of larger than 1 fm^{-1} is considered to be enough for the QFS condition.

Comparison with neutron removal reaction using the nuclear target
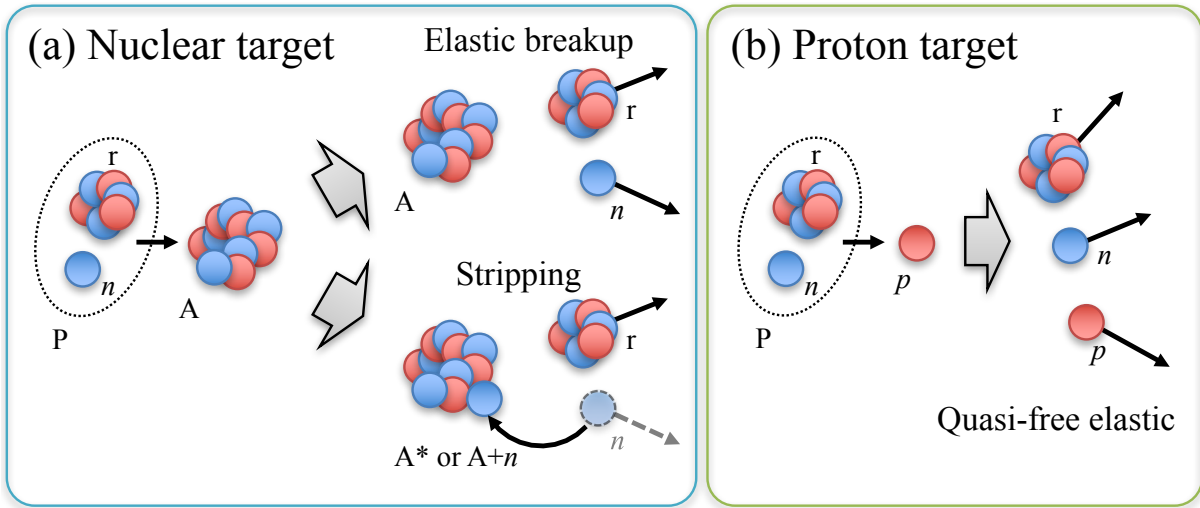
Figure 2.3: Schematic view of three kinds of processes in the neutron removal reactions (a) with a nuclear target and (b) with a proton target. The blue and the red circles represent neutrons and protons, respectively. The groups of nucleons indicated by "P", "A", and "r" represent a projectile, a target nucleus, and a residue, respectively.

There is the other kind of knockout reaction, the so-called removal reaction induced by the nuclear target. This reaction has been commonly used for the study of the single-particle properties [74]. Technically, the treatment of the nuclear target is much easier than that of the proton target. Moreover, the cross section of the nuclear-target-induced removal reaction is much larger than that of the proton-induced knockout reactions. However, the reaction mechanism in the removal reaction is more complex than that in the proton-induced knockout reaction. Figure 2.3 shows the reaction mechanisms in the neutron removal and knockout reactions. Two different kinds of processes can contribute to the removal reactions: the elastic breakup and the stripping processes. In the elastic breakup process, the projectile (P) breaks into a neutron (n) and a residue (r) by exchanging the momentum with a target nucleus (A). Some theoretical

models are available to describe this process, such as the Continuum-Discretized Coupled-Channel (CDCC) method [75, 76], the Dynamical Eikonal Approximation (DEA) [77, 78], the Faddeev–Alt-Grassberger-Sandhas (Faddeev–AGS) theory [79, 80], etc. On the other hand, in the stripping process, the residue and the target nucleus are excited and sometimes the neutron is picked-up by the target nucleus. Although the Glauber model [81] based on the Eikonal reaction theory (ERT) and adiabatic approximations has been developed [82, 83] for this process, the formulation of the parallel momentum distribution (PMD) of residual nucleus and the differential cross sections is not completed [84]. These processes are competitive and it makes the representation complicated [85].

2.2.2 Minimization of the FSIs

We explain the effect of the FSIs by taking the Coulomb breakup reaction as an example. Figure 2.4 shows a conceptual diagram of the Coulomb breakup reaction. A high-Z target, such as a lead, is used in this method to break the system by exciting the $E1$ transition in the nucleus. After the breakup, momentum vectors of all the decay particles can be measured. However, in the transient region, the FSIs between three constituents take place. Due to the three-body FSI, the observed momentum vectors in the final state (k'_{n1}, k'_{n2}, and k'_r) cannot be traced back to those in the initial state (k_{n1}, k_{n2}, and k_r). In other words, the momentum distribution in the initial state is smeared and at least partly lost in the reaction.
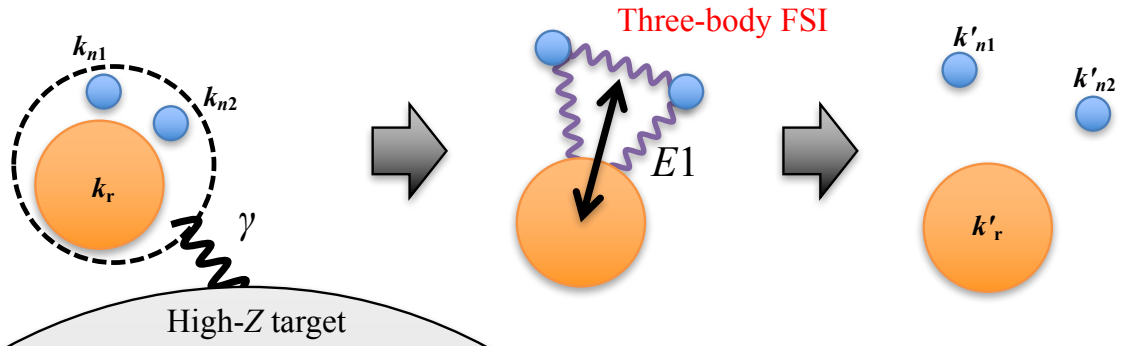
Figure 2.4: Conceptual diagram of the Coulomb breakup reaction. The orange and the blue circles represent a core nucleus and valence neutrons, respectively. Momentum vectors of corresponding particles are shown by bold italic letters.

It should be emphasized that the suppression of the *three-body* FSI is crucial in the present experiment; In the presence of the three-body FSI, energies and momenta can be exchanged among two-body subsystems and thus the their correlations in the initial state can be easily lost. This does not take place in the two-body FSIs; It can be fully described by the Lippmann-Schwinger equation.

As described in Sec. 2.2.1, the quasi-free (p, pn) reaction enables one to remove one of

the valence neutrons in Borromean nuclei without interference in the remaining constituents. Then, only the two-body FSI takes place in the decay process, and therefore, the initial-state information can be extracted.

2.2.3   Kinematically complete measurement

The kinematically complete measurement, the measurement of all the particles involved in the reaction, is required in this work so as to reconstruct the neutron momentum distribution without any uncertainties. In addition, it is also important to investigate the contributions of core excitation component in the ground-state ^{11}Li [23].

Use of the proton target is essential for the kinematically complete measurement. The momentum transfer q and the energy transfer ω can be determined event by event without any uncertainties. One can reconstruct all the momentum vectors without any assumptions.

2.2.4   Transparency

For measuring the momentum distribution, it is important to use the transparent probe so as to investigate the neutron-neutron correlation over the whole nuclear volume. The quasi-free (p, pn) reaction is more transparent than the Coulomb breakup reaction as well as the neutron removal reaction induced by the nuclear target. Coulomb breakup reaction is peripheral because the operator of the Coulomb interaction is proportional to r^n with $n \geq 1$ [86]. In the case of the neutron removal reaction, a strong absorption from the nuclear target takes place. Recent theoretical calculation showed that the strength of the absorption from the nuclear target is 10 times larger than that from the proton target in the case of ^{6}He [73]. Only the quasi-free (p, pn) reaction can probe deeply into inner part of the nucleus.

2.3   Definition of coordinates

In the present study, the spatial correlation of three-body system (two neutrons and a core nucleus) is discussed. For the description of such a system, it is convenient to introduce so-called Jacobi coordinates based on the hyper-spherical basis [87]. Figure 2.5 shows schematic view of the definition of variables. In the beam rest frame, the positions of the ^{9}Li core, the knocked-out neutron, and the decay neutron are denoted as $\boldsymbol{r_r}$, $\boldsymbol{r_{n1}}$, and $\boldsymbol{r_{n2}}$, respectively. The relative position vectors $\boldsymbol{R_Y}$ and $\boldsymbol{r_Y}$, and the opening angle in position space θ_Y^x are defined in

Jacobi coordinates as

$$R_Y = r_{n2} - r_{\mathrm{r}}, \tag{2.2}$$

$$r_Y = r_{n1} - \frac{m_{\mathrm{r}} r_{\mathrm{r}} + m_n r_{n2}}{m_{\mathrm{r}} + m_n}, \tag{2.3}$$

$$\cos \theta_Y^x = \frac{R_Y \cdot r_Y}{|R_Y||r_Y|}, \tag{2.4}$$

where m_n and m_{r} represent the masses of the neutron and the ^{9}Li core, respectively. In a similar way, the relative momentum vector K_Y and the internal momentum vector k_Y, and the opening angle in momentum space θ_Y are defined as follows:

$$K_Y = k_{n2} - k_{\mathrm{r}}, \tag{2.5}$$

$$k_Y = k_{n1} - \frac{m_{\mathrm{r}} k_{\mathrm{r}} + m_n k_{n2}}{m_{\mathrm{r}} + m_n}, \tag{2.6}$$

$$\cos \theta_Y = \frac{K_Y \cdot k_Y}{|K_Y||k_Y|}. \tag{2.7}$$

The opening angles in so-called V-coordinates are also used historically for describing the dineutron correlation [25, 40]. They are defined as

$$\cos \theta_V^x = \frac{R_Y \cdot (r_{n1} - r_{\mathrm{r}})}{|R_Y||r_{n1} - r_{\mathrm{r}}|}, \tag{2.8}$$

$$\cos \theta_V = \frac{K_Y \cdot (k_{n1} - k_{\mathrm{r}})}{|K_Y||k_{n1} - k_{\mathrm{r}}|}. \tag{2.9}$$

Figure 2.5(b) shows the definition of the momentum vectors of all the particles in the laboratory frame. The momentum vectors of the ^{11}Li beam $\tilde{p}_{\mathrm{b}}$ and the proton target p_{t} are defined before the occurrence of the reaction, while those of the recoil proton $\tilde{p}_p$, the knocked-out neutron p_{n1}, the decay neutron p_{n2}, and the ^{9}Li heavy fragment $\tilde{p}_{\mathrm{r}}$ are defined after the occurrence of the reaction.

The Lorentz transformation between the beam rest frame and the laboratory frame is defined by using the momentum vector of the ^{11}Li beam $\tilde{p}_{\mathrm{b}}$.

(a) Beam rest frame

(In coordinate space)   (In momentum space)
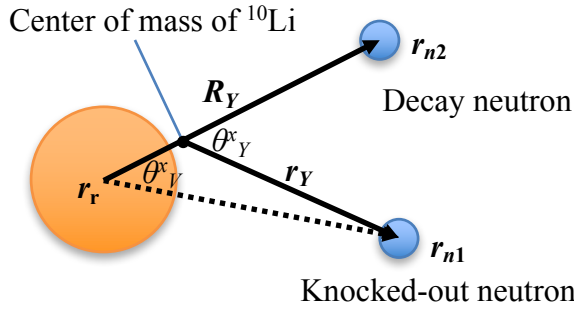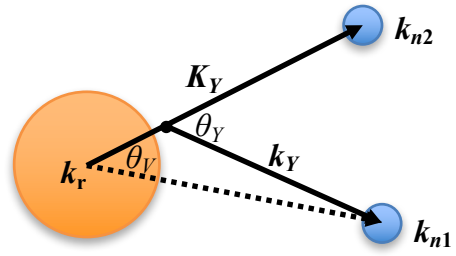
(b) Laboratory frame (in momentum space)
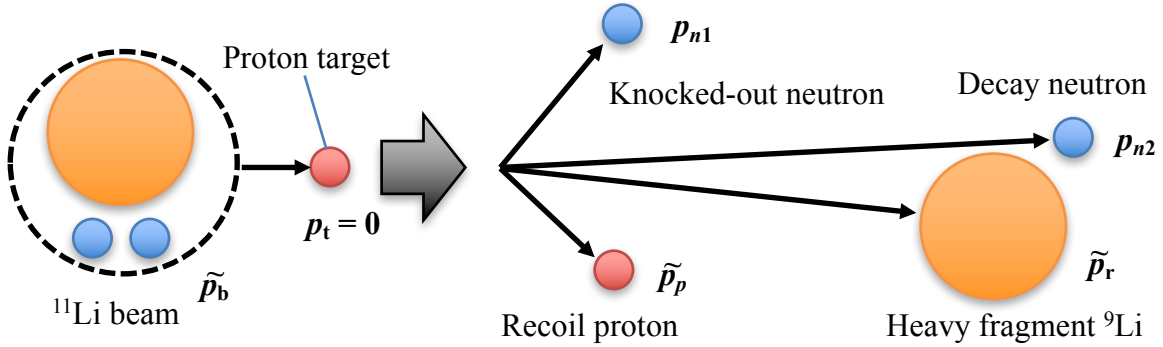
Figure 2.5: Schematic view of the definition of variables. (a) Position and momentum vectors of the three constituents of ^{11}Li. Relative position vectors ($\boldsymbol{R_Y}$ and $\boldsymbol{r_Y}$), a relative momentum vector ($\boldsymbol{K_Y}$), and an internal momentum vector ($\boldsymbol{k_Y}$) are defined. Opening angles between these vectors are also defined (θ_V^x and θ_Y^x for the position space, θ_V and θ_Y for the momentum space). (b) Momentum vectors of all the particles in the laboratory frame. They are defined at the reaction point, just before and just after an occurrence of the quasi-free (p, pn) reaction.

2.4 Experimental requirements

As discussed, the quasi-free (p, pn) reaction followed by the neutron emission is the best suited probe for the study of the dineutron correlation. Herein we summarize the experimental requirements for applying this method to the Borromean nucleus ^{11}Li.

Inverse kinematics.
> ^{11}Li has a short half life of 8.75 ms. Thus, the quasi-free (p, pn) reaction should be performed with ^{11}Li as the energetic projectile and a proton as the stationary target.

Intermediate energy.
> The intermediate energy (100–1000 MeV) is best suited for the (p, pn) reaction, where the QFS picture is valid.

High luminosity.
> High statistics measurement is required for the decomposition of the single-particle orbits with higher angular momentum.

> The cross section of the quasi-free (p, pn) reaction is smaller by 1–2 orders of magnitude than those of the other reactions discussed above. Measured cross sections of those reactions on ^{11}Li are summarized in Table 2.1. The cross section of the Coulomb breakup reaction is the largest because the reaction is caused by the electromagnetic interaction. The cross section of the quasi-free (p, pn) reaction is smaller than that of the neutron removal reaction because only one probe proton contributes to the neutron knockout in the former case, while more than one nucleons of a target nucleus contribute to the neutron removal in the latter case.

> In order to achieve a high luminosity, a high-intense beam and a thick proton target are needed.

Table 2.1: Integrated cross sections of different reactions on ^{11}Li.

Reaction	Energy [MeV/nucleon]	Integrated cross section σ [b] for $E_{\mathrm{rel}} \leq 3$ MeV	for $E_{\mathrm{rel}} \leq 6$ MeV
Coulomb breakup [40]	70	$2.34 \pm 0.05(\mathrm{stat}) \pm 0.28(\mathrm{syst})$	(not given)
Neutron removal [61]	264	0.15^a	(not given)
Quasi-free (p, pn) [64]	280	0.035^a	0.041^a

^{a} Data were read from figures in the articles.

Kinematically complete measurement.
> For reconstructing the neutron momentum distribution, it is needed to determine the momentum vectors of all the particles without any assumptions such as the inert core.

It is inevitable to detect all the particles involved in the reaction including gamma-rays simultaneously.

In summary, the following four requirements should be satisfied practically:

1. High-intensity, intermediate-energy ^{11}Li beam,

2. Thick liquid hydrogen target,

3. Large acceptance spectrometer having multiple particle detection capability, and

4. Dedicated (p, pn) setup.

These are simultaneously available only at the RI Beam Factory at RIKEN; The accelerator complex and the following BigRIPS separator can provide a high-intensity ^{11}Li beam at intermediate energy. Thick liquid hydrogen target MINOS is available at RIKEN. The SAMURAI spectrometer has a large acceptance and a multiple particle detection capability, as well as a flexibility to be combined with the (p, pn) setup newly constructed for this study. Therefore, we performed the present experiment at the RIBF.

Chapter 3

Experiment

In this chapter, the experimental setup is described in detail. The kinematically complete measurement for the quasi-free (p, pn) reaction followed by the neutron emission on the Borromean nucleus ^{11}Li was performed at Radioactive Isotope Beam Factory (RIBF) in RIKEN by using the SAMURAI spectrometer. This measurement required high luminosity to have as much statistics as possible. For this purpose, very thick liquid hydrogen target MINOS was used with a high intense ^{11}Li beam. The (p, pn) setup and auxiliary detectors were newly constructed and combined with the SAMURAI standard detectors for realizing the kinematically complete measurement.

The RIBF facility is introduced in Sec. 3.1. The acceleration of a ^{48}Ca primary beam is explained in Sec. 3.2. The production of a ^{11}Li secondary beam in the BigRIPS is described in Sec. 3.3. The beam transport to the experimental room is presented in Sec. 3.4. Section 3.5 describes overview of the SAMURAI setup. The SAMURAI spectrometer is explained in Sec. 3.6. The MINOS device is described in Sec. 3.7. The recoil particle detectors, the recoil proton detector RPD and the knocked-out neutron detector array WINDS are described in Sec. 3.8 and Sec. 3.9, respectively. The gamma-ray detector array DALI2 is shown in Sec. 3.10. The neutron detector array NEBULA is explained in Sec. 3.11. The electronic circuits for triggering and the data acquisition system are explained in Sec. 3.12. The experimental conditions are summarized in Sec. 3.13.

3.1   RIKEN RI Beam Factory

The Radioactive Isotope Beam Factory (RIBF) in RIKEN provides the world's most intense ion beams over a wide range of elements. Figure 3.1 shows a bird's-eye view of the RIBF. The region enclosed with blue lines shows the RIKEN accelerator complex. The BigRIPS separator is shown by the green rectangle. The experimental room for the present study is indicated by the orange rectangle. The red curved line shows the beam course used in the present experiment from the ion source to the secondary target.

21
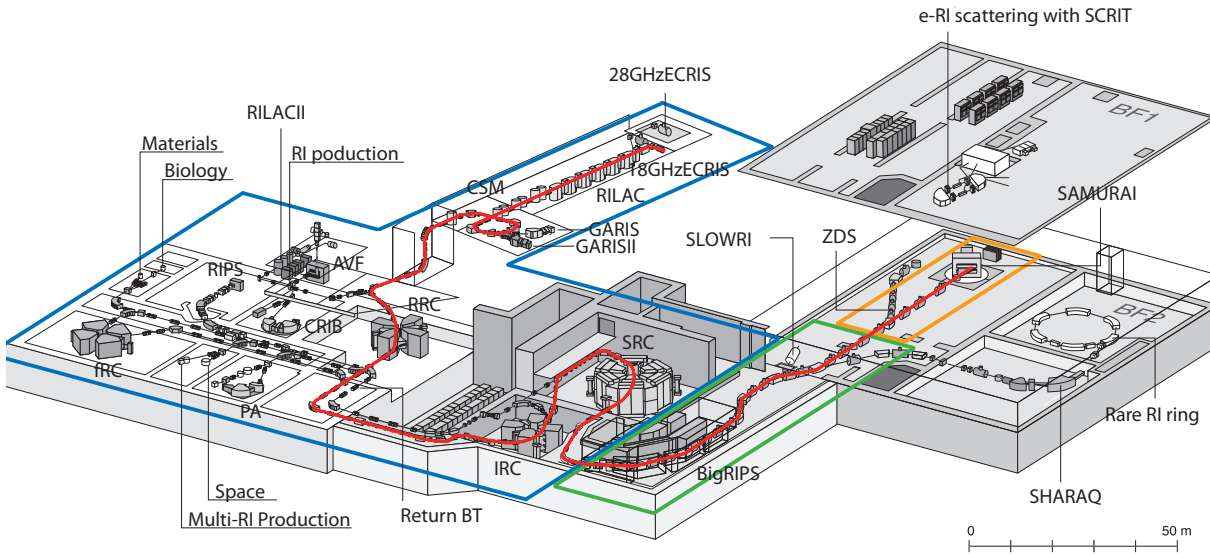
Figure 3.1: Bird's-eye view of the RIBF. The red curved line represents the beam course used in the present experiment. The regions enclosed with blue, green, and orange lines shows the RIKEN accelerator complex, the BigRIPS separator, and the experimental room, respectively.

The accelerator complex was used to provide a ^{48}Ca primary beam at 345 MeV/nucleon. The BigRIPS separator provided secondary beam particles produced from the ^{48}Ca primary beam. From the end of the BigRIPS, the secondary beam was transported onto the liquid hydrogen target in the experimental room, and then, the measurement was performed.

3.2   Acceleration of a ^{48}Ca primary beam

A ^{48}Ca primary beam was accelerated up to 345 MeV/nucleon by the RIBF accelerator complex [88, 89]. The acceleration scheme is shown in Fig. 3.2. A ^{48}Ca^{10+} ion was extracted from the 18-GHz electron cyclotron resonance ion source (ECRIS) [90]. The ion was accelerated up to 2.7 MeV/nucleon by the RIKEN heavy ion linear particle accelerator (RILAC). The accelerated ^{48}Ca^{10+} ion was converted into ^{48}Ca^{16+} ion by the first charge stripper made of a carbon foil. By increasing the valence charge of the ion in the charge stripper, the ion can be accelerated to much higher energy with the same acceleration voltage. The ion was accelerated up to 46 MeV/nucleon by the RIKEN ring cyclotron (RRC). The ^{48}Ca^{16+} ion was again converted into fully-stripped ^{48}Ca^{20+} ion by the second charge stripper made of a carbon foil. The fully-stripped ^{48}Ca was accelerated up to 345 MeV/nucleon by the intermediate-stage ring cyclotron (IRC) and the superconducting ring cyclotron (SRC). All the accelerators were operated with the RF frequency of 35.6 MHz. The beam bunch separation was 28.1 ns. The beam was transported to the production target at F0 focal plane of the BigRIPS. The averaged beam intensity was 400 pnA on the target.
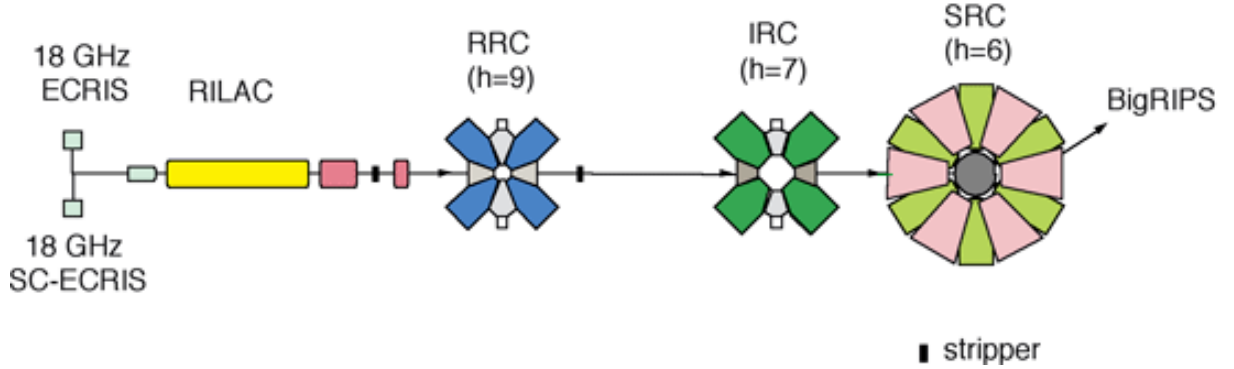
Figure 3.2: Acceleration scheme of the RIBF accelerator complex in variable energy mode [89] for medium-mass ions.

3.3 Production of a ^{11}Li secondary beam

The ^{11}Li secondary beam was produced through the projectile fragmentation reaction from the ^{48}Ca primary beam at 345 MeV/nucleon bombarding on a primary target of ^{9}Be. The secondary beam was purified through the BigRIPS fragment separator [91].

In Sec. 3.3.1, the BigRIPS separator is introduced. The beam line detectors of the BigRIPS are explained in Sec. 3.3.2. Setting parameters of the BigRIPS are summarized in Sec. 3.3.3. The secondary beam used in the present study is contaminated with tritons. Sec. 3.3.4 describes the approach to reduce tritons. The obtained beam intensity and purity are summarized in Sec. 3.3.5.

3.3.1 Fragment separator BigRIPS

The BigRIPS[1] [91] is an in-flight RI beam separator at RIBF RIKEN. Figure 3.3 shows a top view of the BigRIPS. It consists of two stages. The first stage, starting from the primary target station F0, consists of two dipole magnets and four sets of superconducting triplet quadrupole magnets [92], forming the momentum-dispersive (F1) and achromatic (F2) focal planes. The second stage consists of four dipole magnets and eight superconducting triplet quadrupole magnets, forming the five focal planes: an achromatic focal plane (F3), three intermediate dispersive planes (F4, F5, and F6), and a doubly-achromatic focal plane (F7). Wedge-shaped energy degraders made of aluminum are installed at the momentum-dispersive focal planes F1 and F5 so as to improve the isotopic separation.

---

[1]Acronym for "BIG RIken Projectile fragment Separator".
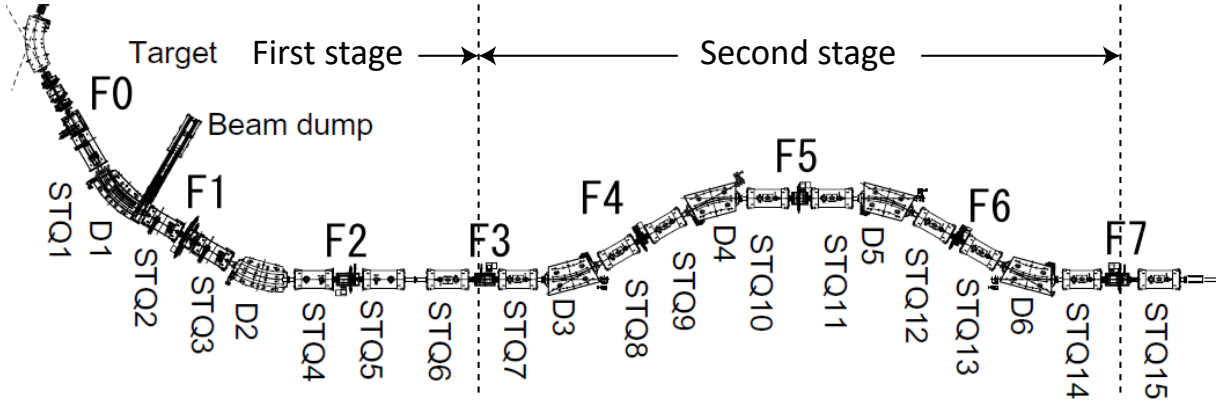
Figure 3.3: Top view of the BigRIPS. D and STQ denote a dipole and a superconducting triplet quadrupole magnets, respectively.

3.3.2 Beam line detectors of BigRIPS

Beam line detectors were installed in the F3, F5, and F7 focal planes, as listed in Table 3.1, so as to obtain the information necessary for the beam tuning as well as the data analysis. The details of the data analysis is given in Sec. 5.1 (the particle identification) and Sec. 5.3 (the momentum analysis).

The plastic scintillators were used to measure the energy loss and the time-of-flight (TOF). The parallel-plate avalanche counters (PPACs) were used to determine the position and the angle of the beam. The beam tuning was performed by using both the plastic scintillators and the PPACs, while the physics run was conducted only by using the plastic scintillators. Below in this subsection, the technical details of the beam line detectors are described.

Table 3.1: List of beam line detectors in the BigRIPS.

Focal plane	Detector	Sensitive area (w mm$\times h$ mm)	Used during Tuning	Physics run
F3	Plastic (3 mm^t)	120×100	○	○
	PPAC	150×150	○	
	PPAC	240×150	○	
F5	Plastic (3 mm^t)	240×100	○	○
	PPAC	240×150	○	
	PPAC	240×150	○	
F7	Plastic (3 mm^t)	120×100	○	○
	PPAC	240×150	○	
	PPAC	150×150	○	

Plastic scintillator

Plastic scintillators were installed at the focal planes F3, F5, and F7 to measure the energy loss and the timing. Each scintillator was made of EJ-230 and had a thickness of 3 mm. The light output was read out by two photomultiplier tubes (PMTs, Hamamatsu H2431-51MOD) attached at both ends of the scintillator. A multichannel power supply CAEN SY2527 was used for providing a high voltage to the PMTs. The typical operation voltage was -1400 V.

The anode signal of the PMT was split into two. One was digitized by using charge-to-digital converter (QDC) modules CAEN V792 to record the charge information of the signal. The other was discriminated by the constant fraction discriminator (CFD) RIS-0330 to generate logic signals, then sent to the time-to-digital converter (TDC) modules CAEN multi-hit TDC V1290 to record the timing information. The width of the logic signal was 50 ns, longer than the bunch separation of 28.1 ns. Since the beam intensity was in the order of 10^6 Hz at F3, about 4.2% of total events had a particle in the neighboring or the same bunches.

Parallel-plate avalanche counters (PPAC)

Two PPACs [93, 94] were installed at the focal planes F3, F5, and F7 to determine the position and the angle of the beam. Each PPAC has two sets of x-axis and y-axis cathode electrodes, which are segmented into strips vertically and horizontally, respectively. The strips were connected in series by delay lines. Signals were read out from both ends of the delay line. An anode signal of the PPAC was amplified by the timing filter amplifier with a gain factor of 12. After the amplification, the signal was sent to the CFD CF8201 to generate logic signals. The timing of the logic signal was recorded by CAEN multi-hit TDC V1190. The position perpendicular to the strip direction was determined from the time difference of the signals. A set of two cathodes with horizontal and vertical strips gives the two-dimensional position information of the incident particles at each PPAC. The angle was determined by combining the position information of two PPACs at each focal plane.

The PPACs were used only for the tuning of the secondary beam production, because the combination of the energy loss and the TOF was enough for the particle identification and the momentum determination. The typical operation voltage was -900 V, resulting the detection efficiency for ^{11}Li particles of 70%. The voltage was not applied during the data run. The PPACs were installed even during the physics run so as not to change the energy loss of the beam particles.

3.3.3 Setting parameters of BigRIPS

The setting parameters of BigRIPS are summarized in Table 3.2. Two production ^{9}Be targets were used. A water cooling system of the 29.8-mm-thick ^{9}Be target was broken during the experiment due to a rapid change of a thermal load. Then the other ^{9}Be target with a thickness of

19.9 mm was used instead, in the latter half of the beam time. The magnetic fields of the dipole magnets, the thicknesses of the degraders, and the openings of the slits were kept the same so as to minimize the change of the secondary beam profiles. The replacement of the production target did not affect the particle identification nor the momentum analysis.

Table 3.2: Production parameters of the BigRIPS used in the present study.

Items	Thick target	Thin target
F0 target	29.8-mm^t ^{9}Be	19.9-mm^t ^{9}Be
D1 dipole	9.112 Tm	
F1 slit	-120–120 mm	
F1 degrader	9.9 mm^t (center), 12.4 mrad	
D2 dipole	8.9165 Tm	
F2 collimator	Iron blocks (Sec. 3.3.4)	
F2 slit	-20–120 mm	
D3 dipole	9.0695 Tm	
D4 dipole	9.0690 Tm	
F5 slit	50–120 mm	
F5 degrader	7.0 mm^t (center), 5.7 mrad	
D5 dipole	8.9015 Tm	
D6 dipole	8.9270 Tm	
F7 slit	-10–10 mm	

3.3.4   Reduction of triton contaminant

As mentioned above briefly, the secondary beam production in the region of the mass-to-charge ratio A/Z close to 3 may contain a large contaminant of tritons. This is mainly because the production yield of tritons is larger by three orders of magnitude than those of the other nuclei in this A/Z region. In addition, it is hard to stop or to energy-degrade tritons with standard BigRIPS beam line slits and wedges. Tritons cannot be removed at the standard setup of BigRIPS and a large amount of tritons can come along with the ^{11}Li secondary beam.

A total beam rate should be less than a maximum rate where beam line detectors work reasonably. Since we needed to maximize the rate of wanted particles to achieve high statics, we reduced the triton contaminant by employing the two methods below.

One is the installation of a thick collimator just before the standard slit at F2. Figure 3.4 shows a top view of the collimator. The thickness of the collimator was designed as 45 cm so that tritons with energies up to 400 MeV/nucleon are stopped in it. It is noteworthy that the use of a thin slit, as usually done, sometimes increases the triton contaminant; it would not stop tritons but only reduce their energies. As a result, the thin slit would make the energy-degraded tritons intrude into the rigidity domain of wanted secondary beam particles, resulting in producing a large contaminant.
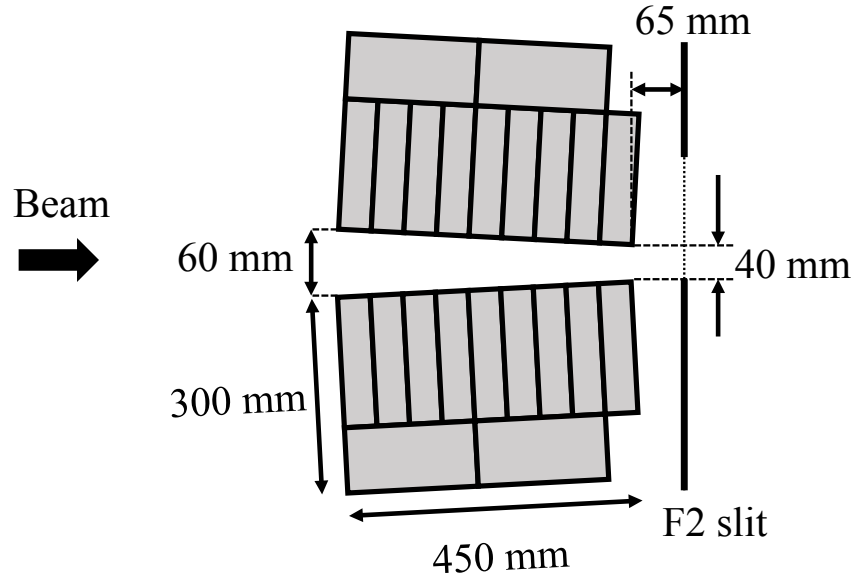
Figure 3.4: Top view of the F2 collimator. The gray shaded boxes represent iron blocks with dimensions of 5 cm $\times$ 10 cm $\times$ 20 cm.

The other is development of an asymmetric beam transport from F3 to F5. The central trajectory of the BigRIPS beam line from F3 to F7 has a symmetric shape with respect to F5 as seen in Fig. 3.3. In the standard setting of BigRIPS, the beam is transported along this central trajectory. However, in this experiment, the magnetic fields of the dipole magnets D3 and D4 were set about 1.7% higher than the nominal values so that the secondary beam was off centered at the F5 focal plane. As a result, tritons having lower rigidity hit the beam pipe from F3 to F5 and were lost.

The contamination of tritons was evaluated as low as 14% of the total beam rate by counting the number of tritons in the SBT beam line plastic scintillators in the experimental room (Sec. 3.6.3). This means that the F2 collimator contributed remarkably to reduce the number of tritons roughly by three orders of magnitude.

3.3.5 Beam intensity and purity

The averaged intensity of the primary beam was 400 pnA. The expected and obtained values of the intensity and purity of the secondary beam particles are summarized in Table 3.3. The secondary beam production was simulated by using the LISE++ [95]. In the simulation, an empirical parameterization for fragmentation cross section (EPAX) 2.15 [96] was used. It was considered to provide reliable cross section for these nuclei. The obtained purity of ^{11}Li was about 70% for both production targets, in good agreement with the expectation. However, the obtained intensity was about one order of magnitude larger than expected.

The details of the particle identification is explained in Sec. 5.1.

Table 3.3: Secondary beam intensity and purity for a 400-pnA primary beam.

Target	Nuclide	Energy [MeV/nucleon]	Expected		Obtained	
			Intensity [s^{-1}]	Purity	Intensity [s^{-1}]	Purity
Thick	^{11}Li	246	1.8×10^4	77%	1.0×10^5	74%
	^{14}Be	265	5.0×10^3	21%	1.8×10^4	13%
	^{17}B	277	5.7×10^2	2.4%	1.0×10^4	7.4%
	^{19}B	224	5.9×10^0	0.02%	7.0×10^1	0.05%
	Total ($Z \geq 3$)		2.4×10^4		1.4×10^5	
Thin	^{11}Li	246	2.4×10^4	70%	1.0×10^5	70%
	^{14}Be	265	8.8×10^3	26%	1.7×10^4	12%
	^{17}B	277	1.2×10^3	3.6%	1.4×10^4	10%
	^{19}B	224	5.1×10^0	0.01%	5.7×10^1	0.04%
	Total ($Z \geq 3$)		3.4×10^4		1.4×10^5	

3.4 Beam transport to a secondary target

The secondary beam was transported from the last focal plane of the BigRIPS (F7) to the location of the secondary target (F13) in the experimental room through the straight beam line, as shown in Fig. 3.5.
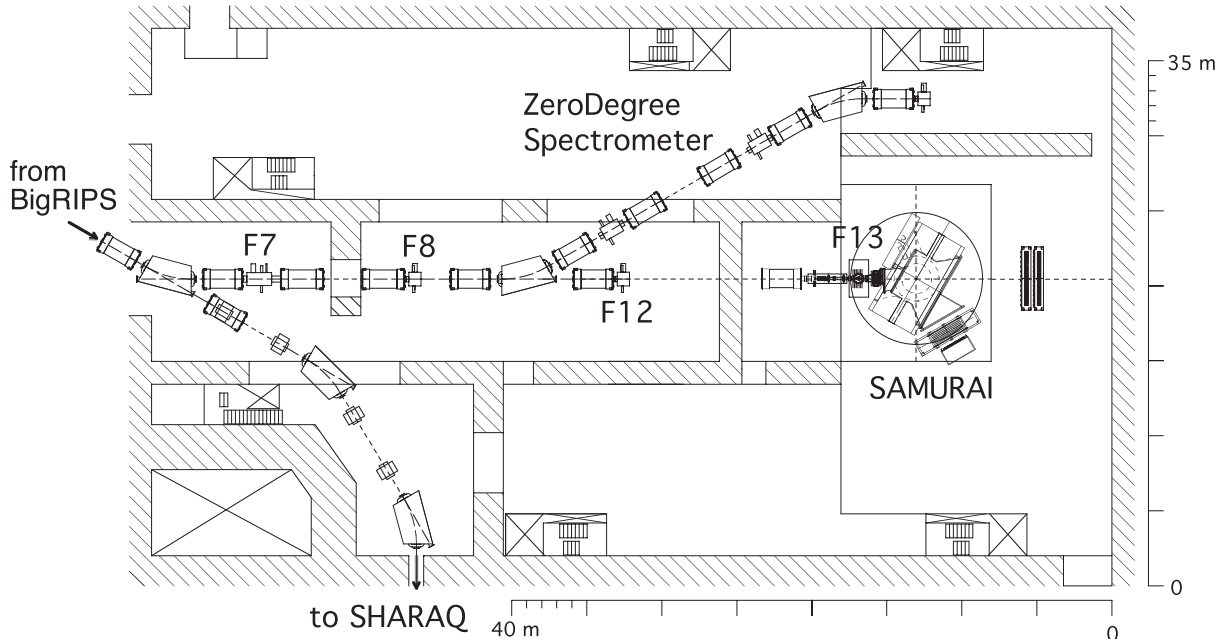
Figure 3.5: Top view of the straight beam line from the BigRIPS to the experimental room.

For the beam transport, we developed a new optics setting to make the beam size on the target as small as possible by minimizing the magnification. It was needed to make the beam spot size on the target as small as possible to minimize background events coming from the surrounding structure especially at the entrance of the MINOS system (Sec. 3.7). To achieve the

small magnification in the position, the last superconducting triplet quadrupole magnet (STQ25) was placed as close to the target location as possible. In this experiment, the target position, i.e. the center of the MINOS liquid hydrogen target, was 4.5 m upstream from the center of the SAMURAI magnet. It was 1 m upstream from the standard of the SAMURAI spectrometer. In addition, the STQ25 magnet was moved to the downstream limit.

Figure 3.6 shows the beam envelopes calculated with the COSY Infinity [97]. The matrix elements are summarized in Table 3.4. The magnification from F7 to F13 was 1.15 and 1.11 for the horizontal and vertical directions, respectively. These values were smaller than those of the standard transport, 1.86 and 2.16 for the horizontal and vertical directions, respectively.
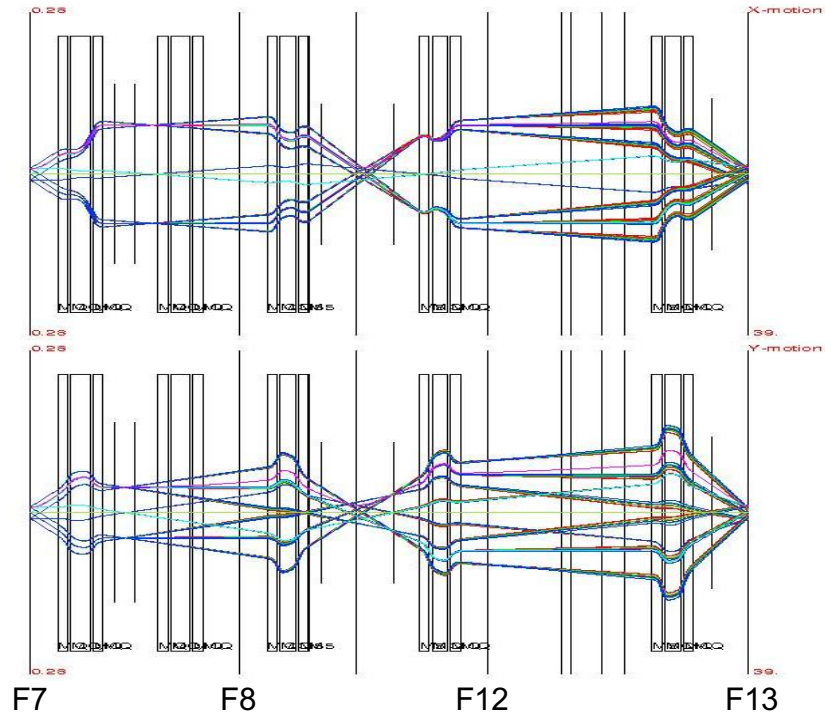
Figure 3.6: Calculated envelopes of a ^{11}Li beam from F7 to F13 for the horizontal (top) and the vertical (bottom) direction. By courtesy of H. Suzuki.

Table 3.4: Transfer matrix elements from F7 to F13. Units for lengths (x and y) and angles (a and b) are mm and mrad, respectively. The δ denotes momentum dispersion defined in Eq. (5.11).

Item	Standard	New
$(x\|x)$	1.86	1.15
$(x\|a)$	-0.43	-0.48
$(x\|\delta)$	1.00	1.00
$(a\|x)$	0.00	0.00
$(a\|a)$	0.54	0.87
$(a\|\delta)$	1.26	1.23
$(y\|y)$	2.16	1.11
$(y\|b)$	-0.66	-1.12
$(b\|y)$	0.00	0.00
$(b\|b)$	0.46	0.90

3.5 SAMURAI setup

The key component of our experiment is the setup to obtain the kinematically complete information on the ^{11}Li(p, pn) reaction. Figure 3.7 shows a top view of the experimental setup. In this figure, the ^{11}Li(p, pn) reaction is schematically drawn. The incident ^{11}Li beam bombarded on a liquid hydrogen target of the MINOS, and then, the ^{11}Li$(p, pn)^{10}$Li$^* \rightarrow ^9$Li $+ n$ reaction took place. In order to reconstruct the momentum vectors of two valence neutrons, all of the relevant momentum vectors, i.e. those of the ^{11}Li beam, the recoil proton, the knocked-out neutron, the heavy fragment ^{9}Li, the decay neutron, and the gamma ray emitted from the heavy fragment ^{9}Li were determined event by event and kinematically complete measurement was realized.
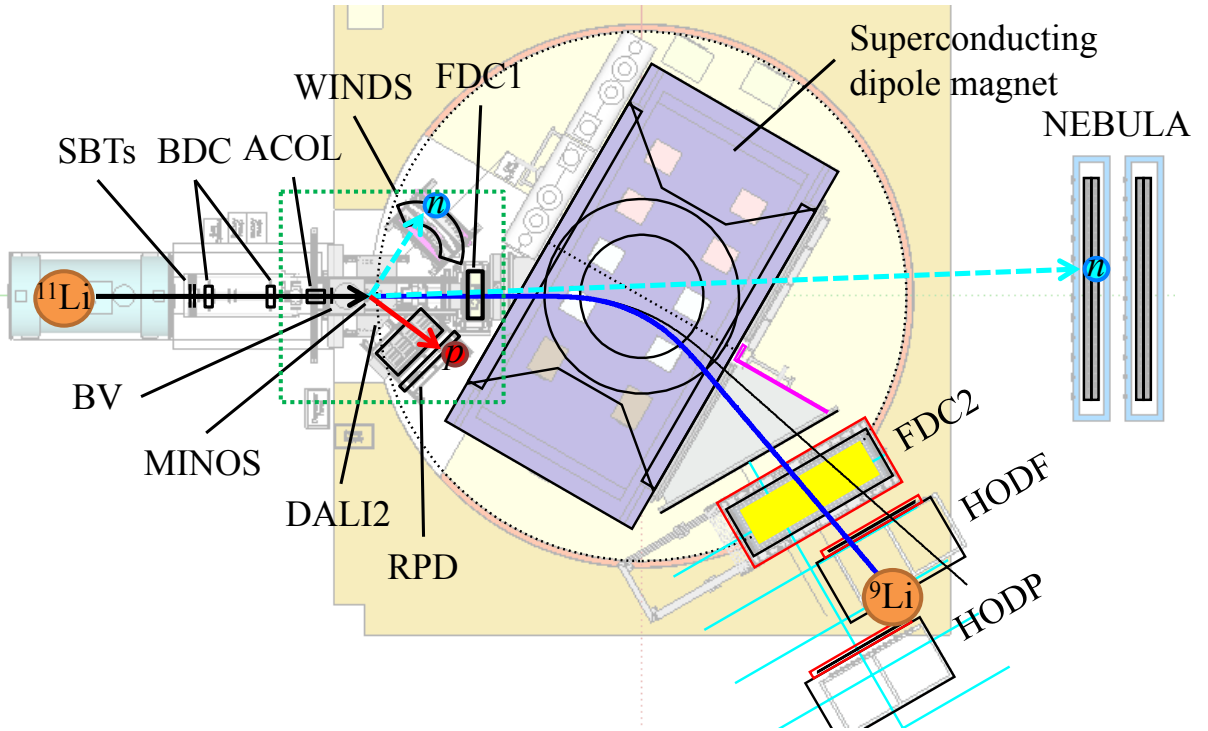
Figure 3.7: Top view of the experimental room. The black solid arrow, the dark blue arrow, the red arrow and the light blue dashed arrows show the trajectories of a ^{11}Li beam particle, a heavy fragment ^{9}Li, a recoil proton, and two neutrons (a knocked-out and a decay neutrons), respectively. See the text for details.

The setup consisted of two parts. One part was the standard setup of the SAMURAI spectrometer and used for determining the momentum vectors of the heavy fragment ^{9}Li and of the decay neutron in a similar manner as in normal invariant mass spectroscopy. The other part was newly developed in this thesis project and used for determining the momentum vectors of the recoil proton and of the knocked-out neutron.

In the below of this section, the role of each component of the setup is described briefly. The details are given in Sec. 3.6 (SAMURAI spectrometer and detectors), Sec. 3.7 (MINOS),

Sec. 3.8 (RPD), Sec. 3.9 (WINDS), Sec. 3.10 (DALI2), Sec. 3.11 (NEBULA), and Sec. 3.12 (electronics and data acquisition).

Starting from the upstream area along the beam direction, plastic scintillators (SBTs, Sec. 3.6.3) and tracking detectors (BDC1 and BDC2, Sec. 3.6.4) were placed to measure the timing and the position of the incident beam ^{11}Li. From that information, the momentum vector of ^{11}Li was determined. The SBTs were used also for the purpose of monitoring the flux of tritons. Just before the secondary target, the active collimator ACOL and the beam veto counter BV were installed so as to stop and to reject the beam particles whose trajectories were out of the target cell (Sec. 3.6.5).

After the occurrence of the quasi-free (p, pn) reaction in the target, a reaction residue ^{10}Li emitted in the very forward direction and immediately decayed into the heavy fragment ^{9}Li and the decay neutron. The superconducting dipole magnet (the SAMURAI magnet, Sec. 3.6.1) was placed to analyze the rigidity of the heavy fragment ^{9}Li. Two tracking detectors (FDC1 and FDC2, Sec. 3.6.6) were installed before and after the SAMURAI magnet to measure the position of the heavy fragment. By reconstructing the trajectory in the SAMURAI magnet, the rigidity of the heavy fragment was determined. The momentum vector of heavy fragment ^{9}Li was determined from the reconstructed rigidity and the position information from the FDC1. Two sets of plastic scintillator hodoscopes (HODF and HODP, Sec. 3.6.7) were installed after the FDC2 to measure the timing and the energy loss for the particle identification of the heavy fragment.

The MINOS was installed so as to achieve high luminosity (Sec. 3.7). The MINOS device is composed of a 15-cm-thick liquid hydrogen target (Sec. 3.7.1) coupled to a cylindrical time projection chamber (TPC, Sec. 3.7.2) for the tracking of the recoil proton. By combining the trajectory information of the incident ^{11}Li beam and the recoil proton, the reaction point in the target was determined with an uncertainty of about 5 mm.

Figure 3.8 shows a magnified view around the MINOS. After the occurrence of the quasi-free (p, pn) reaction, the target proton and one of the valence neutrons of ^{11}Li, the recoil proton and the knocked-out neutron, were scattered at large polar angles of around 45 degrees. The recoil particle detector RPD (Sec. 3.8) was installed at the right hand side of the beam line to detect the recoil proton. The RPD was composed of a multi-wire drift chamber (RPDC) and a plastic scintillator hodoscope (RPTOF). The RPDC and the RPTOF were used for measuring the position and the timing, respectively. The momentum vectors of recoil proton was reconstructed from this information. The neutron detector array WINDS (Sec. 3.9) was installed at the left hand side of the beam line to measure the position and the timing of the knocked-out neutron for the momentum vector reconstruction. The gamma-ray detector array DALI2 (Sec. 3.10) was installed surrounding the MINOS TPC to detect the gamma ray emitted from the heavy fragment.

The neutron detector array NEBULA (Sec. 3.11) was placed at forward angle to measure the timing and position of the decay neutron for determining the momentum vector.
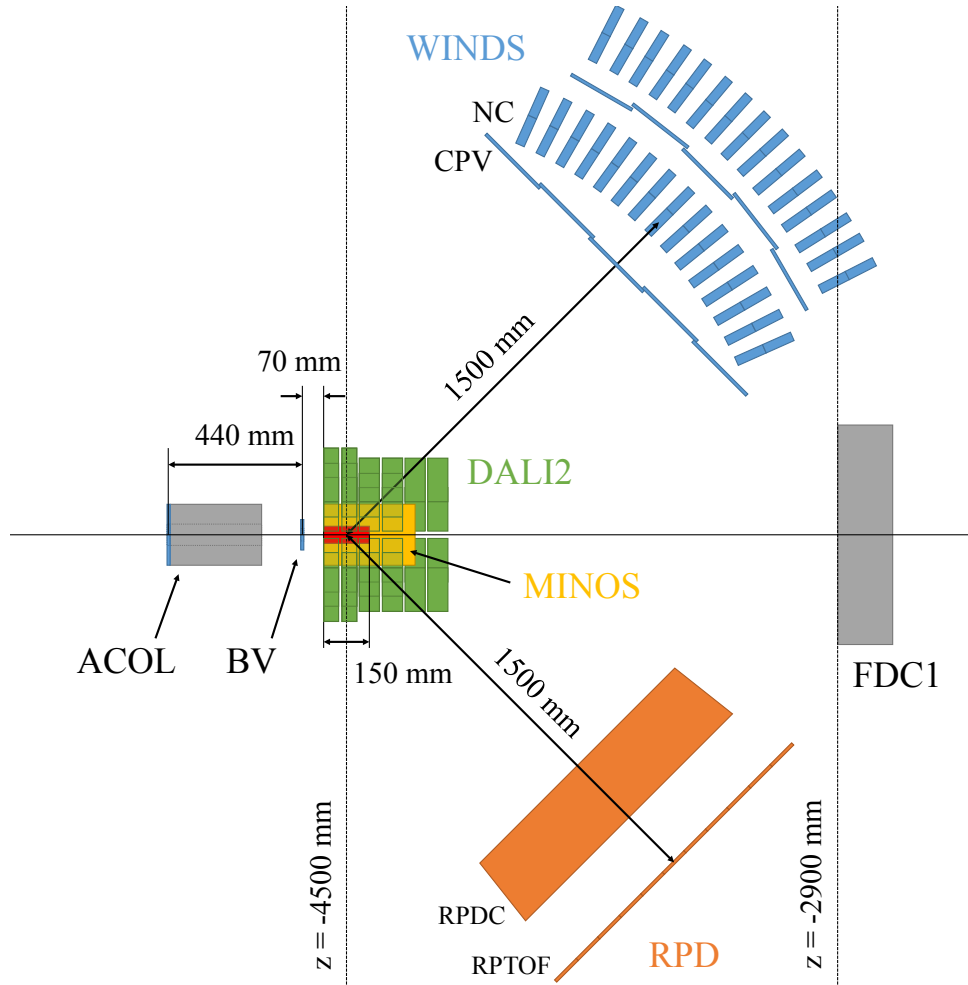
Figure 3.8: Magnified top view of the experimental room, corresponding to the region enclosed with the green dotted rectangle in Fig. 3.7. The MINOS target cell and the surrounding TPC are shown by the red and the yellow boxes, respectively. The effective area of the DALI2, the RPD and the WINDS are shown by the green, the orange and the blue boxes, respectively.

The laboratory frame of reference is centered on the experimental room. Figure 3.9 shows a bird's-eye view of the experimental room. The zero point is placed at the center of the SAMURAI magnet. The z and y axes are defined in parallel to the beam line and in parallel to the vertical direction, respectively.
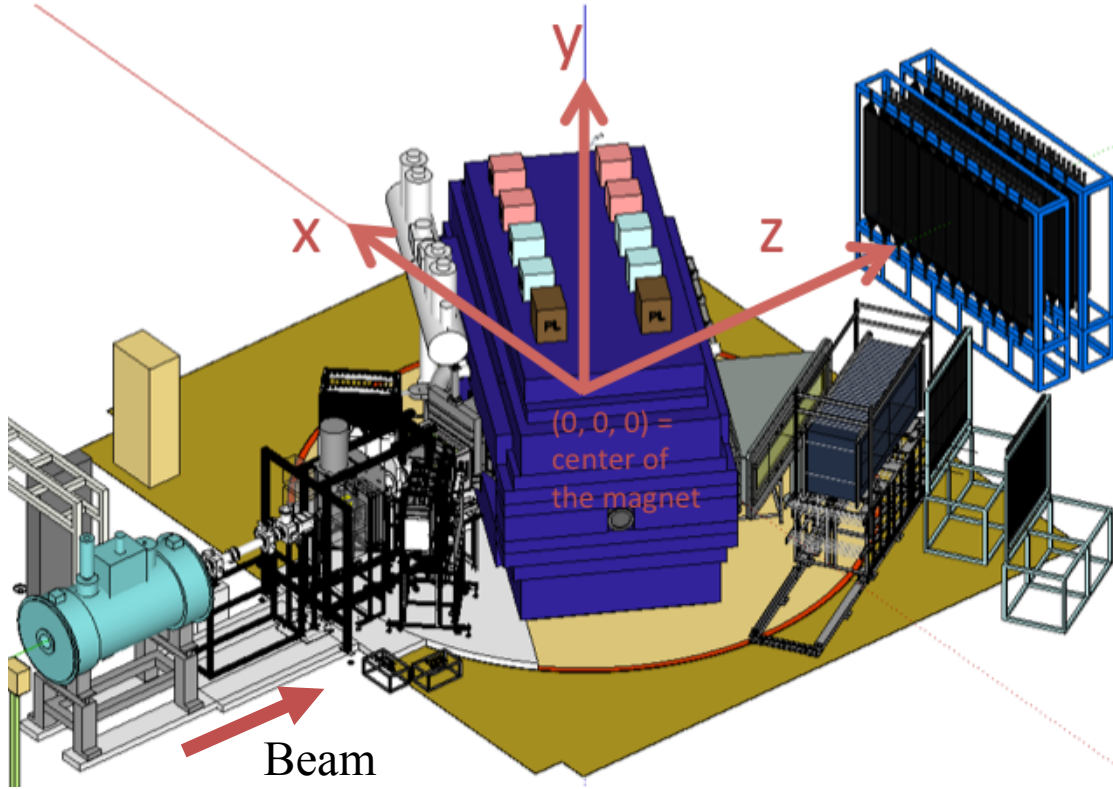
Figure 3.9: Bird's-eye view of the experimental room with the definition of the coordinate. The zero point is placed at the center of the SAMURAI magnet. The z and y axes are defined in parallel to the beam line and in parallel to the vertical direction, respectively.

The STQ25 magnet, the SAMURAI magnet, and the detectors mentioned above were aligned within an uncertainty of 200 μm (FWHM) by employing the photogrammetry system [98, 99].

3.6 Magnetic spectrometer SAMURAI

The SAMURAI[2] spectrometer [100] is designed to perform various kinds of measurements such as invariant-mass spectroscopy. It consists of a superconducting dipole magnet (SAMURAI magnet) [101], a large gap chamber [102], and detectors, as shown in Fig. 3.10. Depending on physics cases, the orientation angle of the SAMURAI magnet can be changed to optimize the resolution and the acceptance for particles to be detected. The positions of the detectors are changed experiment by experiment.

[2]Acronym for "Superconducting Analyzer for MUlti-particles from RAdioIsotope beams".
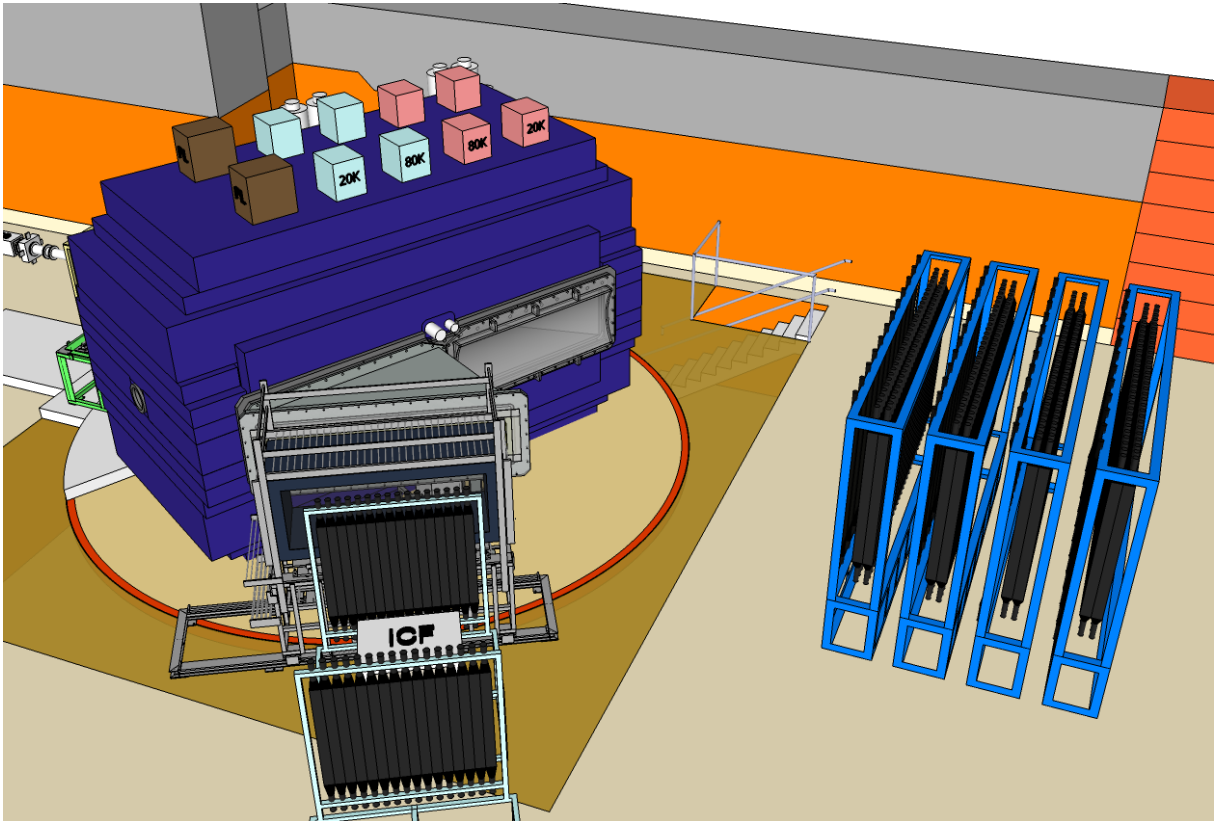
Figure 3.10: Bird's-eye view of the SAMURAI spectrometer. Beam particles come from the left to the right side. The purple polyhedron represents the SAMURAI magnet. The orientation angle of the SAMURAI magnet is 30 degrees.

In this experiment, the configuration of the 30-degree orientation angle was selected so as to maximize the acceptance of the heavy fragments as well as the decay neutrons. The magnetic field of 2.9 T was applied by applying the current of 510 A to the coil in order to bend heavy fragments having rigidity of 6.6 Tm at 60 degrees. The rigidity of the heavy fragment was determined by reconstructing the trajectory in the SAMURAI magnet. The position and angle of the heavy fragment before and after the SAMURAI magnet were separately measured. The trajectory of the fragment and its flight path length in the SAMURAI magnet were uniquely determined from the incident and outgoing momentum vectors of the fragment, by using the magnetic field map along the trajectory (Sec. 5.4). By combining the flight path length with the measured TOF of heavy fragments, the velocity of the heavy fragment was determined.

3.6.1   SAMURAI magnet

Table 3.5 summarizes the specifications of the SAMURAI magnet. The most unique feature is the wide gap space ($\varnothing 2$ m, between magnetic poles 0.88 m^h). Owing to this feature, one can obtain a large acceptance for the detection of reaction-residue fragments including fast neutrons flying at forward angles. In addition, the magnet pole is surrounded by iron yorks (H-type magnet). This helps the confinement of the fringe field.

Table 3.5: Specifications of the SAMURAI magnet.

Type	H-type
Pole	$\varnothing 2$ m, 0.88 m^h (gap)
Maximum field	3.1 T
Maximum field integral	7.1 Tm
Number of turns	3413 turns/coil
Maximum current	563 A
Coil cross section	180 mm $\times$ 160 mm
Gap	800 mm (inner size of a vacuum chamber [102])
Total weight	600 t

3.6.2   Configuration of detectors

In this subsection, the configuration of the detectors of the SAMURAI spectrometer is described. The details of each detector are described in the following subsections, separately.

The upper part of Fig. 3.11(a) shows a side view of the detectors placed before the SAMURAI magnet. At the exit of the STQ25 magnet, two plastic scintillator counters (the SBT1 and the SBT2, Sec. 3.6.3) were placed. Two beam drift chambers (the BDC1 and the BDC2, Sec. 3.6.4) were placed 2.6 m and 1.6 m upstream from the secondary target. Just before the secondary target, the active collimator and the beam veto (the ACOL and the BV, Sec. 3.6.5) were installed.

After the secondary target, the forward drift chamber 1 (the FDC1, Sec. 3.6.6) was installed just before the SAMURAI magnet.

A vacuum configuration before the SAMURAI magnet is shown in the lower part of Fig. 3.11(a). The vacuum system of the present setup was separated from that of the Bi-gRIPS beam line at the exit of the STQ25 magnet. The exit window was made of Kapton film with a thickness of 129 μm. The SBTs were placed in the air. The BDCs were installed in the isolated vacuum system having 129-μm-thick Kapton windows at the entrance and the exit. The ACOL and the BV were placed in the air. The vacuum system of the MINOS was isolated from the others (Sec. 3.7). The vacuum system of the FDC1 was connected to the gap chamber in the SAMURAI magnet. The entrance window was made of 129-μm-thick Kapton film.
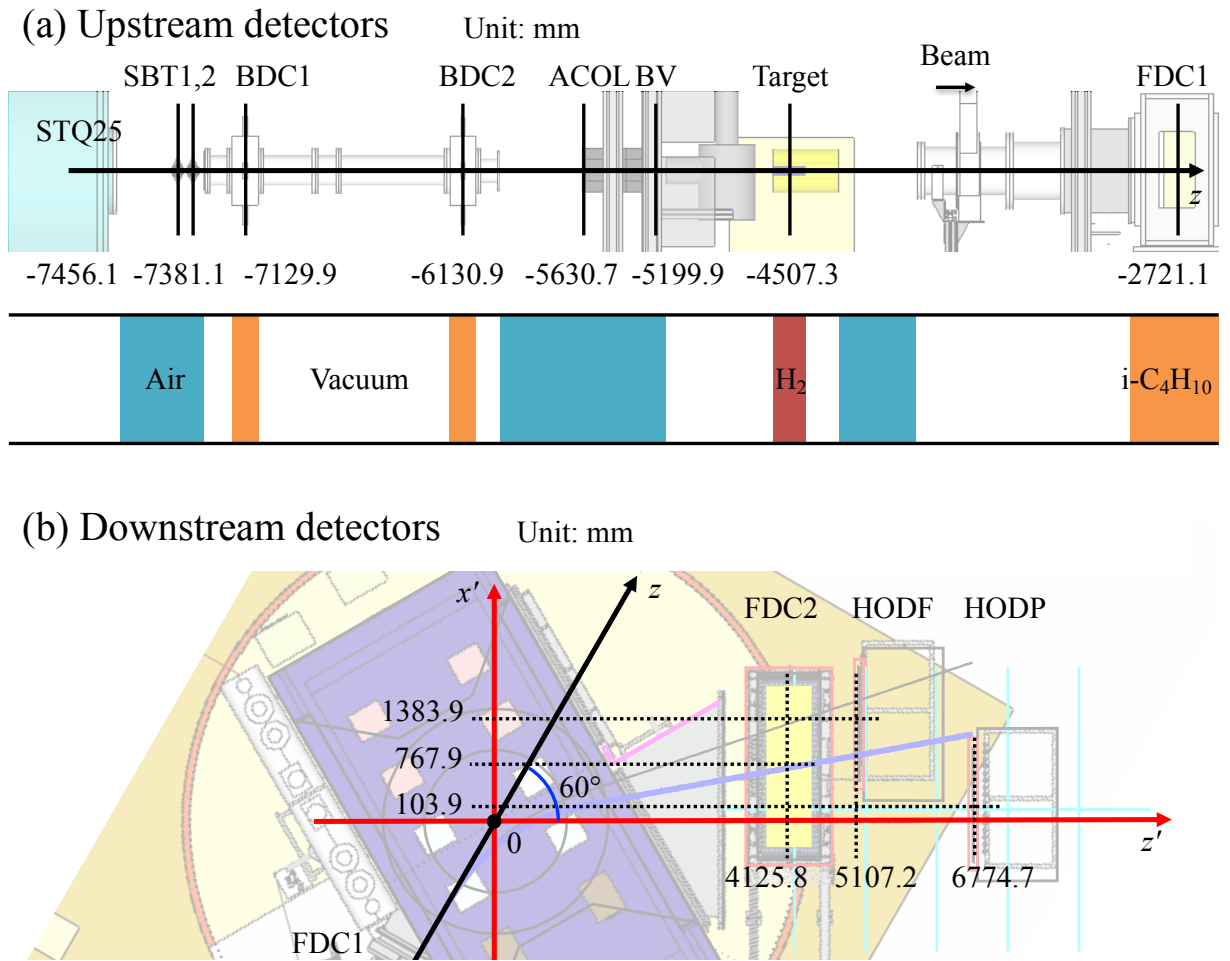
Figure 3.11: (a) Side view of the upstream detectors with a vacuum configuration. The numbers represent z positions of detectors. The blue, the orange, and the red colored areas are filled with the air, the isobutane, and the liquid hydrogen, respectively. The white areas are in vacuum. (b) Top view of the downstream detectors. The (z', x') plane is defined by rotating a (z, x) plane 60 degrees clockwise around the center of the SAMURAI magnet.

Figure 3.11(b) shows a top view of the detectors placed after the SAMURAI magnet. The

SAMURAI magnet was placed with the orientation angle of 30 degrees. The forward drift chamber 2 (the FDC2, Sec. 3.6.6) was installed just after the SAMURAI magnet. Two sets of plastic scintillator hodoscopes (the HODF and the HODP, Sec. 3.6.7) were placed next to the FDC2.

3.6.3   Plastic scintillators SBTs

The SBT1 and SBT2 were used to provide the logic signal that gave the beam timing information as well as severed as a part of the trigger logic (Sec. 3.12.2). The flux of tritons were also monitored in these detectors. As described above, they were located just after the exit of the STQ25 magnet. Therefore, all the particles transported into the experimental room passed through these detectors.

SBT1 and SBT2 each consisted of a 2-mm-thick plastic scintillator EJ-200 and two PMTs attached at the left and right ends. Anode signal of each PMT was split into three. One split signal was input to the QDC modules REPIC RPC-022 to digitize its charge. The others were sent to discriminators to generate logic signals. Two kinds of discriminators with different operation modes were used for determining the timing and for making trigger conditions. One discriminator was Phillips 708. This discriminator was used to provide the timing information of SBT signals with a high precision. The discretized signals were input to the TDC modules REPIC RPC-180 to record their timing information. The other discriminator was Phillips 730. This module provided the logic signal to separate $Z \geq 3$ particles from tritons. The input signals for this discriminator were an arithmetic sum of the two signals of the two PMTs at both ends, made with the linear fan-in fan-out Phillips 740 module. The logic signals discretized by this module were sent to the trigger circuit (Sec. 3.12) and joined the trigger logic driving the whole data acquisition system. The logic signals originating from the left PMT of the SBT1 through the Phillips 708 module defined the trigger timing and the stop timing of the BDCs and FDCs.

3.6.4   Beam drift chambers BDCs

The BDC1 and the BDC2 [100] were used to provide the trajectories of beam particles. They were located just after the SBT1 and SBT2. Each BDC gave the position along both the *x* and *y* directions of the incoming beam particle having $Z \geq 3$ at its location. Combining the the position information at the two location, the trajectories of the beam particles were determined.

Specifications of the BDCs are summarized in Table 3.6. The BDCs are Walenta-type drift chambers with a 2.5 mm half cell size. The operation gas are pure isobutane with a pressure of 50 Torr.

In this experiment, the operation voltage of cathode and potential wires were optimized for $Z \geq 3$ particles and set at around -850 and -900 V, respectively.

The signals from the anode wires were sent to the amp-shaper-discriminators (ASDs) Gnomes

Table 3.6: Specifications of the BDCs.

Anode wire	⌀16 μm Au-W/Re
Potential wire	⌀80 μm Au-Al
Cathode	8 μm^t Al-Kapton
Cell size	2.5 mm × 2.5 mm
Configuration	xx'yy'xx'yy'
Gas window	4 μm^t Aramid
Effective area	80 mm^w × 80 mm^h
Operation gas	i-C$_4$H$_{10}$ at 50 Torr
Cathode volt.	−850 V (typical)
Potential volt.	−900 V (typical)
Readout	128 ch

Design GNA-210 to generate low-voltage differential signaling (LVDS) logic signals. The ASDs were directly mounted on the BDC casing so as to reduce the effect of noise. The timing of the logic signals were recorded by the AMSC AMT-VME TDC.

The stop timing of the drift time was defined by the SBTs (Sec. 3.6.3). The fluctuation of the TOF from SBTs to BDCs was negligible as compared with the drift time.

3.6.5 Active collimator ACOL and beam veto BV

The active collimator ACOL and the beam veto BV were installed just before the MINOS, as already shown in Fig. 3.8. The purpose of the ACOL was to eliminate unwanted triton events in the MINOS TPC. If tritons are incident on the amplification part of the MINOS TPC, they could cause spark in cathode pads. The purpose of the BV was to detect and to reject the beam particles that passed through out of the target cell.

Figure 3.12(a) shows a schematic view of the ACOL. The main part of the ACOL was a lead block with a hole. The hole diameter of 70 mm was optimized so as not to interfere with beam trajectories. The main component of the beam went through the hole, while unwanted particles that may hit the MINOS TPC, mostly tritons, were presumably dumped in the lead block. The dimensions of the lead were $20^w \times 20^h \times 30^d$ cm^3. The depth of the lead block, 30 cm, is enough to energy-degrade and stop tritons with kinetic energies up to 300 MeV.

On the upstream surface of the lead, a 5-mm-thick plastic scintillator EJ-200 was mounted to detect the charged particles. It was wrapped by an aluminum foil with a thickness of 12 μm. The plastic scintillator had a through-hole at the center with a diameter of 68 mm. The signal was read out by two PMTs Hamamatsu H7195 attached on the left and right ends via light guides.

The anode signals from the PMTs were input to the leading edge discriminator to make logic signals. The logic signals were used for vetoing the beam trigger (Sec. 3.12.2).

Figure 3.12(b) shows the schematic view of the BV. The dimensions of the scintillator were 10 cm$^w \times 10$ cm$^h \times 5$ mm^d. It was wrapped by an aluminum foil with a thickness of 12 μm. It

(a)   (b)
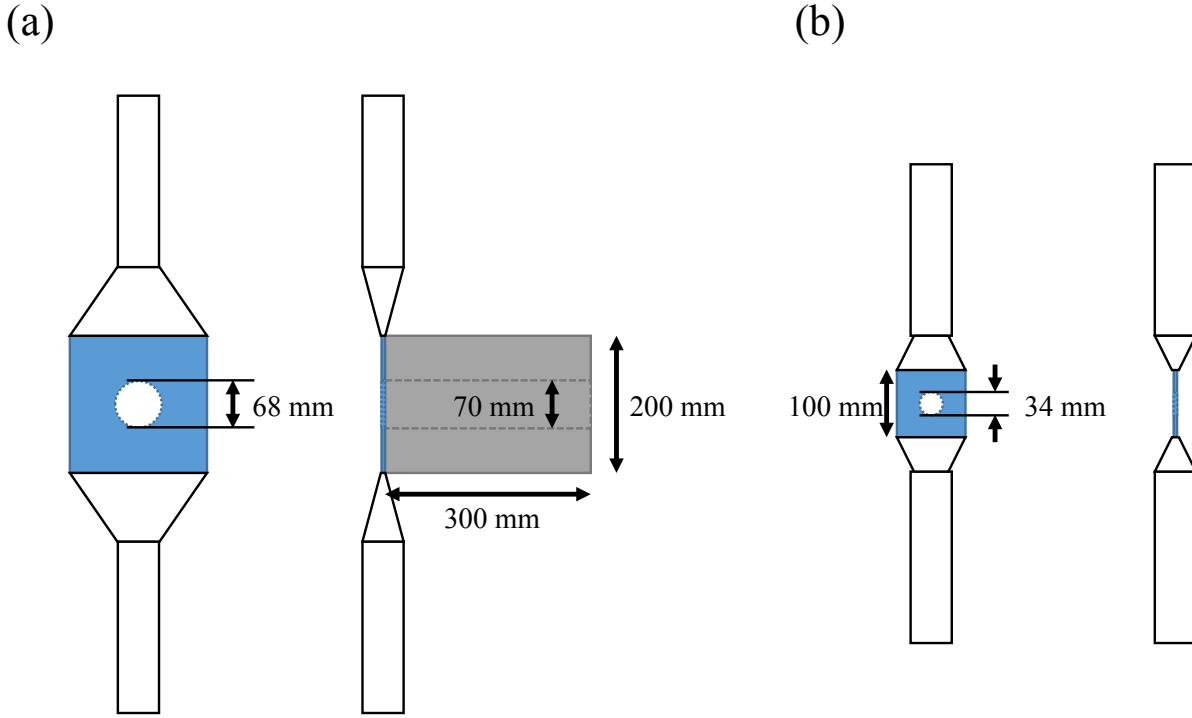
Figure 3.12: Schematic views of (a) the ACOL and (b) the BV. The blue and the gray areas represent plastic scintillators and a lead. Light guides and PMTs are shown by the black lines.

had a through-hole at the center with a diameter of 34 mm. The light output was read out by two PMTs Hamamatsu H7195 attached at both ends via light guides. The signal handling of the BV was done in a similar way as one of the ACOL.

The same settings of the high voltage of the PMTs and of the discriminator threshold were used for the ACOL and the BV. The applied high voltage was -2000 V, while the threshold levels of the discriminators were set to -30 mV. The threshold level was set to 0.6 MeV$_{ee}$, which was sufficiently low compared to the light output by tritons, ~ 1 MeV$_{ee}$. The calibration of the light output was performed by the interpolation of two points: a Compton edge of 1.33-MeV gamma rays from a ^{60}Co source at 1.3 MeV$_{ee}$ and a position of the pedestal at 0 MeV$_{ee}$.

The count rates of the ACOL and the BV for a certain physics run are summarized in Table 3.7. The fractions of 12% and 20% of the incident beam particles were identified to hit the ACOL and the BV, respectively. In total, 28% of incident beam particles were rejected by the ACOL and the BV. The trigger circuit for defining the beam particles is explained in Sec. 3.12.2.

3.6.6   Forward drift chambers FDC1 and FDC2

The FDC1 and the FDC2 [100] were located just before and after the SAMURAI magnet. They were used for determining the x and y position of heavy fragment particles at each of their z locations. As will be explained in Sec. 5.4, the trajectories of the heavy fragments before the

Table 3.7: Count rates of the ACOL and the BV for a certain physics run. SBTs and beam represents the count rate of beam particles defined by the SBTs and that of the beam trigger, respectively. See the text for details.

Item	Count rate [s^{-1}]
ACOL	15×10^3
BV	25×10^3
SBTs ($Z \geq 1$)	123×10^3
SBTs ($Z \geq 3$)	108×10^3
Beam	78×10^3

magnet were determined by combining the position information in the FDC1 with the reaction point information derived from the BDCs and the MINOS TPC (Sec. 4.4). Performing the optics analysis to connect the trajectory before the magnet to the position in the FDC2, the rigidity of the fragment particle was uniquely determined (Sec. 5.4.1). In addition, the trajectory information obtained by the FDC1 gave the information of the direction of the fragment momentum vector.

The FDC1 is a Walenta-type drift chamber with a 5 mm half cell size. Sense wires have three kinds of orientation of $0°$, $+30°$, and $-30°$. The operation gas is pure isobutane with a pressure of 50 Torr. The FDC2 has a hexagonal cell structure having 10 mm half cell size. The plane configuration is the same as FDC1, except for the shield wires with a pitch of 100 mm installed every two anode planes. The specifications are given in Table 3.8. The electronics for FDC1 and FDC2 are the same as BDCs, as described in Sec. 3.6.4.

The FDC1 has an effective area of 62 cm^w $\times$ 34 cm^h. The effective area is limited by the vacuum duct mounted on the FDC1 with a diameter of 31 cm. The effective area of the FDC2 is 2.2 m^w $\times$ 0.8 m^h. More than 99% of the heavy fragment ^{9}Li was in the acceptance of the FDC1 and the FDC2 (Sec. 5.11).

Similarly as in the case of BDCs, the operation voltages for FDC1 and FDC2 were tuned for detection of $Z = 3$ particles. The operation voltage of cathode and potential wires of the FDC1 were set at -900 and -950 V, respectively. The operation voltage of -1900 V was applied for the FDC2.

3.6.7 Hodoscopes HODF and HODP

The HODF and the HODP [100] were install next to the FDC2. They were used for measuring the position and the timing of the heavy fragment for the particle identification.

Each hodoscope consisted of 16 plastic scintillators with sizes of 10 cm^w $\times$ 120 cm^h $\times$ 1 cm^d. The light output of each scintillator was read out by the two PMTs Hamamatsu R7195 attached at the end via light guides. In addition, one detector was added to cover an ineffective area coming from a supporting frame between HODF and HODP.

The PMT voltage and discriminator threshold setting were both optimized so as not to lose

Table 3.8: Specifications of the FDC1 and the FDC2.

Item	FDC1	FDC2
Anode wire	$\varnothing$20 μm Au-W/Re	$\varnothing$40 μm Au-W/Re
Pot./shield wire	$\varnothing$80 μm Au-Al	$\varnothing$80 μm Au-Al
Cath./shield window	8 μm^t Al-Kapton	12 μm^t Al-Mylar
Cell size	5 mm × 5 mm	10 mm (hexagonal)
Configuration	xx′uu′vv′xx′uu′vv′xx′ u: +30°, v: −30°	sxx′suu′svv′sxx′suu′svv′sxx′s s: shield plane
Gas window	80 μm^t Kapton	50 μm^t Mylar
Effective area	$\varnothing$31 cm (62 cm^w × 34 cm^h)	2.2 m^w × 0.8 m^h
Operation gas	i-C_4H_{10} at 50 Torr	i-C_4H_{10} at 1 atm
Operation voltage (typical)	Cathode: −900 V Potential: −950 V	−1900 V
Readout	448 ch	1568 ch

detection efficiency for $Z = 2$ particles. The typical operation voltage and threshold were −1500 V and −150 mV, respectively.

The anode signals from the PMTs were split into two. One split signal, after being cable-delayed by 500 ns, was input to the CAEN QDC V792 to record the charge information. The other was sent to the leading edge discriminator to generate logic signals. The timing of the logic signals was recorded by the CAEN TDC V775 with a cable delay of 500 ns.

3.7 MINOS

This section describes the MINOS[3] [103, 104] device developed by CEA Saclay in collaboration with RIKEN Nishina Center. A 3D sectional drawing of the MINOS device is shown in Fig. 3.13. It is composed of a liquid hydrogen target and a cylindrical time projection chamber (TPC) serving as a vertex tracker.

Figure 3.14 shows cross-sectional views of the MINOS around the target cell. The target cell made of Mylar had a cylindrical shape with a length of 15 cm and a diameter of 56 mm. The target cell was attached on the target support and installed in the vacuum pipe with a diameter of 80 mm. The target support had an entrance hole with a diameter of 38 mm, which limited the effective diameter of the target cell.

Through the (p, pn) reaction in the liquid hydrogen target, a recoil proton, a knocked-out neutron, a heavy fragment, decay neutrons, and gamma rays were emitted. The trajectory of the recoil proton was measured by the MINOS TPC. The acceptance of the MINOS TPC fully covered the scattering angle region of the recoil protons from 30 to 90 degrees with respect to

---

[3]Acronym for "nuclear MagIc Numbers Off Stability".
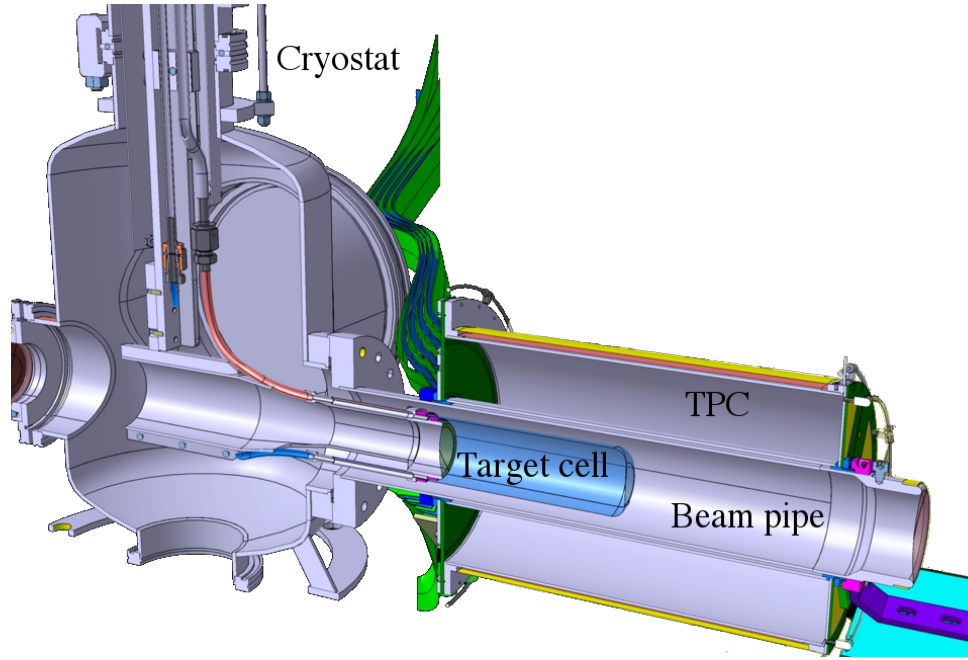
Figure 3.13: 3D sectional drawing of the MINOS device with respect to the beam center is shown. The left side in this figure corresponds to the upstream side along the beam direction, while the right side the downstream side.

the beam direction and, depending on the depth of the reaction point along the beam direction, partially that from 17 to 120 degrees.

Combining the trajectory information of the recoil proton with that of the incident beam, the reaction point was reconstructed (Sec. 4.4).

3.7.1 Liquid hydrogen target

The liquid hydrogen target part consisted of the 2 mm-thick aluminum beam pipe and the target cell attached on the cryostat through the target support. The aluminum beam pipe was isolated from the air by 150 μm Mylar windows at an entrance and an exit.

The target cell was made of the Mylar films with a length of 152.8 mm and an effective diameter of 38 mm. The thicknesses of a straight side, an entrance window, and an exit window were 150 μm, 110 μm, and 150 μm, respectively. It was thermoformed at 160°C by mechanical stamping so that it could maintain the shape without any support even at low temperature and high pressure.

During the experiment, the temperature and the pressure were kept at 15 K and 153 mbar, respectively, resulting the averaged density of the liquid hydrogen of 0.076 g/cm^3 and the target thickness of 1.16 g/cm^2. During the measurement with the empty target, the liquid hydrogen was vaporized by warming up to 45 K, resulting the target thickness of 3.93 mg/cm^2.
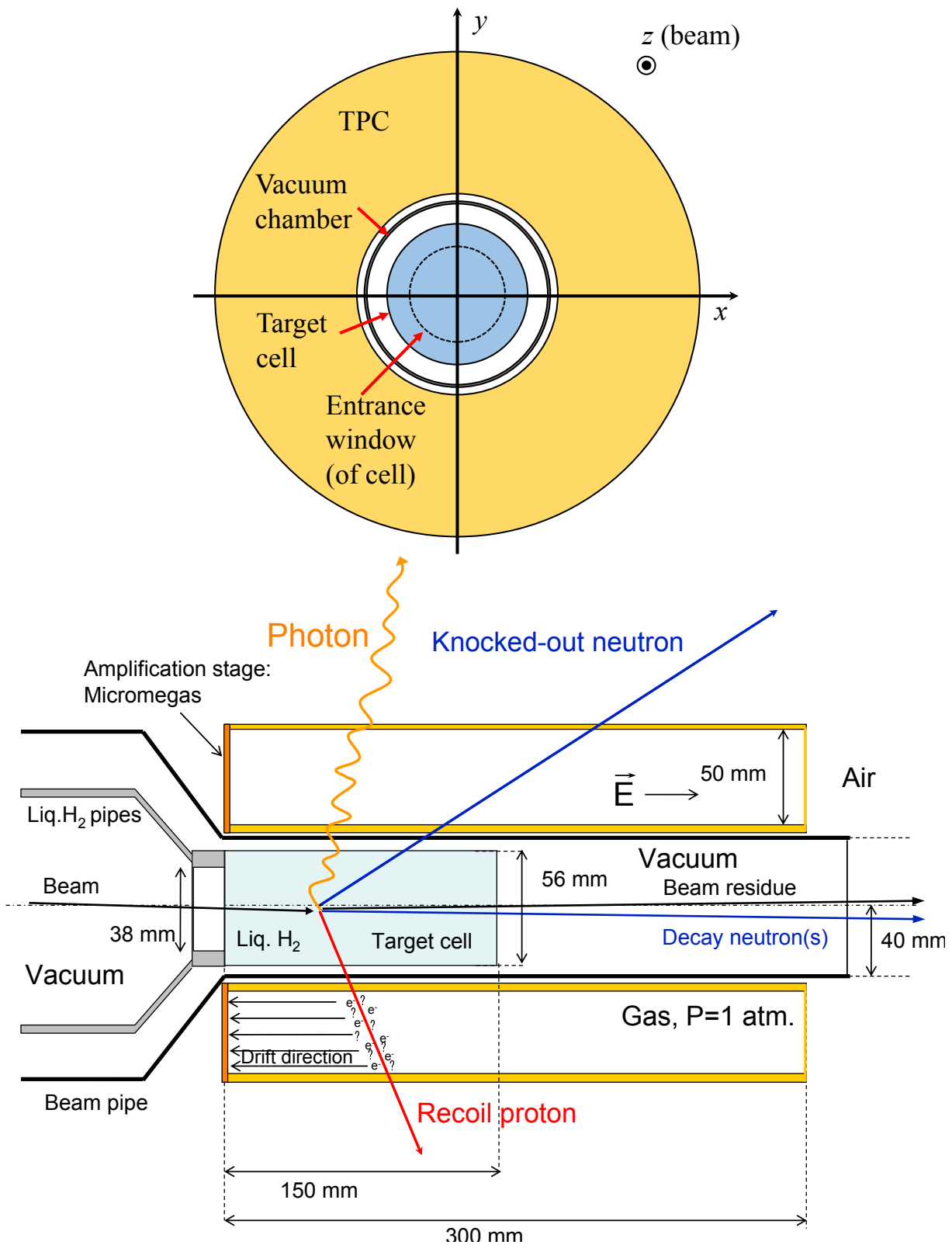
Figure 3.14: Cross-sectional views of the MINOS around the target cell (top) on the (x, y) and (bottom) on the (z, x) planes. The target cell filled with a liquid hydrogen and the MINOS TPC are shown by the blue and the yellow shaded areas, respectively. Particle trajectories are shown by the arrows.

3.7.2 MINOS TPC

The MINOS TPC surrounded the liquid hydrogen target for the determination of the reaction point. The specifications are given in Table 3.9. The recoil proton produced electrons and positive ions in the MINOS TPC along its trajectory. The electrons were drifted to the upstream side and amplified by a Micromegas [105, 106]. A readout electrode of the Micromegas was divided into 4608 pads for the two-dimensional position detection. The proton trajectory on the (x, y) plane was determined by the geometry of fired pads. The proton trajectory along the z axis was determined by the drift time.

Table 3.9: Specifications of the MINOS TPC.

Length	300 mm
Inner radius	45 mm
Outer radius	55 mm
Operation gas	82%Ar + 15%CF$_4$ + 3%i-C$_4$H$_{10}$ at 1 atm
Field voltage (TPC)	-6000 V (typical)
Mesh voltage (Micromegas)	-450 V (typical)
Signal amplification	Micromegas
Number of channels	5120 ch
Resolution (depth)	5 mm (FWHM) [107]
Tracking efficiency	$> 85\%$

Amplified signals from the readout pads were input to Feminos boards [104] for the digitization. The Feminos board was based on a front-end card (FEC) from the T2K experiment [108]. In the Feminos, AFTER chips [109] embedded on the FEC were replaced by the AGET chips [110] developed by the GET collaboration for the fast signal processing. Each chip comprised 64 channels of charge sensitive preamplifier and shaper followed by an external ADC.

The digitized data were transferred to a PC through a Gigabit Ethernet. The data were processed by a dedicated data acquisition software Mordicus [111].

3.8 Recoil proton detector RPD

The timing and position information of the recoil proton was determined by the recoil proton detector (RPD). It consisted of a multi-wire drift chamber (RPDC) and plastic scintillator hodoscopes (RPTOF). A 3D drawing and cross-sectional views of the RPD are shown in Fig. 3.15 and Fig. 3.16, respectively. The geometrical coverage for the recoil proton was about 30–65 degrees in a polar angle (approximately, same as the scattering angle of the recoil proton in the laboratory frame) and about -20 to $+20$ degrees in an azimuthal angle. The kinetic energy of the recoil proton ranged from 30 MeV to about 500 MeV.

Along the direction of the recoil protons, the RPTOF was located behind the RPD at a

distance of 324.8 mm from the center of the RPD. The RPTOF fully covered the solid angle of all the proton particles passing through the RPD from the target.
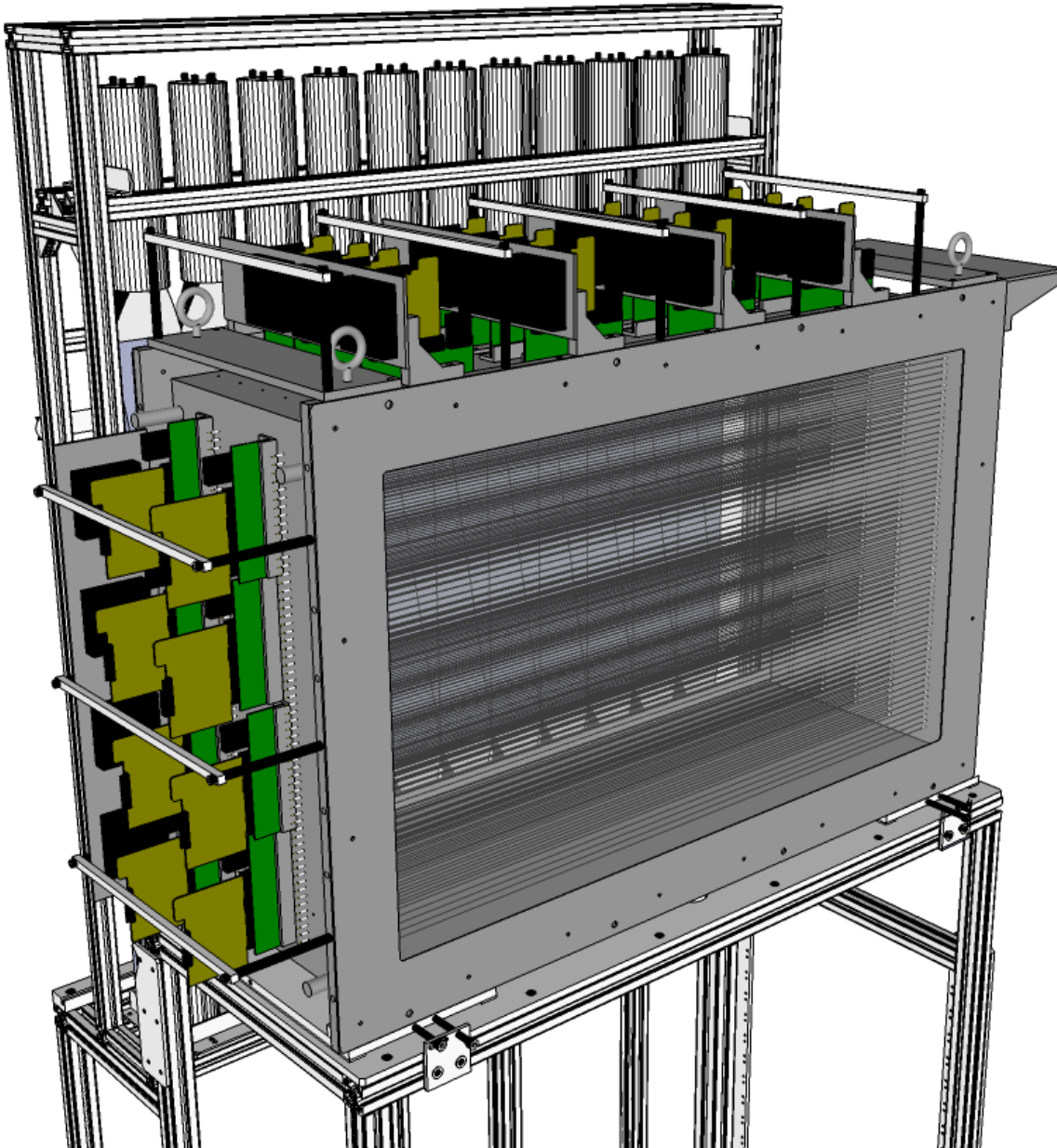
Figure 3.15: 3D drawing of the RPD. The gray box at the center of the figure represents the RPDC. Preamplifier-discriminators are shown by green and ocher parts. The 11 modules of the RPTOF are located behind the RPDC.
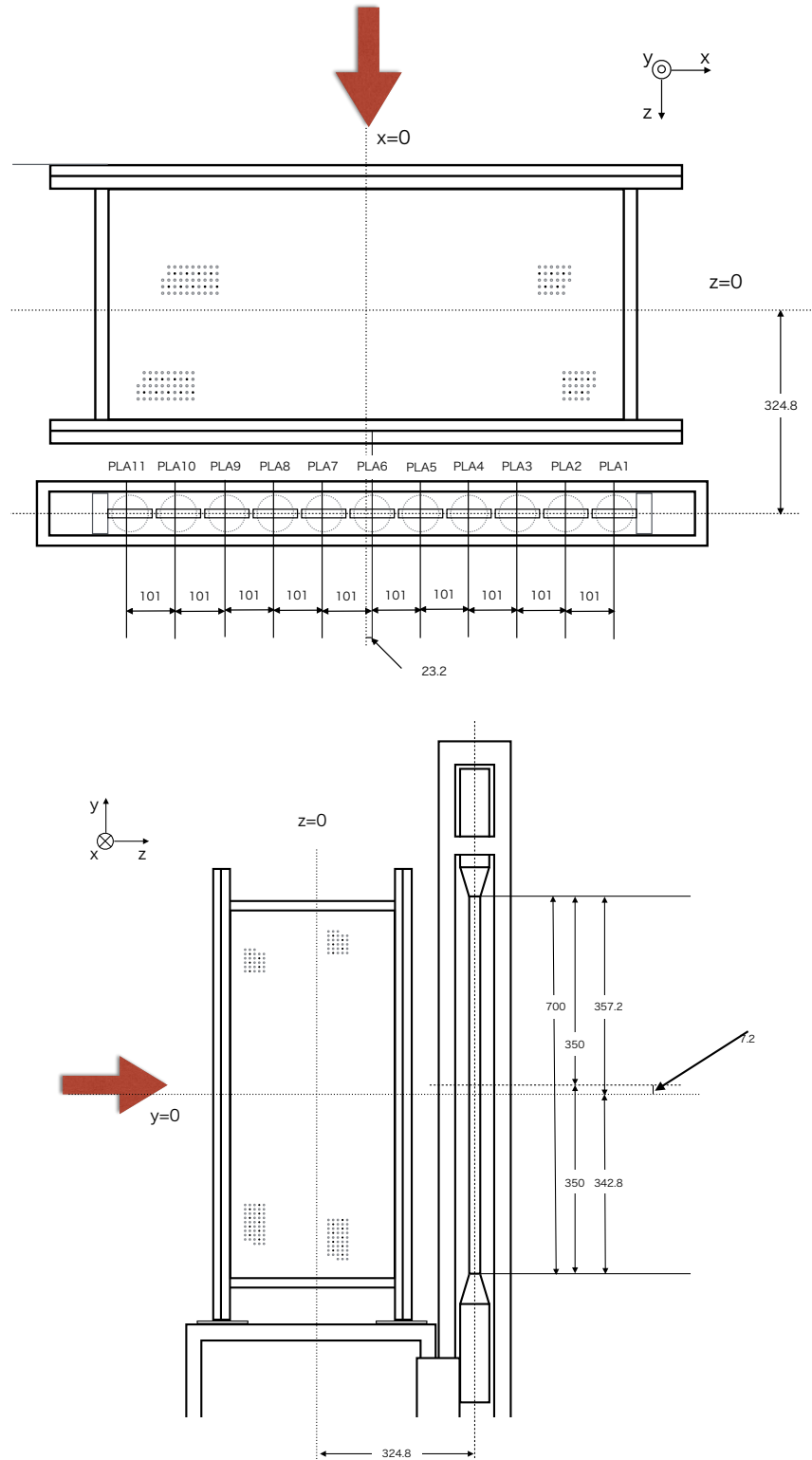
Figure 3.16: Cross-sectional views of the RPD. (Top) top view and (bottom) side view. The red arrows show a direction of the bombarding recoil proton. The unit is mm.

3.8.1   Multi-wire drift chamber RPDC

The RPDC was used to measure the position of the recoil proton. The RPDC had three types of regular tetragonal cell structure with different drift lengths of 7 mm, 7.5 mm, and 8 mm depending on the plane. The specifications are summarized in Table 3.10.

Table 3.10: Specifications of the RPDC.

Anode wire	$\varnothing$30 μm Au-W
Cathode wire	$\varnothing$80 μm Au-Mo
Potential wire	$\varnothing$80 μm Au-Mo
Shield wire	$\varnothing$80 μm Au-Mo
Cell size	x_f: 14 mm $\times$ 14 mm
	y_f: 14 mm $\times$ 14 mm
	x_r: 15 mm $\times$ 15 mm
	y_r: 16 mm $\times$ 16 mm
Configuration	s-$x_f x_f'$-s-$y_f y_f'$-s-$x_r x_r'$-s-$y_r y_r'$-s
Gas window	50 μm^t Al-Mylar
Effective area	896 mm^w $\times$ 448 mm^h (x_f, y_f)
Operation gas	50%Ar + 50%C_2H_6 at 1 atm
Cathode volt.	-2700 V (typical)
Potential volt.	-2700 V (typical)
Readout	768 ch

A two-channel power supply Sato Denshi HV-02W was used for providing a high voltage to cathode and potential wires. The typical voltage applied for the cathode and the potential was -2700 V. The signals from anode wires were sent to preamplifier-discriminator LeCroy 2735DC to generate logic signals. The preamplifier-discriminator modules were directly mounted on the RPDC casing so as to reduce the effect of noise. The timing of the logic signals was digitized by CAEN multi-hit TDC V1190.

The operation voltage was optimized for detecting recoil protons at the highest energy region of interest, 500 MeV. The threshold was set so as not to lose detection efficiency for minimum ionizing particles (MIPs).

3.8.2   Plastic scintillator hodoscope RPTOF

The RPTOF was used to measure the TOF of recoil protons. Since the RPTOF was placed just behind the RPDC, it served also as a time reference in the measurement of the drift time in the RPDC. The RPTOF was composed of 11 plastic scintillators each with sizes of 10 cm^w $\times$ 70 cm^h $\times$ 1 cm^t. The thickness of the scintillator was uniform over the whole area within a precision of 50 μm. The light output of each scintillator was read out by the two PMTs Hamamatsu H7195 attached at both ends via the light guides. Each PMT was electro-magnetically shielded

from the fringe field from the SAMURAI magnet by using a cylinder made of two layers of electromagnetic soft iron (SUY-1) with a thickness of 2 mm [112].

The PMTs were operated with high voltage of -2200 V. A multichannel power supply CAEN SY1527 was used for providing a high voltage to each PMT.

Anode signals from the PMTs were split into three. One split signal was delayed and input to the CAEN QDC V792 to record their charge information. The others were sent to two different discriminators. Two discriminators with different threshold levels were used for determining the timing as well as for making trigger signals. One discriminator was Iwatsu ultra fast discriminator UFD4, with a low threshold of -60 mV for timing information. The timing of the logic signals were recorded by CAEN multi-hit TDC V1290 and CAEN TDC V775. The other discriminator was Fuji Diamond TKY-0230, with a high threshold of -225 mV for triggering. The logic signals were used for making a trigger.

3.9 Knocked-out neutron detector array WINDS

The WINDS[4] [113–115] was used for detecting knocked-out neutrons coming from quasi-free scattering with emission angles from 25 to 60 degrees and kinetic energies from 30 MeV to 500 MeV. The WINDS was composed of 60 modules of plastic scintillators for neutron detection (NC) and 11 modules of plastic scintillators for charged particle veto (CPV1, CPV2). A 3D drawing and a top view of the WINDS are shown in Figs. 3.17 and 3.18, respectively. The NC modules were arranged in four concentric layers: NCL1, NCL2, NCL3, and NCL4. Here, the center of the circles was at the geometrical center of the liquid hydrogen target. The radii of these concentric layers were 1.5 m (NCL1), 1.6 m (NCL2), 1.8 m (NCL3), and 1.9 m (NCL4). Each NC module faced to the center of the target. The NC modules in first two layers were placed at every 3 degrees, while the others were placed at every 2.5 degrees. The PMTs of the NC modules were electro-magnetically shield in the same manner as described in Sec. 3.8.2. The specifications are summarized in Table 3.11.

Multichannel power supply CAEN SY1527 and CAEN SY527 were used for providing a high voltage to each PMT. The anode signals from the PMTs were handled in a similar way as the NEBULA (Sec. 3.11). The leading edge discriminator LeCroy 4413 was used to generate a logic signal, and then, the CAEN TDC V1190 was used to record the timing.

The PMT voltage and discriminator threshold settings were optimized to maximize the neutron detection efficiency. The typical operation voltage and threshold settings were -2500 V and -15 mV, respectively. The threshold was sufficiently lower than the software threshold of 6 MeV$_{ee}$.

---

[4]Acronym for "Wide-angle Inverse-kinematics Neutron Detectors for SHARAQ".
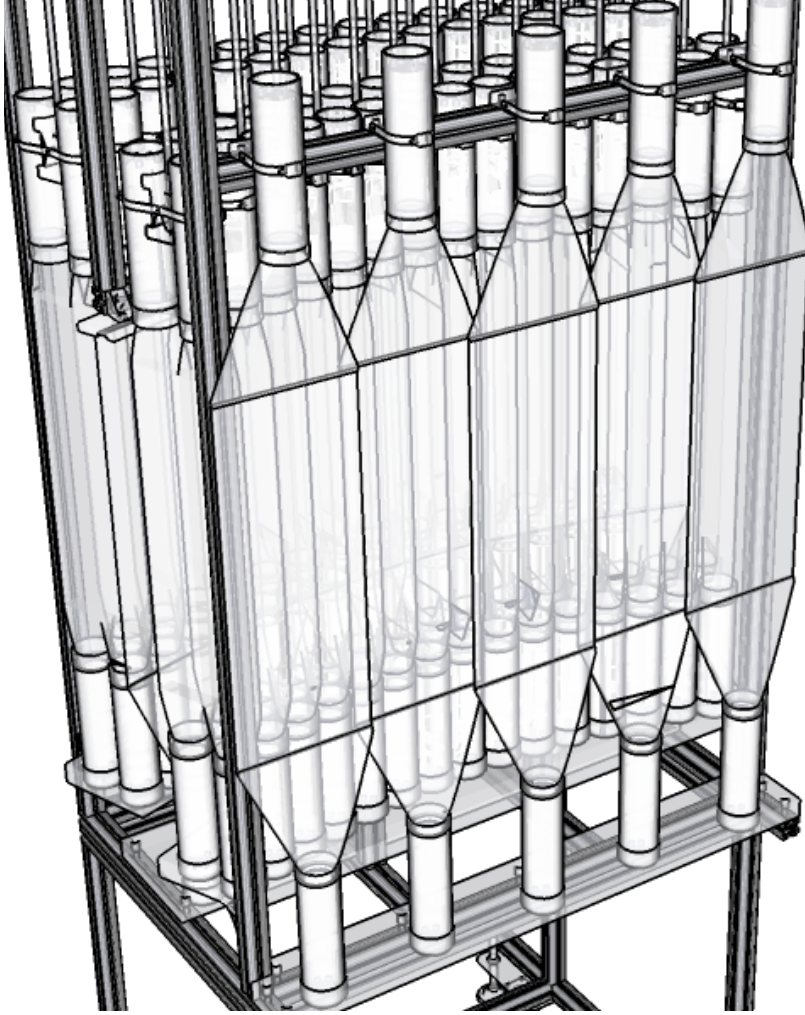
Figure 3.17: 3D drawing of the WINDS. Five CPV1 modules are seen in front of other modules.

Table 3.11: Specifications of the WINDS.

Plastic scintillator	Saint-Gobain BC-408
	$3 \text{ cm}^w \times 60 \text{ cm}^h \times 10 \text{ cm}^t$ (NC)
	$25 \text{ cm}^w \times 65 \text{ cm}^h \times 0.5 \text{ cm}^t$ (CPV1)
	$23 \text{ cm}^w \times 65 \text{ cm}^h \times 0.5 \text{ cm}^t$ (CPV2)
PMT	Hamamatsu H7195
Number of detectors	60 modules (NC)
	5 modules (CPV1)
	6 modules (CPV2)
Configuration	3° pitch (NCL1 and NCL2)
	2.5° pitch (NCL3 and NCL4)
Detection efficiency	13% ($E_{\text{th}} = 6 \text{ MeV}_{\text{ee}}$)
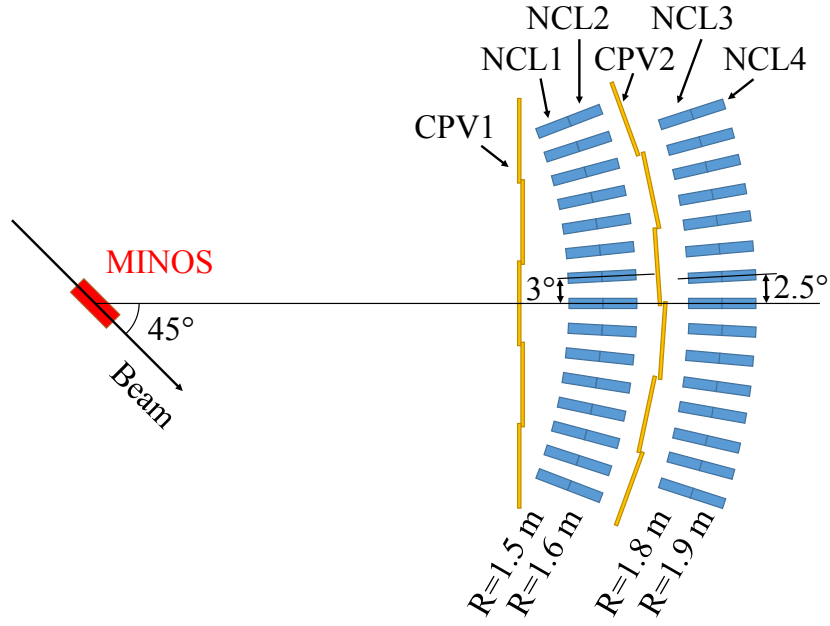
Figure 3.18: Layout of the WINDS. The red, the yellow, and the blue rectangles represent the target cell of the MINOS, CPV modules, and NC modules, respectively.

3.10 Gamma-ray detector array DALI2

The DALI2[5] [116] is a gamma-ray detector array composed of NaI(Tl) scintillator modules and has been widely used in in-beam gamma ray spectroscopy in experiments at RIBF. Each module has a PMT (Hamamatsu R580 or Hamamatsu R1306) and scintillator part (with sizes of 45 mm $\times$ 80 mm $\times$ 160 mm or 60 mm $\times$ 60 mm $\times$ 120 mm).

In this experiment, we reconfigured these modules to detect gamma rays from an excited heavy fragment, i.e. ^{9}Li core in the case of the ^{11}Li(p, pn) reaction. The DALI2 was arranged to surround the MINOS TPC to detect gamma rays from an excited heavy fragment. A schematic view of the DALI2 with the MINOS TPC is shown in Fig. 5.8. Although DALI2 has 186 detector modules as a whole in the standard setup, we used only 68 of them and changed the configuration of the crystals for the detection of the recoil proton and the knocked-out neutron. We used two types of modules having different dimensions and PMTs: 32 "WHITE" modules and 36 "OLD" modules. The modules were arranged in 6 layers in our configuration. From the upstream, each layer had 16, 16, 12, 12, 6, and 6 modules. For the 3rd to 6th layer, the modules were not placed in the region with an azimuthal angle of about -20 to $+20$ degrees so as to make the flight space for the recoil protons and the knocked-out neutrons. The specifications are given in Table 3.12.

A multichannel power supply CAEN SY2527 was used for providing a high voltage to each PMT. Typical HV values applied for the WHITE and the OLD modules were -1200 V and -1400 V, respectively. The anode signals from the PMTs were input to the spectroscopy

---

[5]Acronym for "Detector Array for Low Intensity radiation 2".
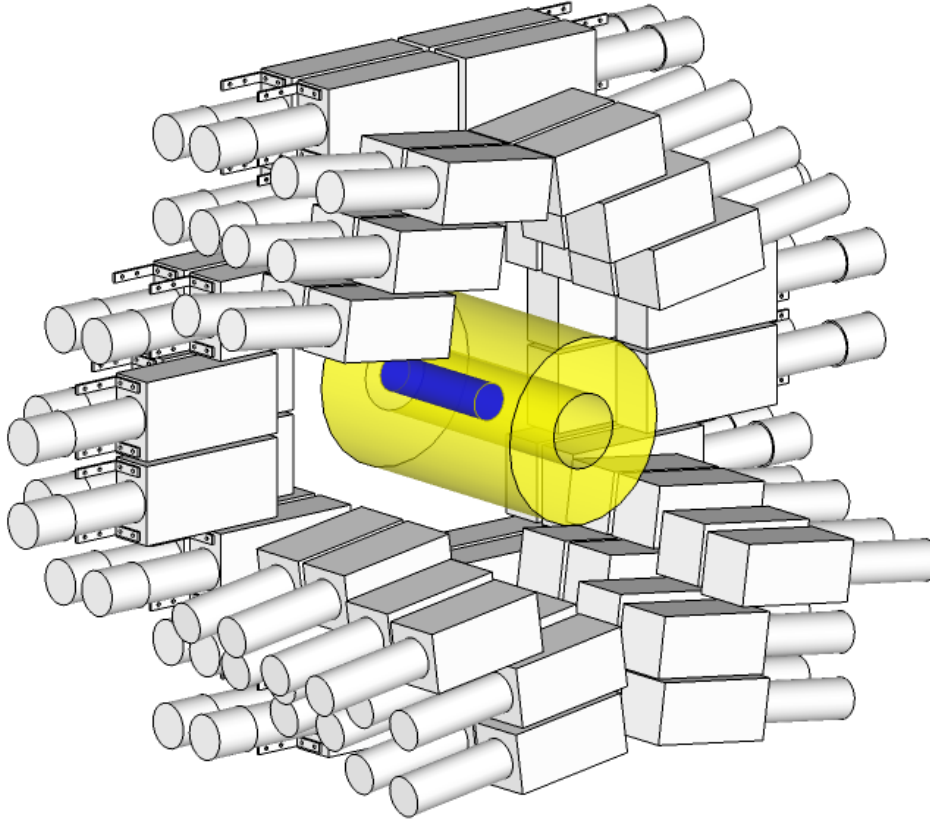
Figure 3.19: Schematic view of the reconfigured DALI2 setup. The white boxes and cylinders show metal housings of NaI(Tl) crystals and PMTs, respectively. The blue and the yellow cylinders represent the liquid hydrogen target and the MINOS TPC, respectively. The beam flew from the top left side to the bottom right side.

Table 3.12: Specifications of the DALI2. The efficiency includes the intrinsic efficiency and the geometrical acceptance.

Crystal	NaI(Tl)
Detector size	45 mm × 80 mm × 160 mm (WHITE)
	60 mm × 60 mm × 120 mm (OLD)
PMT	Hamamatsu R580 (WHITE)
	Hamamatsu R1306 (OLD)
Number of crystals	32 (WHITE) + 36 (OLD)
Efficiency	7% for 2.7 MeV gamma rays (GEANT4 simulation)

amplifier CAEN N568B. Shaping-out signals of N568B with a time constant of 1 μs were sent to peak-sensing analog-to-digital converter Mesytec MADC-32 to record the energy-deposit information. Fast-out signals of N568B shaped with a time constant of 100 ns were sent to the leading edge discriminator CAEN V895 to generate logic signals. The timing of logic signals were recorded by the CAEN multi-hit TDC V1190.

The configuration of the modules was optimized by a simulation based on the GEANT4 framework [117, 118] to maximize the overall detection efficiency including the geometrical acceptance. The overall efficiency was evaluated 7% for the 2.7-MeV gamma rays, by adopting the add-back analysis [116].

3.11   Neutron detector array NEBULA

The neutron detector array NEBULA[6] [119] was placed at 12 m downstream from the secondary target. It was used to measure the position and the timing of the decay neutrons.

It consisted of 120 plastic scintillators for neutron detection (NEUT) and 24 plastic scintillators for charged particle veto (VETO). The whole detector modules were divided into 2 walls each with a VETO layer and two NEUT layers so as to maximize the detection efficiency for more than two neutrons [120]. Figure 3.20 shows the layout of the NEBULA. Specifications are shown in Table 3.13.
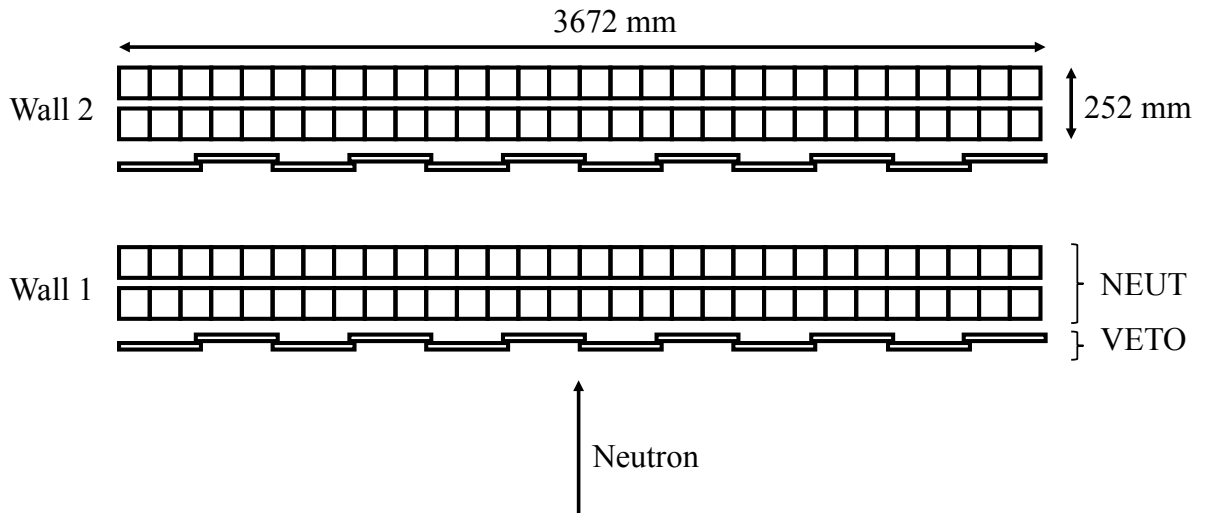
Figure 3.20: Layout of the NEBULA.

Two PMTs (Hamamatsu R7724 Assy.) were attached at the both ends of NEUT and VETO to read out the light output. The anode signals from the PMTs were split into two. One split signal, after being cable-delayed by 500 ns, was input to the CAEN QDC V792 to record the charge

[6]Acronym for "NEutron detection system for Breakup of Unstable nuclei with Large Acceptance".

Table 3.13: Specifications of the NEBULA.

Configuration	2 layers with full width
Plastic scintillator	Saint-Gobain BC-408
	12 cm^w × 180 cm^h × 12 cm^t (NEUT)
	32 cm^w × 190 cm^h × 1 cm^t (VETO)
PMT	Hamamatsu R7724 Assy.
Number of detectors	120 modules (NEUT)
	24 modules (VETO)
Effective area	3.6 m^w × 1.8 m^h
Detection efficiency	34.3% for one neutron (E_{th} = 6 MeV$_{ee}$)

information. The other was sent to the leading edge discriminator CAEN V895 to generate logic signals. The timing of the logic signals was recorded by the CAEN TDC V775 with a cable delay of 500 ns.

A part of the decay neutrons was out of the acceptance of the NEBULA. The acceptance strongly depended on the relative energy (Sec. 5.11).

The PMT voltage for a NEUT module was optimized so that the light output of 200 MeV$_{ee}$ is in the dynamic range of the QDC module. The typical voltage was −1300 V. The discriminator threshold setting was −25 mV, that is sufficiently lower than the software threshold of 6 MeV$_{ee}$. The PMT voltage and discriminator threshold setting for VETO modules were typically −1600 V and −15 mV, respectively, not to lose detection efficiency for protons.

The software threshold of 6 MeV$_{ee}$ was applied to eliminate background events due to gamma rays. The detection efficiency for 250-MeV neutrons was $34.3 \pm 0.7\%$ with the software threshold of 6 MeV$_{ee}$ [121].

3.12   Electronic circuits and data acquisition

In the present experiment, the data acquisition (DAQ) was based on a common trigger scheme, where all the signals from detectors were processed all together so as to keep the correlation among them. The data were handled with the standard framework of RIBF DAQ [122]. This framework is based on the distributed computing and the Gigabit Ethernet for the sake of high flexibility as well as high throughput. However, it was not suited for fast signal processing due to the interrupt latency of the CPU in the order of several or several tens of μs. Since the trigger signal should have been handled within several tens of ns, the electronic modules based on the Nuclear Instrumentation Module (NIM) standard were used for trigger making.

3.12.1 Data acquisition system

As mentioned above, the present DAQ employed the framework of the RIBF standard DAQ [122]. The DAQ system of the MINOS device was based on a different framework (Mordicus [111]). In this experiment, the MINOS DAQ was integrated as one of the subsystems according to the method described in Ref. [123].

The DAQ system in the present experiment comprised a Linux PC serving as a master event builder and fourteen front-end machines serving as DAQ subsystems (event sender) in the slave mode, as listed in Table 3.14. The event senders collected data from the electronics locally attached to the detectors, and after packing the data (event fragment), sent them to the event builder via a local area network. The event builder collected all the event fragments from the event senders, and reconstructed them as an *event*. For each event, the responses of all the detectors based on the common trigger signal were recorded.

Table 3.14: List of components of the DAQ system.

Component	Bus	Front end	Dead time	Detector
sdaq02	-	PC	-	(Event builder)
sva03	VME	VMIVME-7768	50 μs	BigRIPS detectors
sdaq07	VME	SBS-620 + PC	150 μs	HODF
sdaq08	VME	SBS-620 + PC	460 μs	FDC2 (1 of 2)
sdaq09	CAMAC	CC/7700 + PC	300 μs	SBTs
sdaq10	VME	SBS-620 + PC	220 μs	FDC2 (2 of 2)
sdaq11	VME	SBS-620 + PC	200 μs	FDC1
sdaq12	VME	SBS-620 + PC	150 μs	BDC1 and BDC2
sdaq13	VME	SBS-620 + PC	400 μs	HODP
sdaq14	VME	SBS-620 + PC	200 μs	NEBULA
sdaq19	VME	VMIVME-7768	200 μs	WINDS
sdaq20	VME	VMIVME-7807	60 μs	SBTs, ACOL, and BV
sdaq22	VME	VMIVME-7807	60 μs	DALI2
sdaq25	VME	VMIVME-7768	60 μs	RPDC and RPTOF
sdaq26	dedicated	Feminos + PC	60 μs	MINOS

The event senders except sdaq26 (event sender for the MINOS) collected data from individual digitization modules through a Versa Module Europa (VME) bus or a Computer Automated Measurement And Control (CAMAC) bus and sent the data to the event builder (sdaq02). Each event sender had a front end system to communicate with the event builder. The hardware composing each front end system was listed in the third column of the table.

The data stream from the MINOS was first processed by Feminos cards [104] and transferred to the Linux PC via the Gigabit Ethernet, where the dedicated DAQ program Mordicus was running. Newly implemented program in the Mordicus converted the data format to the RIBF data format [124] and sent the data to the event builder as one of the event senders.

The accepted trigger rate was limited by the event sender having the largest dead time. Due to the large number of channels (1568 ch) and slow readout system based on SBS-620, one of the event senders for the FDC2 (sdaq08) had the longest dead time, 460 μs. The averaged accepted trigger rate was 700 cps with a request rate of 1.2 kcps, and a live time was about 60%. The averaged data throughput was 15 MB/s.

3.12.2   Trigger logic

The request trigger signal was generated by making the coincidence between logic signals from SBTs (beam trigger) and those from RPTOF (recoil proton trigger). Figure 3.21 shows a simplified circuit diagram of the beam trigger and the recoil proton trigger signals. The recoil proton trigger was defined as the logical sum of the 11 RPTOF modules. The logic signal of each RPTOF module was the coincidence signal between the two signals from the PMTs at both ends of the module. Thus, the recoil proton trigger signal triggered events where at least one RPTOF module was fired.

The beam trigger was defined as a logical product of SBT1, SBT2, $\overline{\text{ACOL}}$, and $\overline{\text{BV}}$. Thus, the beam trigger signal triggered events where both SBT1 and SBT2 were fired but without firing in ACOL nor BV. The timing of the signal was always defined by the timing of the left PMT of the SBT1.

Figure 3.22 shows a circuit diagram of the trigger logic circuit for making the accepted trigger signal from the requested trigger signal. The accepted trigger signal was produced from the requested trigger signal when all the DAQ subsystems were ready. This function was realized by using a coincidence module with a VETO gate as described below. The accepted trigger signal was distributed to all the DAQ subsystems to start the data acquisition. This signal enabled the VETO gate at the same time so as to suppress following accepted trigger signals. After finishing the data processing, each DAQ subsystem sent an End-of-Busy (EOB) signal so as to disable each latch module. When all the EOB signals were received, the VETO gate was disabled, and then, the next accepted trigger was provided. This VETO circuit was realized by using the GTO module [125, 126].
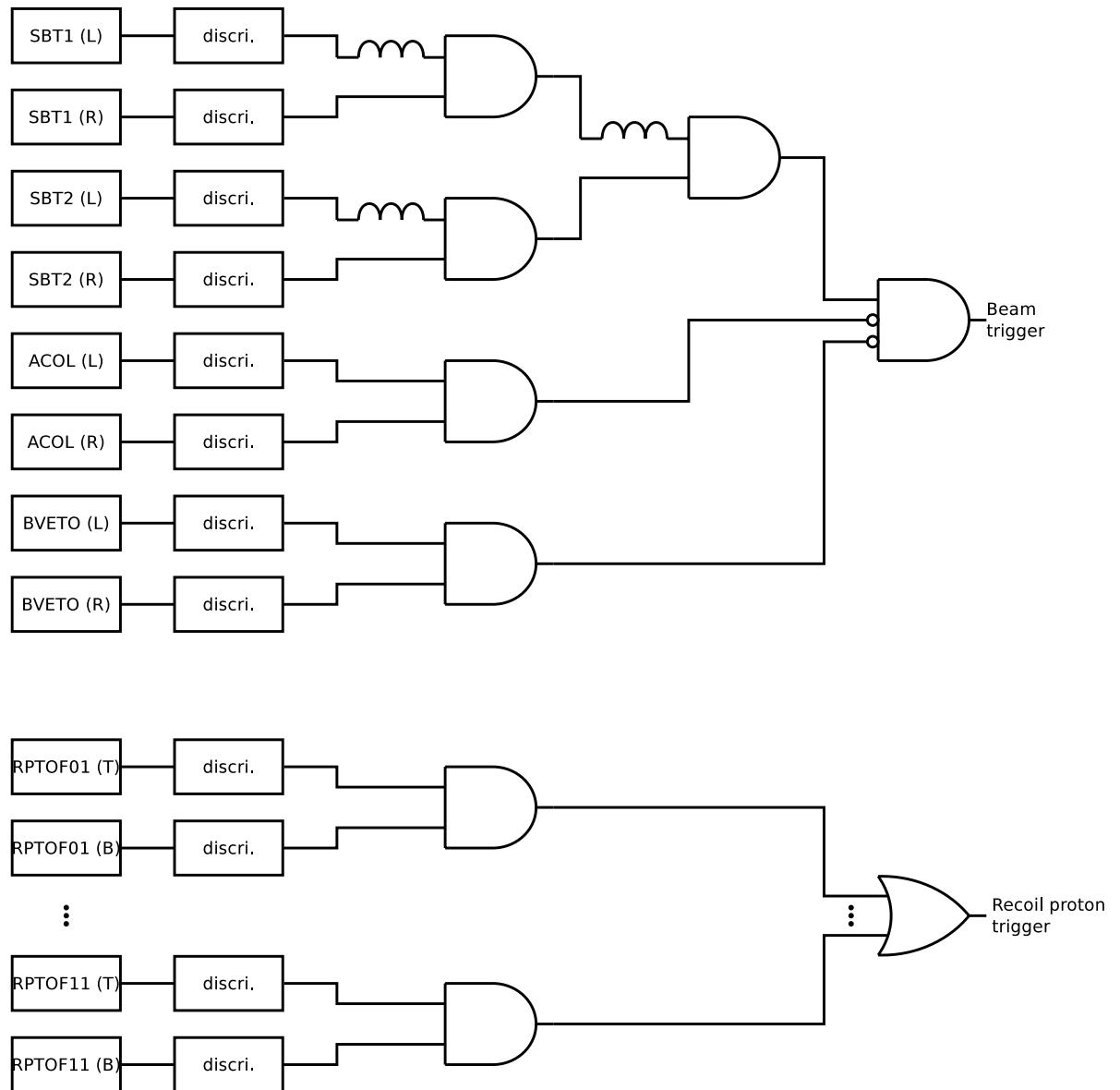
Figure 3.21: Simplified circuit diagram of (top) the beam trigger and (bottom) the recoil proton trigger.
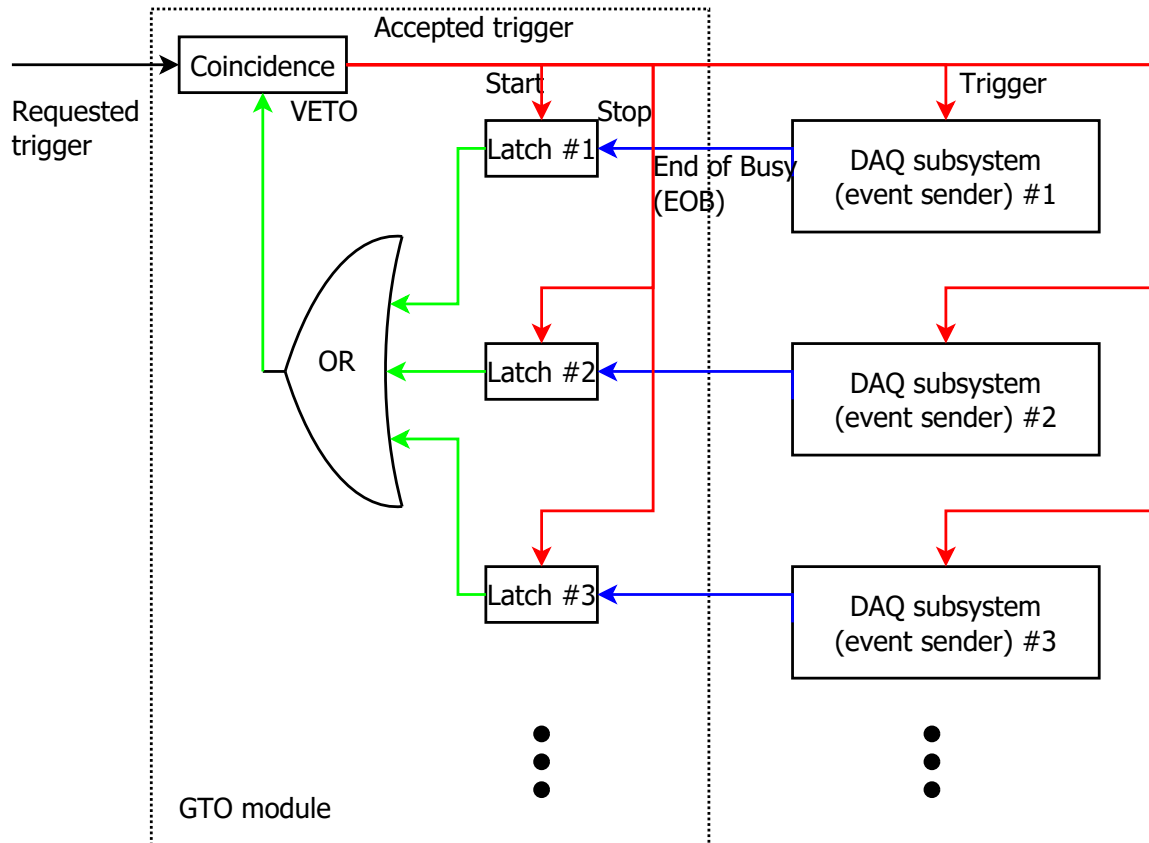
Figure 3.22: Circuit diagram for a trigger logic. The black, the red, the blue, and the green arrows represent signal lines for the requested trigger, the accepted trigger, the EOB signal, and the VETO gate, respectively. The circuits enclosed with the dotted rectangle is implemented in the GTO module.

3.13   Experimental conditions

The experiment was conducted at the end of 2014, from November 27th to December 8th. Due to the trouble of the production target, the beam time was split into two (Sec. 3.3.3). The data run of 36 hours was performed in the first half of the beam time. In the latter half, the data run of 40 hours and the calibration run with an empty target were performed. Through the measurement of 76 hours, the sufficient numbers of incident ^{11}Li particles and of (p, pn) events of 1.6×10^{10} and 9.6×10^{4}, respectively, were obtained. The experimental conditions are summarized in Table 3.15.

Table 3.15: Summary of the experimental conditions.

Item	Physics run (1)	Physics run (2)	Empty target run
Primary beam		^{48}Ca^{20+}	
energy		345 MeV/nucleon	
intensity		400 pnA	
Production target	29.8-mm^{t} ^{9}Be		19.9-mm^{t} ^{9}Be
Secondary beam		^{11}Li (, ^{14}Be, ^{17,19}B)	
energy		246 MeV/nucleon	
total intensity	140 kpps		140 kpps
Secondary target		Liquid H$_2$ 1.16 g/cm^2	Gas H$_2$ 3.93 mg/cm^2
Trigger rate	1.4 kcps	1.2 kcps	< 0.1 cps
Duration	36 h	40 h	0.5 h
Number of ^{11}Li particles on target	6.6×10^{9}	9.8×10^{9}	1.2×10^{8}
Number of (p, pn) events obtained	3.7×10^{4}	5.9×10^{4}	2

Chapter 4

Detector calibration and performance

This chapter describes the detector calibration and performance in detail. Analysis of the beam line plastic scintillators is given in Sec. 4.1. Analysis of the multi-wire drift chambers (MWDCs) is explained in Sec. 4.2. Analysis of the MINOS TPC is described in Sec. 4.3. Reconstruction procedures of the reaction point and the reaction timing are explained in Sec. 4.4. The results of the evaluated performances of the RPD, the WINDS, and the NEBULA are given in Sec. 4.5, Sec. 4.6, and Sec. 4.7, respectively. The performance of the (p, pn) setup composed of the RPD and the WINDS is confirmed in Sec. 4.8.

4.1 Beam line plastic scintillators

4.1.1 TDC channel to time calibration

Three types of TDC modules, REPIC RPC-180, CAEN V775, and CAEN V1290 were used for recording the timing signals from the plastic scintillators. For all these TDC modules, the time calibrator ORTEC 462 was used to determine the function of converting the TDC raw channel to the time unit.

Figure 4.1 shows a 2D plot of time versus TDC channel for one input channel in a REPIC RPC-180 module. The time t_{cal} was calculated from the raw data of the TDC t_{raw} as

$$t_{\text{cal}} = a \cdot t_{\text{raw}}, \tag{4.1}$$

where the coefficient a is a slope of the linear fitting function in Fig. 4.1.

The intrinsic time resolution was determined as 40 ps and 45 ps for REPIC RPC-180 and CAEN V775, respectively.
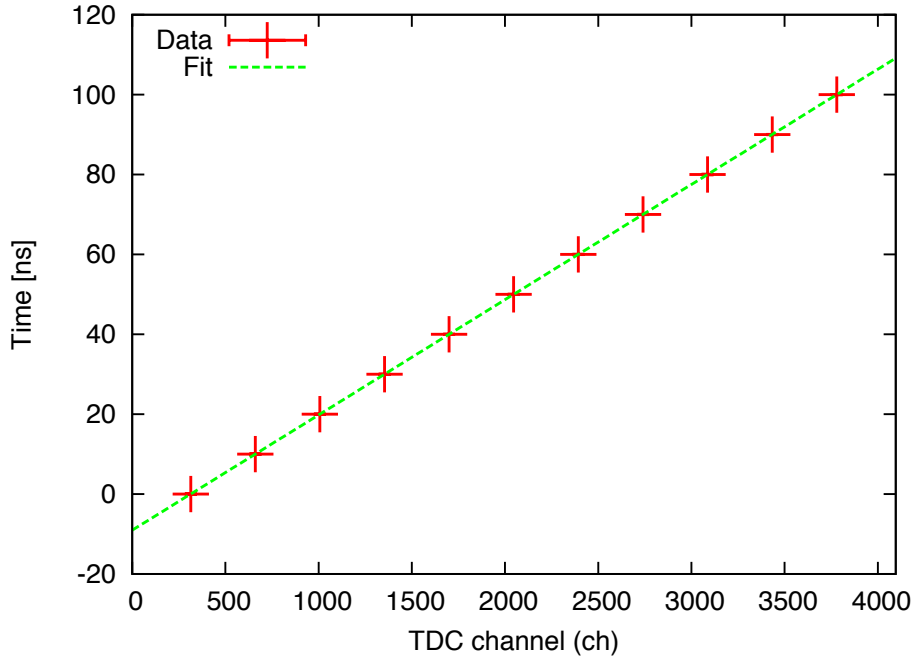
Figure 4.1: 2D plot of time versus TDC channel used for calibrating a channel in the REPIC RPC-180 TDC module. Each data point (red) has a 10-ns interval. The green dashed line represents the linear function to fit the data.

4.1.2   Differential nonlinearity correction for CAEN V1290

This section describes the correction of the differential nonlinearity of the CAEN multi-hit TDC V1290 module and obtained time resolution.

The TDC module has a least significant bit (LSB) size of 25 ps on average [127]. However, its time resolution is about 100 ps because of the variation of the LSB size (nonlinearity). In order to compensate this nonlinearity, the variation of the LSB size was determined as a function of the TDC channel. The variation was corrected for by the software, before performing the TDC channel to time calibration described in Sec. 4.1.1.

Figure 4.2(a) shows a raw TDC data distribution for random input signals. The spike structure is seen in the spectrum before the correction. Since the random input signal has no time structure and is not synchronized with the clock period of the TDC module, the distribution should be flat when the LSB size of all the channels is the same; the non-uniformity reflects the variation of the LSB size. The LSB size of each channel was determined so as to make the distribution flat as schematically shown in Fig. 4.2(b).

The intrinsic time resolution was evaluated from the width of the time difference between two input channels with the same signal. Figure 4.2(c) shows the time differences before and after the correction. The width of the spectrum corresponds to the quadratic sum of the time resolutions of the two channels. The peak structure became sharp after the correction. The intrinsic time resolution of one channel in the CAEN multi-hit TDC V1290 was evaluated as
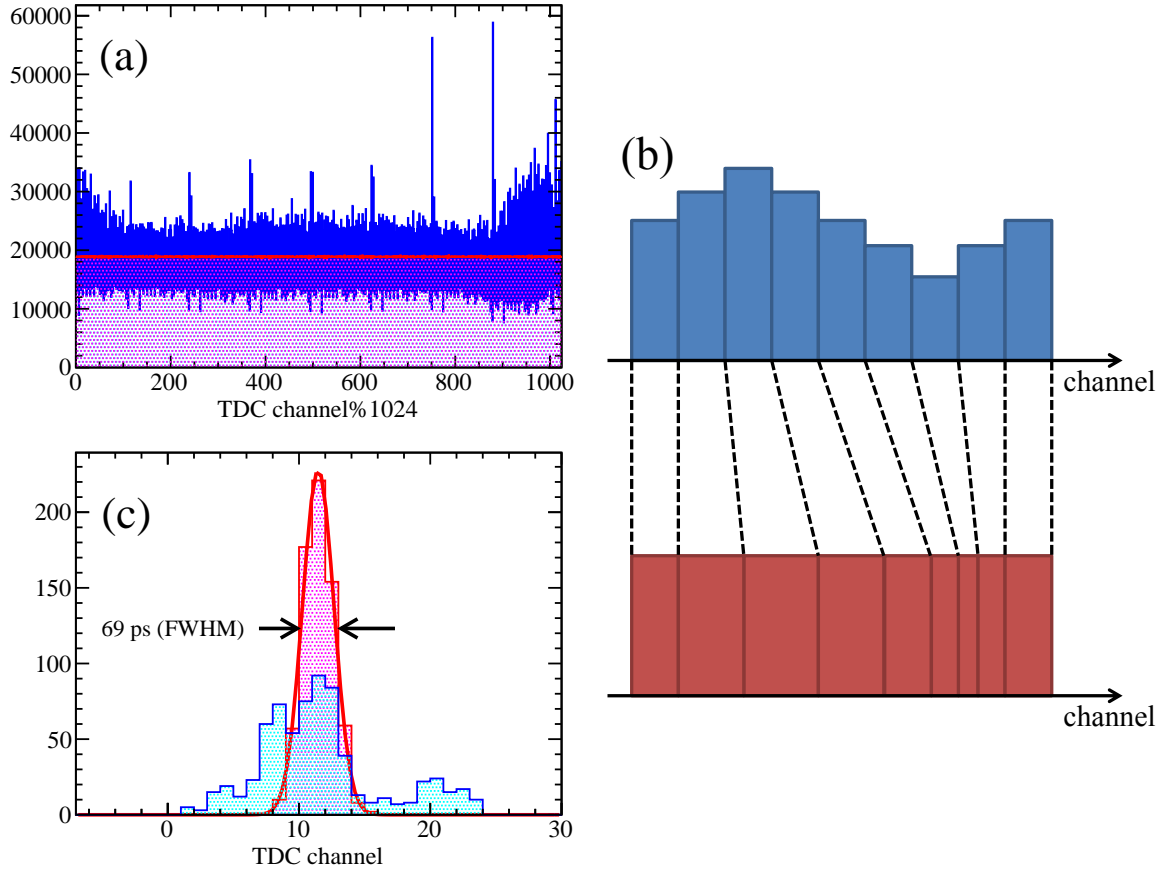
Figure 4.2: (a) Raw data distributions for the random input signals (blue) before the correction and (red) after the correction for one input channel in the CAEN V1290 module. (b) Schematic view of the correction for differential nonlinearity. (c) Time difference between two input channels with the same signal. See the text for details.

50 ps (FWHM).

4.1.3   Slew correction

In the present experiment, most of the signals from the PMTs attached to the plastic scintillators were converted into the logic signals by using leading edge discriminators. A leading edge discriminator outputs the logic signal when the pulse height of the input signal exceeds a certain threshold value. A smaller input signal needs a longer time to exceed the threshold value, while a larger input signals a shorter time. It results in the so-called walk effect, i.e. the discrimination timing relative to the physical timing varies depending on the pulse height.

In order to compensate the walk effect, the timing information was corrected by using the light output information. The incident cocktail beam particles were used for the correction. The slew correction was performed by using the phenomenological correction function of third-degree polynomial $f_{\text{pol3}}(Q)$ as

$$f_{\text{pol3}}(Q) = c_0 + c_1 Q + c_2 Q^2 + c_3 Q^3, \tag{4.2}$$

where Q represents the light output and c_0, c_1, c_2, and c_3 represent coefficients to be calibrated. Figures 4.3(a) and (b) show timing and light output correlation of SBT before and after applying the slew correction. Figure 4.3(c) shows the projection of left two plots onto the vertical axes. The timing resolution of SBT was obtained from the width of the peak as 81 ps (FWHM).

The slew correction was also applied for the plastic scintillator at F7 in a similar way. However, it is difficult to evaluate its intrinsic time resolution because there was only one plastic scintillator at F7. The overall TOF resolution is discussed in Sec. 5.3.

4.1.4   Timing offset calibration

The above mentioned calibration and correction do not give time information having physical meaning such as time of flight. This is because the origin of the time recorded in the TDC modules does not correspond to the physical time origin like the reaction timing. The correction of the difference between the recorded time and the physical time can be done by adding some offset to the recorded time.

The timing offsets of the beam line plastic scintillators were calibrated by using the beam particles having known rigidity. The analysis is explained in Sec. 5.1.1.

4.2   Multi-wire drift chamber

MWDCs are complex systems. Below, their basic structures and functions are quickly described to make the understanding of the analysis procedure easier.
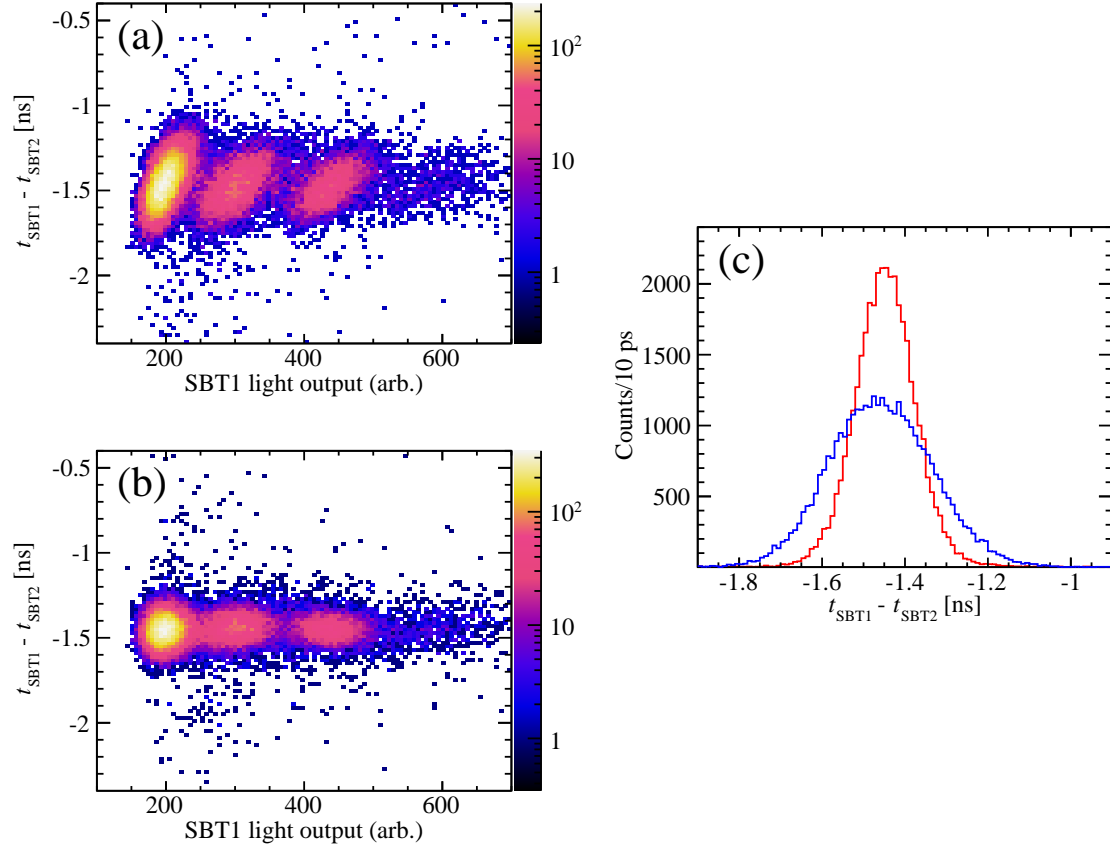
Figure 4.3: Timing and light output correlation of SBT (a) before the slew correction and (b) after applying the slew correction. The horizontal and the vertical axes show the mean light output of the SBT1 and the time difference between SBT1 and SBT2, respectively. Spots having light output of about 200, 300, 450, and 600 correspond to incident beam particles of Li, Be, B, and C isotopes, respectively. (c) The blue and the red lines show the time differences between SBT1 and SBT2 before and after applying the slew correction, respectively.

An MWDC consists of several sets of planes in which anode and potential wires are stretched in parallel, sandwiched between cathode planes. The negative high voltage of typically a few kV is applied for potential wires and cathode planes so as to make a strong electric field around the anode wire. The space between wires and planes is filled with a gas mixture. When charged particles pass through the MWDC, the gas is ionized, and then, produced electrons drift to the anode wires causing a charge avalanche so as to be detected as an electric signal. The drift time gives the distance information of the primary electrons from the anode wire; the position information perpendicular to the wire direction in a plane is determined by calibrating the drift time to the drift length. By combining multiple planes having different wire directions, the two-dimensional position information of incident particle is reconstructed.

In the present experiment, five MWDCs (BDC1, BDC2, FDC1, FDC2, and RPDC) were used for measuring the positions of ^{11}Li beam particle, heavy fragment ^{9}Li, and the recoil proton.

The wire and plane configurations are different detector by detector except for the case of BDC1 and BDC2. Details of the configuration are given in Sec. 3.6.4 for BDCs, Sec. 3.6.6 for FDC1 and FDC2, and Sec. 3.8.1 for RPDC.

4.2.1   Drift time to drift length calibration

Figure 4.4 shows the drift time distribution of each MWDC taken during the data run. The drift time for the RPDC was measured with respect to the RPTOF timing by employing the common start mode, while those for BDC1, BDC2, FDC1, and FDC2 were measured with respect to the SBT timing by employing the common stop mode. As for the RPDC, the left edge of the spectrum corresponds to the drift length of zero, namely the position of the anode wire. In the case of the others, the right edge of the spectra corresponds to the position of the anode wire.

Since the gradient of the electric field was steep around anode wires, the drift velocity around them was faster than that far from them. It results in the sharp peak around the edges mentioned above in the drift time distributions. This tendency was most clearly seen in the case of the RPDC. In the drift time distributions of BDC1 and BDC2, there are slightly smeared peaks. In those of FDC1 and FDC2, the peaks seem to be smoothed out. It was due to the different policy in the optimization of the operation voltage. The RPDC was bombarded only by the $Z = 1$ particles with an intensity of less than 1 kpps. Thus, the applied voltage was set sufficiently high so as to obtain a good position resolution. On the other hand, the MWDCs placed in the beam line, BDC1, BDC2, FDC1, and FDC2, were bombarded by the $Z \geq 3$ cocktail beam with an intensity of a several 100 kpps. When the HV is optimized for the $Z = 3$ particles, the effective beam intensity of the beam taking into the energy loss difference was almost 1 Mpps, which is almost maximum intensity that these MWDCs can accept. Therefore, the operation voltage was optimized so as to achieve enough high efficiencies for $Z = 3$ particles, but not optimized in terms of position resolutions.

During the data run, the position distribution of the bombarding particle was not uniform
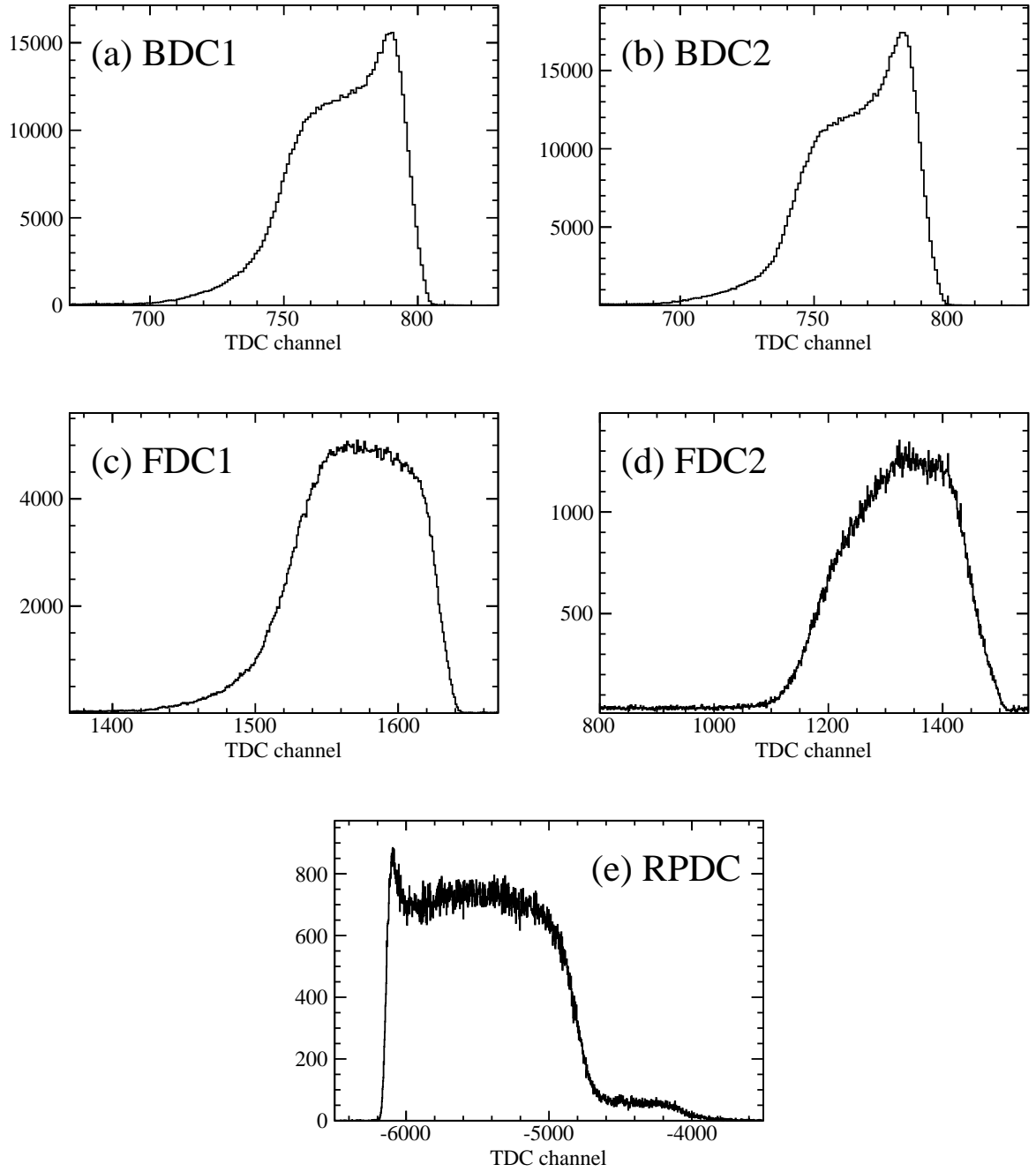
Figure 4.4: Drift time distributions for (a) BDC1, (b) BDC2, (c) FDC1, (d) FDC2, and (e) RPDC.

in the whole effective area of each MWDC as later shown in Sec. 4.2.3. However, the position distribution in each cell could be regarded as uniform because the cell size of each MWDC is smaller enough than the geometrical spread of the bombarding particle on each detector. Thus, we assume that the drift length was uniform in each cell. The drift length was calculated so as to make the drift length distribution flat. Figure 4.5 shows obtained conversion functions from the drift time to the drift length.

The drift length distribution is shown in Fig. 4.6. The spectra for BDC1, BDC2, FDC1, and FDC2 had large distortion. It implies the conversion function was not perfect. However, we did not struggle to improve it because the reasonable position distributions and residues were obtained even with these conversion functions (Sec. 4.2.4). The spectrum for RPDC was flat, suggesting the good conversion function.

4.2.2   Tracking algorithm

For each MWDC, the track of a bombarding particle was reconstructed by combining the position information at each plane. The procedure of the reconstruction was as follows:

1. The tracking is independently performed for each direction: x ($0°$), y ($90°$), u ($30°$), and v ($-30°$) directions. Events having at least two hit layers for each direction are analyzed.

2. All possible combinations of the fired wires in each plane are listed. The possible hit positions are fitted with a straight line, and sorted by the chi square. The list is called 1D track list.

3. Tracks with 10 least chi squares are selected and the others are discarded.

4. The 1D track list for each direction is merged into the 2D track list. The list is sorted by the chi square.

   - In the case of BDC1, BDC2, and RPDC, the 1D track list in x and y planes are simply merged by taking all possible combinations ($\leq 10 \times 10$), because the x and the y directions span a Cartesian coordinate, therefore, the 1D tracks obtained from x planes are independent of those from y planes.

   - FDC1 and FDC2 have x, u, and v planes. All possible combinations of 1D tracks in the x, u, and v planes ($\leq 10 \times 10 \times 10$) are taken to make the 2D track list. The x, u, and v directions make oblique angles, therefore, the 1D track obtained from one plane has correlations with that from the others. The position in x direction is calculated as an average of x, u, and v planes. The position in y direction is calculated as an average of u and v planes.

5. The 2D track candidate having the minimum chi square in the 2D track list is selected as the track.
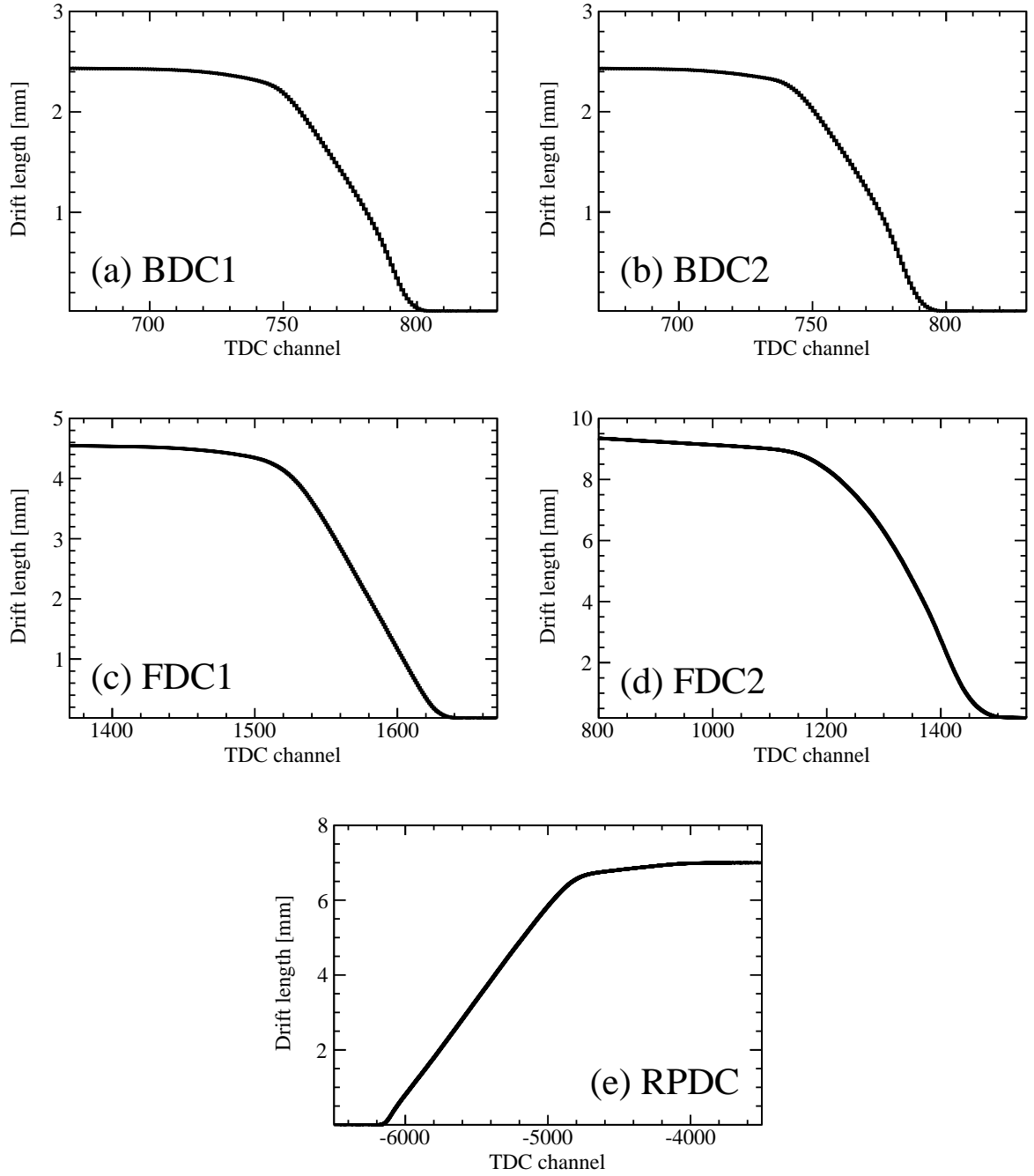
Figure 4.5: Conversion functions from the drift time to the drift length for (a) BDC1, (b) BDC2, (c) FDC1, (d) FDC2, and (e) RPDC.
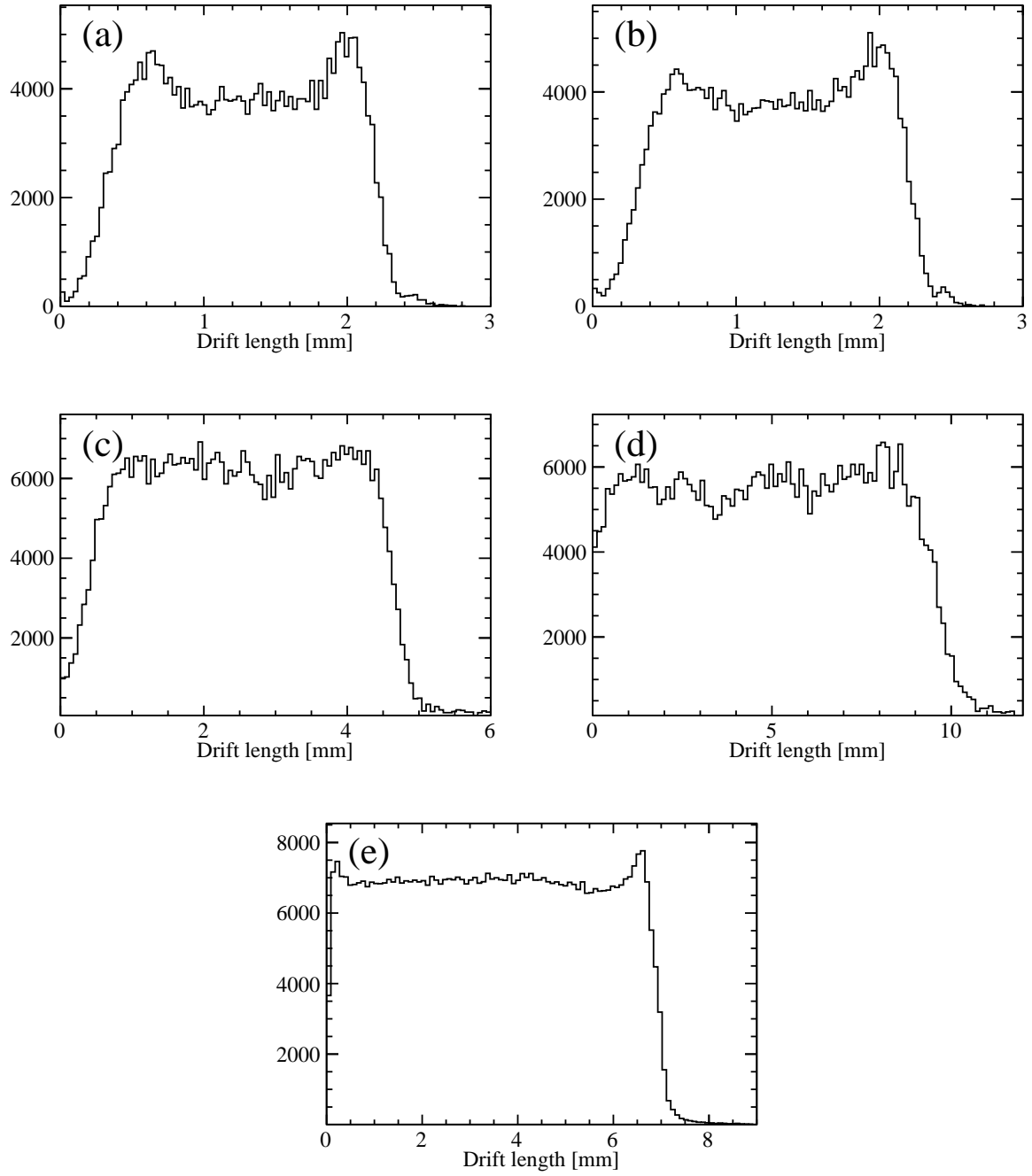
Figure 4.6: Drift length distributions for (a) BDC1, (b) BDC2, (c) FDC1, (d) FDC2, and (e) RPDC.

4.2.3 Incident particle profile of each drift chamber

Figure 4.7 shows the position distributions of the bombarding particle at the center of each MWDC. The effective area of the BDC1 was fully covered by the incident ^{11}Li beam particles, because the effective area was smaller than the beam profile at the position of the BDC1. The situation was almost same in the case of the BDC2. About 78% and 86% of the beam particles flew through the effective areas of the BDC1 and the BDC2, respectively. Events where beam particles passed outside the BDC1 or the BDC2 were not analyzed. The main constituents of the secondary beam used in the present experiment were ^{11}Li, ^{14}Be and ^{17}B, with A/Z values of 3.7, 3.5, and 3.4, respectively. In order to focus all the nuclides with a single configuration of the beam transport, ^{11}Li beam was not centered and had a finite angle with respect to the beam line, as seen in the asymmetric profiles in BDC1 and BDC2.

As compared to the ^{11}Li beam particles, the heavy fragment ^{9}Li particles were fully covered by the effective area of the FDC1. Very small fraction of them having a large spread in y direction was out of the acceptance of the FDC2 (Sec. 5.11). The spread along the x direction was fully covered by the FDC2.

As for the recoil proton, the whole effective area of the RPDC was bombarded. Events were concentrated on the $+x$ direction, which corresponds to the forward angle. This can be explained by the kinematics of the (p, pn) reaction: A scattering angle distribution from the (quasi-)elastic scattering has a peak at forward angle.

4.2.4 Position resolution

The position resolution of each MWDC was evaluated from the residual [128]. Figure 4.8 shows the correlation between the drift length and the residual of each MWDC. In spite of the rough calibration of the drift time to drift length conversion functions (Sec. 4.2.1), the distributions of the residual were reasonable; the residuals did not depend on the drift lengths. We speculate it was due to the high redundancy of the anode planes of these detectors. Although two anode planes for each direction are enough to perform the tracking, the BDC1 and the BDC2 both have four anode planes for each direction. Figure 4.9 shows the residual distributions of the MWDCs. The obtained resolutions are summarized in Table 4.1.

Table 4.1: Position resolutions and tracking efficiencies of the MWDCs. Resolution values are written in FWHM.

MWDC	Δx [μm]	Δy [μm]	ε
BDC1	410	410	99.8%
BDC2	430	430	99.6%
FDC1	420	460	98.8%
FDC2	540	540	93.1%
RPDC	220	190	92.3%
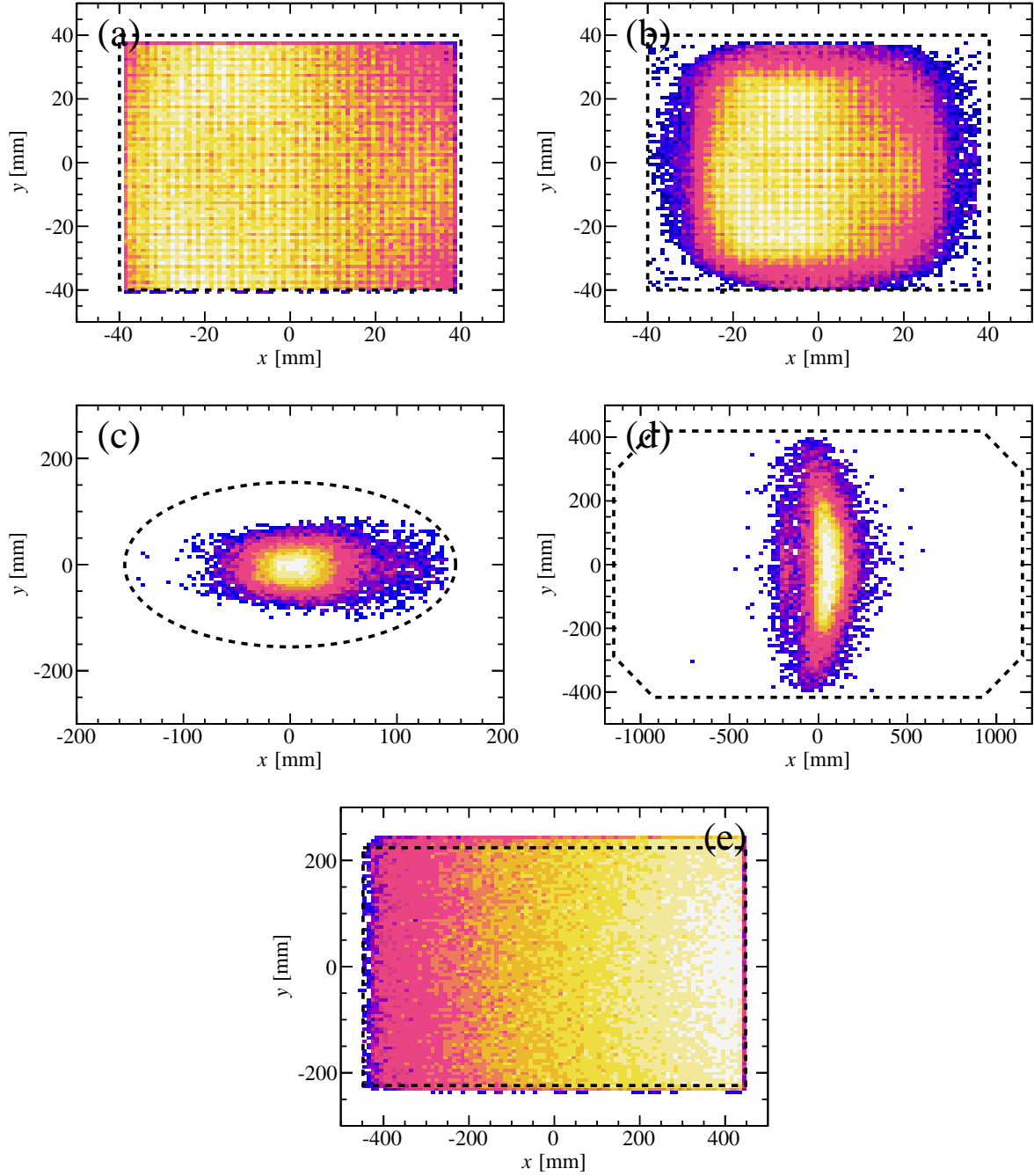
Figure 4.7: Position distributions of bombarding particles at the center of the MWDCs. ^{11}Li beam particles for BDC1 (a) and BDC2 (b), ^{9}Li heavy fragments for FDC1 (c) and FDC2 (d), recoil protons for RPDC (e). The dotted circle in (c) shows the acceptance of the entrance window of FDC1. The dotted lines in the other panels show the acceptances of the MWDCs.
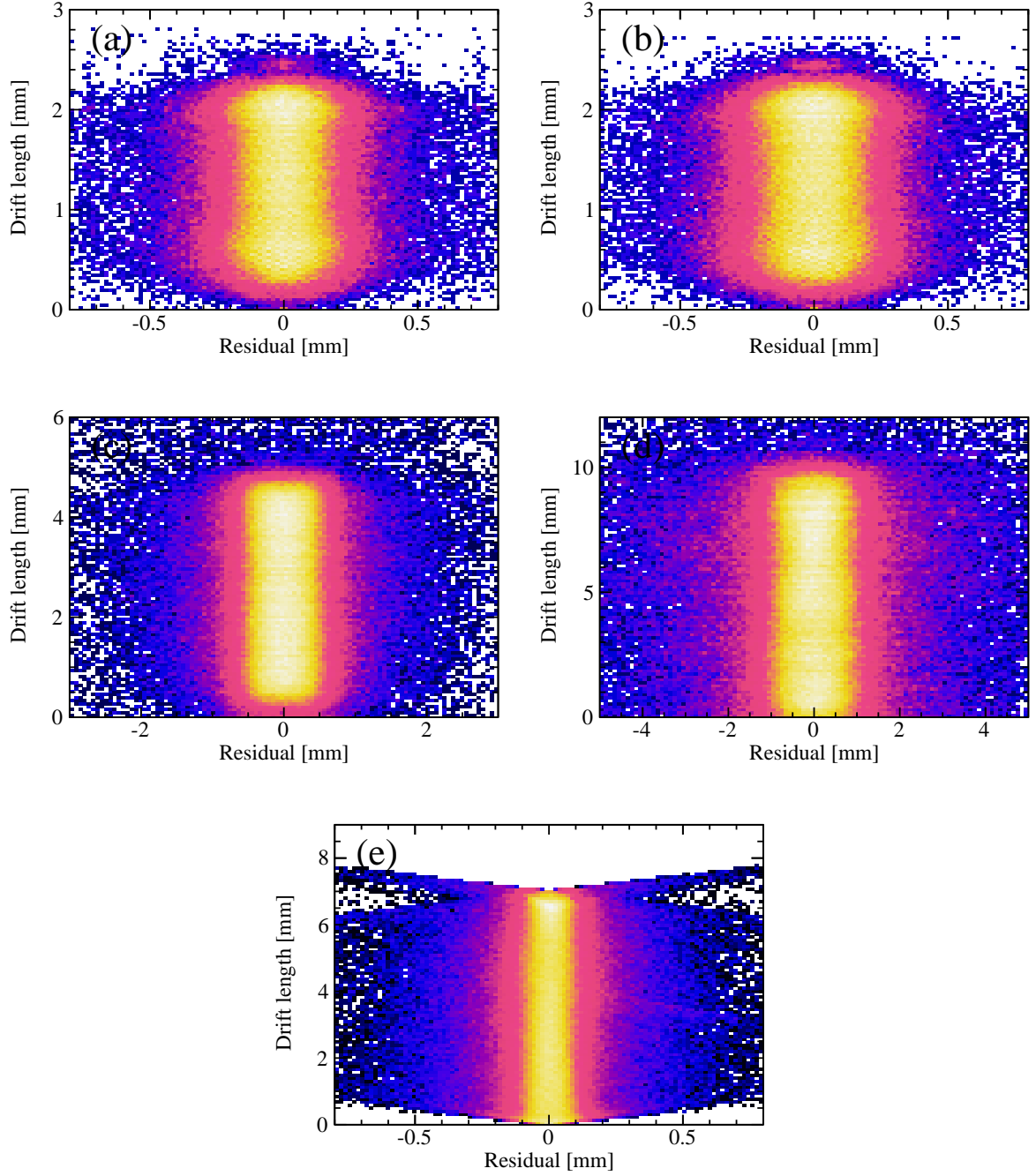
Figure 4.8: Correlation between the drift lengths and the residuals for (a) BDC1, (b) BDC2, (c) FDC1, (d) FDC2, and (e) RPDC.
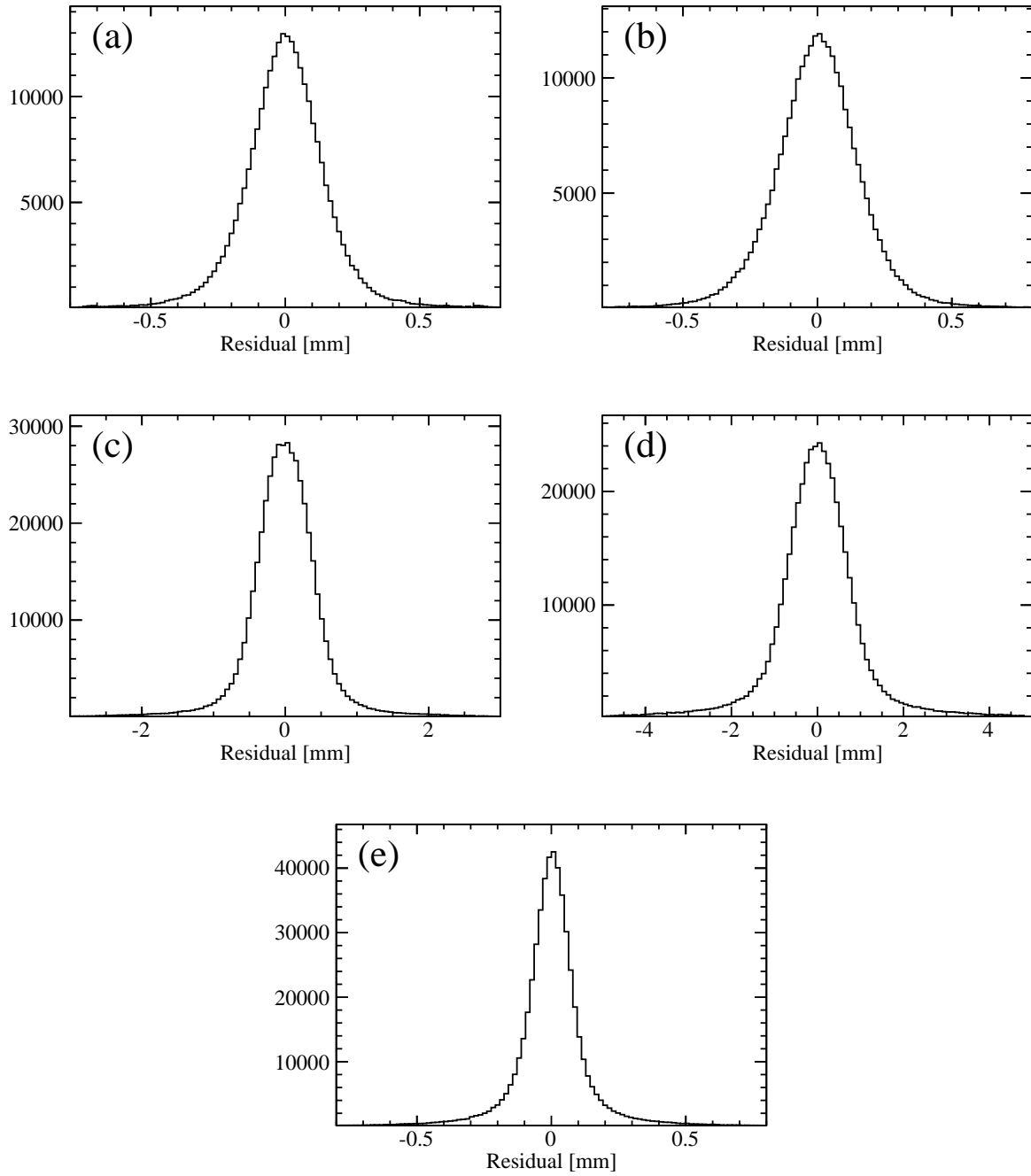
Figure 4.9: Residual distributions for (a) BDC1, (b) BDC2, (c) FDC1, (d) FDC2, and (e) RPDC.

4.2.5 Tracking efficiency

The tracking efficiencies of the BDC1 $\varepsilon_{\text{BDC1}}$ and the BDC2 $\varepsilon_{\text{BDC2}}$ were evaluated by using the number of count in the SBTs as the definition of the number of incident beam particles. In addition, the BDC2 or the BDC1 was used to select the beam spot so as to guarantee that the beam particle hit the BDC1 or the BDC2, respectively, because the beam profile was larger than the effective areas of BDCs (Sec. 4.2.3). The definitions of the $\varepsilon_{\text{BDC1}}$ and $\varepsilon_{\text{BDC2}}$ are

$$\varepsilon_{\text{BDC1}} = \frac{N\left(\text{BDC1} \cap \text{PID}(^{11}\text{Li}) \cap \text{BDC2}|_{\sqrt{x^2_{\text{BDC2}}+y^2_{\text{BDC2}}}<10 \text{ mm}}\right)}{N\left(\text{PID}(^{11}\text{Li}) \cap \text{BDC2}|_{\sqrt{x^2_{\text{BDC2}}+y^2_{\text{BDC2}}}<10 \text{ mm}}\right)}, \tag{4.3}$$

$$\varepsilon_{\text{BDC2}} = \frac{N\left(\text{BDC2} \cap \text{PID}(^{11}\text{Li}) \cap \text{BDC1}|_{\sqrt{x^2_{\text{BDC1}}+y^2_{\text{BDC1}}}<10 \text{ mm}}\right)}{N\left(\text{PID}(^{11}\text{Li}) \cap \text{BDC1}|_{\sqrt{x^2_{\text{BDC1}}+y^2_{\text{BDC1}}}<10 \text{ mm}}\right)}. \tag{4.4}$$

where $N(condition)$ denotes the number of events satisfying the *condition*. It should be noted that the condition "PID(^{11}Li)" implicitly requires the hit of the SBTs (Sec. 5.1.1).

The tracking efficiencies of the FDC1 $\varepsilon_{\text{FDC1}}$ and the FDC2 $\varepsilon_{\text{FDC2}}$ for the heavy fragment ^{9}Li were evaluated by using ^{11}Li beam particles; we assumed that the tracking efficiencies for $Z = 3$ particles were the same. Since ^{11}Li beam particles distributed from 3rd to 5th modules of HODF (Sec. 5.1.2), the number of incident ^{11}Li particles was defined by the number of counts with reasonable light output in the 4th module of the HODF. The definitions of the $\varepsilon_{\text{FDC1}}$ and $\varepsilon_{\text{FDC2}}$ are

$$\varepsilon_{\text{FDC1}} = \frac{N(\text{FDC1} \cap \text{Beam} \cap \text{HODF}|_{\text{ID}=4,Z=3})}{N(\text{Beam} \cap \text{HODF}|_{\text{ID}=4,Z=3})}, \tag{4.5}$$

$$\varepsilon_{\text{FDC2}} = \frac{N(\text{FDC2} \cap \text{Beam} \cap \text{HODF}|_{\text{ID}=4,Z=3})}{N(\text{Beam} \cap \text{HODF}|_{\text{ID}=4,Z=3})}, \tag{4.6}$$

$$\text{Beam} := \text{PID}(^{11}\text{Li}) \cap \text{BDC1}|_{\sqrt{x^2_{\text{BDC1}}+y^2_{\text{BDC1}}}<10 \text{ mm}} \cap \text{BDC2}|_{\sqrt{x^2_{\text{BDC2}}+y^2_{\text{BDC2}}}<10 \text{ mm}}. \tag{4.7}$$

The tracking efficiency of RPDC was obtained using RPTOF as a reference of the number of incident protons. The effective area of the RPDC was smaller than that of the RPTOF. For the tracking efficiency evaluation, events in an area smaller than the effective area of the RPDC were selected so as to reject protons outside the effective area of the RPDC; seven RPTOF modules placed at the middle ($2 < \text{ID} < 10$) was selected to limit the position along the x direction. The position along the y direction was limited by selecting the $|y_{\text{RPTOF}}| < 100$ mm region. The selected y region is smaller enough than the effective area of the RPDC, after taking into account the position resolution of the RPTOF in y direction of 6.5 cm (FWHM). In addition, the light output larger than 6 MeV$_{\text{ee}}$ was required for rejecting events due to gamma rays in the RPTOF.

Thus, the tracking efficiency of the RPDC was calculated as

$$\varepsilon_{\text{RPDC}} = \frac{N(\text{RPDC} \cap \text{RPTOF}|_{2<\text{ID}<10,\ |y_{\text{RPTOF}}|<100\ \text{mm},\ Q>6\ \text{MeV}_{\text{ee}}})}{N(\text{RPTOF}|_{2<\text{ID}<10,\ |y_{\text{RPTOF}}|<100\ \text{mm},\ Q>6\ \text{MeV}_{\text{ee}}})}. \tag{4.8}$$

The $\varepsilon_{\text{RPDC}}$ was evaluated for each RPTOF module separately so as to evaluate the uniformity of the efficiency. The standard deviation of $\varepsilon_{\text{RPDC}}$ values was as low as 0.7%.

The obtained tracking efficiencies are summarized in Table 4.1. All the MWDCs worked reasonably well.

4.3 MINOS TPC

Proton track information of the MINOS TPC was obtained through the analysis procedure based on the Hough transform [129] and the pattern recognition [130, 131], as given in Ref. [132]. This section describes the calibration performed specifically for the present experiment.

4.3.1 Drift velocity

The blue colored spectrum in Fig. 4.10 shows a drift time distribution of the MINOS TPC. There are two edges around 1.5 and 8.5 μs in the drift time distribution. Since the trajectory of the recoil proton covered all the effective area of the TPC, these edges corresponded to the both ends of the TPC. The drift velocity was calibrated by comparing the drift time difference between two edges to the known distance of 30 cm. The edge positions were defined by the peak positions in the derivative of the distribution, as shown in the green colored spectrum in Fig. 4.10. The drift velocity was determined as 4.61 cm/μs. The uncertainty of the edge position was evaluated from the widths of the peaks as 7.8 mm (FWHM). Therefore, the systematic uncertainty for the drift velocity was evaluated as 2.6%.

4.3.2 Tracking efficiency

The kinetic energy of the recoil proton ranged from about 50 to 300 MeV. Although all the recoil proton passed through the TPC, the energy loss varied between 0.2 and 0.8 MeV depending on the kinetic energy. This energy loss difference could result in the non-uniform tracking efficiency of the MINOS TPC. The energy loss dependence of the tracking efficiency was investigated through the scattering angle dependence since the kinetic energy and the scattering angle of the recoil proton were strongly correlated (Sec. 4.5.4).

The tracking efficiency of the MINOS TPC $\varepsilon_{\text{MINOS}}$ was evaluated by comparing the numbers of events detected by the MINOS TPC and by the RPD. By employing the same notation in
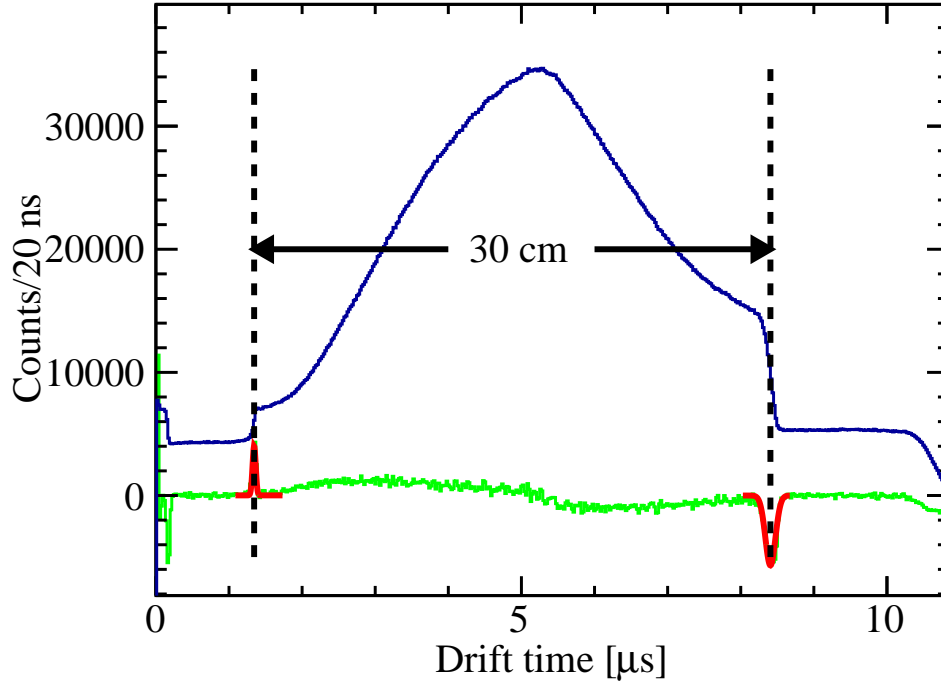
Figure 4.10: Drift time distribution of the MINOS TPC (blue) and its derivative (green). The vertical dashed lines show the both ends of the TPC.

Sec. 4.2.5, the definition of the $\varepsilon_{\text{MINOS}}$ is written as

$$\varepsilon_{\text{MINOS}} = \frac{N\,(\text{MINOS} \cap \text{RPD})}{N\,(\text{RPD})}. \tag{4.9}$$

It should be noted that the detection efficiency of the RPD ε_{RPD} had no scattering angle dependence, because the detection efficiencies of the components of the RPD, the RPDC and the RPTOF, were uniform for recoil protons having various scattering angles and kinetic energies. The discriminator threshold for the RPTOF was set to sufficiently low so that the $\varepsilon_{\text{RPTOF}}$ value was 100% (Sec. 3.8.2), and the standard deviation of $\varepsilon_{\text{RPDC}}$ values for different scattering angles was evaluated as low as 0.7% (Sec. 4.2.5).

Figure 4.11 shows the tracking efficiency of the MINOS TPC $\varepsilon_{\text{MINOS}}$ as a function of the scattering angle of the recoil proton θ_p. The tracking efficiency was uniform and larger than 90% for the region, which was covered by the RPD. The averaged $\varepsilon_{\text{MINOS}}$ value was 92.6% and the standard deviation was 1.1%. By subtracting the contribution from the RPD, the non-uniformity was evaluated as low as 0.8%. Although the tracking efficiency for the effective region of the TPC which was not covered by the RPD was not evaluated, the region was not used in the present study.
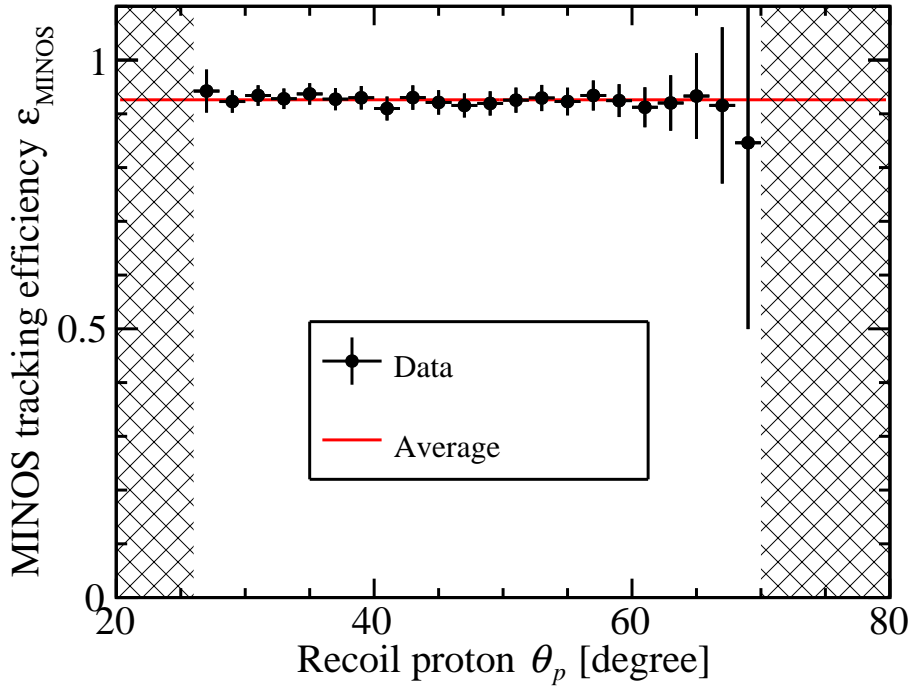
Figure 4.11: Tracking efficiency of the MINOS TPC as a function of the scattering angle of the recoil proton. The hatched areas represent ineffective areas of the RPD.

4.4   Reaction point and reaction timing reconstruction

In this experiment, the 15-cm-thick liquid hydrogen target was used. This section describes how to determine the reaction point in the time and space coordinate system, $(t_0, \mathbf{r_0})$.

The MINOS is originally designed to be used in the $(p, 2p)$ measurement, where two protons are emitted from the liquid hydrogen target at large polar angle and both detected in the TPC. The reaction point is reconstructed from the trajectories of the two protons [132]. However, in the present experiment, only one proton is emitted through the (p, pn) reaction. Therefore, we used the trajectory information of incident beam particles to determine the reaction point.

The reaction point $\mathbf{r_0}$ in the liquid hydrogen target was derived by combining the tracks of the incident beam particle and the recoil proton. Ideally, the trajectories of the incident beam particle and the recoil proton should always have a crossing point just at the reaction point. However, in reality, that is not the case because of the finite resolution of each detector and the angular straggling of the particles. Thus, the reaction point $\mathbf{r_0}$ was derived as

$$\mathbf{r_0} = \frac{\mathbf{r_{b0}} + \mathbf{r}_{p0}}{2},\tag{4.10}$$

where the position vectors, $\mathbf{r_{b0}}$ and $\mathbf{r}_{p0}$, are on the trajectories of the beam and the recoil proton, respectively, and are chosen such that the norm $|\mathbf{r_{b0}} - \mathbf{r}_{p0}|$ become minimal, therefore corresponding the minimum distance between the two trajectories. Figure 4.12 shows a schematic

view of the definition of the reaction point.
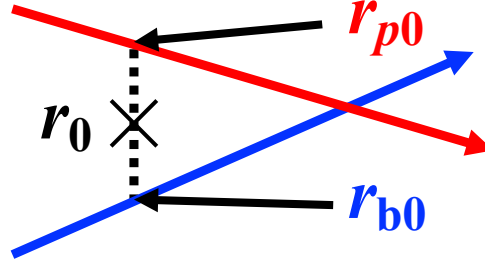
Figure 4.12: Schematic view of the definition of the reaction point r_0. The blue and the red arrows represent trajectories of the beam particle and the recoil proton, respectively. The dotted line gives the minimum distance between two trajectories.

The beam trajectory was reconstructed from the beam position measured by the BDC1 and the BDC2. A beam trajectory unit vector $\hat{u}_b$ and the trajectory x_b were defined as

$$\hat{u}_b = \frac{r_{BDC1} - r_{BDC2}}{|r_{BDC1} - r_{BDC2}|}, \tag{4.11}$$

$$x_b = \alpha r_{BDC1} + (1 - \alpha) r_{BDC2}, \tag{4.12}$$

where r_{BDC1} and r_{BDC2} are the detection position of the beam particle at BDC1 and BDC2, as obtained in Sec. 4.2.

The reaction timing t_0 was determined as

$$t_0 = t_{F13} + \frac{|r_0 - r_{F13}|}{\beta_b c}, \tag{4.13}$$

where t_{F13}, r_{F13}, and $\beta_b c$ represents a beam timing at the SBT, a beam position at the SBT, and the beam velocity, respectively. The position of the SBT was defined as the middle point between the SBT1 and the SBT2, i.e. $z = -7418.6$ mm. The beam timing at the SBT was defined as the mean timing of the SBT1 and SBT2. The beam position at the SBT was determined by the extrapolation of the beam trajectory x_b to the SBT position. The derivation of the beam velocity is explained in Sec. 5.3.

4.4.1 Resolution and uncertainty

The position resolution of the reaction point r_0 was evaluated by using the $^{11}\text{Li}(p, 2p)$ channel. In this reaction channel, two protons were emitted from the target and both detected in the MINOS TPC. Therefore, there are three different ways to obtain the reaction point, as shown in Table 4.2, thereby giving the redundancy to check the resolution.

Figure 4.13 shows the differences between reconstructed reaction points $(r_{0,1} - r_{0,2})$ projected onto the x, y, and z direction. From the widths of the peaks, the position resolution of the

Table 4.2: List of combinations of two trajectories to obtain the reaction point in the ^{11}Li$(p, 2p)$ channel.

Trajectory 1	Trajectory 2	Analysis scheme	Reaction point
Recoil proton #1	Recoil proton #2	Standard [132]	$r_{0,1}$
Recoil proton #1	Incident beam	Sec. 4.4	$r_{0,2}$
Recoil proton #2	Incident beam	Sec. 4.4	$r_{0,3}$

reaction point projected onto the x, y, and z direction were determined as 4.6, 1.6, and 6.0 mm (FWHM), respectively. This resolution was reasonable as compared to the designed value of 5 mm (FWHM) in z direction [107]. This result also gave the validation of the reaction point reconstruction newly introduced in Sec. 4.4. It should be noted that the same result could be obtained by comparing the $r_{0,1}$ and $r_{0,3}$ because the kinematics of the recoil proton #1 and #2 were the same.
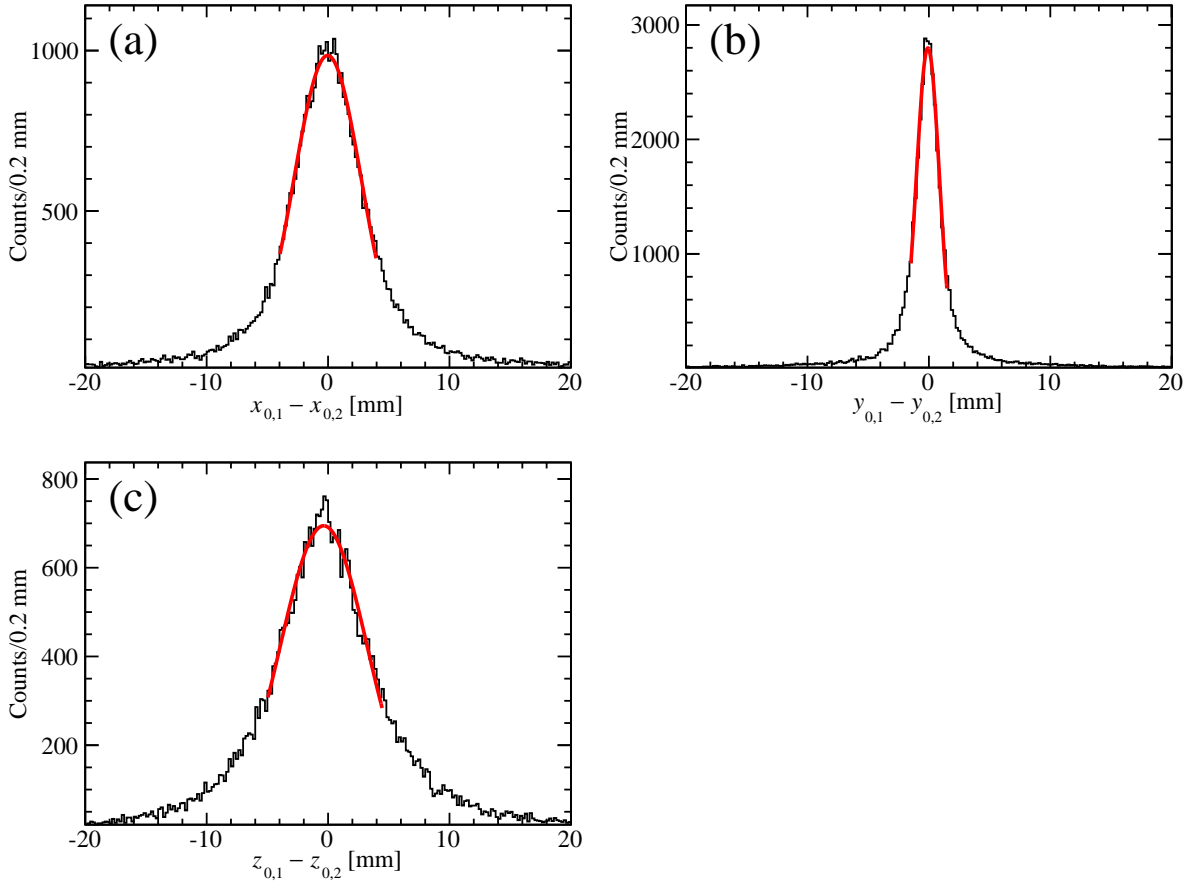
Figure 4.13: Differences between reconstructed reaction points ($r_{0,1} - r_{0,2}$) (a) projected onto the x, (b) the y, and (c) the z directions.

The resolution in x direction was worse than that in y direction in spite of the symmetries of the detectors. It is because the asymmetric distribution of the recoil proton due to a biased trigger defined by the RPD. Most recoil proton trajectories are approximately parallel to the (z, x) plane. In such a case, a small mismatching of the two trajectories coming from the resolution and the straggling results in large deviation in the x direction.

The systematic uncertainty of the reaction point r_0 mainly came from the extrapolation of the beam trajectory x_b from the BDCs. The positions of the BDCs were aligned within an uncertainty of 200 μm (FWHM) by employing the photogrammetry system [98, 99]. Thus, the most pessimistic estimation gave the uncertainty on the reaction point of 610 μm (FWHM).

The resolution of the reaction timing came from both the time resolution of the SBTs and the reaction point resolution as Eq. (4.13). The resolution was estimated as 88 ps (FWHM).

4.4.2 Event selection

Figure 4.14 shows the minimum distance between the tracks of the incident ^{11}Li beam particle and the recoil proton $|r_{b0} - r_{p0}|$. The events having the minimum distances less than 5 mm were selected for further analysis. The criterion of 5 mm was double of the FWHM of the minimum distance distribution shown in Fig. 4.14. This selection covered 89% of the total events. The other events in the tail were assumed as spurious events.
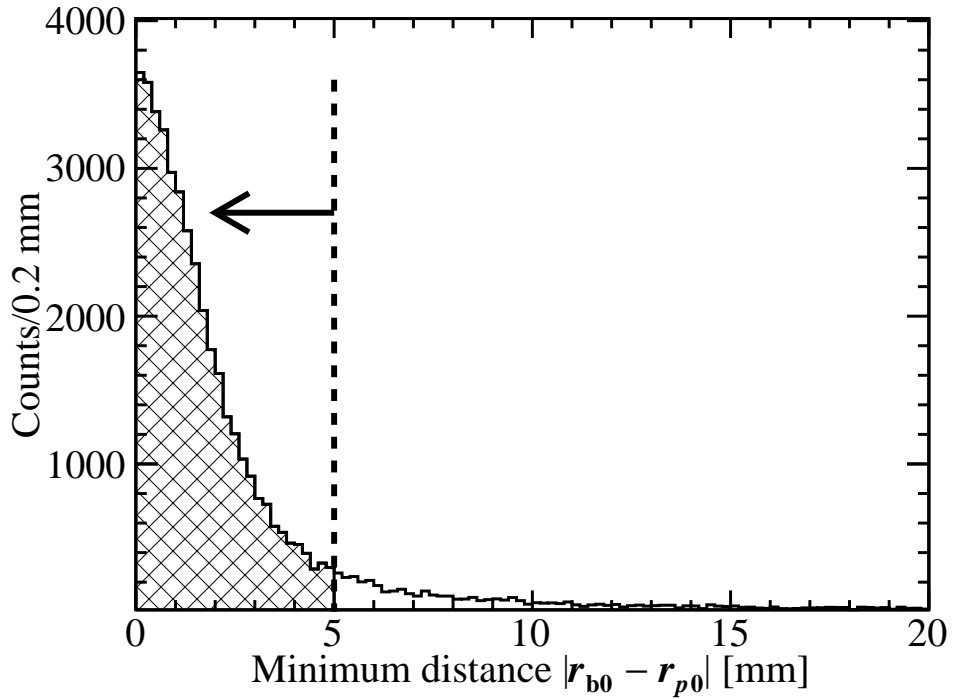
Figure 4.14: The minimum distance between tracks of the incident ^{11}Li beam particle and the recoil proton. The events with shaded area were selected for further analysis.

Figure 4.15 shows the reaction point distribution r_0. Because the reaction point has a finite resolution (Sec. 4.4.1), the cylindrical region, which has 5 mm smaller radius and 12 mm shorter length than the target cell, was selected for further analysis. 11% of the total events were rejected by this selection.
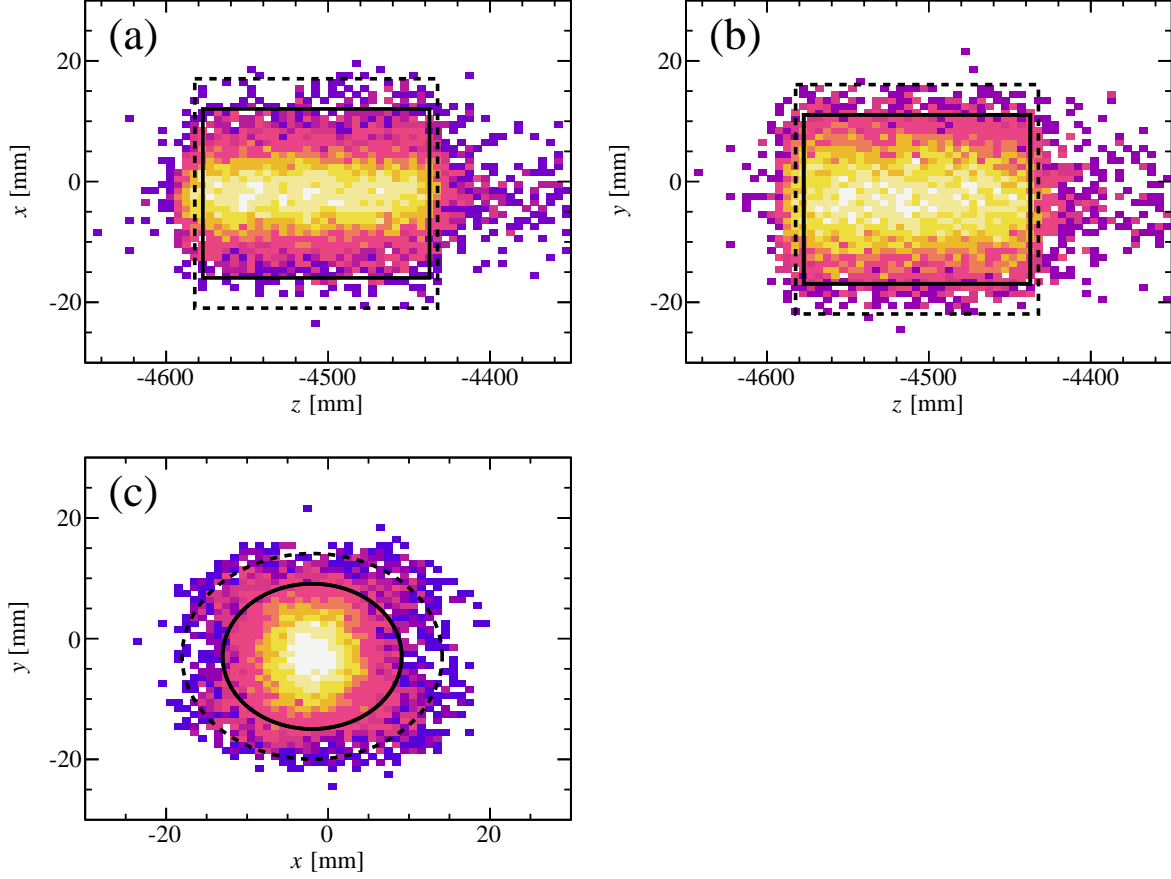
Figure 4.15: Reaction point r_0 distributions (a) in the (z, x), (b) the (z, y), and (c) the (x, y) planes. The black dotted lines shows the size of the target cell. The events enclosed with black solid line are selected as those where the reaction occurred in the target.

4.5 RPD

The performance of the RPDC is summarized in Sec. 4.2. This section describes the calibration of the RPTOF. The performance of the RPD by using the (p, pn) events is described in Sec. 4.8.

4.5.1 Slew correction

Slew correction of the RPTOF was performed by using the events taken during the physics run, in which the neighboring two detector modules were hit by one proton. In such an event, the

timing of the two detector modules should be the same.
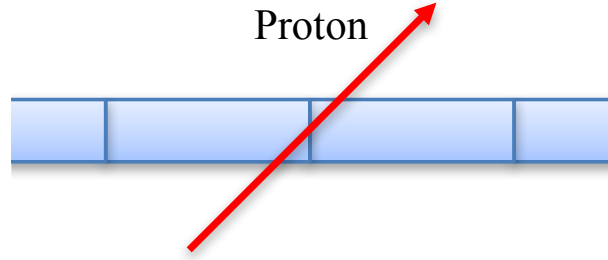
Figure 4.16: Schematic view of the event in which the neighboring two detector modules were hit by one incident proton. The blue boxes and the red arrow represent the detector modules and the incident proton, respectively.

The light output dependence of the time difference between neighboring detector modules was corrected by using the function $f(Q)$ defined as

$$f(Q) = c_0 + \frac{c_1}{(Q - c_2)^{1/2 + c_3}}, \tag{4.14}$$

where c_0, c_1, c_2, and c_3 are fitting parameters and Q is the light output. The parameters were independently determined for top and bottom PMTs. Figures 4.17(a) and (b) show the time difference between neighboring detector modules before and after applying the slew correction. Figure 4.17(c) shows the comparison of the time difference with and without the slew correction. The walk effect was successfully compensated by the correction.

4.5.2 TOF offset calibration

The TOF offset was calibrated by using gamma rays produced in the metal target in a calibration run. Figure 4.18 shows a TOF spectrum of one detector module of the RPTOF. The peak at zero corresponding to the gamma rays from the metal target was clearly identified so that the TOF offset was successfully calibrated. The precedent peak around -2 ns corresponds to the gamma rays produced in the SBT.

4.5.3 Resolution and uncertainty

In this subsection, the resolution and uncertainty of the TOF information obtained by RPTOF are shown.

The time resolution of the RPTOF strongly depended on the light output in scintillators. Since the kinetic energies of recoil protons ranged from 30 to 500 MeV, the light output of the recoil proton was widely spread from about 1.2 MeV$_{\text{ee}}$ to 12 MeVee depending on the recoil proton momentum (Sec. 5.1.3). Thus, the resulting time resolution also depended strongly on
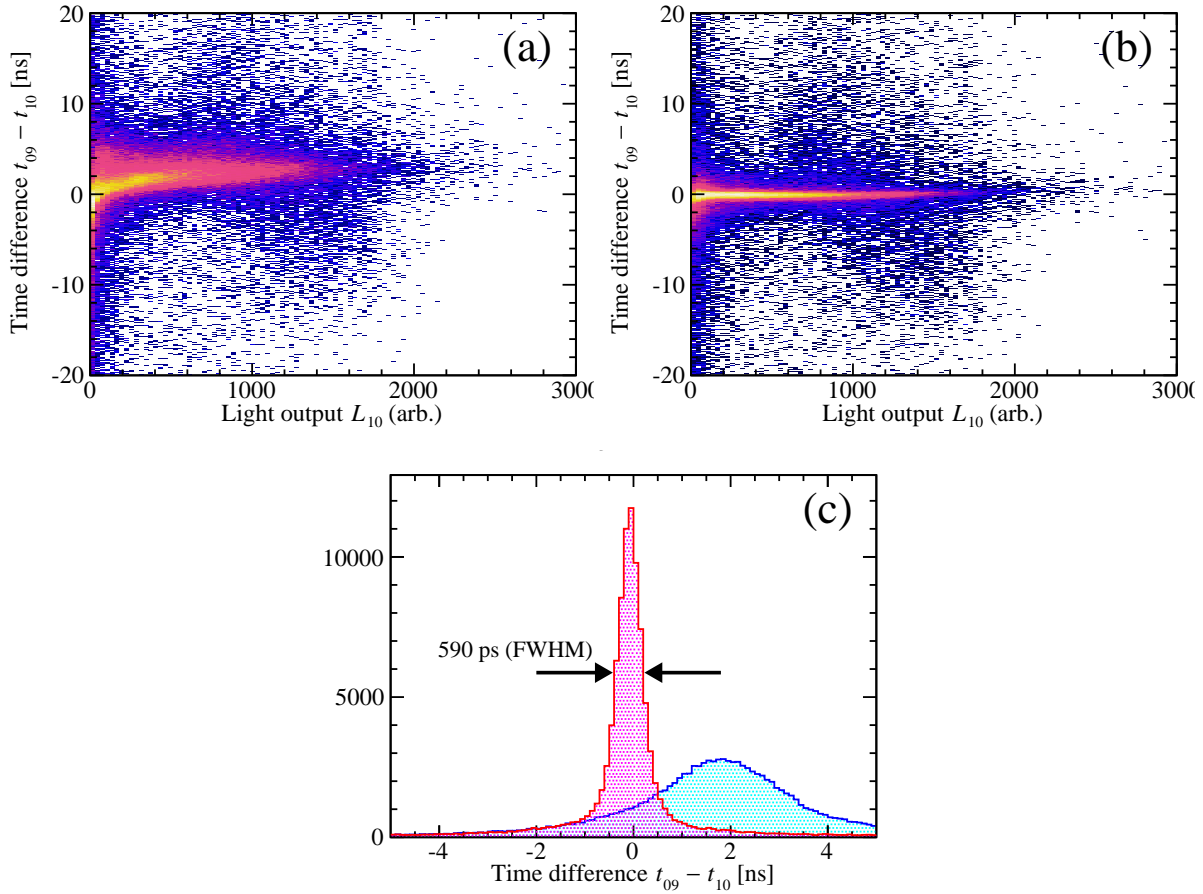
Figure 4.17: Time difference vs light output plots of RPTOF modules (a) before slew correction and (b) after applying the slew correction. The horizontal axis shows the mean light output of one detector module and vertical axis shows the time difference between neighboring detector modules. (c) Time difference spectra (blue) before the slew correction and (red) after applying the slew correction.
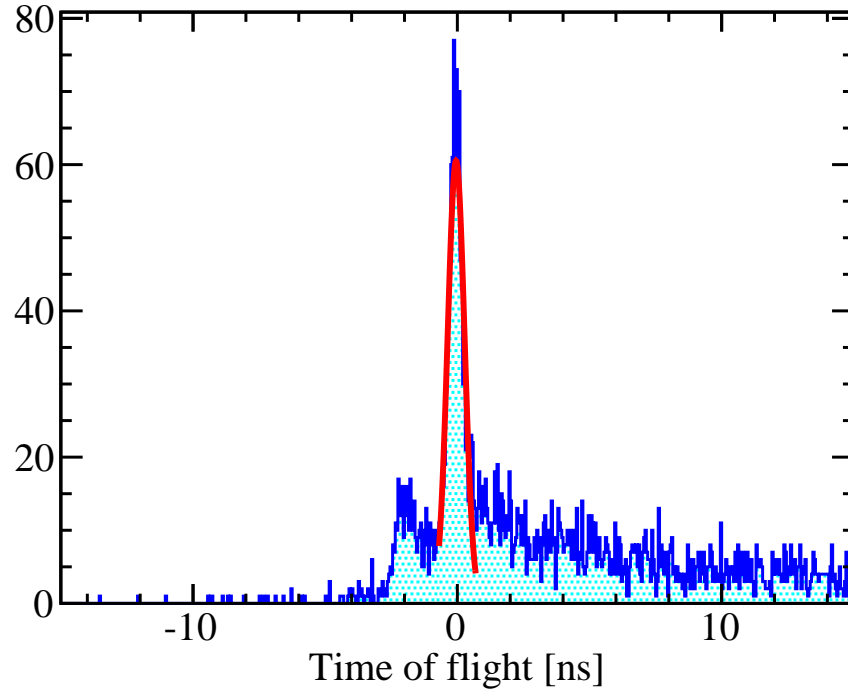
Figure 4.18: TOF spectrum of RPTOF module for the TOF offset calibration. See the text for details.

the recoil proton momentum as shown in Fig. 4.19. The recoil proton with smaller momentum gave the larger energy loss in the RPTOF so that the resolution was better.

The RPTOF is originally designed to have the time resolution of 200 ps (FWHM). This resolution was achieved during the construction, even for the ^{90}Sr beta-ray source, which made smaller light output than the proton. We speculate the worse resolution during the experiment is due to relatively lower setting of applied voltages. The typical voltage applied to each PMT was -2700 V during the construction, while that was -2200 V during the experiment.

The uncertainty of the timing information came from the difference in the response for protons and gamma rays, which was used for the TOF offset calibration (Sec. 4.5.2). Since the slew correction had been performed for entire region of the light output including the those for gamma rays and recoil protons at the same time (Sec. 4.5.1), the uncertainty of the timing information was considered to be smaller than the time resolution. The time resolution was 580 ps (FWHM) at the worst case, as shown in Fig. 4.19. Therefore, the uncertainty was evaluated as 580 ps (FWHM).

4.5.4 Validation with (p, pn) events

The functions of the RPD, the detection of the recoil proton and the measurement of its position and TOF, were confirmed by using the data taken during the physics run. Figure 4.20 shows the
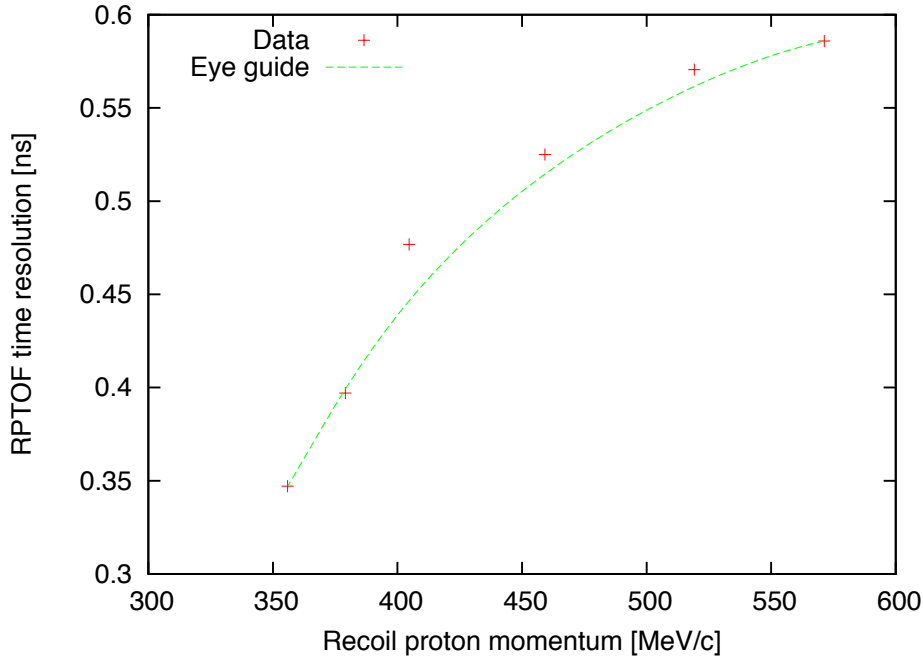
Figure 4.19: Time resolution of the RPTOF as a function of the recoil proton momentum. The resolution is given in FWHM.

correlation between the kinetic energy and the scattering angle of the recoil proton. The kinetic energy and the scattering angle were determined from the TOF and the detection position, respectively. The detail is described in Sec. 5.7. Kinematic locus was clearly seen in the spectrum after performing the particle identification (Sec. 5.1). The spread perpendicular to the kinematic line came both from the resolution of detectors and the missing momentum (Eq. (2.1)). The RPD successfully identified the (p, pn) events.

4.6 WINDS

Figure 4.21 shows the hit pattern of knocked-out neutrons in the WINDS. As described in Sec. 3.9, the detection part of the WINDS consisted of four layers: NCL1, NCL2, NCL3, and NCL4 for the detector ID of 1–15, 16–30, 31–45, and 46–60, respectively. In each layer, the detector module with smaller ID was placed at forward angles.

Two tendencies can be seen in the plot. One is that higher yields are observed in more upstream layer. It came from the finite detection efficiency of the WINDS; The neutron flux was reduced due to the detection in the former layers. It resulted in smaller yields in the latter layers. The other is that higher yields are observed in detector modules placed at forward angles. It can be explained with the kinematics; A scattering angle distribution from the (quasi-)elastic scattering has a peak at forward angle.
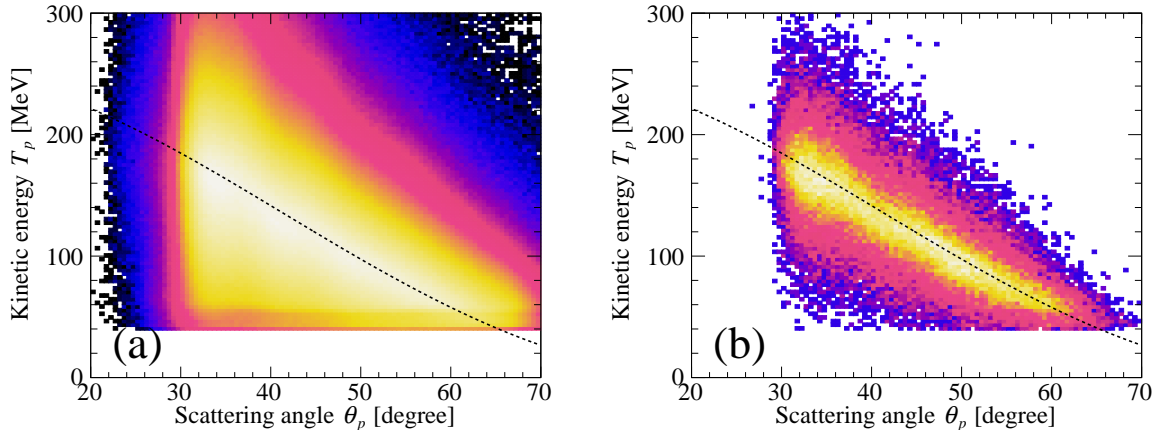
Figure 4.20: Correlation between the kinetic energy and the scattering angle of the recoil proton for all events (a) and after applying the particle identification (Sec. 5.1) (b). The horizontal and the vertical axes represent the scattering angle and the kinetic energy of the recoil proton, respectively. The black dashed lines represent the kinematical correlation for the quasi-free (p, pn) reaction.
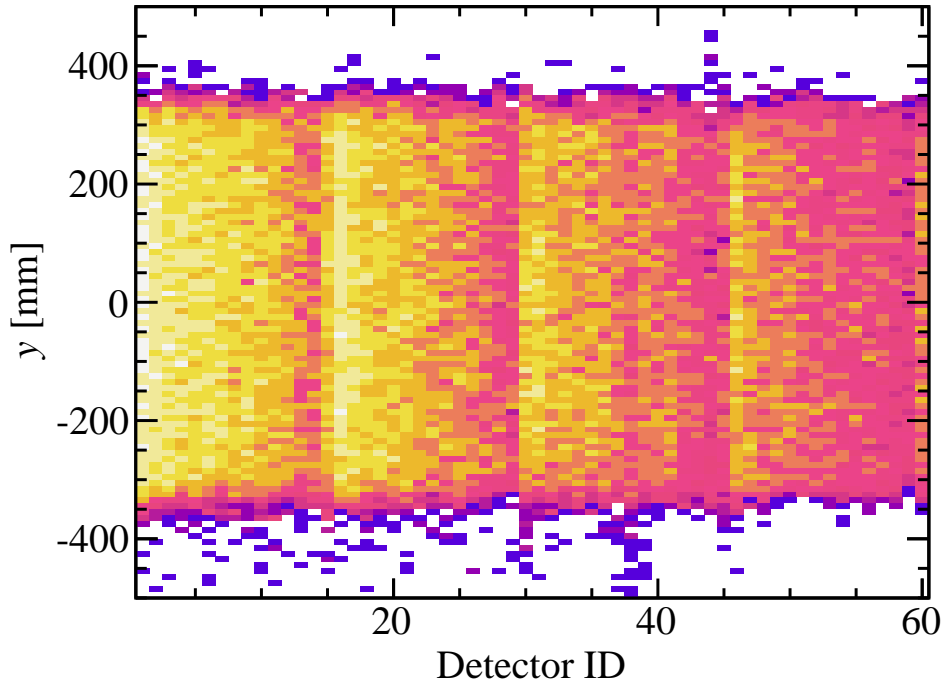
Figure 4.21: Hit pattern of the knocked-out neutron in the WINDS. The four layers of NCL1, NCL2, NCL3, and NCL4 were consisted of detector modules with IDs of 1–15, 16–30, 31–45, and 46–60, respectively. The horizontal and the vertical axes show the ID of the NC module and the detection position in y direction in each NC module, respectively.

4.6.1　Light output calibration

The digitized information of the electric charge of the signals from the scintillator detectors were converted to the light output (L) information. The light output was calibrated so as to define the detection threshold because the detection efficiency of the neutron detector strongly depends on the threshold for the light output.

It is known that the differential light output (dL/dx) and the differential energy loss per the traveling distance (dE/dx) in a plastic scintillator have a non-linear correlation [133, 134]. There are various parameterizations such as

$$\frac{dL}{dx} = \frac{A\frac{dE}{dx}}{1 + kB\frac{dE}{dx}}, \tag{4.15}$$

$$\frac{dL}{dx} = \frac{A\frac{dE}{dx}}{1 + B\frac{dE}{dx} + C(\frac{dE}{dx})^2}, \tag{4.16}$$

$$\frac{dL}{dx} = \frac{A}{2B}\ln\left(1 + 2B\frac{dE}{dx}\right). \tag{4.17}$$

In addition, the nonlinearity of the charge digitization modules and PMT responses also matter.

If the absolute value of light output in a wide dynamic range is needed, the nonlinearity should be taken into account. However, in the case of the neutron detector, the absolute value is needed around the threshold value of $6\,\mathrm{MeV_{ee}}$. Therefore, instead of calibrating the nonlinearity for a wide range, the light output was calibrated for the region around the threshold level by employing a linear function as

$$\frac{dL}{dx} = A\frac{dE}{dx} + B. \tag{4.18}$$

The calibration was performed by using 4.4-MeV gamma rays from a ^{241}Am-^{9}Be neutron source and cosmic rays. A Compton edge of 4.4-MeV gamma rays give the light output of $4.2\,\mathrm{MeV_{ee}}$, while cosmic rays make a peak at $18.6\,\mathrm{MeV_{ee}}$. The light output threshold of $6\,\mathrm{MeV_{ee}}$ was determined by the interpolation of these two points.

By assuming the non-linearity of the light output of 10% in this region, the threshold of $6\,\mathrm{MeV_{ee}}$ was determined within $1.4\,\mathrm{MeV_{ee}}$. 1.4-$\mathrm{MeV_{ee}}$ difference of the threshold value changed the detection efficiency of 6%. Therefore, the uncertainty of the detection efficiency was evaluated as 6%.

4.6.2　Slew correction

The slew correction of the WINDS was performed in a similar manner as that of the RPTOF (Sec. 4.5.1) by using the same correction function of Eq. (4.14). The slew correction was performed by using the events taken during the physics run, in which a neutron was converted

to a secondary proton in the module in the NCL1 or the NCL3, and the secondary proton hit
the neighboring module in the NCL2 or the NCL4, respectively. In such an event, the timing of
the two detector modules should be the same within an uncertainty of the time of flight of the
secondary proton in the first detector module (Sec. 4.6.5).

Neutron   Proton
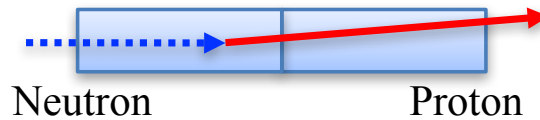
Figure 4.22: Schematic view of the event in which the two detector modules belonging to
neighboring to layers were fired by one proton produced in the first layer. The blue boxes, the
blue dotted and the red straight arrows represent the detector modules, the incident neutron, and
the secondary proton, respectively.

Figure 4.23 shows the timing spectra before and after applying the slew correction. The
walk effect was successfully compensated by the correction.

4.6.3   TOF offset calibration

Figure 4.24 shows a TOF spectrum of one detector module of the WINDS. The peak at zero
corresponding to the gamma rays from the metal target was clearly identified, so that the TOF
offset was successfully calibrated. The precedent peak around -2 ns corresponds to the gamma
rays produced in the SBT.

4.6.4   Detection position

The detection position was determined as is the case with the NEBULA (Sec. 4.7.4), where
the incident angle of the neutron with respect to the detector was assumed as about zero
degrees. In contrast to the decay neutron detected by the NEBULA, the knocked-out neutron
had various scattering angles from 25 to 60 degrees. However, the analysis method applied for
the NEBULA is still valid for the WINDS, because the detector modules of the WINDS were
arranged in concentric layers so as to face the module surface perpendicular to the incident
neutron (Sec. 3.9).

Figure 4.23: Time difference vs light output plots of WINDS modules before slew correction (a) and after applying the slew correction (b). The horizontal axis shows the mean light output of one detector module and vertical axis shows the time difference between neighboring detector modules. (c) Time difference spectra (blue) before the slew correction and (red) after applying the slew correction.

Figure 4.24: TOF spectrum of WINDS for the TOF offset calibration.

4.6.5 Resolution and uncertainty

The time resolution of the WINDS was evaluated as 550 ps (FWHM) in total. The intrinsic time resolution of WINDS was evaluated using secondary protons as 320 ps (FWHM), in the same manner as RPTOF (Sec. 4.5.3). However, this value may be different from the real performance when WINDS was bombarded by neutrons. A major difference is that, in the case of neutron detection, the light output has a continuous distribution from zero to maximum energy deposits. The light output region realized by the secondary protons are overlapping with that of the neutron detection. Therefore, we suppose the value of 320 ps should be close to the truth. This value was almost comparable with the design value of 300 ps, and acceptable.

In addition, there was an uncertainty on the detection position, coming from the thickness of the detector of 10 cm. By assuming the velocity of the neutron of $\beta = 0.5$, the time resolution due to the uncertainty on the detection position was evaluated as 450 ps (FWHM).

The systematic uncertainty of TOF was evaluated as 460 ps (FWHM) in total. A half of this uncertainty was due to the uncertainty in the TOF offset (320 ps), which was deduced in the same manner as in RPTOF (Sec. 4.5.3). The other half of the uncertainty came from the slew correction. As already explained in Sec. 4.6.2, the slew correction was done in a similar manner as RPTOF (Sec. 4.5.1). In the case of RPTOF, the hit timing of two neighboring detectors was considered to be the same because the thickness of the detector was sufficiently thin. However, in the case of WINDS, the detector were thick (10 cm); It took secondary protons time to reach

the neighboring detector. Thus, the hit timing of the first detector and that of the second detector is not the same. It should be noted that this time difference might depend on the light output; if the secondary proton scattered near the neighboring detector, the time difference got shorter, and the light output became smaller because the flight path length got shorter, vice versa. This made an additional uncertainty between the timing of a proton penetrating two neighboring bars, which cannot be compensated and was treated as a systematic uncertainty of 330 ps. This value was evaluated by assuming the velocity of the proton of $\beta = 0.5$ and the flight path length of 5 cm, the half depth of the NC module. The uncertainty was smaller than the overall time resolution of 550 ps (FWHM).

4.6.6   Validation with (p, pn) events

The functions of the WINDS, the detection of the knocked-out neutron and the measurement of its position and TOF, were confirmed by using the data taken during the physics run. Figure 4.25 shows the correlation between the kinetic energy and the scattering angle of the knocked-out neutron. The kinetic energy and the scattering angle were determined from the TOF and the detection position, respectively. The detail is described in Sec. 5.6. Kinematic locus was clearly seen in the spectrum after performing the particle identification (Sec. 5.1). The spread perpendicular to the kinematic line came both from the resolution of detectors and the missing momentum (Eq. (2.1)). It should be noted that vertical stripe patterns came from the gaps between the WINDS detector modules (Sec. 3.9). The WINDS successfully identified the (p, pn) events.
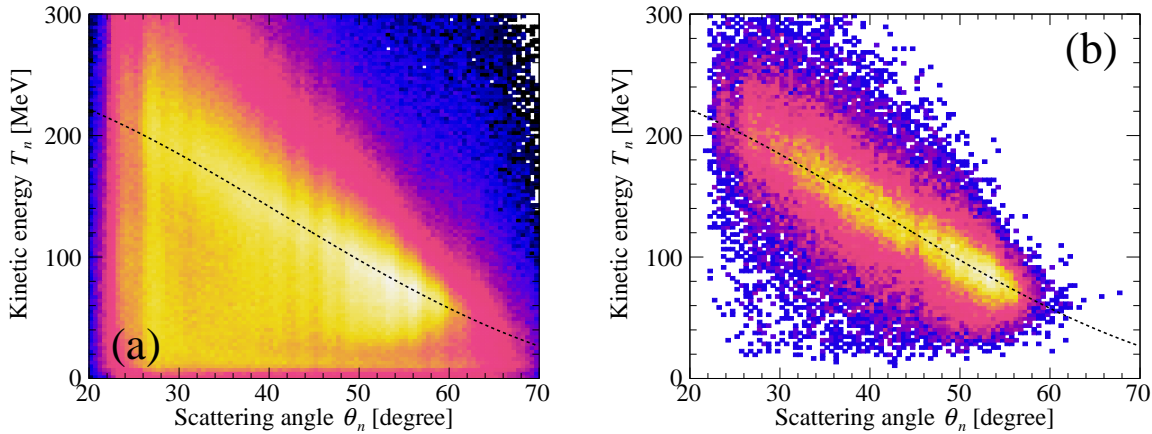
Figure 4.25: Correlation between the kinetic energy and the scattering angle of the knocked-out neutron for all events (a) and after applying the particle identification (Sec. 5.1) (b). The horizontal and the vertical axes represent the scattering angle and the kinetic energy of the knocked-out neutron, respectively. The black dashed lines represent the kinematical correlation for the quasi-free (p, pn) reaction.

4.7 NEBULA

Figure 4.26 shows the hit pattern of decay neutrons in the NEBULA. As described in Sec. 3.11, the detection part of the NEBULA consisted of four layers, two NEUT layers in two walls, for the detector ID of 1–30, 31–60, 61–90, and 91–120, respectively. The layers placed upstream had larger yields as compared to those placed downstream, in common with the WINDS (Sec. 4.6).
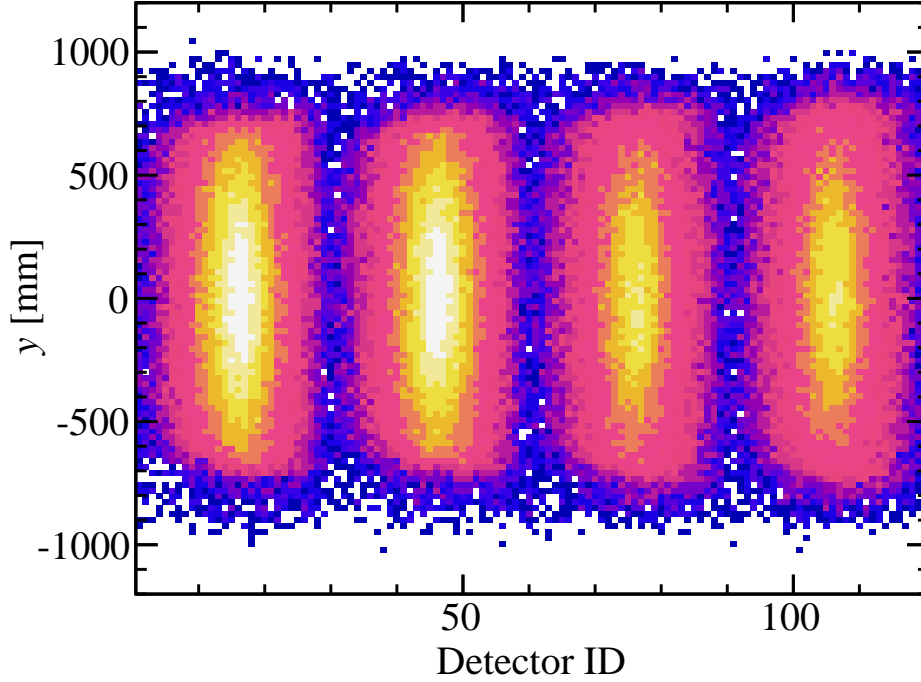
Figure 4.26: Hit pattern of the decay neutron in NEBULA. The horizontal and the vertical axes show the ID of the NEUT module and the detection position in *y* direction in each NEUT module, respectively.

4.7.1 Light output calibration

The light output calibration of the NEBULA was performed in the same manner as WINDS (Sec. 4.6.1). The calibration was performed by using 4.4-MeV gamma rays from a ^{241}Am-^{9}Be neutron source and cosmic rays. A Compton edge of 4.4-MeV gamma rays give the light output of 4.2 MeV$_{ee}$, while cosmic rays make a peak at 30 MeV$_{ee}$. The light output threshold of 6 MeV$_{ee}$ was determined by the interpolation of these two points.

By assuming the non-linearity of the light output of 10% in this region, the threshold of 6 MeV$_{ee}$ was determined within 2.6 MeV$_{ee}$. 2.6-MeV$_{ee}$ difference of the threshold value changed the detection efficiency of 7%. Therefore, the uncertainty of the detection efficiency was evaluated as 7%.

4.7.2 Slew correction

The slew correction of the NEBULA was performed in the same manner as WINDS (Sec. 4.6.2) by using the same correction function of Eq. (4.14). Figure 4.27 shows the timing spectra before and after applying the slew correction.
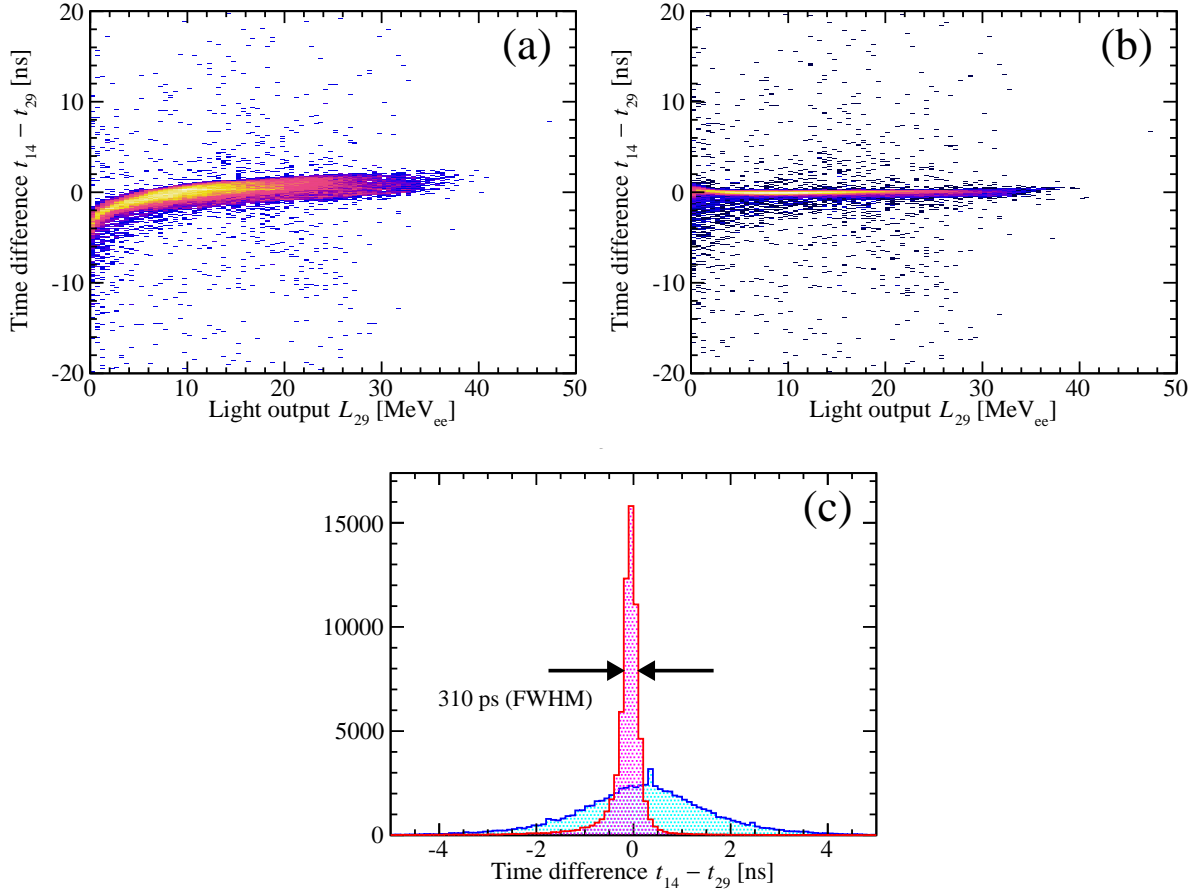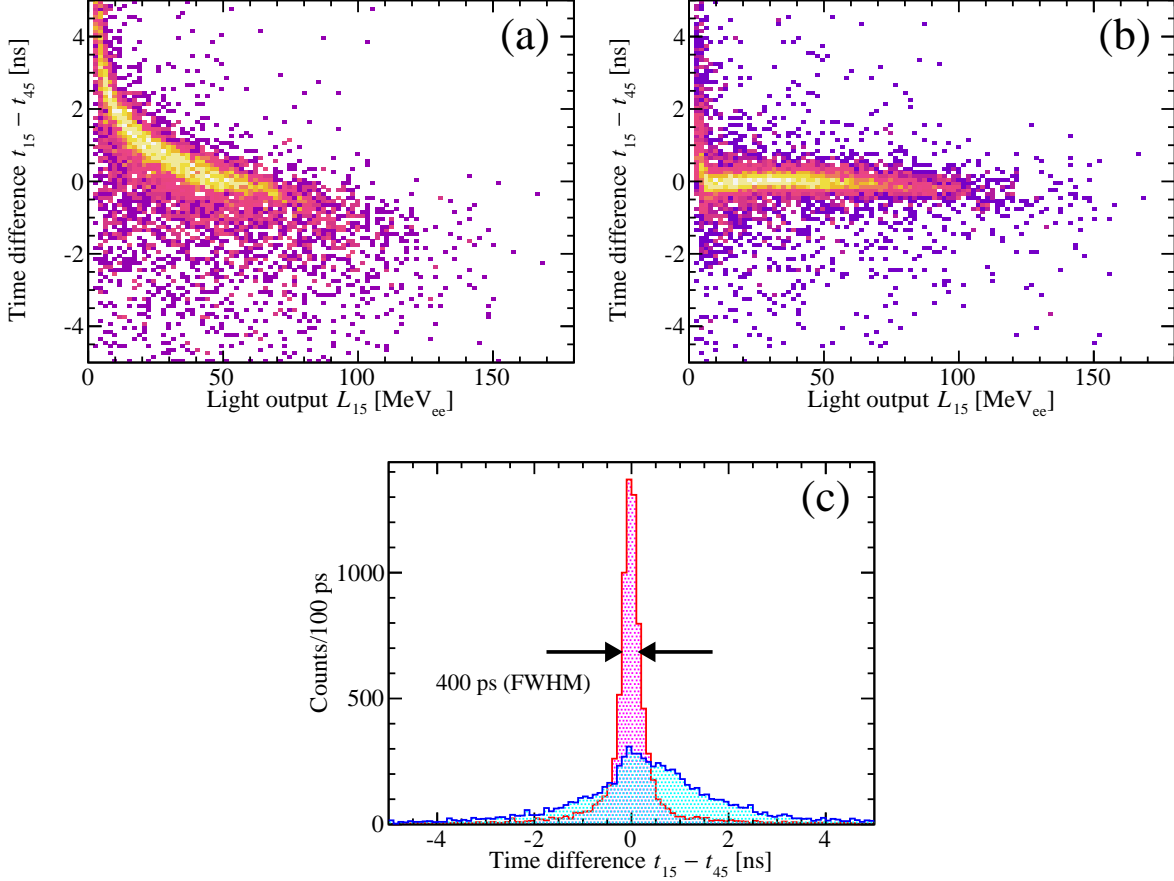

Figure 4.27: Time difference vs light output plots of NEBULA modules before slew correction (a) and after applying the slew correction (b). The horizontal axis shows the mean light output of one detector module and vertical axis shows the time difference between neighboring detector modules. (c) Time difference spectra (blue) before slew correction and (red) after applying the slew correction.
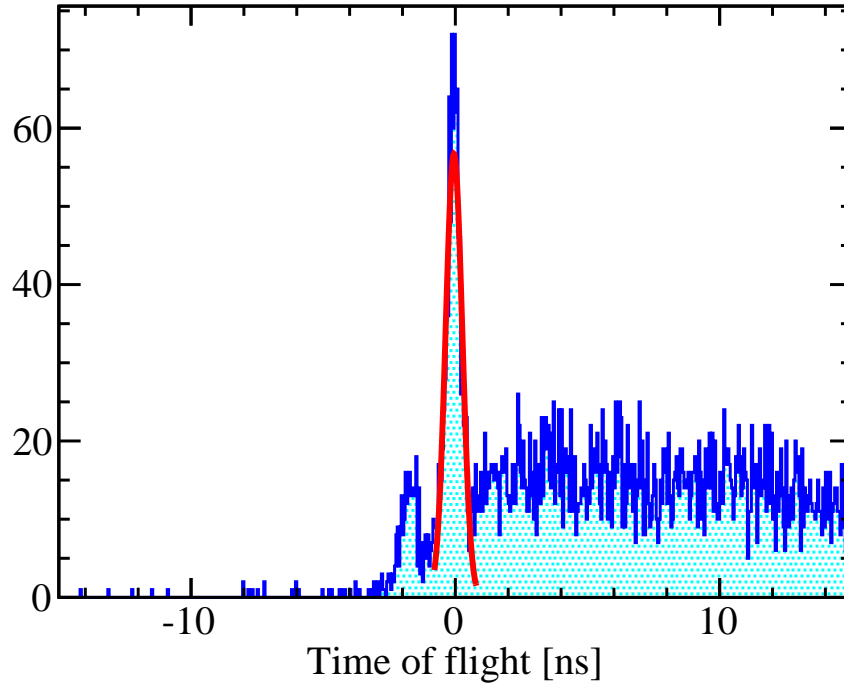
4.7.3 TOF offset calibration

The calibration of the TOF offset was performed in following two steps. (i) The TOF offset was relatively aligned between neighboring NEUT modules by using cosmic rays. (ii) The TOF offset for all NEUT modules was adjusted to the beam timing at the same time by using gamma rays from the metal target by using the beam.

As is the case with the RPTOF (Sec. 4.5.2) and the WINDS (Sec. 4.6.3), the TOF offset can be adjusted only by the step (ii) in principle for bar by bar. However, the step (i) is additionally needed due to the limited statistics of gamma rays. In the case of the RPTOF and the WINDS, the distance between the target and the detector was about 1.5 m. In contrast, the distance between the target and the NEBULA was about 12 m. It resulted in the poor statistics of gamma rays.

By summing up TOF spectra of detector modules in the same layer, the gamma rays from the metal target was identified and the TOF offset was calibrated.

4.7.4 Detection position

The NEUT module of NEBULA had two PMTs at top and bottom ends (Sec. 3.11). Thus, the detection position along the y axis, the vertical direction, was determined from the time difference between two PMTs as

$$y = y_i + \frac{t_\text{T} - t_\text{B}}{2v_\text{eff}}, \tag{4.19}$$

where y_i, v_eff, t_T, and t_B represent the center position of i-th module, the light velocity in the NEUT module, and the signal timings of top and bottom PMTs, respectively.

On the other hand, the NEUT module had no sensitivity on the (z, x) plane. As for the x direction, the direction perpendicular to the bombarding decay neutron, the detection position was calculated as

$$x = x_i + \text{Uniform}[-1/2, 1/2) \times \text{Thickness}, \tag{4.20}$$

$$\text{Thickness} = 12 \text{ cm}, \tag{4.21}$$

where x_i and $\text{Uniform}[-1/2, 1/2)$ denote the center position of i-th module and the random number having uniform distribution defined in a half-bounded interval of $[-1/2, 1/2)$. Since there was no other information correlated to the x position, it was calculated with an assumption of the uniform distribution along the x direction.

As for the z direction, the direction parallel to the bombarding decay neutron, the detection position was defined as

$$z = z_i, \tag{4.22}$$

where z_i represents the center position of i-th module. By contrast to the x direction, the information of the detection position was included in the TOF. Thus, this uncertainty was treated as the uncertainty of the TOF, and was not taken into account for the position determination.

4.7.5   Resolution and uncertainty

The time resolution of the NEBULA was evaluated as 530 ps (FWHM) in total. As is the case with the WINDS (Sec. 4.6.5), the time resolution of the NEBULA was evaluated from the Fig. 4.27 by using the secondary protons, as 280 ps (FWHM). It was acceptable.

In addition, there was an uncertainty on the detection position, coming from the thickness of the detector of 12 cm. By assuming the velocity of the neutron of $\beta = 0.6$, the time resolution due to the uncertainty on the detection position was evaluated as 450 ps (FWHM).

The overall systematic uncertainty of TOF was evaluated as 430 ps. The uncertainty of the timing information came from the difference in the response for protons and gamma rays, which was used for the TOF offset calibration (Sec. 4.5.2). The systematic uncertainty coming from the difference in the response for neutrons and gamma rays was evaluated as same with the time resolution of 280 ps, in common with the WINDS (Sec. 4.6.5).

The slew correction was performed by assuming the detection timings of the secondary proton in two detector modules were same (Sec. 4.6.2). As already discussed (Sec. 4.6.5), there was an uncertainty in the procedure of the slew correction due to an uncertainty of the neutron hit position. In the case of the NEBULA, the deviation was evaluated as 330 ps, by assuming the velocity of the proton of $\beta = 0.6$ and the flight path length of 6 cm, which is the half depth of the NEUT module. The uncertainty was smaller than the overall time resolution of 530 ps (FWHM).

4.8   Correlation between recoil proton and knocked-out neutron

The intrinsic performances of the RPD and the WINDS were evaluated separately in Sec. 4.5 and Sec. 4.6, respectively. The kinematic loci for the (p, pn) reaction were seen in events obtained by the RPD and the WINDS. Herein we confirm whether the (p, pn) events were correctly obtained by checking the correlation between the recoil proton and the knocked-out neutron. The data taken in the physics run were used for this analysis.

Figure 4.28 shows the angular correlation between the recoil proton and the knocked-out neutron, determined by the RPD and the WINDS, respectively. Kinematic locus was clearly seen in the angular correlation after performing the particle identification (Sec. 5.1). The overall angular resolution of 52 mrad (FWHM) at $\theta_p = \theta_n \sim 43$ degree was obtained from the width of the spectrum. It was consistently explained by the contributions from the RPD of 30 mrad (FWHM) including both the resolution and the multiple scattering (Sec. 5.7.3) and from the WINDS of 45 mrad (FWHM, Sec. 5.6). Therefore, we concluded that the (p, pn) setup composed of the RPD and the WINDS successfully worked for the (p, pn) measurement.

It should be noted that vertical stripe patterns in Fig. 4.28 came from the gaps between the

WINDS detector modules (Sec. 3.9). The geometrical acceptance was studied and corrected for (Sec. 5.11).
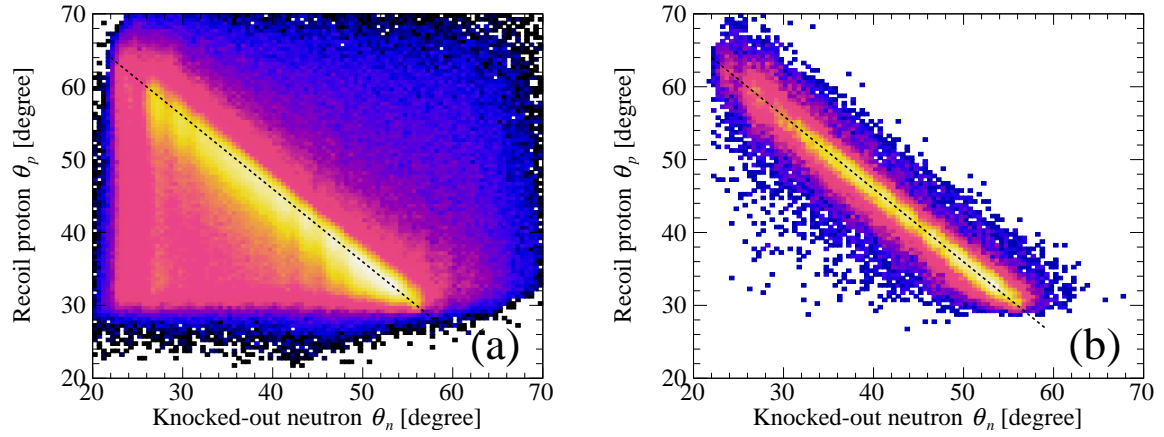
Figure 4.28: Angular correlation between the recoil proton and the knocked-out neutron. (a) The polar angle correlation for all events and (b) that after applying the particle identification (Sec. 5.1). The horizontal and the vertical axes represent the scattering angles of the knocked-out neutron and the recoil proton, respectively. The black dashed lines represent the kinematical correlation for the quasi-free (p, pn) reaction.

Chapter 5

Analysis

The analysis is described in details in this chapter. The flow chart of the data analysis is shown in Fig. 5.1. In the previous chapter, all the parameters in the raw data are calibrated and converted to variable corresponding observables in each detector as listed on the left side of Fig. 5.1. Starting from these physical parameters, in this chapter, we perform particle identification (Sec. 5.1) of all the particles, i.e. involved in the quasi-free (p, pn) reaction, the incident beam (Sec. 5.1.1), the heavy fragment (Sec. 5.1.2), the recoil proton (Sec. 5.1.3), the decay neutron (Sec. 5.1.4), and the knocked-out neutron (Sec. 5.1.5). Section 5.2 describes the analysis of the gamma rays from the heavy fragment ^{9}Li. Section 5.3, Sec. 5.4, Sec. 5.5, Sec. 5.6, and Sec. 5.7 explain how to reconstruct the momentum vectors of the ^{11}Li beam, the heavy fragment ^{9}Li, the decay neutron, the knocked-out neutron, and the recoil proton, respectively. Section 5.8 shows the consistency check of the reconstructed momentum vectors based on the momentum conservation law. Section 5.9 presents the derivation of the relative energy based on the invariant mass method. Section 5.10 gives the derivation of the internal momentum and the opening angle. Section 5.11 explains the evaluation of the geometrical acceptance of the present setup. Section 5.12 and Sec. 5.13 show the achieved experimental resolution and systematic uncertainties, respectively. Section 5.14 shows the momentum transfer distribution for the confirmation of the QFS condition.
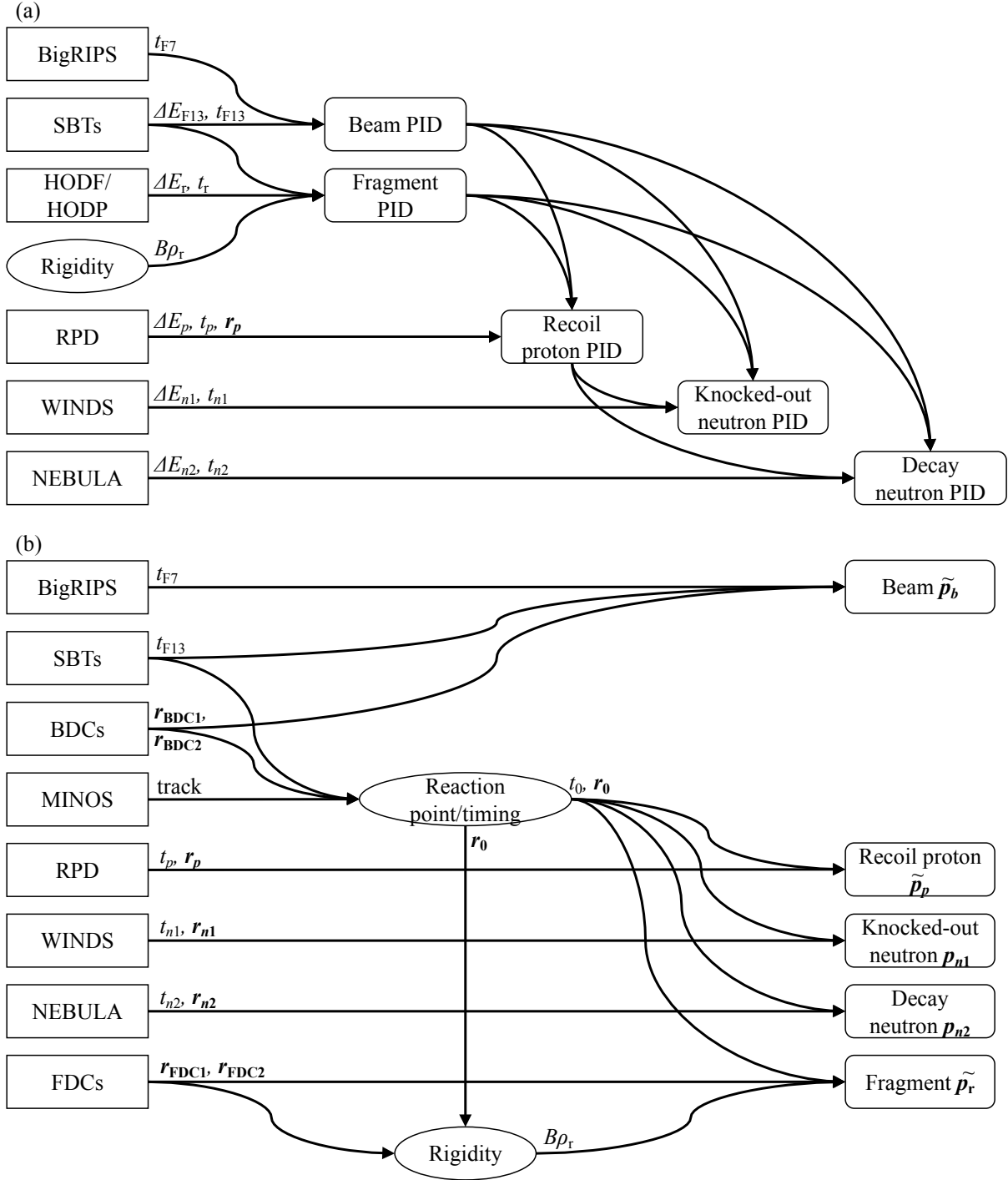
Figure 5.1: Flow charts of the data analysis for (a) the particle identification and (b) the momentum derivation. The rectangles and the ellipses represent detectors and intermediate information, respectively. The arrows and the characters next to them represent the data flow and the variables. See the text for details.

5.1   Particle identification

The particle identification (PID) was performed on an event-by-event basis for

- Incident ^{11}Li beam in the BigRIPS,

- Emitted heavy fragment ^{9}Li in the SAMURAI spectrometer,

- Scattered target proton in the RPD,

- Knocked-out neutron from the ^{11}Li beam in the WINDS,

- Forward emitted neutron from the reaction residue ^{10}Li in the NEBULA.

The former two items, ^{11}Li and ^{9}Li, were done by employing the TOF–$B\rho$–ΔE method. After gating the PID cuts of these two items, the events were selected. The latter three were analyzed for the selected events, as shown in Fig. 5.1(a). These are described in the following subsections.

5.1.1   Incident ^{11}Li beam

The atomic number Z and the mass-to-charge ratio A/Q of ^{11}Li beam particles were determined from the time-of-flight (TOF), the magnetic rigidity $B\rho$, and the energy loss ΔE, through following three formula: equations of motion and Bethe-Bloch formula

$$\text{TOF} = \frac{\text{(Flight path length)}}{\beta c}, \tag{5.1}$$

$$B\rho = \frac{p}{q} = \frac{m\gamma v}{q} = \frac{A}{Q}\frac{u\gamma\beta c}{e}, \tag{5.2}$$

$$\Delta E = \int_{\Delta x} dx \left(-\frac{dE}{dx}\right)$$

$$= \int_{\Delta x} dx \frac{4\pi}{m_e c^2} \frac{nZ^2}{\beta^2} \left(\frac{e^2}{4\pi\epsilon_0}\right)^2 \left[\ln\left(\frac{2m_e c^2 \beta^2}{I(1-\beta^2)}\right) - \beta^2\right], \tag{5.3}$$

with the parameters:

β	velocity (v/c) of the particle,
c	the light velocity,
p	momentum of the particle,
q	electric charge of the particle,
$\gamma = 1/\sqrt{1 - \beta^2}$	Lorentz factor,
m	rest mass of the particle,
u	mass per nucleon in the rest frame,
e	elementary charge,
Δx	thickness of the material,
m_e	electron mass,
ϵ_0	vacuum permittivity,
I	mean excitation energy of the material.

From Eq. (5.3), the atomic number Z can be written as

$$Z^2 = C\frac{\Delta E}{f(\beta)}, \tag{5.4}$$

$$f(\beta) = \frac{1}{\beta^2} \ln\left(\frac{2m_e c^2 \beta^2}{I(1 - \beta^2)}\right) - 1, \tag{5.5}$$

where C is a constant.

In the present experiment, the beam velocity β was determined from the TOF from F7 to F13 by using Eq. (5.1). The timing information at each focal plane ($t_{\mathrm{F}i}$) was calculated by averaging the timing signals from the left and the right PMTs ($t_{\mathrm{F}i}^L$, $t_{\mathrm{F}i}^R$). The timing at F13 was obtained by averaging the timing information of the two scintillators, SBT1 and SBT2, to improve the resolution.

$$t_{\mathrm{F}7} = \frac{t_{\mathrm{F}7}^L + t_{\mathrm{F}7}^R}{2}, \tag{5.6}$$

$$t_{\mathrm{F}13} = \frac{t_{\mathrm{SBT1}} + t_{\mathrm{SBT2}}}{2}, \tag{5.7}$$

$$t_{\mathrm{SBT1}} = \frac{t_{\mathrm{SBT1}}^L + t_{\mathrm{SBT1}}^R}{2}, \tag{5.8}$$

$$t_{\mathrm{SBT2}} = \frac{t_{\mathrm{SBT2}}^L + t_{\mathrm{SBT2}}^R}{2}. \tag{5.9}$$

By taking the average of the left and the right timing, the hit position dependence of the timing $t_{\mathrm{F}i}$ was canceled out. The TOF between F7 and F13 was derived as

$$\mathrm{TOF}_{713} = t_{\mathrm{F}13} - t_{\mathrm{F}7} + t_{\mathrm{ofs}}, \tag{5.10}$$

where t_{ofs} is a constant to be calibrated.

The TOF offset t_{ofs} was calibrated by using the beam with a small momentum spread of 0.063%. The spread of the beam momentum was controlled by closing the F5 slit. The absolute value of the beam momentum from F5 to F7 (p_{57}) was determined from the NMR value of the dipole magnet D5 (8.9015 Tm) by employing Eq. (5.2). The beam momentum from F7 to F13 (p_{713}) was calculated from the p_{57} taking account the energy loss in the detectors at F7. The flight path length between the two plastic scintillators at F7 and F13 was 35.849 m.

The mass-to-charge ratio A/Q was determined by using Eq. (5.2). The magnetic rigidity $B\rho$ was derived from the momentum dispersion δ and the magnetic rigidity of the central trajectory $B\rho_0 = 8.9015$ Tm as

$$B\rho = (1 + \delta)B\rho_0. \tag{5.11}$$

By considering the optical transmission from F3 to F5 in the BigRIPS, the position at F5 (x_{F5}) was written as

$$x_{\text{F5}} = (x|x)x_{\text{F3}} + (x|a)a_{\text{F3}} + (x|\delta)\delta \tag{5.12}$$

where x_{F3} and a_{F3} respectively denote the position and the angle of the beam at F3. $(x|x)$, $(x|a)$, and $(x|\delta)$ represent the optical matrix elements from F3 to F5 [135]. By replacing the momentum dispersion by the observables by the beam line detectors, the magnetic rigidity $B\rho$ was obtained as

$$B\rho = \left(1 + \frac{x_{\text{F5}} - (x|x)x_{\text{F3}} - (x|a)a_{\text{F3}}}{(x|\delta)}\right)B\rho_0. \tag{5.13}$$

In the present experiment, x_{F5} was obtained from the plastic scintillator at F5, while x_{F3} and a_{F3} were not measured during the physics run (Sec. 3.3.2). By omitting the F3-dependent terms, one could get

$$B\rho \approx \left(1 + \frac{x_{\text{F5}}}{(x|\delta)}\right)B\rho_0. \tag{5.14}$$

Figure 5.2 shows a PID plot of the secondary beam. Pile up events indicated by arrows included multiple particles in one event. The ratio of the pile up events for ^{11}Li beam particles to the total ^{11}Li beam events was 1.0% for the beam intensity of 80 kcps. It was consistently understood with the pile up probability of 1.1% for 80-kcps beam at the RF frequency of 35.6 MHz and the logic pulse width of 50 ns. The obtained resolution for the atomic number Z and the mass-to-charge ratio A/Q were $\sigma_Z = 1.2 \times 10^{-2}$ and $\sigma_{A/Q} = 1.4 \times 10^{-1}$, respectively, which was sufficiently high to select the ^{11}Li. The events having deviation of $\pm 2.5\sigma$ both in the Z and the A/Q distributions were selected. Assuming the Gaussian distribution, 97.5% of ^{11}Li were included in the PID gate.
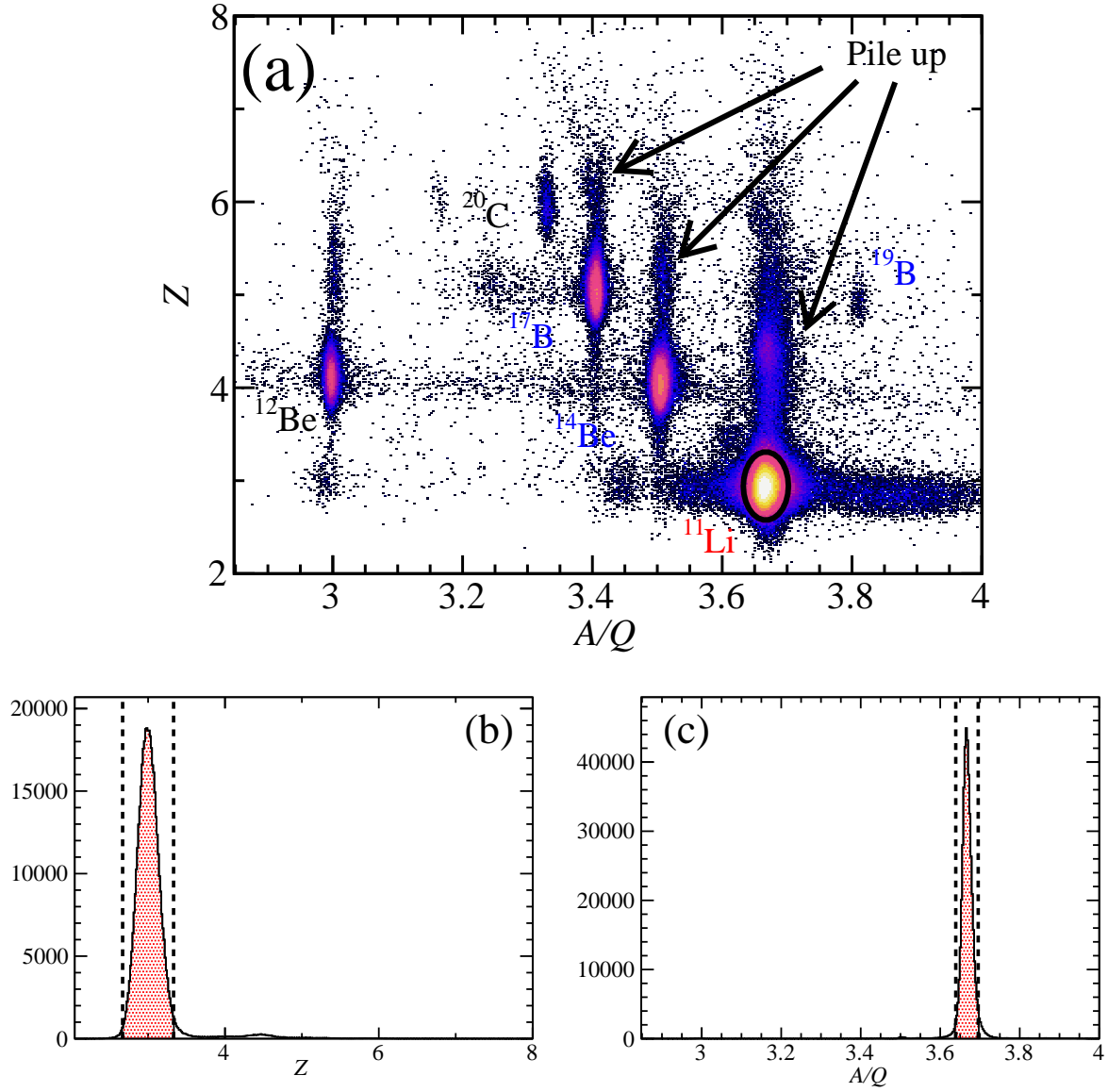
Figure 5.2: PID plots for the beam particles. (a) Two-dimensional plot of the Z value versus A/Q value. The region in the solid line was identified as ^{11}Li particles. The arrows indicate the pile up events. (b) The Z distribution with the selection of the A/Q value and (c) the A/Q distribution with the selection of the Z value. The red shaded events were selected as ^{11}Li.

5.1.2 Heavy fragment ^{9}Li

The heavy fragment, ^{9}Li decaying from ^{10}Li, was particle identified through the TOF–$B\rho$–ΔE method similarly as described in Sec. 5.1.1.

The atomic number Z was derived by using Eq. (5.4). The fragment velocity β_r was determined from the TOF from F13 to HODF or HODP. Similarly as in the case of plastic scintillators at each focal plane, the timing information of HODF or HODP was defined by the arithmetic mean of the timings of the top and the bottom PMTs, while the energy loss information was defined by the geometric mean of the light output of the PMTs.

For the purpose of the derivation of β_r, a mean flight path length was evaluated module by module of the HODF and HODP. The evaluation took into account the variation of the flight path length due to the differences in the emission angle and momentum of the heavy fragments hitting each detector module, as shown in Fig. 5.3.
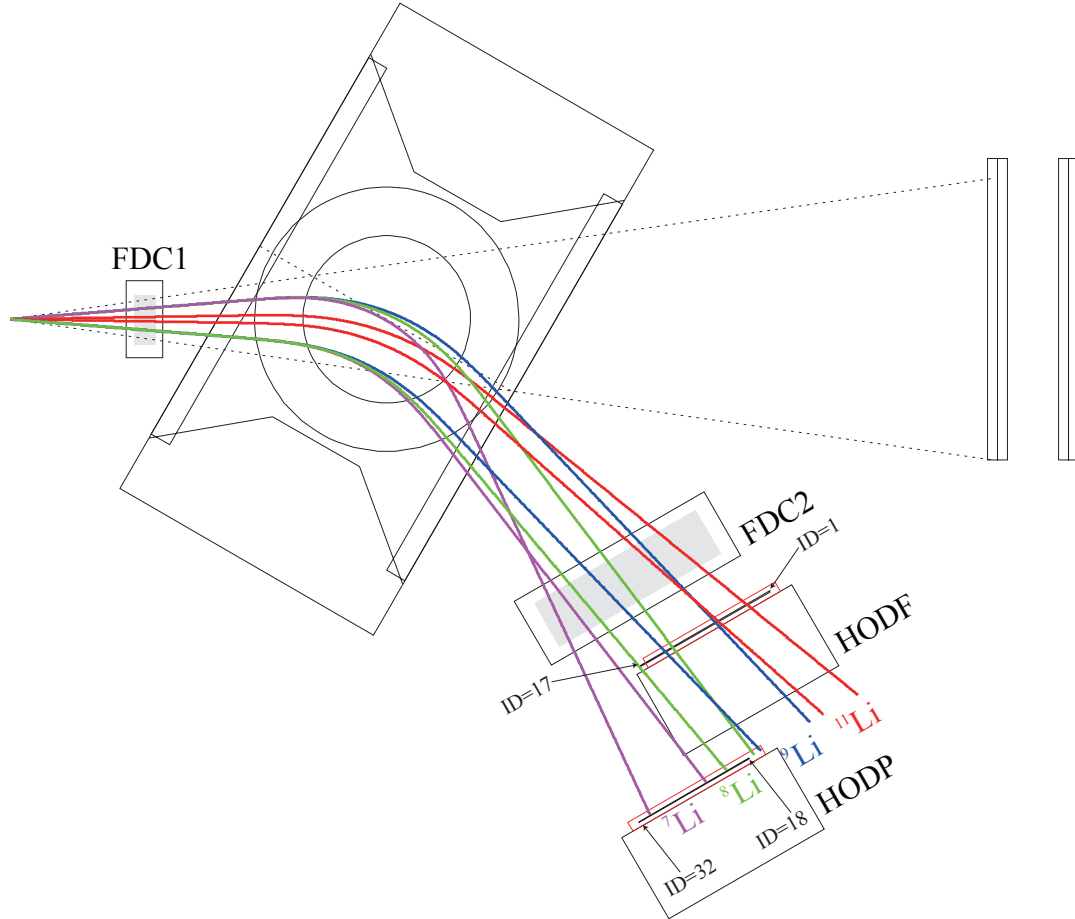
Figure 5.3: Top view of the SAMURAI detectors for heavy fragment. The shaded rectangles show the effective areas of FDC1 and FDC2. The effective areas of HODF and HODP are shown by the black solid lines surrounded by the red rectangles. The colored curves represent simulated envelopes of the beam particle and the heavy fragments.

The A/Q was determined by using Eq. (5.2). The $B\rho$ and the momentum of the heavy fragment p_r follow the relation

$$B\rho = \frac{p_r}{q} = \frac{p_r}{Qe} = \frac{p_r}{Ze}.$$ (5.15)

Here the charge states were ignored since the heavy fragments around $Z < 10$ with kinetic energies of around 250 MeV/nucleon could be assumed to be fully stripped. The rigidity analysis of the heavy fragment is explained in Sec. 5.4.

The hodoscopes HODF and HODP were used for the TOF measurement and the atomic number Z determination for the heavy fragment. The atomic number Z was derived from the energy loss in the HODF and the HODP, same as the PID for the beam described in Sec. 5.1.1. The TOF was measured from the SBT to the HODF or the HODP for calculating the velocity β_r and the Lorentz factor γ_r.

Figure 5.4 shows a PID plot for the 14th module of HODF. The number of events for ^{3}H was quite small because the tracking efficiencies of FDC1 and FDC2 for ^{3}H were low. The obtained resolution for the atomic number Z and the mass-to-charge ratio A/Q was $\sigma_Z = 7.9 \times 10^{-2}$ and $\sigma_{A/Q} = 3.7 \times 10^{-2}$, respectively, which was sufficiently high to separate ^{9}Li from the nearest neighbor nuclide ^{8}Li. The events having deviation of $\pm 2\sigma$ both in the Z and the A/Q distributions were selected. Assuming the Gaussian distribution, 91.1% of ^{9}Li were included in the PID gate.

5.1.3   Recoil proton

The recoil proton was identified by using the recoil proton detector RPD. The plastic scintillator hodoscope RPTOF was sensitive not only to the charged particles but to gamma rays and neutrons, while the multi-wire drift chamber RPDC was sensitive only to charged particles. Thus, by selecting events in which RPDC had tracks, events due to electrically neutral particles or gamma rays hitting the RPTOF were eliminated.

Figure 5.5 shows a PID plot of the recoil proton. The horizontal and the vertical axes represent the TOF and the light output of the RPTOF, respectively. The TOF and the light output were calculated similarly as in the case of HODF or HODP. The locus of the recoil proton was clearly observed. The kink of the locus at the TOF of around 17 ns is explained by the kinematical condition; the fast protons passed through the RPTOF while the slow protons stopped in the RPTOF depositing the total kinetic energy.

Although loci of deuterons and tritons cannot be seen in the plot, one cannot completely exclude deuterons nor tritons by this selection because the fast protons, deuterons and tritons can make events in the proton PID gate in the timing region shorter than 17 ns. By applying the PID conditions for neutrons (Sec. 5.1.4 and Sec. 5.1.5), events from deuterons or tritons were fully excluded because of the neutron number conservation.
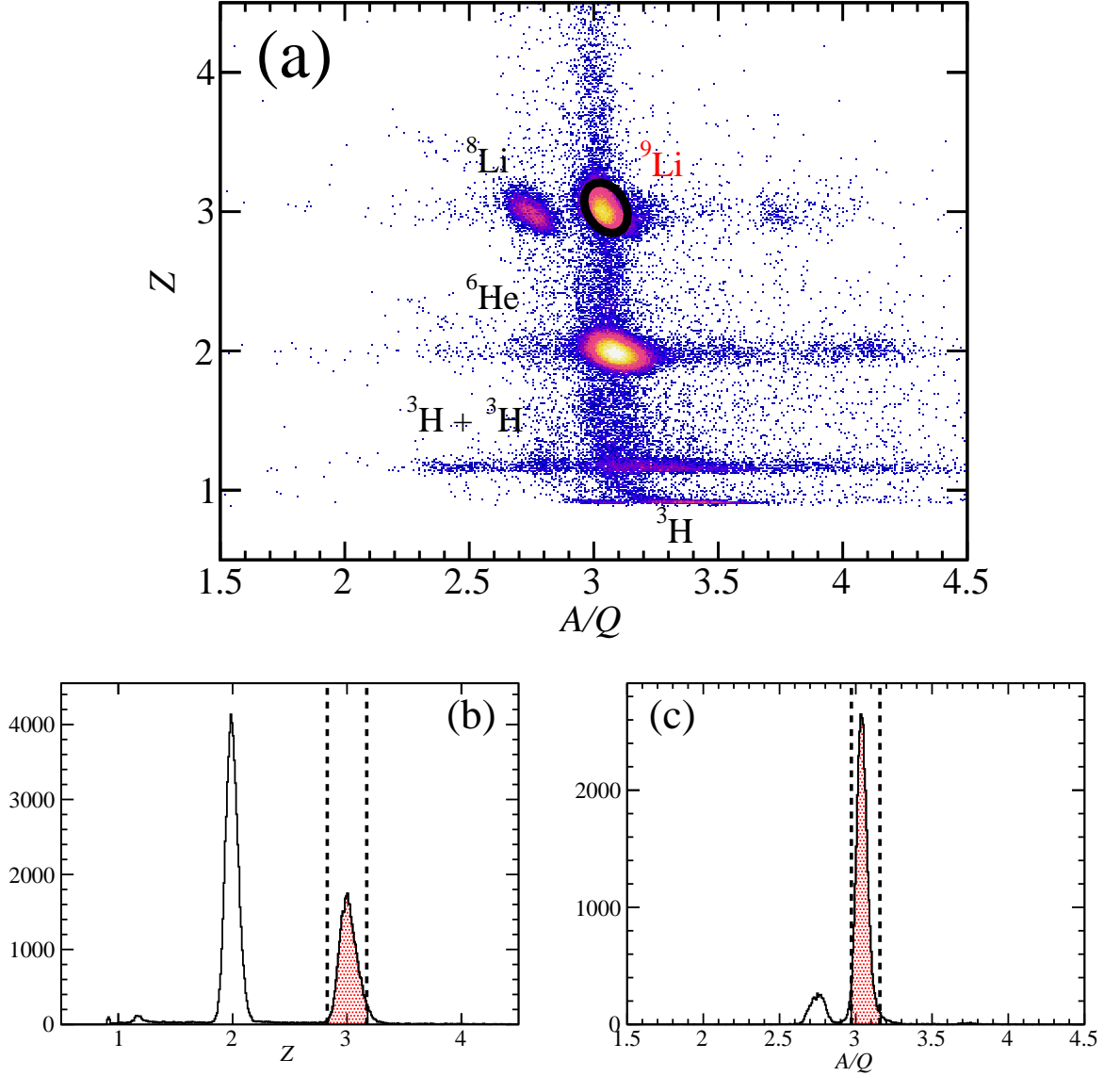
Figure 5.4: PID plot for the heavy fragments at the 14th module of HODF. (a) Two-dimensional plot of the Z value versus A/Q value. The ^{11}Li beam was selected. The region in the solid line was identified as ^{9}Li heavy fragment. The arrows indicate the pile up events. (b) The Z distribution with the selection of the A/Q value and (c) the A/Q distribution with the selection of the Z value. The red shaded events were selected as ^{9}Li.
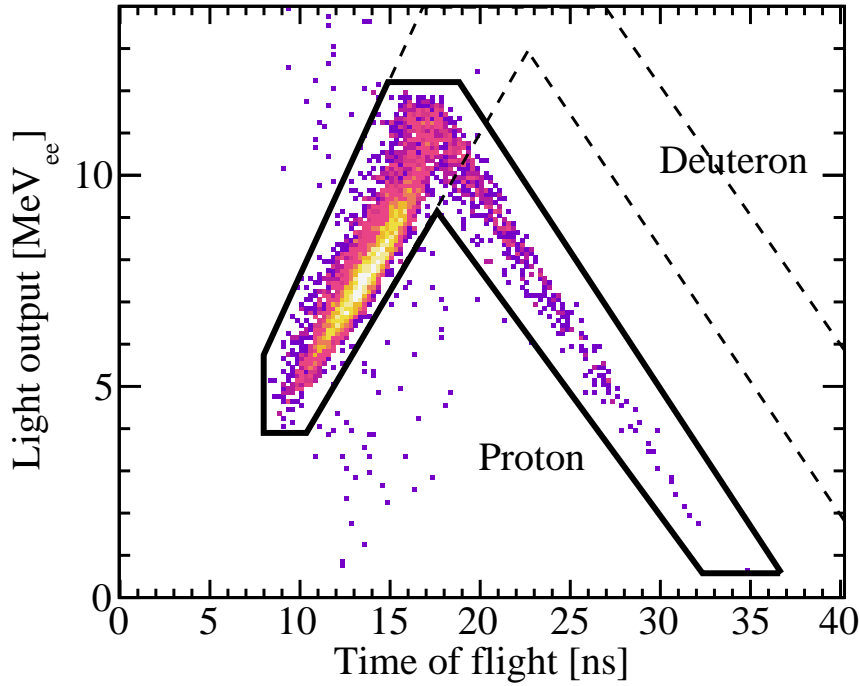
Figure 5.5: PID plot for the recoil proton. The ^{11}Li beam particle and ^{9}Li heavy fragment were selected. The events in the region enclosed with the solid line were selected as recoil proton events. The dashed line show the region where the deuteron-induced events appear, if any.

5.1.4 Decay neutron

The decay neutron detected in the NEBULA was identified by using the information of the TOF, the light output, and VETO counter. Neutron detectors based on plastic scintillators are sensitive to gamma rays and charged particles, which can have background events due to gamma rays or secondary neutrons and protons coming from neighboring bars.

In a plastic scintillator, neutrons are firstly converted to charged particles through neutron-induced nuclear reactions, such as the *n-p* elastic scattering or the ^{12}C(n, np) reaction. The secondary charged particles, protons in most cases, immediately start to deposit the energy through the electromagnetic interaction so that the scintillation photons are generated and converted to signals. Thus produced secondary neutrons or protons have relatively high energy and can fly to neighboring bars to make background events (cross talk).

Neutrons can also excite the ^{12}C in the plastic scintillator through the nuclear reaction. Gamma rays emitted from the excited ^{12}C make a background, because they are not detected where they are generated, but are detected somewhere around in the plastic scintillator.

To select the neutron events, following conditions were applied.

1. When a VETO module fired, the event was considered to be caused by an incident charged particle, and rejected.

2. When the light output was smaller than the threshold of 6 $\mathrm{MeV_{ee}}$, the event was considered to be caused by a gamma ray, and rejected.

3. When the velocity β is larger than 0.9 (Detection timing $t_{n2} < 40$ ns), the event was considered to be caused by a gamma ray from the secondary target, and rejected.

Following condition was applied so as to reject cross-talk events.

- When more than two NEUT modules fired, the module with fastest timing was selected as the hit one.

Figure 5.6 shows a PID plot of the decay neutron after selecting the ^{11}Li beam, the ^{9}Li heavy fragment, and the recoil proton. The axes are defined as same as Fig. 5.5. The locus of the decay neutron can clearly be be seen. Gamma rays from the target and the SBTs can be seen in the region with light output smaller than 6 $\mathrm{MeV_{ee}}$ and with TOF shorter than 43.5 ns. These background events are rejected by the PID conditions.
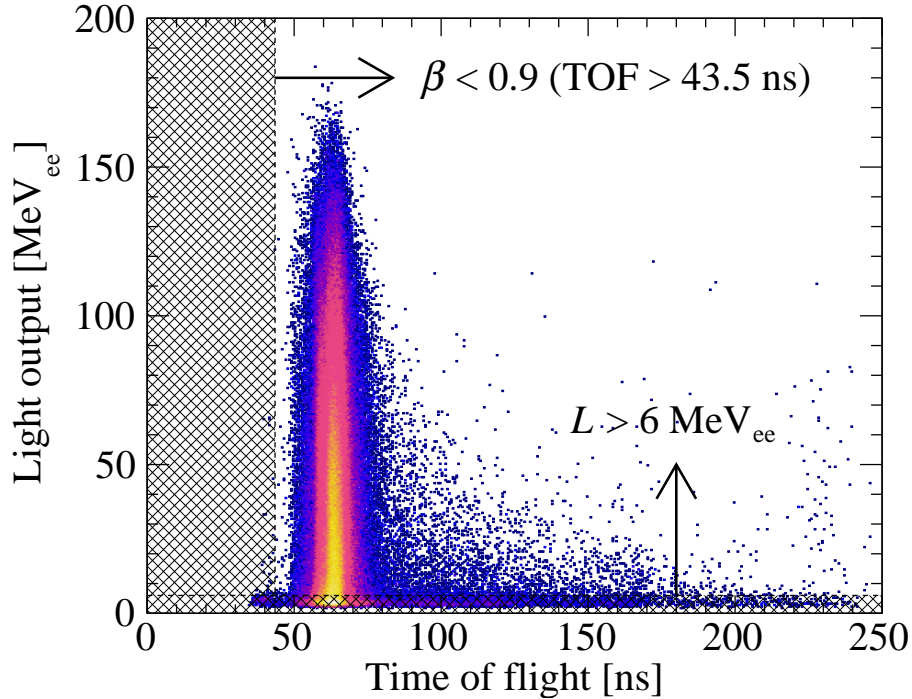
Figure 5.6: PID plot of the decay neutron for the first NEUT layer of the NEBULA. The ^{11}Li beam, the ^{9}Li heavy fragment, and the recoil proton were selected. The hatched area represents events with light output smaller than 6 $\mathrm{MeV_{ee}}$ or with TOF shorter than 43.5 ns, which were excluded in the analysis.

5.1.5 Knocked-out neutron

The knocked-out neutron was detected and identified by the WINDS, in the same as in the case of the NEBULA (Sec. 5.1.4).

Figure 5.7 shows a PID plot of the knocked-out neutron after selecting the ^{11}Li beam, the ^{9}Li heavy fragment, and the recoil proton. The axes are defined as same as Fig. 5.6. The locus of the knocked-out neutron can clearly be be seen. Gamma rays from the target and the SBTs can be seen in the region with light output smaller than 6 MeV$_{ee}$ and with TOF shorter than 5.6 ns. These background events are rejected by the PID conditions.
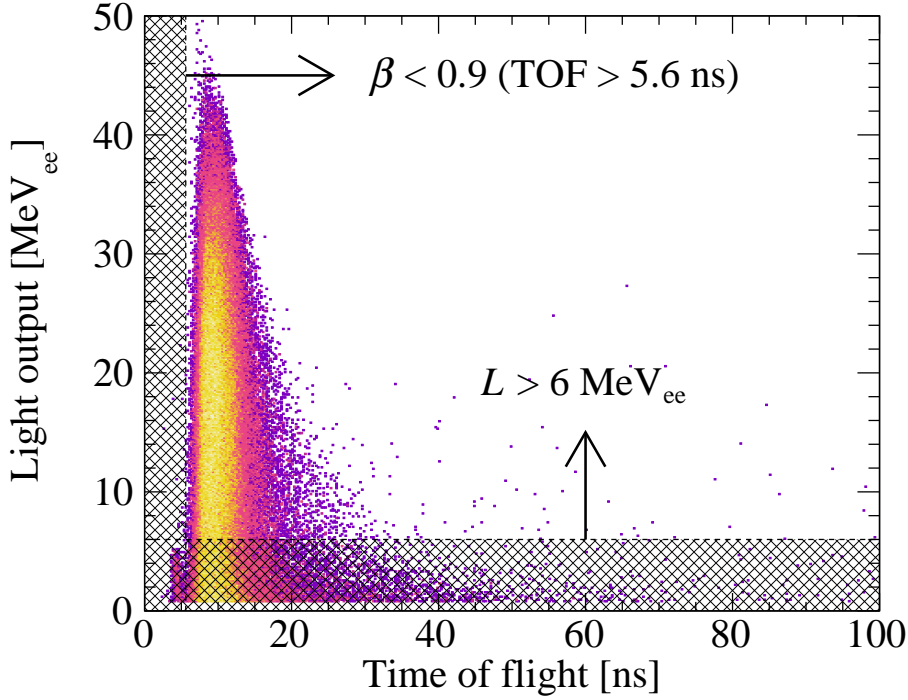
Figure 5.7: PID plot of the knocked-out neutron for the NCL1 layer of the WINDS. The ^{11}Li beam, the ^{9}Li heavy fragment, and the recoil proton were selected. The hatched area represents events with light output smaller than 6 MeV$_{ee}$ or with TOF shorter than 5.6 ns, which were excluded in the analysis.

5.2 Gamma rays from heavy fragment ^{9}Li

The de-excitation gamma rays from the heavy fragment ^{9}Li were measured by employing the in-beam gamma-ray spectroscopy technique [136]. Since the gamma rays were emitted from the heavy fragment ^{9}Li having a velocity of $\beta \sim 0.61$, the Doppler effect had to be considered. The de-excitation energy E_γ was obtained by performing the Doppler correction for the measured gamma-ray energy E'_γ using the formula

$$\frac{E'_\gamma}{E_\gamma} = \frac{\sqrt{1 - \beta^2}}{1 - \beta \cos \theta_\gamma}, \tag{5.16}$$

where θ_γ represents the emission angle of the gamma ray in the laboratory frame. The θ_γ value was determined from the reaction point r_0 (Sec. 4.4) and the detection position of the gamma ray. The detection position was defined as the center of the DALI2 crystal. The ^{11}Li beam velocity β at the reaction point, which is identical to the heavy fragment ^{9}Li velocity at the reaction point, was used for the correction. The derivation is explained in Sec. 5.3.

Figure 5.8 shows gamma-ray spectra of ^{9}Li and ^{12}Be from the ^{11}Li(p, pn) and the ^{14}Be(p, pn) reactions, respectively. The de-excitation gamma rays from the first excited state of ^{9}Li were not clearly observed in the ^{11}Li(p, pn) channel, while those from the excited states of ^{12}Be were observed in the ^{14}Be(p, pn) channel.
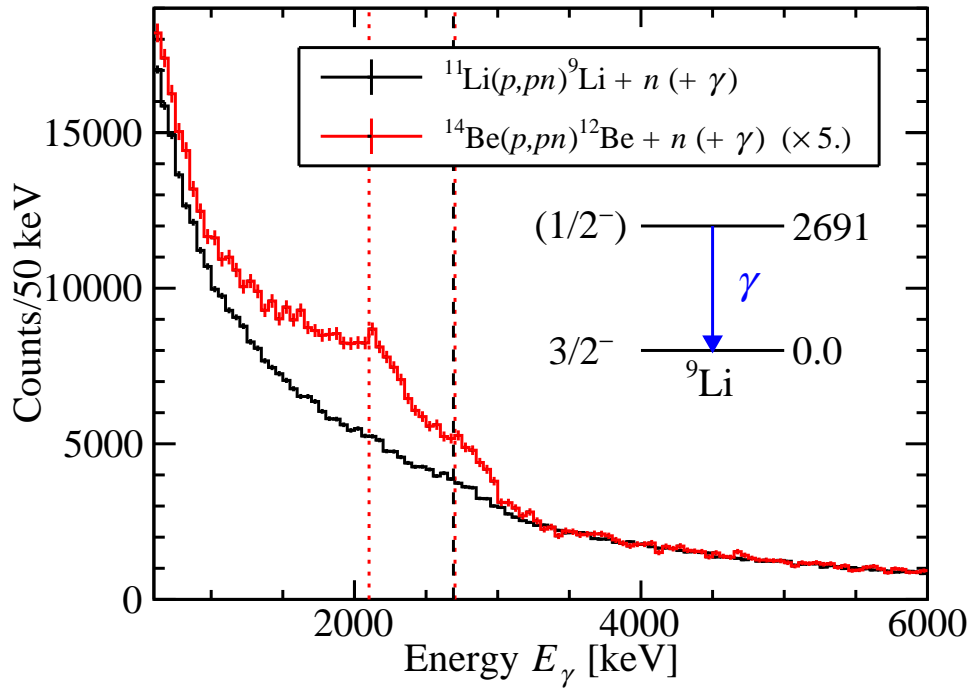
Figure 5.8: Doppler-corrected gamma-ray spectra of ^{9}Li and ^{12}Be from the ^{11}Li(p, pn) and the ^{14}Be(p, pn) reactions, respectively. The red dotted lines indicate the locations of the full energy peak of the 2102- and 2702-keV gamma rays from the excited states of ^{12}Be. The black dashed line indicates that of the 2691-keV gamma rays from the first excited state of ^{9}Li.

We conclude that the heavy fragment ^{9}Li observed in the present experiment was in the ground state. Thus, the excited ^{9}Li core in the ^{11}Li ground state decays with neutron emission, and can be observed as ^{8}Li, etc.

5.3   Momentum analysis of incident ^{11}Li beam

A momentum vector of the ^{11}Li beam particle $\boldsymbol{p}_{\mathbf{b}}$ was determined as

$$\boldsymbol{p}_{\mathbf{b}} = m_{\mathrm{b}}\gamma_{\mathrm{b}}\beta_{\mathrm{b}}c\hat{\boldsymbol{u}}_{\mathbf{b}}, \tag{5.17}$$

where m_{b} denotes a mass of the ^{11}Li beam particle. The $\hat{\boldsymbol{u}}_{\mathbf{b}}$ is the unit vector representing the direction of the beam trajectory and is defined by Eq. (4.11). A velocity β_{b} was determined by the TOF from F7 to F13. A flight path length from F7 to F13 was 35.849 m.

The ^{11}Li beam particle lost its energy in the beam line detectors and also in the target. A momentum vector of the ^{11}Li beam particle $\tilde{\boldsymbol{p}}_{\mathbf{b}}$ at the reaction point was derived by taking account the energy loss.

5.3.1   Beam momentum at the reaction point

The magnitude of the beam momentum p_{b} was defined using the magnetic rigidity from F5 to F7. Since the ^{11}Li beam lost its energy in the liquid hydrogen target, the magnitude of the beam momentum defined at the reaction point $\tilde{p}_{\mathrm{b}}$ was smaller than p_{b}. A momentum vector of the ^{11}Li beam at the reaction point $\tilde{\boldsymbol{p}}_{\mathbf{b}}$ was derived by taking account the energy loss. The energy loss was calculated by employing the Bethe-Bloch formula. The thicknesses of materials in the flight path were calculated by using the direction of the fragment trajectory unit vector $\hat{\boldsymbol{u}}_{\mathbf{b}}$ and the reaction point $\boldsymbol{r}_{\mathbf{0}}$.

5.3.2   Resolution and uncertainty

The TOF resolution was evaluated as 240 ps (FWHM) by using the beam with a small momentum spread of 0.063%. It resulted in the intrinsic momentum resolution of 1/820 (FWHM) for the averaged TOF of 193.7 ns. It should be noted that the multiple scattering of the beam particle contributed the momentum resolution at the reaction point. Since the TOF was measured from the plastic scintillator at the F7 to the SBTs, the energy straggling after the SBTs should be taken into account. The energy straggling was evaluated as 1/950 (FWHM) and did not depend on the beam momentum because of the small momentum spread of 3.2%. Thus, the overall momentum resolution at the reaction point was evaluated as $\mathrm{d}\tilde{p}_{\mathrm{b}}/\tilde{p}_{\mathrm{b}} = 1/620$ (FWHM). The obtained resolution was acceptable.

The intrinsic resolution of 1/820 (FWHM) was worse than the nominal resolution of the BigRIPS of about 1/1500 (FWHM). It was because we did not measure the position and the angle at F3 for the analysis of the optics.

The absolute value of the TOF was calibrated by using the magnetic rigidity $B\rho$ value from F5 to F7 (Sec. 5.1.1). The $B\rho$ value was determined by using the NMR value of the dipole magnet D5, whose NMR value was 0.29% lower than that of D6 (Sec. 3.3). This 0.29%

difference was regarded as the uncertainty of the absolute value of the beam momentum. The flight path length difference also contributed to the uncertainty, but it was no more than 0.01%.

5.4 Rigidity analysis of heavy fragment ^{9}Li

A momentum vector of the heavy fragment $\boldsymbol{p_r}$ was reconstructed by combining the Eq. (5.2) and a fragment trajectory unit vector $\boldsymbol{\hat{u}_r}$ as

$$\boldsymbol{p_r} = qB\rho\boldsymbol{\hat{u}_r}. \tag{5.18}$$

The electric charge of the heavy fragment was determined from the energy loss measured by the HODF and the HODP. The fragment trajectory unit vector $\boldsymbol{\hat{u}_r}$ was defined as

$$\boldsymbol{\hat{u}_r} = \frac{\boldsymbol{r_{FDC1}} - \boldsymbol{r_0}}{|\boldsymbol{r_{FDC1}} - \boldsymbol{r_0}|}, \tag{5.19}$$

where $\boldsymbol{r_{FDC1}}$ and $\boldsymbol{r_0}$ are the detection position of the heavy fragment at FDC1 and the reaction point, as obtained in Sec. 4.2 and in Sec. 4.4, respectively.

5.4.1 $B\rho$ reconstruction by using the SAMURAI spectrometer

The rigidity $B\rho$ was determined by reconstructing the trajectory of the heavy fragment in the SAMURAI magnet. The incoming trajectory of the heavy fragment $\boldsymbol{x_r}$ was calculated by using the fragment trajectory unit vector $\boldsymbol{\hat{u}_r}$ and the detection position at FDC1 $\boldsymbol{r_{FDC1}}$ as

$$\boldsymbol{x_r} = \boldsymbol{r_{FDC1}} + \alpha\boldsymbol{\hat{u}_r}. \tag{5.20}$$

The trajectory of the heavy fragment in the SAMURAI magnet was traced starting from the incoming vector $\boldsymbol{x_r}$ using the Runge-Kutta method for the best position matching with the detection position at FDC2 $\boldsymbol{r_{FDC2}}$. The magnetic field used for the tracing was calculated by the OPERA-3D/TOSCA [137]. A convergence condition for the calculation was

$$|x_{FDC2} - x_{FDC2}^{tr}| < 0.5 \text{ mm}, \tag{5.21}$$

where x_{FDC2} and x_{FDC2}^{tr} represent the positions of the heavy fragment at FDC2 measured by the FDC2 and reconstructed by the tracing, respectively. An error tolerance of 0.5 mm was employed since the position resolution of FDC2 was about 0.5 mm (Sec. 4.2.4).

5.4.2 Heavy fragment momentum at the reaction point

The magnitude of the heavy fragment momentum p_r was defined by the rigidity in the SAMURAI spectrometer as Eq. (5.18). Since the ^{9}Li heavy fragment lost its energy in the target, the magnitude of the heavy fragment momentum defined at the reaction point $\tilde{p}_r$ was larger than p_r in common with the beam momentum at the reaction point (Sec. 5.3.1).

When the initial momentum $\tilde{p}_r$ is known, the calculation of p_r is straightforward, because the energy loss can be directly calculated from $\tilde{p}_r$. However, in this case, p_r was known and $\tilde{p}_r$ was unknown. Therefore, a momentum vector of the ^{9}Li heavy fragment $\boldsymbol{\tilde{p}_r}$ at the reaction point was calculated by employing the bisection method described below.

1. The lower limit of the heavy fragment momentum $\tilde{p}_r^{\text{inf}}$ is initialized by the heavy fragment momentum after the target p_r.

2. The upper limit of the heavy fragment momentum $\tilde{p}_r^{\text{sup}}$ is initialized by the beam momentum before the target p_b.

3. The heavy fragment momentum at the reaction point $\tilde{p}_r$ is iteratively calculated as follows.

    (a) A trial momentum $\tilde{p}_r^{\text{trial}}$ is updated as $\tilde{p}_r^{\text{trial}} = (\tilde{p}_r^{\text{sup}} + \tilde{p}_r^{\text{inf}})/2$.

    (b) An energy loss ΔE in the target is calculated from $\tilde{p}_r^{\text{trial}}$ and a flight path in materials. The flight path is calculated by using the fragment trajectory unit vector $\boldsymbol{\hat{u}_r}$.

    (c) A trial momentum after the target p_r^{trial} is calculated from $\tilde{p}_r^{\text{trial}}$ by subtracting the energy loss ΔE.

    (d) If the trial momentum after the target p_r^{trial} is larger than the p_r, the upper limit $\tilde{p}_r^{\text{sup}}$ is updated by $\tilde{p}_r^{\text{trial}}$. If not, the lower limit $\tilde{p}_r^{\text{inf}}$ is updated by $\tilde{p}_r^{\text{trial}}$.

    (e) If the difference $\tilde{p}_r^{\text{sup}} - \tilde{p}_r^{\text{inf}}$ is larger than 1 MeV/c, one goes back to the step 3a. If not, the heavy fragment momentum at the reaction point $\tilde{p}_r$ is determined as $\tilde{p}_r = (\tilde{p}_r^{\text{sup}} + \tilde{p}_r^{\text{inf}})/2$.

It should be noted that the error tolerance on the momentum of 1 MeV/c we employed herein was sufficiently smaller than the actual momentum resolution of the SAMURAI spectrometer of 15.6 MeV/c (FWHM) for the heavy fragment ^{9}Li having the averaged momentum of 6700 MeV/c (Sec. 5.4.3).

5.4.3 Resolution and uncertainty

The resolution of the heavy fragment momentum p_r was evaluated by using a non-reacted ^{11}Li beam. Although the reaction point could not be defined without the (p, pn) reaction, it was fixed at $z = -4500$ mm, the center of the target, for convenience. In such a case, the beam momentum

at the reaction point $\tilde{p}_b$ and the heavy fragment momentum at the reaction point $\tilde{p}_r$ should be identical.

Figure 5.9 shows the normalized difference of the two momenta $(\tilde{p}_b - \tilde{p}_r)/\tilde{p}_b$. The width of the spectrum was 1/300 (FWHM); it came from the momentum resolution of the beam, that of the heavy fragment, and the energy straggling in the target. By subtracting the contribution of the beam of the $dp_b/p_b = 1/820$ (FWHM) (Sec. 5.3.2) and that of the energy straggling of 1/820 (FWHM), the resolution of the heavy fragment was evaluated as $dp_r/p_r = 1/350$ (FWHM). Since the momentum spread of the heavy fragment was less than 3% (FWHM), the momentum dependence of the energy straggling was negligible. This resolution was acceptable and even better than the design value of the SAMURAI spectrometer of 1/300 (FWHM).
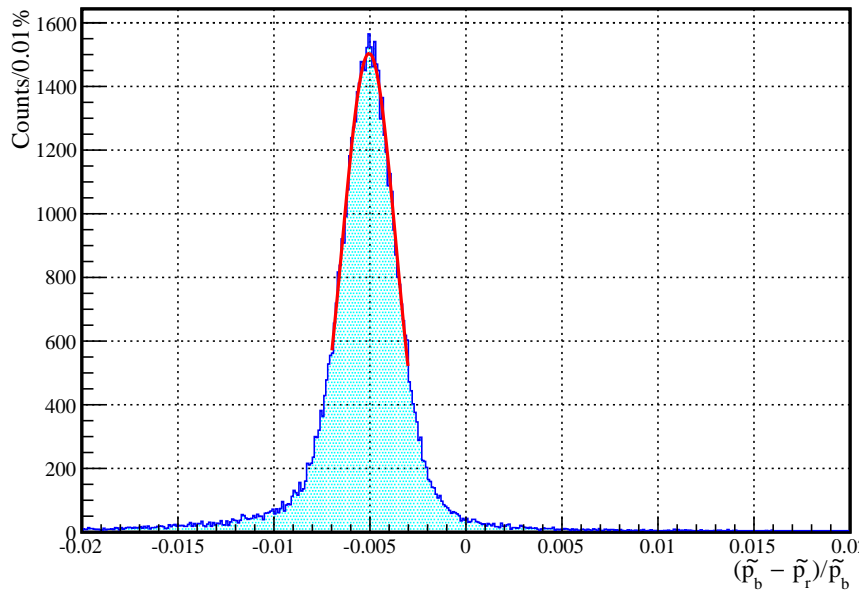
Figure 5.9: Normalized difference of the ^{11}Li beam momentum calculated from the TOF from F7 to F13 $\tilde{p}_b$ and that reconstructed from the rigidity analysis of the SAMURAI spectrometer $\tilde{p}_r$.

The position resolutions of the reaction point were 4.6 and 1.6 mm along the x and y directions, respectively (Sec. 4.4.1). As shown in Sec. 4.2.4, the position resolutions of FDC1 along x and y directions were 420 and 460 μm. Combining them, the position resolutions for heavy fragments along the x and y directions were 4.6 and 1.7 mm, respectively. Since the distance from reaction point to FDC1 was almost 1.8 m, the angular resolutions along the x and y directions were 2.6 and 0.9 mrad, respectively.

The absolute value of the rigidity relied on the calculated magnetic field map [137] and the actual field strength at the center of the SAMURAI magnet monitored by the current in the coil. The systematic uncertainty of the heavy fragment momentum was evaluated as 1/200 from the shift of the peak in Fig. 5.9.

The reaction point had a systematic uncertainty of 610 μm (Sec. 4.4.1). Since the FDC1 was

aligned within an accuracy of 200 μm, the systematic angular uncertainty was evaluated as 0.36 mrad.

5.5   Momentum analysis of decay neutron

The momentum vector of a decay neutron $\boldsymbol{p_{n2}}$ was calculated as

$$\boldsymbol{p_{n2}} = m_n \gamma_{n2} \beta_{n2} c \hat{\boldsymbol{u}}_{n2}, \tag{5.22}$$

$$\beta_{n2} c = \frac{\text{Flight path length (FPL)}}{\text{Time of flight (TOF)}}, \tag{5.23}$$

$$\gamma_{n2} = \frac{1}{\sqrt{1 - \beta_{n2}^2}}, \tag{5.24}$$

$$\text{TOF} = t_{n2} - t_0, \tag{5.25}$$

$$\text{FPL} = |\boldsymbol{x_{n2}} - \boldsymbol{r_0}|, \tag{5.26}$$

$$\hat{\boldsymbol{u}}_{n2} = \frac{\boldsymbol{x_{n2}} - \boldsymbol{r_0}}{\text{FPL}}, \tag{5.27}$$

where m_n denotes a neutron mass. A detection position of the decay neutron $\boldsymbol{x_{n2}}$ and a detection timing of the decay neutron t_{n2} were measured by the NEBULA (Sec. 4.7). By combining the information of the reaction point $\boldsymbol{r_0}$ and the reaction timing t_0, the length and the direction of the trajectory $\boldsymbol{x_{n2}} - \boldsymbol{r_0}$ and the TOF $t_{n2} - t_0$ were calculated so that the momentum vector of the decay neutron $\boldsymbol{p_{n2}}$ was determined.

Figure 5.10 shows a detection position distribution of the decay neutron on the (x, y) plane. The whole effective area was bombarded by the decay neutron. The acceptance is discussed in Sec. 5.11. The hit position had a peak around the center. The peak position in the x axis was slightly off-centered because the geometrical position of the NEBULA had an offset of 12.6 cm. The decrease of the hit frequency along the x axis was not continuous, while that along the y axis was continuous. It was because the x-position distribution was discretized by the size of the NEUT module of 12 cm (Sec. 4.7.4).

The time resolution of the NEBULA was evaluated as 280 ps (FWHM) (Sec. 4.7). By combining the time resolution of the reaction point of 88 ps (FWHM), the TOF resolution was evaluated as 300 ps (FWHM). Besides, the NEBULA had an uncertainty on the detection position in z direction of 12 cm due to the thickness of the detector. This uncertainty was equivalent to the TOF resolution of 670 ps in rectangular distribution, corresponding to 450 ps (FWHM). As a result, the overall TOF resolution and momentum resolution were 540 ps (FWHM) and 1/77 (FWHM), respectively.

The position resolution in the x direction was limited by the width of the detector of 12 cm in rectangular distribution, i.e. 8.1 cm (FWHM). The position resolution in y direction was 4.3 cm (FWHM), by assuming the light velocity of 15.2 cm/ns. The position resolutions of
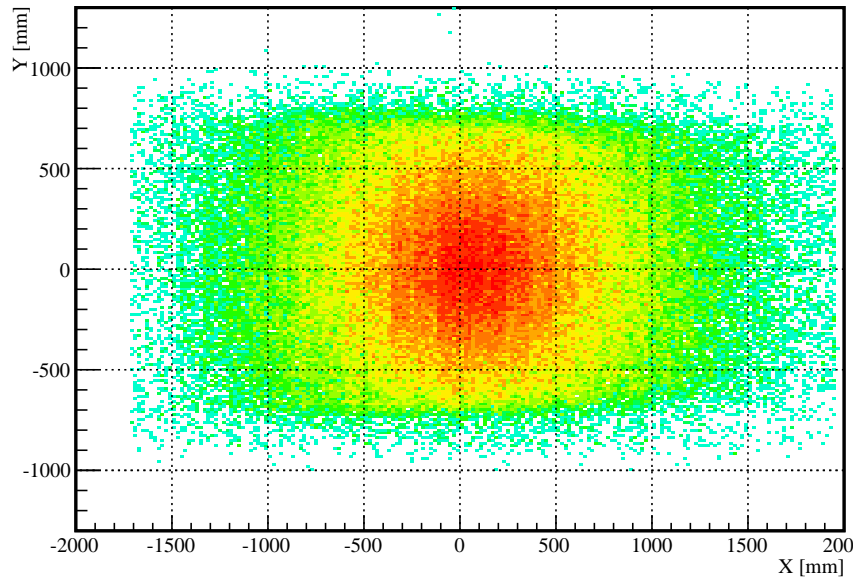
Figure 5.10: Detection position distribution of the decay neutron on the (*x*, *y*) plane.

the reaction point of 4.6 and 1.6 mm along the *x* and *y* directions were negligible as compared with the position resolution of the NEBULA. Thus, the angular resolution along the *x* and the *y* directions was respectively evaluated as 6.7 and 3.6 mrad along the *x* and *y* directions, only by taking into account the position resolution of the NEBULA. The sufficient resolution was achieved as expected.

5.6 Momentum analysis of knocked-out neutron

A momentum vector of the knocked-out neutron p_{n1} was reconstructed by using the neutron detector WINDS. The analysis scheme was the same as one for the NEBULA, as described in Sec. 5.5.

Figure 5.11 shows detection position distributions of the knocked-out neutron. In the top panel, the rectangular shape of each NC module was seen since each NC module was placed with some gaps (Sec. 3.9). In the bottom panel, the NC modules arranged in concentric four layers were clearly seen. As already explained (Sec. 4.6.4), the detection position along the bar width was smeared with the uniform distribution, while that parallel to the incident neutron was not. It was clearly seen in the bottom panel of Fig. 5.11. In addition, the enhanced yields in modules placed at forward angle were also seen.

The intrinsic time resolution of the WINDS was evaluated as 320 ps (FWHM) (Sec. 4.6). By combining the time resolution of the reaction point of 88 ps (FWHM), the TOF resolution was evaluated as 340 ps (FWHM). The WINDS had an uncertainty on the detection position in depth direction of 10 cm due to the thickness of the detector. This uncertainty was equivalent to the TOF resolution of 440 ps to 1 ns in rectangular distribution, depending on the kinetic
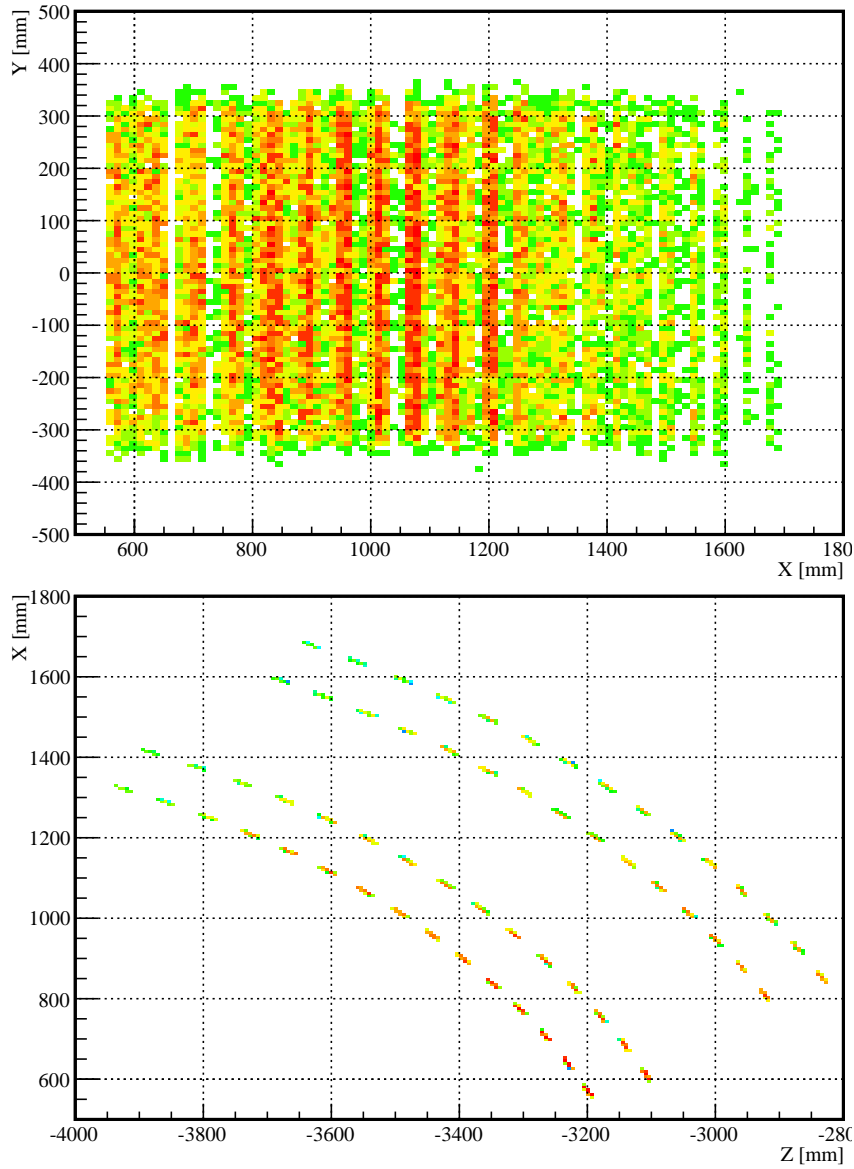
Figure 5.11: Detection position distributions of the knocked-out neutron (top) on the (x, y) and (bottom) the (z, x) planes. The color of the histograms represents the hit frequency. The bottom panel also shows the top view of the geometrical configuration of the NC modules given in Fig. 3.18.

energy of the knocked-out neutron. In FWHM, the uncertainty ranges from 300 ps to 680 ps. The momentum resolution was better for the knocked-out neutron having smaller momentum. This dependence was visually shown in Fig. 5.12.
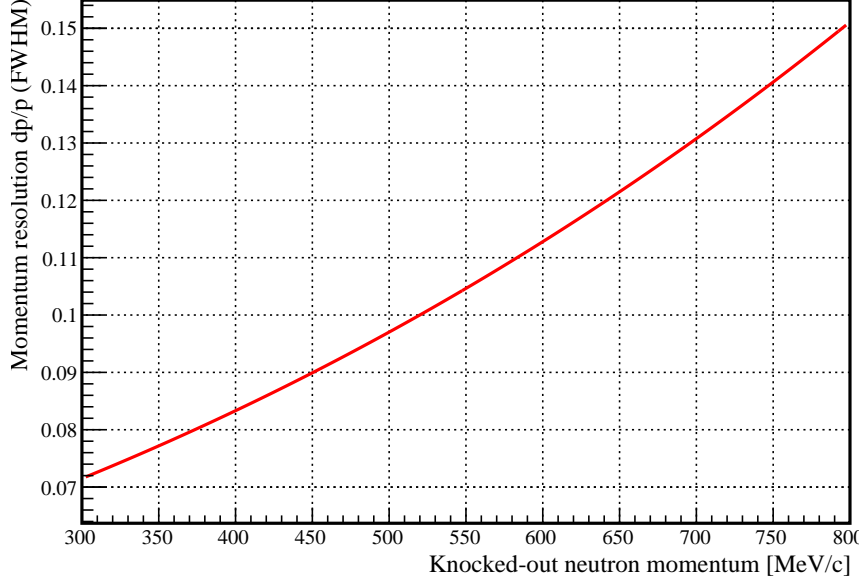
Figure 5.12: Momentum resolution of the knocked-out neutron as a function of the neutron momentum.

Herein, we introduce the x' axis along the width of each scintillator bar. The position resolution in x' direction was limited by the width of the detector of 10 cm in rectangular distribution, i.e. 6.8 cm (FWHM). The position resolution in y direction was 4.9 cm (FWHM), by assuming the light velocity of 15.2 cm/ns. The position resolutions of the reaction point of 4.6 and 1.6 mm along the x' and y directions were negligible as compared with the position resolution of the WINDS. Thus, the angular resolution along the x' and the y directions was respectively evaluated as 45 and 33 mrad along the x' and y directions, only taking into the contribution of the position resolution of the WINDS. The obtained resolution was acceptable.

5.7   Momentum analysis of recoil proton

The momentum vector of a recoil proton $\boldsymbol{p_p}$ was reconstructed by using the recoil proton detector RPD as

$$\boldsymbol{p_p} = m_p \gamma_p \beta_p c \hat{\boldsymbol{u}}_{\boldsymbol{p}}, \tag{5.28}$$

$$\beta_p c = \frac{\text{FPL}}{\text{TOF}}, \tag{5.29}$$

$$\gamma_p = \frac{1}{\sqrt{1 - \beta_p^2}}, \tag{5.30}$$

$$\text{TOF} = t_p - t_0, \tag{5.31}$$

$$\text{FPL} = |\boldsymbol{x_p} - \boldsymbol{r_0}|, \tag{5.32}$$

$$\hat{\boldsymbol{u}}_{\boldsymbol{p}} = \frac{\boldsymbol{x_p} - \boldsymbol{r_0}}{\text{FPL}}, \tag{5.33}$$

where m_p denotes a proton mass. A detection position of the recoil proton $\boldsymbol{x_p}$ and a detection timing of the recoil proton t_p were respectively measured by the RPDC and the RPTOF. By combining the information of the reaction point $\boldsymbol{r_0}$, the length and the direction of the trajectory $\boldsymbol{x_p} - \boldsymbol{r_0}$ and the TOF $t_p - t_0$ were calculated. In order to calculate the proton velocity from consistent TOF and flight path length (FPL), the detection position $\boldsymbol{x_p}$ was defined as the detection position on the RPTOF, and was obtained by extrapolation from the RPDC along the trajectory.

Since the recoil proton loses its energy passing out of the target, the momentum vector of the recoil proton $\tilde{\boldsymbol{p}}_{\boldsymbol{p}}$ at the reaction point was reconstructed taking account of the energy loss in the MINOS and its surrounding materials.

The procedure of the reconstruction is described in the following subsections. The uncertainty coming from the energy loss and from the multiple scattering is also discussed.

5.7.1   Detection position extrapolated onto the RPTOF

The RPDC gives the detection position $\boldsymbol{r}_{\textbf{RPDC}}$ of the recoil proton at the RPDC (Sec. 4.2). The detection position of the recoil proton at the RPTOF $\boldsymbol{r}_{\textbf{RPTOF}} = \boldsymbol{r_p}$ was derived by the extrapolation.

The detection position of the recoil proton $\boldsymbol{r_p}$ is implicitly written as

$$\boldsymbol{r_p} = \boldsymbol{r}_{\textbf{RPDC}} + \hat{\boldsymbol{u}}_{\boldsymbol{p}} \cdot |\boldsymbol{r}_{\textbf{RPTOF}} - \boldsymbol{r}_{\textbf{RPDC}}| \tag{5.34}$$

$$= \boldsymbol{r}_{\textbf{RPDC}} + (\boldsymbol{r}_{\textbf{RPDC}} - \boldsymbol{r_0}) \cdot \frac{|\boldsymbol{r}_{\textbf{RPTOF}} - \boldsymbol{r}_{\textbf{RPDC}}|}{|\boldsymbol{r}_{\textbf{RPDC}} - \boldsymbol{r_0}|} \tag{5.35}$$

$$= \boldsymbol{r}_{\textbf{RPDC}} + (\boldsymbol{r}_{\textbf{RPDC}} - \boldsymbol{r_0}) \cdot \frac{z'_{\textbf{RPTOF}} - z'_{\textbf{RPDC}}}{z'_{\textbf{RPDC}} - z'_0}, \tag{5.36}$$

where z'_{RPTOF}, z'_{RPDC}, and z'_0 denote the position in a RPD local coordinate for the RPTOF, the RPDC, and the reaction point, respectively. The RPD local coordinate is defined in Fig. 3.16.

Figure 5.13 shows obtained detection position distribution of the recoil proton. The larger yield was seen in the right side of the plot, corresponding to the forward angle. It was due to the kinematical condition (Sec. 4.2.3).
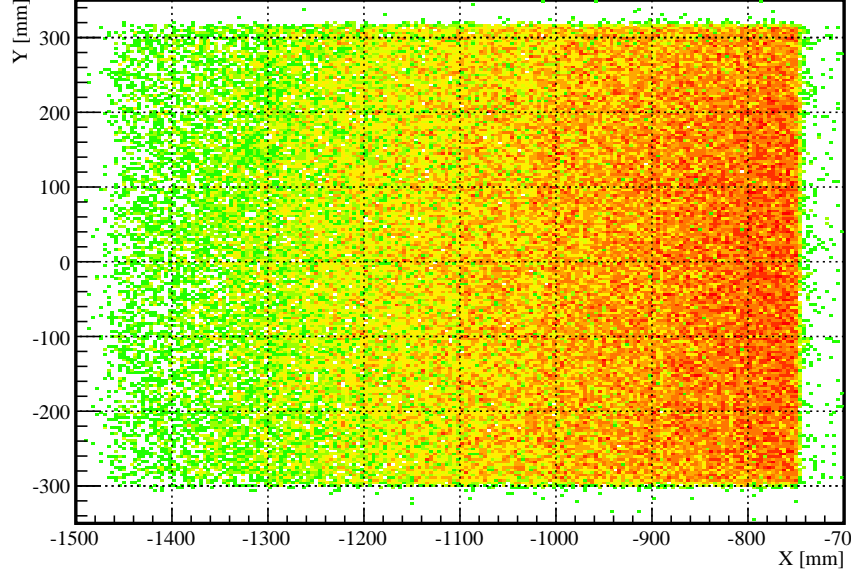
Figure 5.13: Detection position distribution of the recoil proton on the (x, y) plane.

5.7.2 Momentum reconstruction with energy loss correction

The magnitude of the recoil proton momentum p_p calculated from the measured TOF $t_p - t_0$ and the measured FPL is smaller than that at the reaction point $\tilde{p}_p$, since the recoil proton loses its energy passing out of the MINOS. The mean value of the energy loss was about 10 MeV. It resulted about 7% systematic underestimation for the recoil proton momentum $\tilde{p}_p$ at the reaction point.

In this experiment, the liquid hydrogen target with a diameter of 52 mm was used. A scattering angle of the recoil proton ranged from 25 to 65 degrees. It made it difficult to find a clear relation between $\boldsymbol{p_p}$ and $\tilde{p}_p$; thicknesses of materials in the flight path of the recoil proton strongly depends on the reaction point $\boldsymbol{r_0}$ and the scattering angle $\hat{\boldsymbol{u}}_{\boldsymbol{p}}$. Therefore, the recoil proton momentum $\tilde{p}_p$ at the reaction point was reconstructed event by event, by employing the bisection method as described below. The scheme was basically same with that for the heavy fragment (Sec. 5.4.2).

1. The recoil proton momentum p_p out of the MINOS is calculated from the measured TOF $t_p - t_0$ and the measured FPL $\left| \boldsymbol{x_p} - \boldsymbol{x_0} \right|$.

2. The lower limit of the recoil proton momentum $\tilde{p}_p^{\mathrm{inf}}$ is initialized by p_p.

3. The upper limit of the recoil proton momentum $\tilde{p}_p{}^{\text{sup}}$ is initialized by the beam momentum p_{b}.

4. The recoil proton momentum $\tilde{p}_p$ at the reaction point is iteratively calculated as follows.

   (a) A trial momentum $\tilde{p}_p{}^{\text{trial}}$ is updated as $\tilde{p}_p{}^{\text{trial}} = (\tilde{p}_p{}^{\text{sup}} + \tilde{p}_p{}^{\text{inf}})/2$.

   (b) An energy loss ΔE in the MINOS is calculated from $\tilde{p}_p{}^{\text{trial}}$ and a flight path in materials. The flight path is calculated by using the reaction point $\boldsymbol{r_0}$ and the direction $\hat{\boldsymbol{u}}_p$ of the recoil proton.

   (c) A recoil proton momentum $p_p{}^{\text{trial}}$ out of the MINOS is calculated from $\tilde{p}_p{}^{\text{trial}}$ by subtracting the energy loss ΔE.

   (d) A corresponding TOF $t_{\text{TOF}}^{\text{trial}}$ is calculated by using $p_p{}^{\text{trial}}$ and the measured FPL $\left| \boldsymbol{x_p} - \boldsymbol{x_0} \right|$.

   (e) If the TOF $t_{\text{TOF}}^{\text{trial}}$ is shorter than the measured TOF $t_p - t_0$, the upper limit $\tilde{p}_p{}^{\text{sup}}$ is updated by $\tilde{p}_p{}^{\text{trial}}$. If not, the lower limit $\tilde{p}_p{}^{\text{inf}}$ is updated by $\tilde{p}_p{}^{\text{trial}}$.

   (f) If the difference $\tilde{p}_p{}^{\text{sup}} - \tilde{p}_p{}^{\text{inf}}$ is larger than 1 MeV/c, one goes back to the step 4a. If not, the recoil proton momentum $\tilde{p}_p$ at the reaction point is determined as $\tilde{p}_p = (\tilde{p}_p{}^{\text{sup}} + \tilde{p}_p{}^{\text{inf}})/2$.

The momentum resolution of the RPD was 3 MeV/c (FWHM) at the highest (Sec. 5.7.3). The smaller value, 1 MeV/c, was used as the error tolerance on the momentum of the recoil proton.

5.7.3 Resolution and uncertainty

Figure 5.14 shows the resolutions of the magnitude and the angle of the recoil proton momentum vector. The momentum resolution got worse with increasing the recoil proton momentum. Since the TOF depended on the momentum, the momentum resolution was not constant as a function of the recoil proton momentum. In addition, the time resolution of the RPTOF got worse for the recoil proton with larger momentum due to the small light output (Sec. 4.5.3). Therefore, this kind of tendency was obtained.

On the other hand, the effect of multiple scattering on the angular resolution had an opposite tendency; it was more serious for the recoil proton having a smaller momentum. The effect of this angular straggling was larger than the angular resolution of about 2 mrad coming from the uncertainty of the reaction point (Sec. 4.4.1). The angular resolution coming from the position resolution of the RPDC of better than 0.2 mrad was quite small and the effect was negligible.

The resolution of the reaction point caused the systematic uncertainty on the recoil proton momentum; The energy loss of the recoil proton was calculated by using the flight path length based on the reaction point information (Sec. 5.7.2). The reaction point uncertainty was smaller
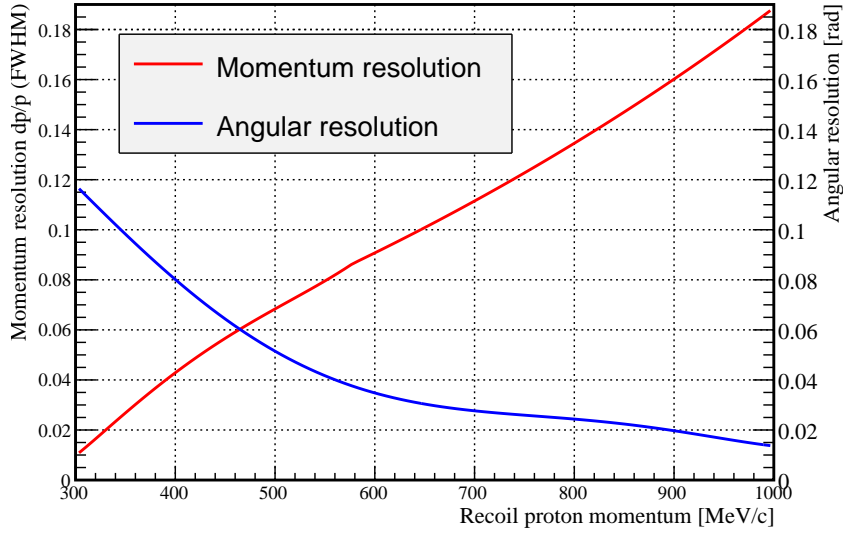
Figure 5.14: Momentum and angular resolutions of the recoil proton as a function of the momentum.

than 1 cm (Sec. 4.4.1), which resulted in the shift of 0.03–0.2% on the recoil proton momentum. This shift was within the resolution and negligible, as shown in Fig. 5.14.

The RPD was aligned within an accuracy of 200 μm thanks to the photogrammetry system [98, 99]. It resulted in about 1 mrad systematic uncertainty. It was negligible as compared to the angular resolution.

5.8 Momentum conservation condition

Momentum vectors of all the particles involved in the reaction were determined (the ^{11}Li beam particle for Sec. 5.3, the ^{9}Li heavy fragment for Sec. 5.4, the decay neutron for Sec. 5.5, the knocked-out neutron for Sec. 5.6, and the recoil proton for Sec. 5.7). These momentum vectors should satisfy the momentum conservation law as

$$\tilde{\boldsymbol{p}}_{\mathbf{b}} + \boldsymbol{p}_{\mathbf{t}} = \tilde{\boldsymbol{p}}_p + \boldsymbol{p}_{n1} + \boldsymbol{p}_{n2} + \tilde{\boldsymbol{p}}_{\mathbf{r}}, \tag{5.37}$$

where $\boldsymbol{p}_{\mathbf{t}}$ denotes the target proton momentum. The left hand and the right hand sides respectively represent the states before and after the occurrence of the quasi-free (p, pn) reaction. Since the target was not a nucleus but a proton, $\boldsymbol{p}_{\mathbf{t}}$ was always zero. A momentum difference d$\boldsymbol{p}$ was defined as

$$\mathrm{d}\boldsymbol{p} = \tilde{\boldsymbol{p}}_{\mathbf{b}} - \left(\tilde{\boldsymbol{p}}_p + \boldsymbol{p}_{n1} + \boldsymbol{p}_{n2} + \tilde{\boldsymbol{p}}_{\mathbf{r}} \right) = 0. \tag{5.38}$$

In order to reject the background, events satisfying the momentum conservation law ($\pm 2\sigma$) were selected for the analysis.

Figure 5.15 shows the momentum difference dp projected onto the x, y, and z directions. The widths of the spectra for x, y, and z directions were 48.9, 44.4, and 59.4 MeV/c (FWHM), respectively. They were consistently explained by the resolution and the straggling (Sec. 5.12). The shifts of the spectra for x, y, and z directions were 5.8, 3.8, and 9.1 MeV/c, respectively. They were smaller than the resolution and the straggling. They may be come from the incomplete calibration of detectors. The systematic uncertainty coming from these shifts are discussed in Sec. 5.13.

It was also confirmed that there was no correlation between the momentum difference dp and each momentum ($\tilde{p}_\mathrm{b}$, $\tilde{p}_p$, p_{n1}, p_{n2}, and $\tilde{p}_\mathrm{r}$) for x, y, and z directions.
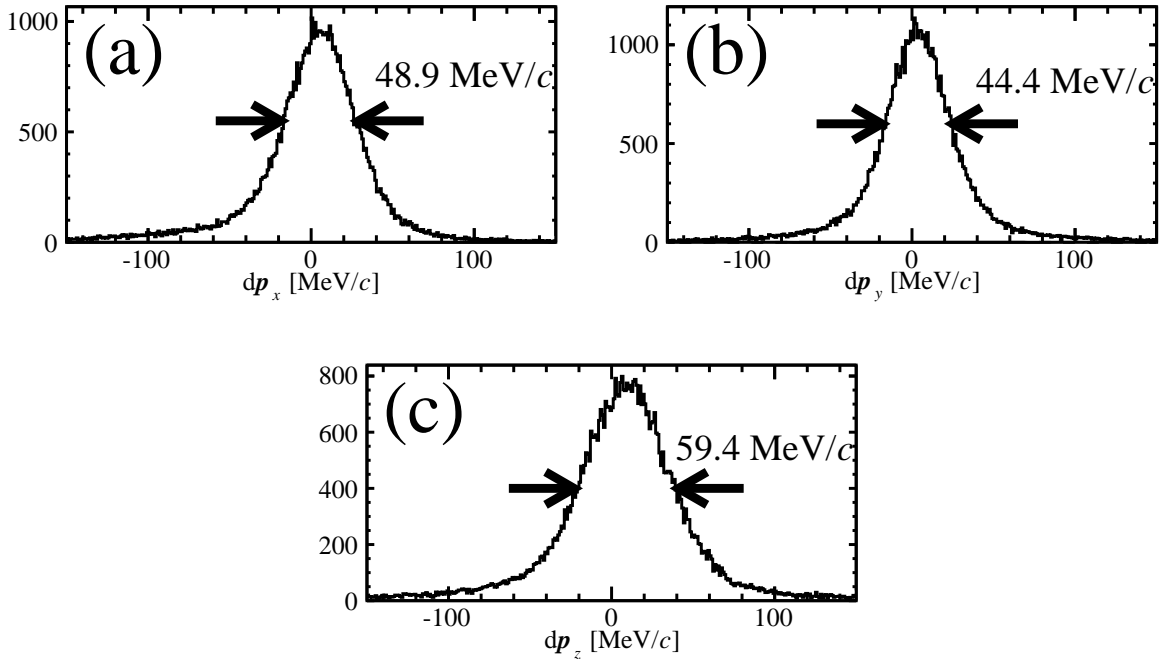
Figure 5.15: Momentum difference dp distribution (a) in the x, (b) the y, and (c) the z directions.

5.9 Relative energy

A relative energy E_{rel} is defined with respect to the invariant mass m_{inv} as

$$E_{\mathrm{rel}} = m_{\mathrm{inv}} - \sum_i m_i, \tag{5.39}$$

$$m_{\mathrm{inv}} = \sqrt{\left(\sum_i E_i\right)^2 - \left|\sum_i \boldsymbol{p}_i c\right|^2}, \tag{5.40}$$

where m_i, E_i, and $\boldsymbol{p}_i$ denote a mass, an energy, and a momentum of a decay fragment i. The relative energy resolution ΔE_{rel} is obtained as

$$\Delta E_{\mathrm{rel}} \approx \sqrt{2E_{\mathrm{rel}}E_{\mathrm{b}}}\sqrt{\left(\frac{\Delta p_{\mathrm{r}}}{p_{\mathrm{r}}}\right)^2 + \left(\frac{\Delta p_n}{p_n}\right)^2 + \Delta\theta_{\mathrm{r}\text{-}n}^2}, \tag{5.41}$$

where E_{b} and $\Delta\theta_{\mathrm{r}\text{-}n}$ denote the beam energy per nucleon and the angular resolution between fragments.

In this experiment, the decay fragments denoted by i were the heavy fragment ^{9}Li and the decay neutron. The masses of these particles were known. The momenta of these particles were obtained in Sec. 5.4 and Sec. 5.5. The energies of these particles were calculated through the energy-momentum relation as

$$E^2 = m^2 + |\boldsymbol{p}c|^2. \tag{5.42}$$

The ^{11}Li beam energy was 246 MeV/nucleon. The momentum resolution of the heavy fragment ^{9}Li was 1/330 (FWHM) if the multiple scattering in the target is taken into account (Sec. 5.4.3). The momentum resolution of the decay neutron was 1/77 (FWHM) (Sec. 5.5). The angular resolution between two particles was about 5.7 mrad on average, dominated by the position resolution of the decay neutron. Therefore, the relative energy resolution was evaluated as

$$\Delta E_{\mathrm{rel}} \approx 0.3\sqrt{E_{\mathrm{rel}}} \text{ MeV (FWHM)}. \tag{5.43}$$

The obtained resolution of 0.3 MeV (FWHM) at $E_{\mathrm{rel}} = 1$ MeV was better than the designed value of the SAMURAI spectrometer of 0.5 MeV (FWHM) at $E_{\mathrm{rel}} = 1$ MeV [100].

It should be noted that Eq. (5.43) slightly underestimates the resolution near the relative energy around zero. For higher relative energies of $E_{\mathrm{rel}} \gtrsim 0.1$ MeV, it is empirically known that the present approximation works well.

5.10   Opening angle reconstruction

The definitions of the variables and the coordinates are explained in Sec. 2.3. The opening angle θ_Y between the relative momentum $\boldsymbol{K}_Y$ and the internal momentum $\boldsymbol{k}_Y$ in Jacobi coordinates was defined by Eq. (2.7). The relative momentum and the internal momentum in Jacobi coordinate $\boldsymbol{K}_Y$ and $\boldsymbol{k}_Y$ were derived from the momentum vectors of two neutrons and the heavy fragment ^{9}Li by using Eq. (2.5) and Eq. (2.6).

In the laboratory frame, the initial momentum vector of the knocked-out neutron $\boldsymbol{p}_{n1}^{\mathbf{0}}$ was derived by using Eq. (2.1) as

$$\boldsymbol{p}_{n1}^{\mathbf{0}} = \boldsymbol{p}_{n1} + \tilde{\boldsymbol{p}}_p - \boldsymbol{p}_{\mathbf{t}} = \boldsymbol{p}_{n1} + \tilde{\boldsymbol{p}}_p. \tag{5.44}$$

This $\boldsymbol{p}_{n1}^{\mathbf{0}}$ was identical to the missing momentum $\boldsymbol{k}$ defined in Eq. (2.1) except for the frame: $\boldsymbol{p}_{n1}^{\mathbf{0}}$ was defined in the laboratory frame while $\boldsymbol{k}$ was defined the beam rest frame. Then, the momentum vectors of the knocked-out neutron $\boldsymbol{p}_{n1}^{\mathbf{0}}$, the decay neutron $\boldsymbol{p}_{n2}$, and the ^{9}Li core $\tilde{\boldsymbol{p}}_{\mathbf{r}}$ were converted to the $\boldsymbol{k}_{n1}$, $\boldsymbol{k}_{n2}$, and $\boldsymbol{k}_{\mathbf{c}}$ respectively, through the Lorentz transformation by using the beam momentum $\tilde{\boldsymbol{p}}_{\mathbf{b}}$.

5.11   Acceptance correction

A Monte-Carlo based simulation was performed so as to evaluate the acceptance of the present setup. Since the correlation of the momentum vectors of two neutrons were directly observed and discussed in the present study, it was important to consider the effect of the geometrical acceptance on the observables.

The procedure of the simulation is first introduced in Sec. 5.11.1. For simplicity, the acceptances of recoil particles (the recoil proton and the knocked-out neutron) and of decay particles (the heavy fragment and the decay neutron) are separately discussed in Sec. 5.11.2 and Sec. 5.11.3, respectively, even they are not independent. The result was discussed in Sec. 5.11.4. The uncertainty of the simulation is discussed in Sec. 5.11.5.

5.11.1   Monte-Carlo simulation

The simulation was based on the Monte Carlo method. It consisted of following components: (i) event generation, (ii) reaction generation, (iii) multiple scattering evaluation, (iv) detection evaluation, and (v) acceptance evaluation. In this subsection, these are explained in detail.

The event generation was performed using the theoretical calculation based on the framework in Ref. [73] as well as the experimental data. The initial state of the ^{11}Li beam particle, the momentum vectors of the ^{9}Li core and of the two valence neutrons, was determined in the beam rest frame so as to reproduce the calculated density [138] as a function of the internal momentum

k_Y, the relative momentum K_Y, and the opening angle θ_Y. These variables are introduced in Sec. 2.3. The momentum vectors defined in the beam rest frame were transformed into the laboratory frame isotropically, since the ^{11}Li beam was not polarized nor aligned in the present experiment. The momentum and the angular distributions of the ^{11}Li beam were determined so as to reproduce those obtained from the experimental data. The reaction point distribution in the target was also determined based on the experimental data.

The reaction part was separated into two steps: the quasi-free (p, pn) reaction on ^{11}Li and the neutron emission from the unbound reaction residue ^{10}Li (Sec. 2.2). The quasi-free (p, pn) reaction was imitated with the n-p elastic scattering by taking the distortion effect into account. The reaction was calculated event by event from the momentum vectors of incident neutron and the target proton by using two parameters: the polar angle θ_{NN} and the azimuthal angle ϕ_{NN} defined in the center of mass frame of the neutron and the proton. The θ_{NN} distribution was assumed to be identical to that in the free space. The ϕ_{NN} distribution was assumed to be uniform since the ^{11}Li beam and the target proton were not polarized. The distortion effect was taken into account by introducing the damping factor (Sec. 6.2.2).

During the neutron emission from the reaction residue ^{10}Li, the momentum vectors of the heavy fragment ^{9}Li and of the decay neutron were distorted due to the two-body FSI [73]. This effect was taken into account in the theoretical calculation of the density distribution used for the event generation.

The multiple scattering of charged particles was taken into consideration since the target was quite thick (15 cm) and the flight paths of particles were not always in vacuum. The energy and the angular straggling for the ^{11}Li beam, for the recoil proton, and for the heavy fragment ^{9}Li were evaluated event by event. On the other hand, nuclear reactions of neutrons were not taken into consideration. It would result no more than 6% error in the final result, which was sufficiently smaller than the total systematic uncertainty of 19% (Sec. 5.11.5).

The particle detection was determined whether the particle passed through the effective volume of the detector. In order to reduce the computational cost, physical processes involved in the detection were not evaluated event by event. Instead, the efficiencies and the intrinsic resolutions of the detectors obtained from the experimental data (Chap. 4 and Chap. 5) were implemented so as to mimic the realistic responses.

The acceptance was evaluated by counting the number of events where all the particles were detected. The acceptance factor $\varepsilon_{\mathrm{acc}}$ was defined as a function of three important quantities in this study: the internal momentum k_Y, the relative energy of ^{10}Li E_{rel}, and the opening angle $\cos \theta_Y$. The definition of the $\varepsilon_{\mathrm{acc}}$ is

$$\varepsilon_{\mathrm{acc}}(k_Y, E_{\mathrm{rel}}, \cos \theta_Y) = \frac{N'(k_Y, E_{\mathrm{rel}}, \cos \theta_Y)}{N(k_Y, E_{\mathrm{rel}}, \cos \theta_Y)}, \tag{5.45}$$

where N and N' respectively represent the number of all the generated events and the number of events where all the particles were detected. The evaluated $\varepsilon_{\mathrm{acc}}$ value was used for the

acceptance correction as

$$Y(k_Y, E_{\text{rel}}, \cos\theta_Y) = \frac{\tilde{N}(k_Y, E_{\text{rel}}, \cos\theta_Y)}{\varepsilon_{\text{acc}}(k_Y, E_{\text{rel}}, \cos\theta_Y)}, \tag{5.46}$$

where Y and $\tilde{N}$ denote the yield and the number of counts obtained experimentally, respectively.

5.11.2   Recoil particles: RPD and WINDS

Among all the detectors used in the present experiment, the detectors for the recoil particles had limited and non-uniform geometrical acceptances. Thus, the acceptances of the recoil particles played significant role to determine the overall acceptance. In this subsection, the geometrical configurations of the recoil particle detectors are first explained. Then, the uncertainty is evaluated which comes from the treatment that nuclear reactions of the knocked-out neutron are ignored in the simulation. Finally, the simulation is validated by comparing the simulation and the experimental data.

The recoil proton and the knocked-out neutron were detected by the RPD (Sec. 3.8) and the WINDS (Sec. 3.9), respectively. The scattering angle of the recoil proton of about $30 < \theta_p < 65$ degrees was geometrically covered by the RPD. The azimuthal angle of about $|\phi_p + 180| < \pm 20$ degrees was covered. The situation was the same with the detection of the knocked-out neutron by the WINDS, which was installed at the opposite side of the beam line from the RPD. The scattering angle of the knocked-out neutron of about $25 < \theta_n < 60$ degrees and the azimuthal angle of about $|\phi_n| < \pm 20$ degrees was geometrically covered by the WINDS. The realistic geometrical configuration of each detector module of the RPD and the WINDS determined by the photogrammetry system [98, 99] was implemented in the simulation.

The reaction loss of the knocked-out neutron along the flight path was evaluated by assuming the reaction point at the center of the liquid hydrogen target and the scattering angle of 45 degrees. Among materials along the flight path, the liquid hydrogen of 40 mm, the aluminum target chamber of 2.8 mm, and the plastic frame of the TPC of 5.6 mm mainly contributed to the reaction. The total interaction cross sections of neutron with these materials at 30–500 MeV were 0.05, 1, and 0.5 b, respectively. Thus, totally 2.1% of the neutrons were scattered or lost in these materials. The reactions in this energy region were dominated by the elastic scattering, which might distort the neutron angular distribution. However, the effect on the following analysis was negligible because the fraction was sufficiently small.

In order to validate results of the simulation, the distribution of the initial neutron momentum in the beam rest frame (missing momentum) $\boldsymbol{k}$ was compared with the data. The missing momentum was selected because its realistic distribution could be predicted without any knowledge on the structure of the ^{11}Li beam particle: Since the ^{11}Li beam was not polarized nor aligned in the present experiment, it had no specific direction in the laboratory frame. In such a condition, the missing momentum had an isotropic distribution in the laboratory frame.

The missing momentum in the beam rest frame k was calculated from the initial neutron momentum in the laboratory frame p_{n1}^0 by applying the Lorentz transformation using the beam momentum vector $\tilde{p}_{\mathbf{b}}$. The p_{n1}^0 was derived by employing the Eq. (5.44).

Figure 5.16 shows angular distribution of the missing momentum. The number of events detected in the experiment without any correction is shown in the plot. The vertical axis was scaled to fit the mean values of the data and the simulation. The shape of the distribution was well reproduced by the simulation within an error of 5%. This disagreement is discussed later in Sec. 5.11.5.
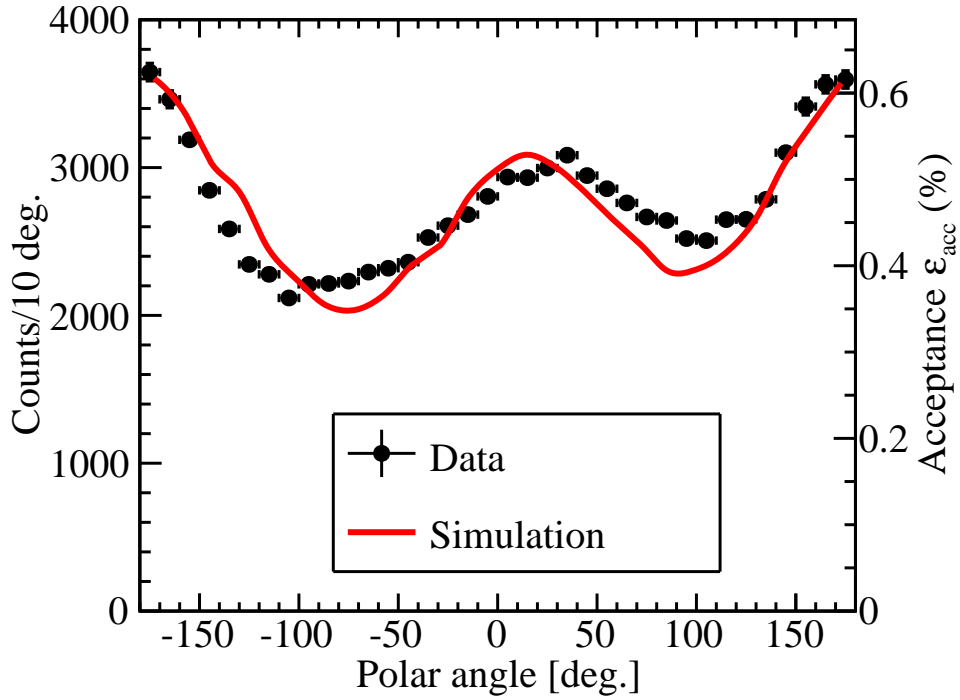
Figure 5.16: Angular distribution of the missing momentum in the polar angle. The black dots show the experimental data. The red curve represents the simulation.

5.11.3 Decay particles: SAMURAI and NEBULA

The decay particles were measured by using the so-called standard setup of the SAMURAI spectrometer. The geometrical configurations of the detectors are explained first in this subsection. Then, the uncertainty is evaluated which comes from the treatment that nuclear reactions of the decay neutron are ignored in the simulation. Finally, the qualitative explanation is given for the result of the simulation.

The heavy fragment was bent by the SAMURAI magnet and detected by the FDCs (Sec. 3.6.6) followed by the HODF and the HODP (Sec. 3.6.7). The decay neutron was detected by the NEBULA (Sec. 3.11). The realistic geometrical configurations of the SAMURAI magnet, the

FDCs, the HODF, the HODP, and the NEBULA were determined by using the photogrammetry system [98, 99] and were implemented in the simulation.

The reaction loss of the decay neutron along the flight path was evaluated by assuming the reaction point at the center of the liquid hydrogen target. Among materials along the flight path, the liquid hydrogen of 75 mm and the air of 11 m mainly contributed to the reaction, in which the total interaction cross sections of neutrons were 0.05 and 0.4 b, respectively. 3.9% of the neutrons were lost mainly by the elastic scattering. The effect of the reaction loss of the decay neutron on the following analysis was negligible, in common with that of the knocked-out neutron.

Figure 5.17 shows the acceptance of the decay particles. The acceptance gradually dropped with increasing the relative energy E_{rel}. Since the mass of the decay neutron was almost 10 times smaller than that of the heavy fragment ^{9}Li, the recoil for the decay neutron due to the relative energy was almost 10 times larger than that for the heavy fragment ^{9}Li. Thus, the acceptance of the decay particles part was limited by the geometrical acceptance of the NEBULA used for the decay neutron detection. The acceptance of the decay particles was 100% for $E_{rel} < 2$ MeV as shown in Fig. 5.17.
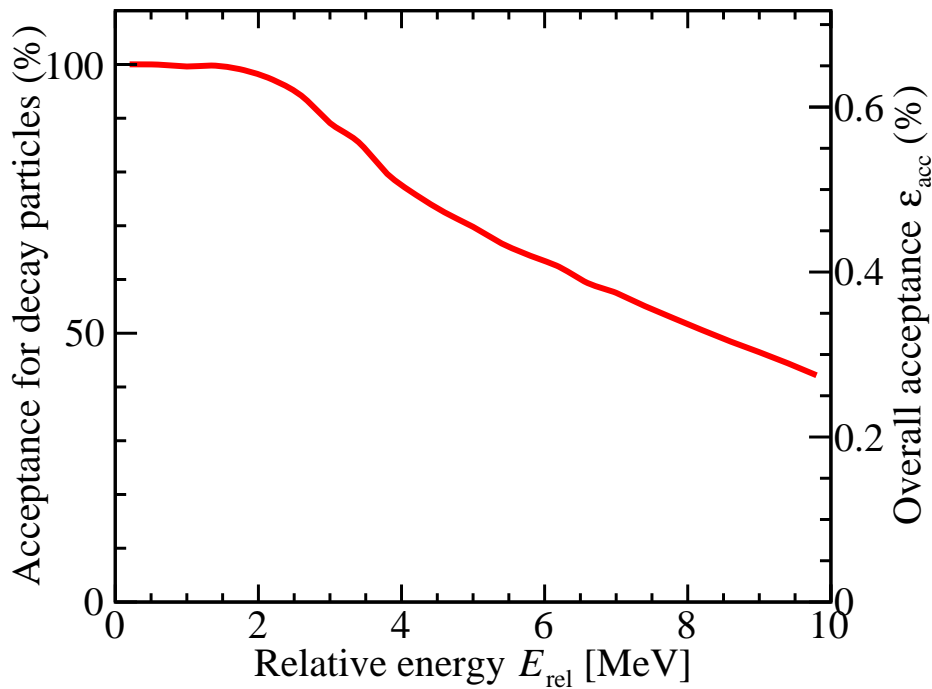

Figure 5.17: Acceptance of the decay particles as a function of the relative energy. The left and right vertical axes represent the acceptance for the decay particles and the overall acceptance including the recoil particles, respectively.

5.11.4   Acceptance dependence of correlation investigation

The acceptance factor $\varepsilon_{\mathrm{acc}}$ was defined in the three-dimensional space of $(k_Y, E_{\mathrm{rel}}, \cos\theta_Y)$. In this subsection, the behavior of the $\varepsilon_{\mathrm{acc}}$ is discussed in the (k_Y, E_{rel})- and $(\cos\theta_Y, E_{\mathrm{rel}})$-space.

Figure 5.17, the bottom panel of Fig. 5.18, and the bottom panel of Fig. 5.19 show the evaluated experimental acceptances of the present setup as a function of the relative energy E_{rel}, the internal momentum k_Y, and the opening angle $\cos\theta_Y$, respectively.

The acceptance drastically dropped with increasing the internal momentum k_Y, as shown in Fig. 5.18. It was due to the small acceptance for the recoil particles (Sec. 5.11.2). The RPD and the WINDS were placed so as to maximize the acceptance for the events with internal momentum of $k_Y = 0$, which has a same kinematics with the n-p elastic scattering. In such a condition, the scattering angles of the recoil proton and the knocked-out neutron are perfectly correlated; e.g., when the recoil proton has an azimuthal angle of ϕ_p, the knocked-out neutron has an azimuthal angle of $\phi_n = \phi_p + \pi$. Thus, most of the events with the recoil proton detection in the RPD resulted in the detection of the knocked-out neutron in the WINDS simultaneously, because the azimuthal angular coverage of the WINDS and the RPD were $|\phi_n| \lesssim \pm 20$ degrees and $|\phi_p + \pi| \lesssim \pm 20$ degrees, respectively. However, by increasing the internal momentum k_Y, in other words, by taking into account the Fermi motion of the knocked-out neutron, the scattering angle between the recoil proton and the knocked-out neutron gradually loses the correlation. In such a case, the knocked-out neutron is often out of the acceptance of the WINDS even if the recoil proton is detected in the RPD, and vice versa.

Although the internal momentum k_Y dependence of the acceptance was large, it had no singularity and the behavior was smooth as shown in Fig. 5.18. Thus, the acceptance could be compensated by dividing the obtained spectrum by the acceptance factor $\varepsilon_{\mathrm{acc}}$.

As shown in Fig. 5.19, the opening angle $\cos\theta_Y$ dependence of the acceptance was moderate as compared with the internal momentum k_Y dependence. It was because the definition of the opening angle was not fixed at the laboratory frame; The opening angle was derived from the internal momentum $\boldsymbol{k_Y}$ and the relative momentum $\boldsymbol{K_Y}$ by employing the Eq. (2.7). Although the directions of these two momentum vectors were partly limited by the geometrical acceptance, basically they could head in any direction, and therefore, the opening angle between these two momentum vectors could have any value.

The acceptance had a larger value at $\cos\theta_Y = 1$, i.e. $\theta_Y = 0$ degrees, especially with the higher relative energy E_{rel}. This enhancement came from events where the directions of the both momentum vectors $\boldsymbol{k_Y}$ and $\boldsymbol{K_Y}$ aligned to the beam direction. It could be qualitatively understood as follows. When the yz-component of the internal momentum $\boldsymbol{k_Y}$ was the zero, the probability that both the recoil proton and the knocked-out neutron were detected in the RPD and the WINDS, was maximized because the azimuthal angles of the recoil particles had the same correlation with the n-p elastic scattering as $\phi_n = \phi_p + \pi$. Thus, the acceptance is maximized when the direction of the $\boldsymbol{k_Y}$ was parallel or anti-parallel to the beam direction. By

Figure 5.18: Evaluated experimental acceptance as a function of the internal momentum k_Y. (Top) Two-dimensional plot of the relative energy E_{rel} versus the internal momentum k_Y. (Bottom) The projection onto the internal momentum k_Y distribution at every 1 MeV.
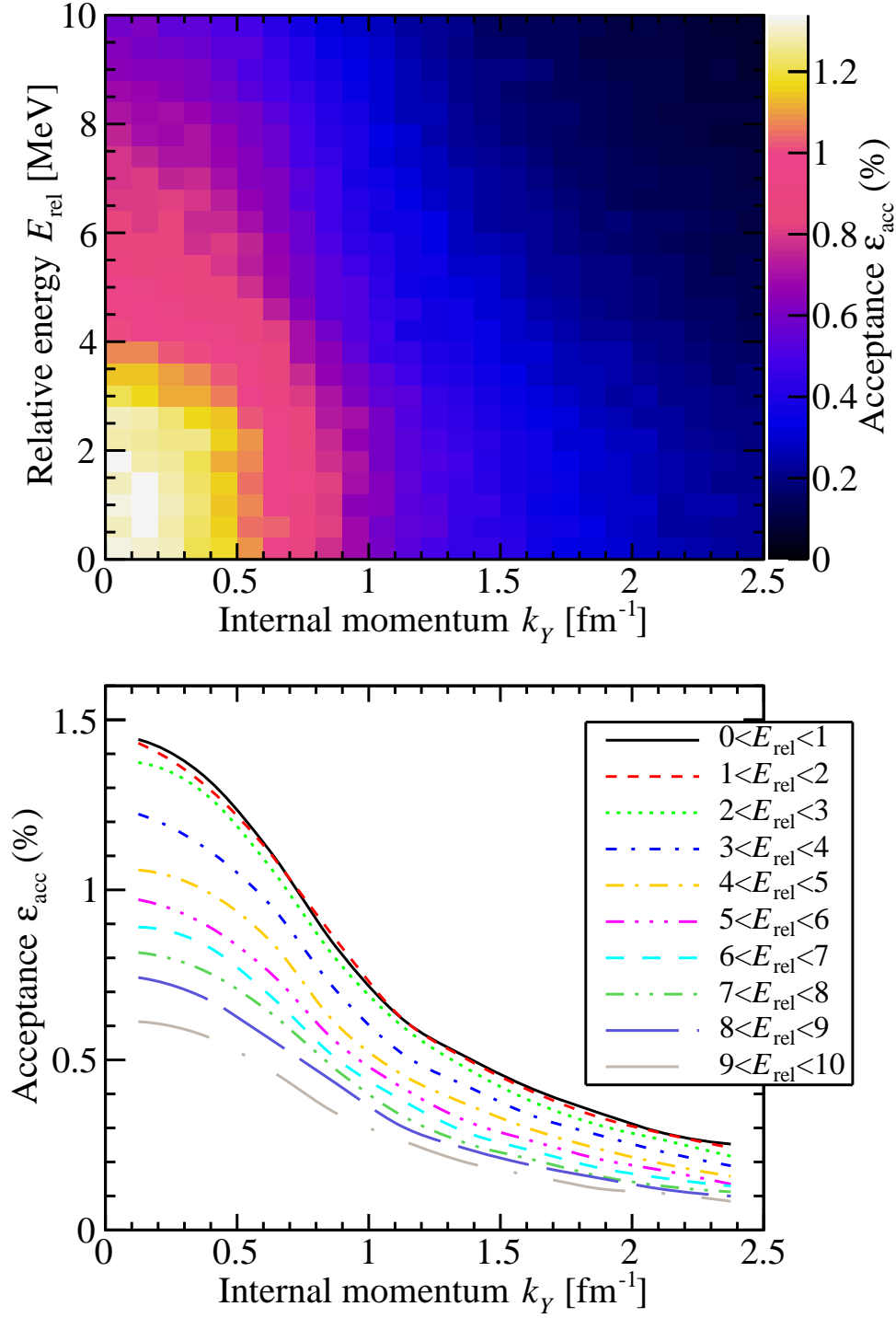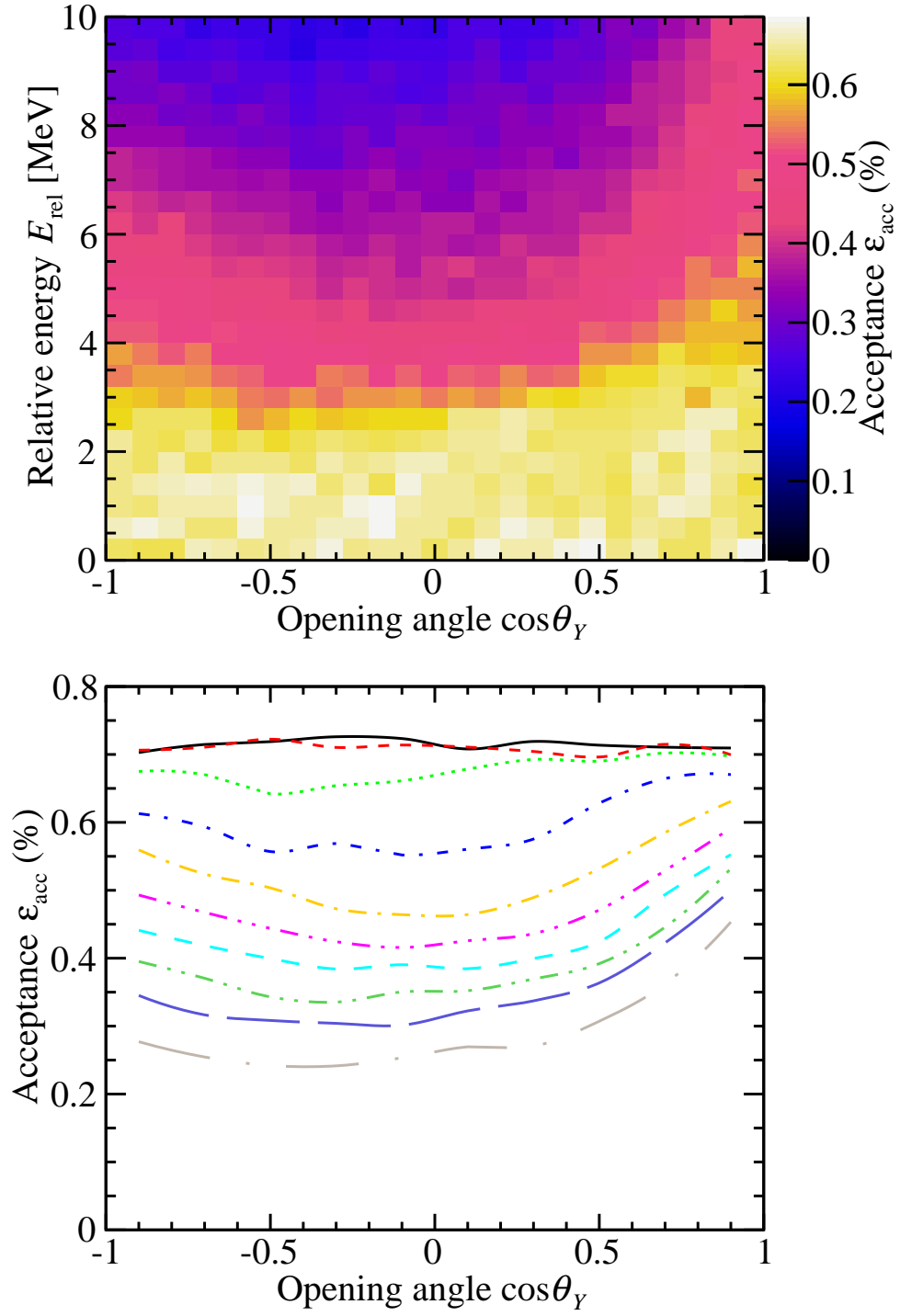
Figure 5.19: Evaluated experimental acceptance as a function of the opening angle $\cos\theta_Y$. (Top) Two-dimensional plot of the relative energy E_{rel} versus the opening angle $\cos\theta_Y$. (Bottom) The projection onto the opening angle $\cos\theta_Y$ distribution at every 1 MeV. The color scheme is same as Fig. 5.18.

comparing the parallel and the anti-parallel cases, the angular acceptance was maximized in the former case, because stronger Lorentz boost focused the trajectories of the recoil particles into the effective areas. This tendency was enhanced when the magnitude k_Y was large. In the same manner, the relative momentum $\boldsymbol{K_Y}$ tended to be parallel to the beam direction due to the forward-focused acceptance of the NEBULA used for the decay neutron detection. Therefore, the directions of the $\boldsymbol{k_Y}$ and the $\boldsymbol{K_Y}$ tended to be parallel to the beam direction, when their magnitudes were large. It should be noted that the relative energy E_{rel} was directly connected to the relative energy $\boldsymbol{K_Y}$ as $(E_{\mathrm{rel}} + M_Y)^2 = K_Y^2 + M_Y^2$, where the M_Y denotes the reduced mass of the decay neutron and the heavy fragment ^{9}Li. Thus, the directions of the $\boldsymbol{k_Y}$ and the $\boldsymbol{K_Y}$ tended to be parallel to the beam direction at higher relative energy region. This tendency disappeared at lower relative energy region, as shown in Fig. 5.19.

In common with the internal momentum k_Y, the opening angle θ_Y dependence of the acceptance was also smooth and had no singularity. Thus, the acceptance could be compensated by dividing the obtained spectrum by the acceptance factor $\varepsilon_{\mathrm{acc}}$.

In conclusion, the acceptance depended on the important observables, the internal momentum k_Y and the opening angle θ_Y, but acceptance was smooth and had no singularity. The relative energy E_{rel} dependence of the acceptance was also smooth and had no singularity (Sec. 5.11.3). Therefore it could be corrected for by employing Eq. (5.46). This correction was applied for further analysis in Chapter 6.

5.11.5 Uncertainty

The systematic uncertainty on the acceptance factor $\varepsilon_{\mathrm{acc}}$ was dominated by the geometrical acceptances and by the detection efficiencies for the particles. In addition, the multiple scattering of charged particles and nuclear reactions of neutrons contributed to modify the $\varepsilon_{\mathrm{acc}}$.

The positions of the detectors were determined within an uncertainty of 200 μm (FWHM) by using the photogrammetry system [98, 99]. These contributions were negligible because 200 μm was sufficiently smaller than the uncertainty coming from the multiple scattering; e.g. the multiple scattering of the recoil proton resulted in the smearing of several tens of mm at the RPD (Sec. 5.7.3).

The non-uniformity of the detection efficiencies of the MWDCs used for tracking charged particles was less than 1% (Sec. 4.2.5), while that of the neutron detectors was 6–7% (Sec. 4.6.1 and Sec. 4.7.1).

The uncertainty coming from the resolution and the multiple scattering were evaluated as 10% (Sec. 5.12.1). By assuming the same contributions of the resolution and of the multiple scattering, the uncertainty of the multiple scattering was evaluated as 7%. By assuming the uncertainty of the nuclear reactions of neutrons of 10%, the contributions of the knocked-out neutron and of decay neutron were 0.2% and 0.4%, respectively, which were negligible as compared with that of the multiple scattering.

In total, the acceptance factor $\varepsilon_{\mathrm{acc}}$ was modified by 19% when all the components described above constructively contributed to change the $\varepsilon_{\mathrm{acc}}$ value. We pessimistically evaluated the systematic uncertainty on the acceptance factor $\varepsilon_{\mathrm{acc}}$ as 19%. It should be noted that the disagreement between the simulation and the data for the recoil particles was determined as 5% (Sec. 5.11.2). By assuming the same disagreement for decay particles, the overall disagreement was 10%. The disagreement of 10% was smaller than the evaluated systematic uncertainty of 19% and agreed within a factor of two.

5.12 Experimental resolution

A Monte-Carlo simulation was performed so as to evaluate the resolution of the present setup. Realistic events were generated by taking into account the detector acceptance (Sec. 5.11), the measured relative energy distribution (Sec. 6.1.1), and the measured internal momentum distribution (Sec. 6.2.1). Figure 5.20 shows resolutions of the internal momentum k_Y and the opening angle θ_Y. As shown in the top panel of Fig. 5.20, the resolution of the internal momentum and of the opening angle did not strongly depend on the relative energy, because the correlations between the relative energy and these observables were very small by definition.

On the other hand, the opening angle resolution strongly depended on the internal momentum, as shown in the middle panel of Fig. 5.20. Since the opening angle was derived from the internal momentum $\boldsymbol{k_Y}$ and the relative momentum $\boldsymbol{K_Y}$ by employing the Eq. (2.7), the angular resolutions of these momentum vectors impacted on its resolution. The angular resolution of the internal momentum $\boldsymbol{k_Y}$ became poor for $k_Y \sim 0$, because a small difference of $\boldsymbol{k_Y}$ due to the resolution resulted in a large difference on the direction of $\boldsymbol{k_Y}$. Therefore, the opening angle resolution got worse for smaller internal momentum k_Y.

As shown in the bottom panel of Fig. 5.20, the opening angle resolution weakly depended on the opening angle and had a worst value at $\theta_Y \sim 90$ degrees. It was simply because the $\cos\theta_Y$ rapidly changes as a function of θ_Y at 90 degrees, and did not change at 0 and 180 degrees.

The overall resolutions of the internal momentum k_Y and the opening angle θ_Y were evaluated as 0.17 fm^{-1} (FWHM) and 30 degrees (FWHM), respectively.

5.12.1 Comparison with experimental data

It was difficult to evaluate the experimental resolutions of the internal momentum k_Y and the opening angle θ_Y directly from the experimental data. Thus, the momentum difference $\mathrm{d}\boldsymbol{p}$ defined in Eq. (5.38) obtained experimentally and that calculated by the simulation were compared so as to validate the simulation.

Figure 5.15 shows the momentum difference $\mathrm{d}\boldsymbol{p}$ projected onto the x, y, and z directions. Due to the momentum and energy conservation law, in each spectrum the peak should have been centered at zero; this was the test of the consistency of both the measurement and of the analysis
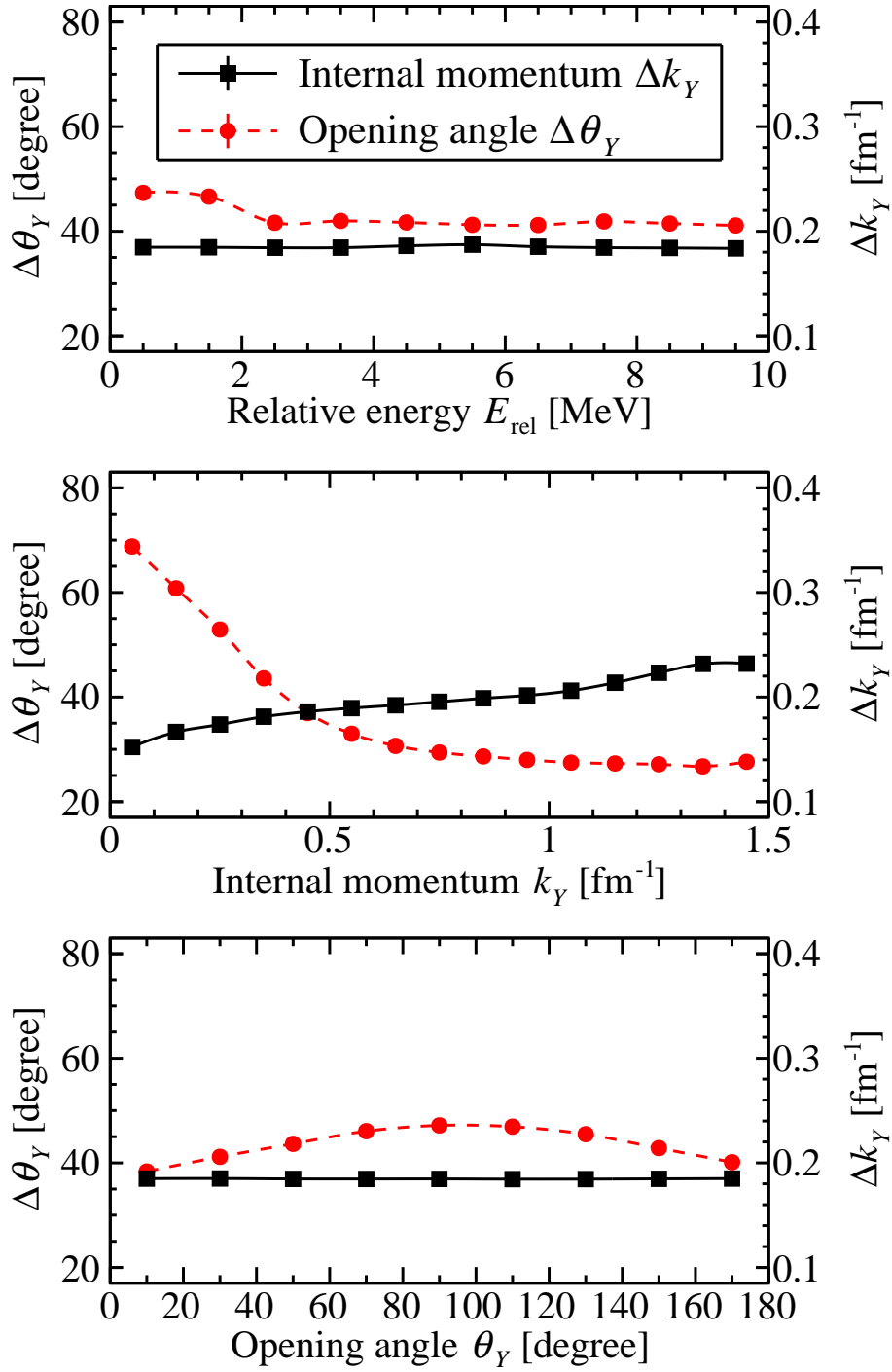
Figure 5.20: Simulated resolutions of the internal momentum k_Y and the opening angle θ_Y as a function of (top) the relative energy E_{rel}, (middle) the internal momentum k_Y, and (bottom) the opening angle θ_Y. The black solid and the red dotted lines represent the resolutions of the internal momentum and the opening angle, respectively. The resolutions are given in FWHM.

(Sec. 5.8). The experimental resolutions including the straggling were obtained from the widths of the spectra.

Table 5.1: Widths of the momentum difference dp in the x, the y, and the z directions. Experimental data and evaluated values from the simulation are listed. The contributions from the straggling and the resolution are decomposed in the case of the simulation. The unit is MeV/c. The values are written in FWHM.

Direction	Data	Straggling	Resolution
		Simulation	
x	48.9	31.0	43.7
		53.1	
y	44.4	31.5	29.0
		43.4	
z	59.4	19.9	59.0
		61.7	

The simulated resolutions were evaluated in the same manner. The widths of the momentum difference dp for x, y, and z directions obtained from the experimental data and the simulation were summarized in Table 5.1. In the case of the simulation, the contributions from the straggling and the resolution were decomposed. The width in y direction was narrower than that in x direction because of the asymmetry in the reaction point resolution (Sec. 4.4.1). The width in z direction was broadest, since most of the momentum was carried along this direction by the beam and the heavy fragment.

The simulation could reproduce the experimental resolution within an accuracy of 90%. Therefore, we concluded that the resolution and the straggling were well understood and implemented in the simulation.

5.13 Systematic uncertainties

In the present experiment, momentum vectors of all the particles involved in the reaction were measured. Systematic uncertainty for each momentum vector was already discussed (the ^{11}Li beam for Sec. 5.3.2, the heavy fragment ^{9}Li for Sec. 5.4.3, the decay neutron for Sec. 5.5, the knocked-out neutron for Sec. 5.6, and the recoil proton for Sec. 5.7.3). However, it was difficult to evaluate the overall uncertainty from these values because the acceptance of the detectors and its dependence of the systematic uncertainty were very complicated in the present experiment. Moreover, possible inconsistencies between independent calibrations could bring an unexpected uncertainty; e.g. the magnetic fields of the D5 magnet in the BigRIPS beam line and of the SAMURAI magnet were not consistent, which were used as references of the the absolute

values of the momentum of the ^{11}Li beam and the heavy fragment ^{9}Li, respectively (Sec. 5.4.3). Therefore, we evaluated the overall uncertainty by employing the different method as described below.

Since it was kinematically complete measurement, any momentum vector could be reconstructed from the other momentum vectors owing to the momentum conservation law (Eq. (5.37)). Thus, following 6 analyses with different combinations of detectors were performed for the same data sets in parallel. These analyses were expected to provide the same result, in principle.

1. All the detectors,

2. without the BigRIPS (the incident ^{11}Li beam),

3. without the RPD (the recoil proton),

4. without the WINDS (the knocked-out neutron),

5. without the NEBULA (the decay neutron).

6. without the SAMURAI (the heavy fragment ^{9}Li),

The discrepancies between the same observable derived from different analyses was regarded as the overall systematic uncertainty. By employing this method, the systematic uncertainty on the internal momentum k_Y and the opening angle θ_Y were evaluated as 0.02 fm^{-1} and 10 degrees, respectively.

5.14   Momentum transfer distribution

The QFS picture is essential in the quasi-free (p, pn) reaction (Sec. 2.2.1). The QFS condition was confirmed so as to guarantee the validity of the QFS picture in the present study.

In the quasi-free (p, pn) reaction in the inverse kinematics, the momentum transfer q is identical to the momentum of the recoil proton in the laboratory frame $\tilde{p}_p$. Figure 5.21 shows the momentum transfer and the missing momentum (Eq. (2.1)) distributions obtained in the present experiment. The momentum transfer was sufficiently larger than the missing momentum, without applying any additional conditions. It was because the geometrical configurations of the RPD and the WINDS were optimized to detect the recoil particles scattered with large momentum transfer. The QFS condition of $q > 1$ fm^{-1} (Sec. 2.2.1) was satisfied in the present experiment.
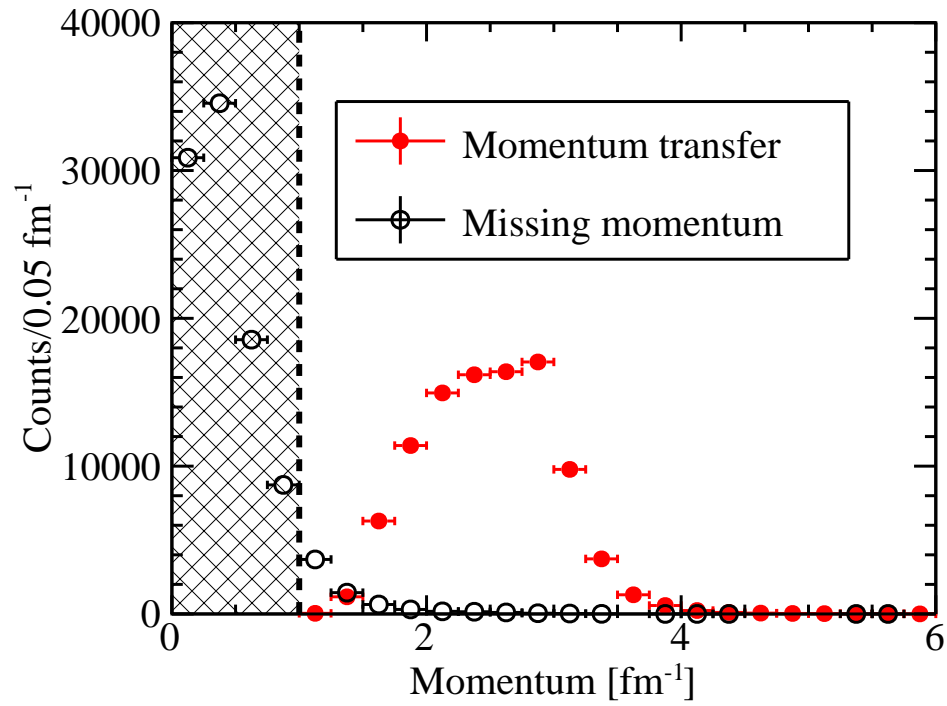
Figure 5.21: (Red closed circle) Momentum transfer and (black open circle) missing momentum distributions. The dotted line represents the lower limit of the momentum transfer satisfying the QFS condition. The events having momentum transfer in the hatched region does not satisfy the QFS condition.

Chapter 6

Results and discussion

In this chapter, the obtained distributions of the relative energy E_{rel} of ^{10}Li, the internal momentum k_Y of the knocked-out neutron, and the opening angle $\cos\theta_Y$ are presented. In Sec. 6.1, the relative energy spectrum of ^{10}Li obtained in this study is presented. In addition to the known s- and p-wave states, a possible d-wave resonance state has been newly found at 5.52 MeV. The structure of ^{10}Li is discussed according to the obtained resonance parameters. In Sec. 6.2, the k_Y distribution is shown as a function of the relative energy. For every relative energy bin, the above-mentioned s-, p-, and d-wave components can be separated from each other through the multipole decomposition analysis (MDA). The MDA results further enforces the evidence of the new d-wave state. Section 6.3 shows the $\cos\theta_Y$ distribution as a function of the relative energy. The result indicates an enhancement of dineutron component near the nuclear surface.

6.1   Spectroscopy of ^{10}Li

In this section, the structure of ^{10}Li is discussed. In Sec. 6.1.1, the relative energy spectrum of ^{10}Li is presented. The resonance parameters for observed peaks are determined by the fitting. In Sec. 6.1.2, the results for known low-lying structures are compared with the previous works. In Sec. 6.1.3, the newly-found resonance is discussed.

6.1.1   Relative energy

The relative energy spectrum of ^{10}Li is presented in this subsection. The known resonances and an unknown peak are respectively found in the lower and higher energy regions. The resonance parameters for these structures are determined by the fitting.

The top panel of Fig. 6.1 shows the relative energy spectrum for the ^{10}Li reconstructed from the heavy fragment ^{9}Li and the decay neutron (Sec. 5.9). The resolution of the relative energy was 0.3 MeV at the relative energy of 1 MeV. The spectra are given in the binning of 0.04 MeV. The experimental acceptance was corrected for (Sec. 5.11).

The bottom panel of Fig. 6.1 shows the same spectrum obtained in the previous experiment at GSI [64]. Both the resolution and the statistics are remarkably improved in this experiment.
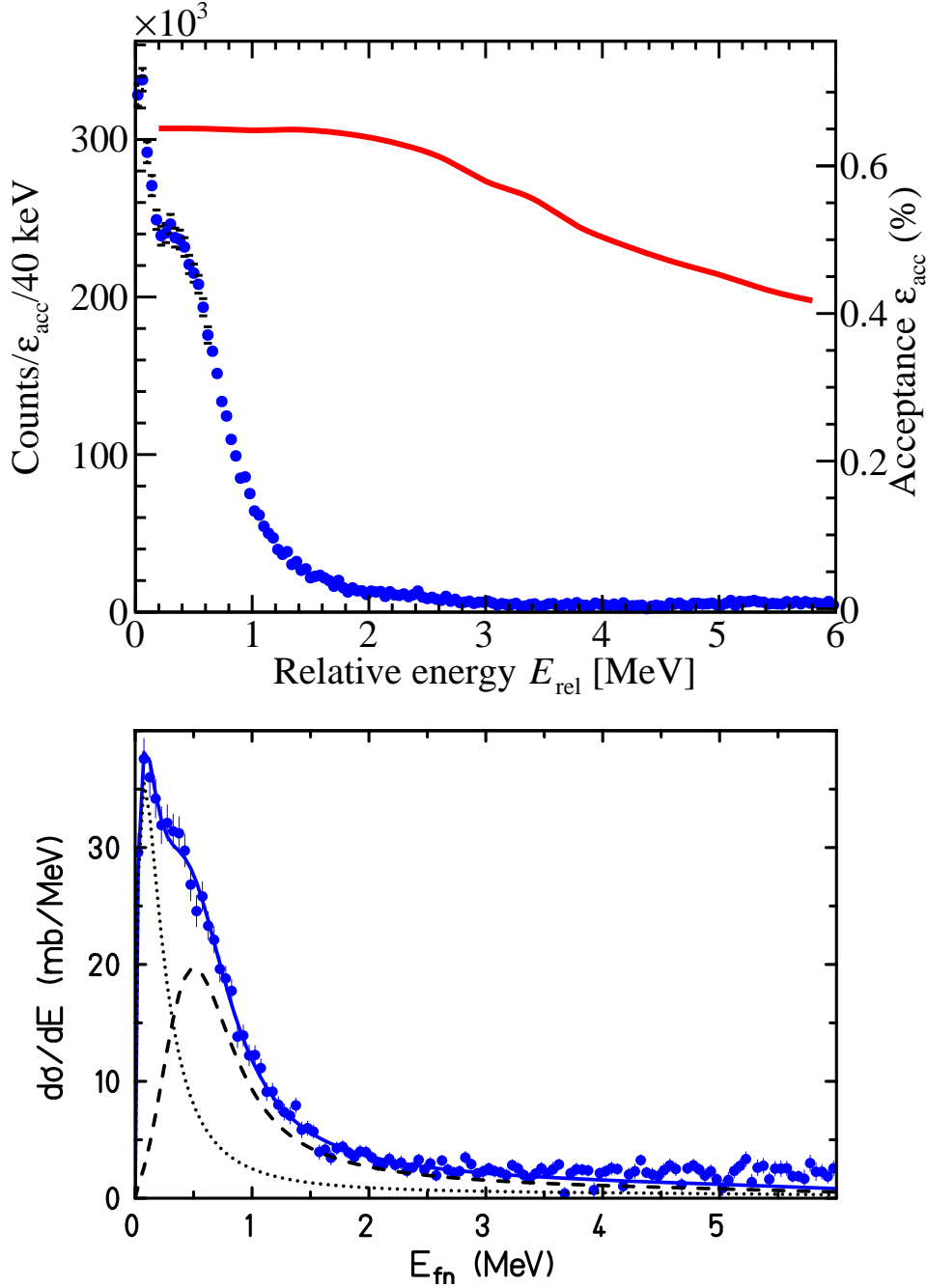

Figure 6.1: (Top) A relative energy spectrum for ^{10}Li obtained in the present study. The horizontal and the vertical axes show the relative energy and the counts divided by the acceptance factor, respectively. The red curved line represents the acceptance factor. (Bottom) Same spectrum obtained in the previous work. Taken from Ref. [64]. The horizontal and the vertical axes show the relative energy and the differential cross section, respectively.

The top panel of Fig. 6.2 shows the relative energy spectrum from 0 to 1.7 MeV. Two known

low-lying structures, *s*-wave virtual state and the *p*-wave resonance state, were observed at $E_{\text{rel}} \sim 0$ and at ~ 0.5 MeV, respectively. The bottom panel of Fig. 6.2 shows the relative energy spectrum from 3 to 7.5 MeV. The broad peak at 5.52 MeV was newly observed in the present experiment, which is assigned to the *d*-wave resonance state (Sec. 6.2.2).

The relative energy spectrum up to 1.1 MeV was fitted with a sum of contributions from the *s*-wave virtual state and the *p*-wave resonance state. The fitting function was convoluted by the response function obtained from the simulation (Sec. 5.11 and Sec. 5.12).

In the fitting, the shape of the *s*-wave virtual state was parameterized by using the expression given in Ref. [139]

$$\frac{\mathrm{d}\sigma}{\mathrm{d}E_{\text{rel}}} \propto K_Y \left[\frac{1}{\kappa^2 + K_Y^2} \right]^2 \left[\cos\delta + \frac{\kappa}{K_Y} \sin\delta \right]^2, \tag{6.1}$$

$$K_Y \cot\delta = -\frac{1}{a_s} + \frac{1}{2} r_0 K_Y^2 + O(r_0^3 K_Y^4), \tag{6.2}$$

where δ is the phase shift with the scattering length a_s and the effective range parameter r_0. The momentum parameter κ is related with the energy parameter ϵ as $\kappa = \sqrt{2\mu\epsilon}$, where μ denotes the reduced mass of ^{9}Li and neutron. These three parameters for describing the *s*-wave virtual state, a_s, r_0, and ϵ, were determined by the fitting.

The Breit-Wigner shape was employed for describing the *p*-wave resonance state as

$$\frac{\mathrm{d}\sigma}{\mathrm{d}E_{\text{rel}}} \propto \frac{\Gamma(E_{\text{rel}})}{(E_{\text{rel}} - E_r)^2 + \frac{1}{4}\Gamma(E_{\text{rel}})^2}. \tag{6.3}$$

The energy dependent decay width $\Gamma(E_{\text{rel}})$ was parameterized around the threshold energy with

$$\Gamma(E_{\text{rel}}) = \frac{g_1 \cdot E_{\text{rel}}^{3/2}}{1 + g_2 \cdot E_{\text{rel}}}, \tag{6.4}$$

where the g_1 and g_2 were the width parameters [62].

The relative energy spectrum from 3.5 to 6.5 MeV was fitted with a sum of a single resonance having a Breit-Wigner shape (Eq. (6.3)) and continuum described by a linear function. We assumed the existence of the continuum in this region because the energy is above the neutron separation energy of ^{9}Li of 4 MeV. A linear function was selected to describe the continuum because it is the simplest function to fit the distribution having no prominent structures. The fitting function was also convoluted by the response function so as to reproduce the experimental response.

The results of the fitting are shown in Fig. 6.2. The fitting function in the top panel well reproduces the experimental data. The fitting function in the bottom panel quite well reproduced the experimental data around 5 MeV. The obtained resonance parameters does not change if we slightly change the slope or the strength of the continuum, since the resonance was clearly
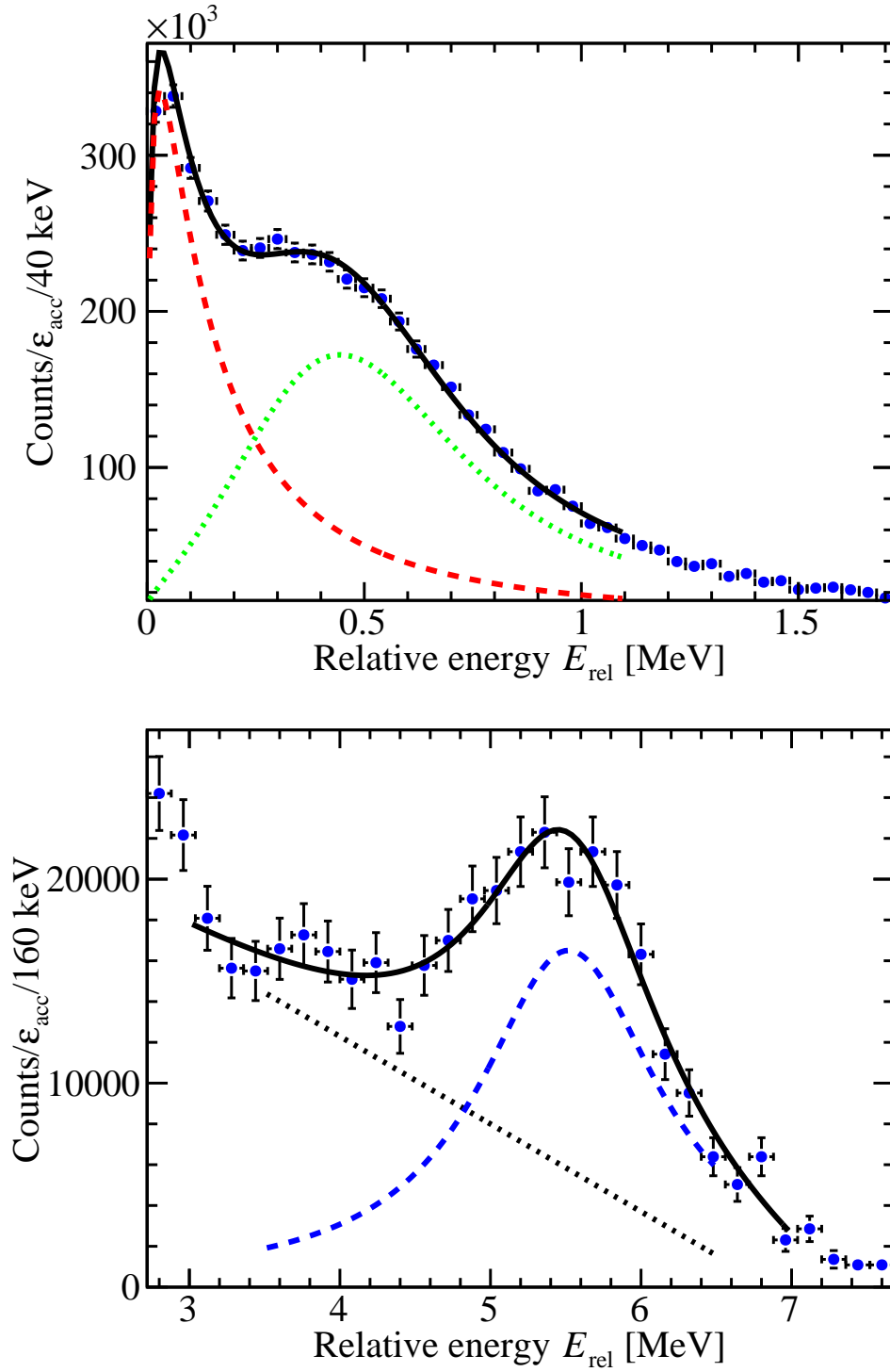
Figure 6.2: Relative energy spectra for ^{10}Li with different regions. The horizontal and the vertical axes show the relative energy and the counts divided by the acceptance factor, respectively. (Top) The red dashed, the green dotted, and the black solid lines represent *s*-wave virtual state, *p*-wave resonance state, and sum of these two components, respectively. (Bottom) The blue dashed, the black dotted, and the black solid lines represent *d*-wave resonance state, continuum state, and sum of these two components, respectively.

observed and well separated from the other structure. The obtained peak energies and widths
are summarized in Table 6.1.

Table 6.1: Obtained resonance parameters for ^{10}Li.

a_s [fm]	ϵ [MeV]	r_0 [fm]	E_r [MeV]	$\Gamma(E_r)$ [MeV]	Angular momentum
-18.8 ± 3.0	0.305 ± 0.1	2.9 ± 0.5			s-wave
			0.494 ± 0.008	0.53 ± 0.20	p-wave
			5.52 ± 0.04	0.72 ± 0.10	d-wave

6.1.2 *s*-wave virtual state and *p*-wave resonance state in ^{10}Li

In this subsection, the obtained resonance parameters for low-lying structures are compared
with those obtained in previous experiments as well as with those predicted by theoretical
calculations. The data are summarized in Table 6.2. Theoretical calculations are summarized in
Table 6.3. The resonance parameters of *p*-wave resonance are visually compared with previous
studies in Fig. 6.3.

Table 6.2: Comparison of the resonance parameters for ^{10}Li. The scattering length a_s, the
energy parameter ϵ, and the effective range r_0 for *s*-wave virtual state, and the resonance energy
E_r and the decay width Γ for *p*-wave resonance state.

Probe			*s*-wave virtual state		*p*-wave resonance state
Quasi-free (p, pn)	This work	a_s	-18.8 ± 3.0 fm	E_r	0.494 ± 0.008 MeV
		ϵ	0.305 ± 0.1 MeV	Γ	0.53 ± 0.20 MeV
		r_0	2.9 ± 0.5 fm		
Quasi-free (p, pn)	Ref. [62]	a_s	-22.4 ± 8 fm	E_r	0.566 ± 0.014 MeV
		ϵ	0.352 ± 0.022 MeV	Γ	0.548 ± 0.030 MeV
		r_0	(fixed at 3 fm)		
Neutron removal	Ref. [61]	a_s	-30^{+12}_{-31} fm	E_r	0.510 ± 0.044 MeV
		ϵ	0.3 MeV	Γ	0.54 ± 0.16 MeV
		r_0	(fixed at 3 fm)		
Neutron transfer (d, p)	Ref. [140]	a_s	-24 to -13 fm	E_r	≈ 0.38 MeV
		ϵ	(not given)	Γ	≈ 0.2 MeV
		r_0	(not given)		

This study considerably improved the reliability of the resonance parameters thanks to
the better resolution in the present study. The resolving power was important since the *s*-wave
virtual state and the *p*-wave resonance state were situated close to each other as shown in Fig. 6.1.

Previously, the spectroscopy of ^{10}Li was performed at GSI by employing the removal [61] and the knockout [62] reactions. The experimental methods used in the present study and in those studies were similar, but resolution and the statistics of the present experiment were considered to be 2–3 times better and about 100 times larger than those of the most recent work [63]. These improvements contributed to the reduction of the uncertainties in the present study. At CERN/ISOLDE, ^{10}Li was studied by employing the neutron transfer ^{9}Li(d, p) reaction at 2.36 MeV/nucleon [140]. The Coupled-channel Born approximation (CCBA) formalism was employed to fit the data without any a priori assumption about positions or shapes of the resonances. Contributions of the *s*- and the *p*-wave states were identified. However, the results had large uncertainties.
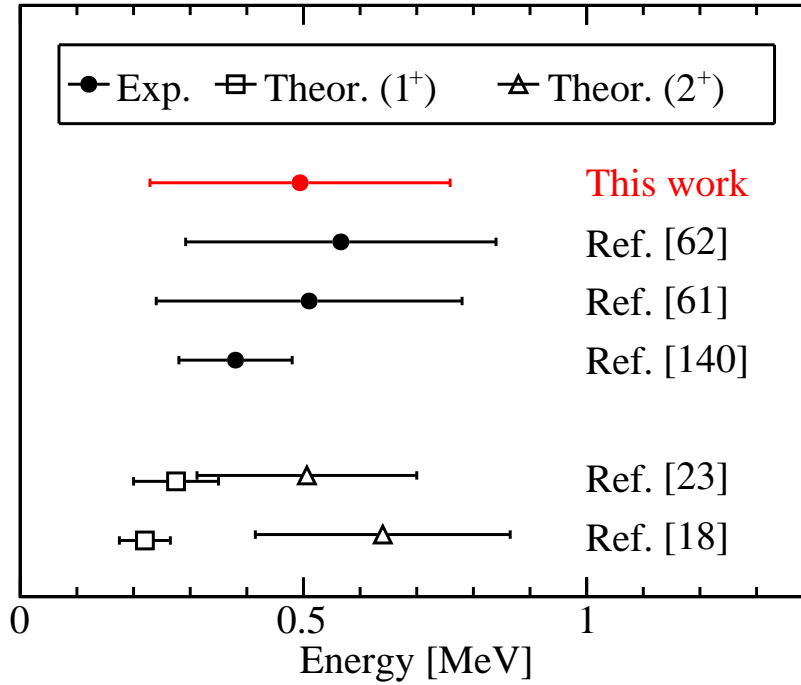

Figure 6.3: Resonance parameters of *p*-wave resonance in ^{10}Li. The resonance energy E_r and the width Γ are shown by the data points and the horizontal bars, respectively. The errors for the resonance energy in experimental data of this work and Refs. [61, 62] are smaller than the symbols, while the error was not given in Ref. [140].

The present study showed slightly larger scattering length parameter a_s for the *s*-wave virtual state, but it is consistent with previous results within the errors. The effective range parameter r_0 was determined by the fitting for the first time. The obtained value of 2.9 ± 0.5 fm is consistent with the assumption of 3 fm in the previous studies [61, 62]. The energy parameter ϵ of 0.305 ± 0.1 MeV was comparable with the S_{2n} value of ^{11}Li of 0.369 MeV, which is consistent with the previous studies [61, 62].

Regarding the resonance energy and the width of the *p*-wave resonance state, this work and Refs. [61, 62] gave similar results, while Ref. [140] gave different ones. It might be due to the different sensitivity of the probes: In the former three experimental studies, ^{10}Li was produced from ^{11}Li by using high-energetic probes. In such a case, not only the structure of ^{10}Li but also that of ^{11}Li would come into the picture. On the other hand, in the latter study, ^{10}Li was produced from ^{9}Li by using the transfer reaction at low energy. In this case, the structure of ^{9}Li as well as the reaction mechanism of the transfer reaction should be taken into consideration.

Table 6.3: Theoretical predictions of the ^{10}Li low-lying states. The resonance energies E_r and the decay widths Γ for *p*-wave resonance states and the scattering lengths a_s for *s*-wave virtual states. Taken from Refs. [18, 23].

	Coupled-channel three-body model [23]	TOSM [18]
$(E_r, \Gamma)(1^+)$ [MeV]	(0.275, 0.150)	(0.22, 0.09)
$(E_r, \Gamma)(2^+)$ [MeV]	(0.506, 0.388)	(0.64, 0.45)
$a_s(1^-)$ [fm]	-6.8	-5.6
$a_s(2^-)$ [fm]	-45.0	-17.4

Theoretically, it has been considered that there must be the other resonances in this region, even though the current experimental consensus of the resonances in this region is that there is a single *s*-wave virtual state near 0 MeV and a single *p*-wave resonance state around 0.5 MeV. The *p*-wave resonance state is expected to be doublet since the $0p_{3/2}$ proton and the $0p_{1/2}$ neutron can make 1^+ and 2^+ states. Similarly, as for the *s*-wave virtual state, the $0p_{3/2}$ proton and the $0s_{1/2}$ neutron can make 1^- and 2^- states. Some theoretical calculations based on the coupled-channel three-body model [23] and the tensor-optimized shell model (TOSM) [18] predicted the doublets for the *s*-wave virtual state and for the *p*-wave resonance state as listed in Table. 6.3. However, current experimental studies failed to separate these doublets due to a poor energy resolution. Although the energy resolution in this study was improved 2–3 times better than the previous studies, the achieved resolution of about 0.2 MeV (FWHM) around the region of interest was not sufficient to identify the predicted *p*-wave doublets.

6.1.3 *d*-wave resonance state in ^{10}Li

In this subsection, the newly-found resonance state is discussed. This new state is assigned to the *d*-wave resonance state by employing the MDA. It is described in detail in Sec. 6.2.2. First, the spectrum is compared with the previous work employing the same reaction. Next, known resonance states having similar energies observed by using different reactions are compared. Finally, the result is discussed with theoretical predictions summarized in Table 6.4.

The *d*-wave resonance state was newly found at the relative energy E_{rel} of 5.52 MeV. In the previous work at GSI [64], this state was not observed although the *s*-wave virtual state and the

p-wave resonance state were reported. In addition, the transverse-momentum profile in their data hinted at possible existence of a *d*-wave state. However, their relative energy spectrum shown in the bottom panel of Fig. 6.1 does not have any structure corresponding to this new state. We speculate it was due to the lack of both the statistics and the resolution in the previous work. The luminosity and the resolution in the previous work were 5×10^4 times smaller and 2–3 times worse than those in the present work, respectively. Although the obtained statistics in the previous work was not explicitly given [63], it could have not exceeded 1/100 of that in the present work. In such a condition, the newly found *d*-wave resonance state shown in the bottom panel of Fig. 6.1 could not be identified.

In the previous work on the missing mass spectroscopy of ^{11}Li(p, pn) reaction at RIKEN [141], the resonance state around the neutron separation energy S_n of 5.15 MeV was observed in the ^{11}Li$(p, pn)^8$Li $+ 2n$ channel, and assigned to the $p_{3/2}$ state. It is unlikely that this state at 5.15 MeV is identical with the new state at 5.52 MeV, although the resonance energies are close to each other. A $p_{3/2}$ state in ^{10}Li can exist only when having a neutron-hole $0p_{3/2}$ orbit in the ^{9}Li core, in a simple shell-model picture. Therefore, it should have structures of ^{8}Li$^* + 2n$ and decays into these components. Since the new state at 5.52 MeV is observed in the ^{9}Li emission channel, it is more likely that the structure of this state consists of the ^{9}Li core and a valence neutron in the orbit higher than the $0p_{3/2}$ single-particle level. In addition, the internal momentum distribution of the state at 5.52 MeV does not show the behavior of the $p_{3/2}$ state (Sec. 6.2.2). These two points strongly support the view that the resonance state found in the previous study [141] and that found in this study are two different states.

In the Ref. [142], the resonance state at 5.2 ± 0.2 MeV was observed through the ^{14}C(π^-, dd) reaction by employing the missing mass spectroscopy. In their study, the spin parity was not assigned. In addition, there was no information on the reaction channel since the reaction residue was not measured. Therefore, it is difficult to speculate the correspondence of their state with those reported in other works.

The resonance states around 5 MeV were studied by using the multi-nucleon transfer reactions [143, 144]. Through the ^{10}Be$(^{12}$C,^{12}N$)^{10}$Li measurement, the resonance states at 4.19 and 4.64 MeV with decay widths of 0.12 and 0.2 MeV were observed [144]. From the ^{9}Be$(^{13}$C,^{12}N$)^{10}$Li measurement, the resonance states at 4.64 and 5.7 MeV with decay widths of 0.2 MeV were observed [144]. Because the signal-to-noise (S/N) ratio was poor in both cases, the possible small structure at around 5.52 MeV is hardly to be discussed.

We can claim this is the newly discovered *d*-wave resonance state in ^{10}Li. The existence of the *d*-wave resonance state was theoretically predicted [145, 146]. Resonance parameters of predicted *d*-wave resonance states by employing the tensor-optimized shell model (TOSM) calculation [147, 148] and the microscopic coupled-channel model [146] are summarized in Table 6.4. The resonance energy E_r fairly agrees with the present result. However, the calculated decay width is larger than 3 MeV and does not agree with one obtained in the present study of 0.72 ± 0.10 MeV. No theoretical model could reproduce the energy and the width of the *d*-wave

resonance state in ^{10}Li.

Table 6.4: Resonance parameters of predicted *d*-wave resonance states in ^{10}Li. Taken from Refs. [145, 146].

	TOSM [145]		Microscopic coupled channel [146]	
J^π	E_r [MeV]	Γ [MeV]	E_r [MeV]	Γ [MeV]
1^-	5.84	5.16	4.73	3.27
2^-	5.81	5.20	5.27	4.37
3^-	6.57	6.31	6.05	5.63
4^-	5.30	3.84	4.70	3.17

In ^{11}Li, the ^{9}Li + n + n system, two kinds of interactions take place: the $n + n$ and the ^{9}Li + n interactions. Although the neutron-neutron interaction in vacuum has long been studied, little is known about the structure of the ^{9}Li + n system. As we discussed in Sec. 6.1.2, even the low-lying resonances are still in discussion. It is important to understand the ^{9}Li + n interaction so as to understand the neutron-neutron correlation in ^{11}Li, the ^{9}Li + n + n system. The newly found d-wave resonance state must reflect the nature of the ^{9}Li + n interaction, and must be a benchmarking case for validating theoretical models.

It should be noted that the disagreement between the obtained result and the theoretical calculations mentioned above does not directly indicate the incompletion of the theoretical models. Those models describe the structure of pure ^{10}Li. On the other hand, the final state of ^{10}Li in this study was produced from ^{11}Li via the quasi-free (p, pn) reaction. Thus, the final spectrum reflects not only the structure of ^{10}Li but also that of ^{11}Li as well as the effect of the reaction mechanism of the quasi-free (p, pn) reaction: A part of the wave function of ^{10}Li can be hindered in the final spectrum. Recently a theoretical model which can treat both the structure information as well as the reaction mechanism has been developed and first applied to the calculation of ^{6}He [73]. Such an approach is required to check the consistency between the experimental data and theoretical calculations.

6.2 One-neutron ground-state momentum of ^{11}Li

In this section, the one-neutron ground-state momentum of ^{11}Li is discussed. In Sec. 6.2.1, the internal momentum k_Y distribution is presented with the relative energy E_{rel} of ^{10}Li. In Sec. 6.2.2, the multipole decomposition analysis (MDA) for the determination of relative fractions of each multipole components $S_{\ell j}$ is explained. In Sec. 6.2.3, the obtained $S_{\ell j}$ values are compared with the previous works.

6.2.1 Internal momentum k_Y

A two-dimensional plot of the yield of the $^{11}\text{Li}(p, pn)^9\text{Li} + n$ reaction is shown in Fig. 6.4. The vertical and horizontal axes represent the relative energy E_rel and the internal momentum k_Y, respectively. The spectra are given in the binning of 0.2 MeV and 0.1 fm^{-1}. The resolutions of the internal momentum and the relative energy were 0.17 fm^{-1} (Sec. 5.12) and 0.3 MeV at the relative energy of 1 MeV (Sec. 5.9), respectively. The experimental acceptance was corrected for (Sec. 5.11).

Figure 6.5 shows internal momentum distributions having different relative energies. The spectra were fitted with the DWIA calculation for the multipole decomposition analysis (Sec. 6.2.2).

6.2.2 Multipole decomposition analysis

In this subsection, the fraction of each single-particle wave function $S_{\ell j}$ is determined by employing the multipole decomposition analysis (MDA). The MDA is first introduced. The distortion effect coming from the reaction mechanism is evaluated. The restrictions for the fitting are explained. Finally, the obtained $S_{\ell j}$ values are presented.

The MDA enables us to extract the $S_{\ell j}$ values from the momentum distribution of knocked-out neutron [149]. The k_Y distribution is a good signature of orbital angular momentum of the knocked-out neutron in ^{11}Li. It is quite characteristic depending on the multipolarity of the orbit. This can be used to reliably decompose the experimentally-obtained momentum distribution into different multipole components. It is noteworthy that even the spin-parity can be determined from the momentum dependence of the analyzing power. In the present study, however, only the momentum distribution is discussed because the target was not spin-polarized.

The one-neutron wave function of the knocked-out neutron $|\Phi(n)\rangle$ is written as a sum of the single-particle wave functions $|\ell j\rangle$ as

$$|\Phi(n)\rangle = c_{s_{1/2}} |s_{1/2}\rangle + c_{p_{3/2}} |p_{3/2}\rangle + c_{p_{1/2}} |p_{1/2}\rangle + c_{d_{5/2}} |d_{5/2}\rangle + \cdots, \tag{6.5}$$

$$c_{\ell j} = \sqrt{S_{\ell j}}\, e^{i\phi_{\ell j}}, \tag{6.6}$$

where $S_{\ell j}$ and $\phi_{\ell j}$ denotes the fraction and the relative phase of each single-particle wave function. The $S_{\ell j}$ values are determined by fitting the experimental data with the calculated momentum distribution. Figure 6.6 shows the calculated k_Y distribution of ^{11}Li by employing the DWIA [73, 138].

The effect of the distortion was taken into account by multiplying the calculated cross section by the damping factor $D(k_Y)$. The damping factor represented the absorption of the knocked-out neutron by the reaction residue ^{10}Li. It was calculated with the eikonal approximation [73] and,
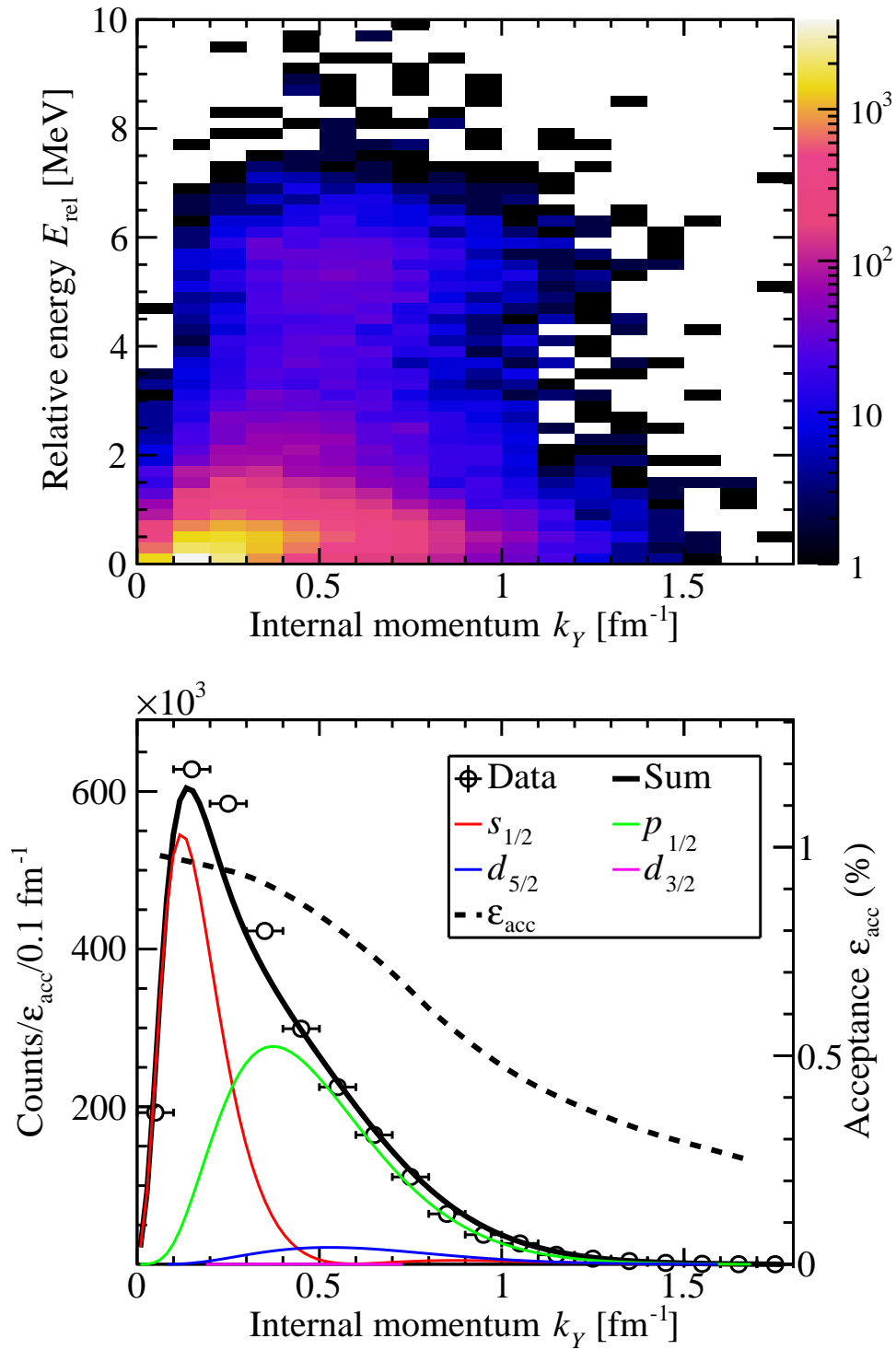
Figure 6.4: (Top) Two-dimensional plot of the yield of the ^{11}Li$(p, pn)^9$Li $+ n$ reaction. The horizontal and the vertical axes represent the relative energy E_{rel} and the internal momentum k_Y, respectively. (Bottom) The projection of top panel onto the x axis. The horizontal and the vertical axes show the internal momentum and the counts divided by the acceptance factor, respectively. The black dotted curved line represents the acceptance factor. The functions showing the result of the MDA are explained in Sec. 6.2.2.
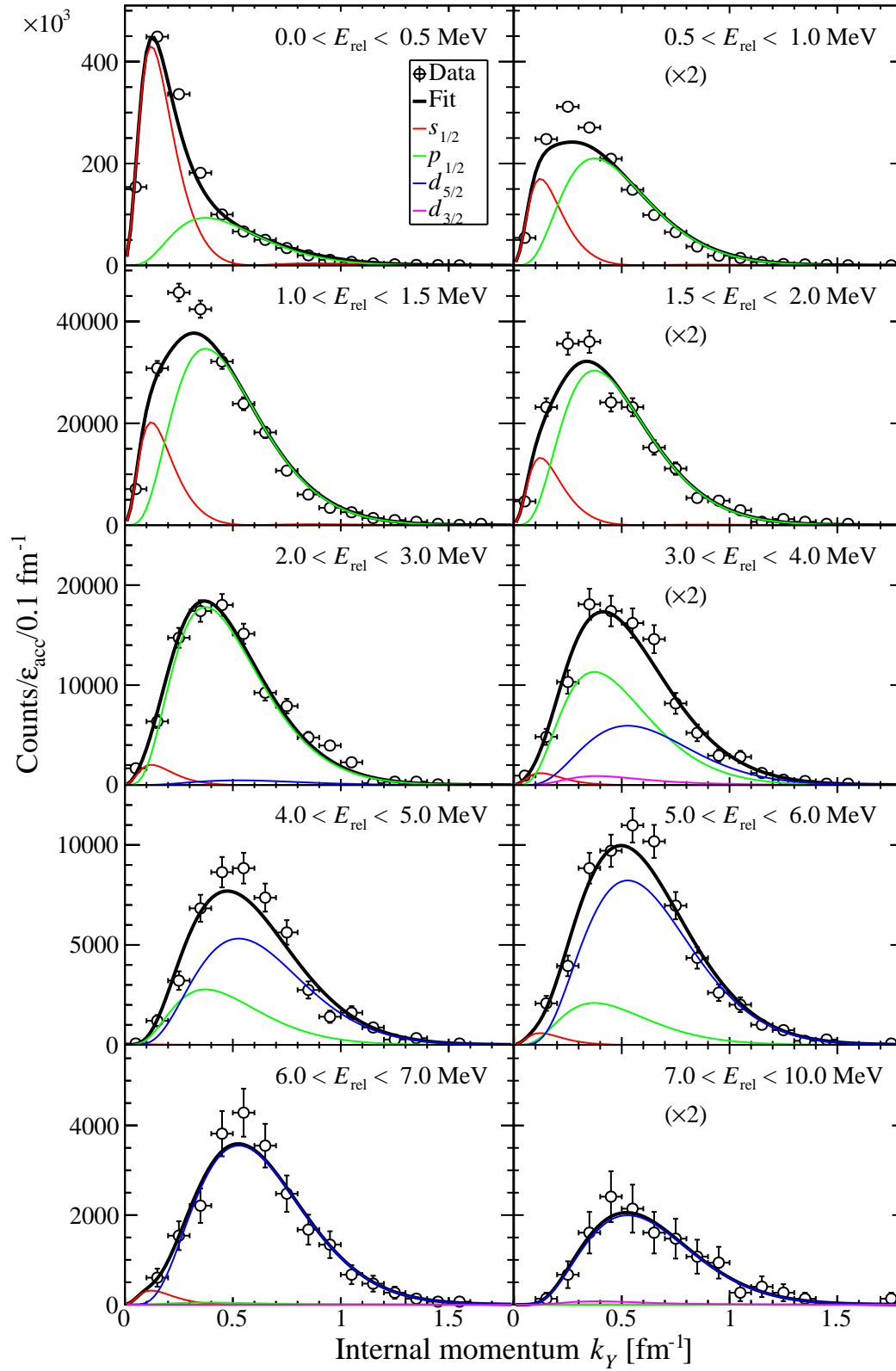
Figure 6.5: Internal momentum k_Y distribution for each relative energy $E_{\rm rel}$. The horizontal and the vertical axes show the internal momentum and the counts divided by the acceptance factor, respectively. The fitting functions are explained in Sec. 6.2.2.
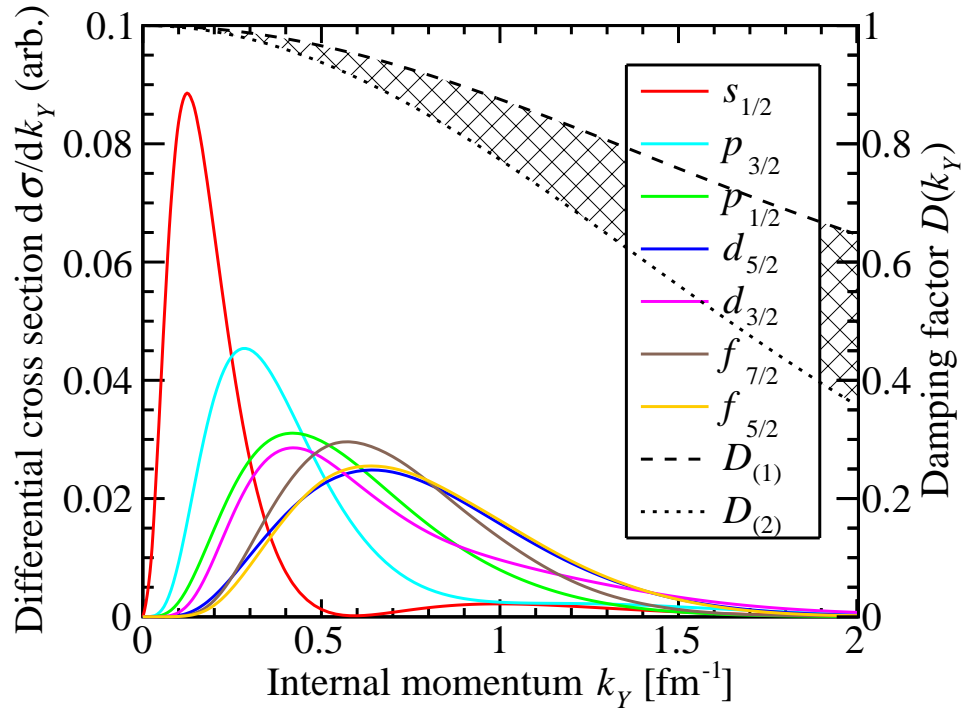
Figure 6.6: Internal momentum k_Y distributions calculated by employing the DWIA. The parameter set (1) is employed for the calculation of the damping factor $D(k_Y)$. The integration of each DWIA calculation is normalized to 1. The damping factors with two different sets of parameters are also shown by the black dashed and dotted lines. By courtesy of Y. Kikuchi [138].

for the convenience, parameterized by fitting it with the Gaussian-type function defined as

$$D(k_Y) = 1 - b \left[1 - \exp\left(-\frac{k_Y^2}{4a} \right) \right],$$ (6.7)

where the parameters a and b denotes the size of the heavy fragment ^{9}Li and the strength of the absorption from the ^{9}Li core, respectively. Two sets of parameters were prepared as summarized in Table 6.5. The damping factors calculated with these two parameter sets are shown as dashed and dotted curves in Fig. 6.6. The parameter set (1) was determined by scaling those optimized for describing the ^{4}He + $2n$ system. In the parameter set (2), the strength of the absorption was assumed to be 100% at the limit of large k_Y. The realistic parameter b is expected to lie between these two parameters, because the absorption of the heavy fragment ^{9}Li is considered to be stronger than that of the ^{4}He particle. Thus, the realistic damping factor is expected to be found inside the hatched area in Fig. 6.6. The difference of the results with these two parameters was considered as a systematic uncertainty.

Table 6.5: Parameters sets for calculating the distortion effect. See the text for details.

Set	a	b
(1)	$0.228 \times (9/4)^{2/3}$	0.55
(2)	$0.228 \times (9/4)^{2/3}$	1.00

In the present study, the four orbits, $1s_{1/2}$, $0p_{1/2}$, $0d_{5/2}$, and $0d_{3/2}$ were included for the fitting. The contributions of the $0s_{1/2}$ and $0p_{3/2}$ components were assumed to be 0% because such components were out of the scope of the present analysis. When the 0^+-neutron pair in the $0s_{1/2}$ or the $0p_{3/2}$ orbit was removed by the knockout and the simultaneous neutron emission, the final state of the heavy fragment ^{9}Li could not be bound and decayed by neutron emission. The contributions from f- and more higher orbits were assumed to be negligible.

The MDA was independently performed for each relative energy bin. The fitting result is shown in the Fig. 6.5. The integrated fractions were summarized in Table 6.6. Figure 6.7 shows the fraction of each multipole component as a function of relative energy. The $1s_{1/2}$ and the $0p_{1/2}$ component are found at the relative energy $E_{\rm rel} \sim 0$ MeV and $0 < E_{\rm rel} < 1$ MeV, respectively. It agrees with the existence of the s-wave virtual state and the p-wave resonance state at $E_{\rm rel} \sim 0$ and ~ 0.5 MeV, respectively (Sec. 6.1.2). The $0d_{5/2}$ component is found at the relative energy $E_{\rm rel}$ of larger than 2 MeV, and forms a peak around 5 MeV. This result suggests the peak found in the relative energy spectrum at 5.52 MeV is the d-wave resonance state (Sec. 6.1.3).

6.2.3 Comparison with other methods to deduce $S_{\ell j}$

In this subsection, the obtained $S_{\ell j}$ values are compared with those obtained in the previous works using different reactions. The data are summarized in Table 6.6. Then, the advantage
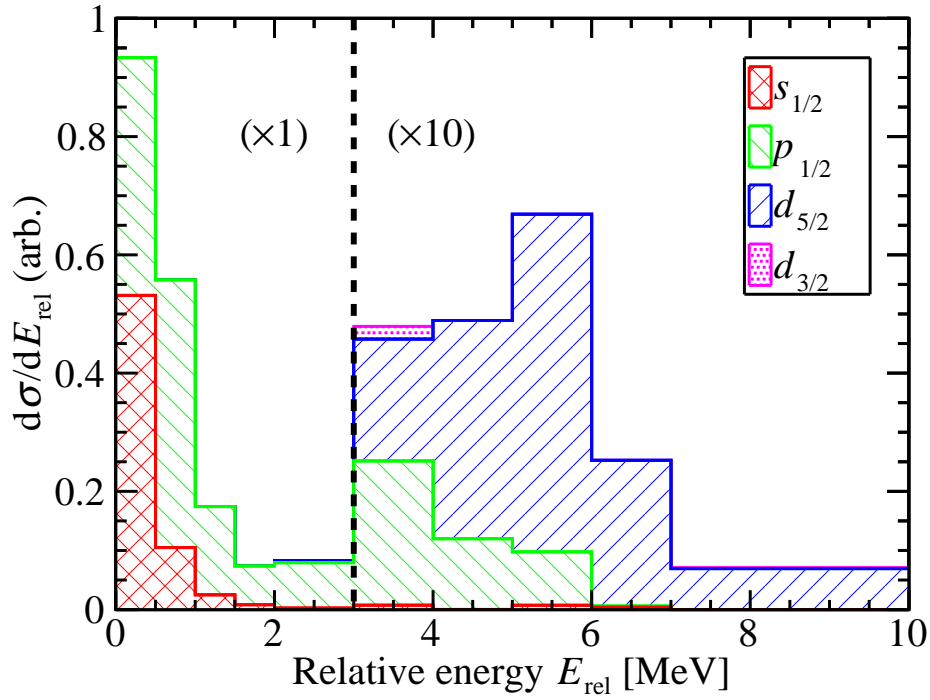
Figure 6.7: Fraction of each multipole of knocked-out neutron as a function of the relative energy of ^{10}Li, obtained through the multipole decomposition analysis.

of the MDA we employed in this study is explained. Finally, an indication of the dineutron correlation in ^{11}Li is discussed.

As we discussed in Sec. 6.1.2, the *s*- and *p*-wave states are considered to be doublets. However, these doublet states have not yet been discriminated experimentally. Thus, each $S_{\ell j}$ value in Table 6.6 represents the sum of the relative fractions of the doublet.

From an experimental point of view, the s/p ratio was shown for the first time in the study based on the carbon-induced neutron removal reaction [60]. Contributions of $(1s_{1/2})^2$ and $(0p_{1/2})^2$ were determined as $45 \pm 10\%$ and $55 \pm 10\%$, respectively, by fitting the parallel momentum distribution (PMD) of ^{10}Li. In this fitting, only up to the *p*-wave contributions were taken into consideration. The fraction of the $(p_{3/2})^2$ component was also evaluated as 3–5% at a maximum from the fitting of the opening angle distribution.

In the Ref. [61], another interpretation was provided for the same data set. Since the interference term $p_{1/2} \otimes p_{3/2}$ gives nearly the same opening angle distribution as the $s_{1/2} \otimes d_{5/2}$, a part of the $p_{1/2}$ component can be reinterpreted as the $d_{5/2}$ component. The $10 \pm 8\%$ admixture of the $d_{5/2}$ state was determined by assuming the same contribution of the the $s_{1/2}$ and the $p_{1/2}$ components.

The contribution of the $d_{5/2}$ components was also evaluated in a different method by using the proton-induced knockout reaction [64]. The fraction of the $d_{5/2}$ component was determined as $11 \pm 2\%$ from the excess of the momentum profile compared with the calculation including

only the *s* and the *p* components. Contributions from the others were not shown.

In the previous studies mentioned above, the parallel momentum distribution (PMD) was compared with the calculation so as to determine the contributions of multipoles. However, it turned out recently that the PMD can be distorted by some experimental conditions [84]. Because the behavior of the tail of the parallel momentum distribution strongly affects the angular momentum assignment, it should be carefully considered. In contrast, the reliability of the MDA for the internal momentum based on the DWIA framework is confirmed (Sec. 2.2.1).

Table 6.6: The fraction $S_{\ell j}$ of each multipole. The unit is percent (%).

		$(1s_{1/2})^2$	$(0p_{3/2})^2$	$(0p_{1/2})^2$	$(0d_{5/2})^2$	$(0d_{3/2})^2$
Exp.	This work	35 ± 4	0^a	59 ± 1	6 ± 4	
	Ref. [60]	45 ± 10	3–5	55 ± 10		
	Ref. [61]	45 ± 10	3–5	45 ± 10	10 ± 8	
	Ref. [64]				11 ± 2	
Theor.	Ref. [23]	44.0	2.5	46.9	3.1	1.7
	Ref. [150]	33^{+3}_{-5}				
	Ref. [145]^b	46.9	2.5	42.7	4.1	1.9

^{a} Fixed.
^{b} 0.6% and 0.5% contributions for $(f_{7/2})^2$ and $(f_{5/2})^2$ in Ref. [145].

The multipole fractions $S_{\ell j}$ determined in this study were consistent with those obtained in the previous experimental studies within the uncertainty as shown in Table 6.6. The uncertainties were dramatically reduced in this study. This is owing to the simple reaction mechanism of the quasi-free (p, pn) reaction and the higher reliability of the present MDA (Sec. 2.2.1). In addition, the present analysis was done for each relative energy bin. This enhanced the sensitivity to the small *d*-wave component lying in the high relative energy region.

The central value of the s/p ratio was determined as 0.6 in the present study. It was slightly smaller than the previous values of 0.8–1.0, even though the previous results had large uncertainties. It might be due to the difference of the probe: The probe used in the previous studies [60, 61] was peripheral so that the contribution of the *s*-wave might be overestimated. The smaller s/p ratio obtained in this study implies the weaker dineutron correlation because the admixture of the different parity states is necessary to make a spatial localization of two neutrons. This result supports the weaker dineutron correlation than in the previous works, as also shown in a different manner in Sec. 6.3.2.

The magnitude of $s_{1/2}$ and $p_{1/2}$ components is still an open question. Theoretically, the comparable contributions of these components, i.e. the s/p ratio of about 1.0, were predicted by the coupled-channel three-body model [23] as well as by the TOSM [145]. The present results of s/p ratio of about 0.6 did not agree with these calculations. Fortune [150] evaluated the $s_{1/2}$ contribution of 33^{+3}_{-5}% by calculating the cross section of two-neutron transfer (t, p) reaction.

The calculation agreed with the present result of 35 ± 4%, however, contributions of the other components were not given.

6.3 Neutron-neutron correlation in ^{11}Li

The spatial configuration of two valence neutrons in ^{11}Li is discussed in this section. In Sec. 6.3.1, the opening angle θ_Y distribution is presented. The relative energy dependence of the opening angle is shown for the first time. In Sec. 6.3.2, the dineutron correlation in ^{11}Li is discussed by comparing the result with previous works.

6.3.1 Opening angle θ_Y

In this subsection, the opening angle θ_Y distribution in momentum space and its expectation value $\langle\theta_Y\rangle$ is presented as a function of the relative energy E_{rel} of ^{10}Li. The expectation values of the opening angle in position space $\langle\theta_Y^x\rangle$ and $\langle\theta_V^x\rangle$ are obtained.

The opening angle in momentum space θ_Y was derived from the internal momentum vectors as described in Sec. 5.10. In order to remove the phase space factor, the $\cos\theta_Y$ distribution instead of the θ_Y distribution is shown and discussed. A two-dimensional plot of the yield of the ^{11}Li$(p, pn)^9$Li $+ n$ reaction is shown in the top panel of Fig. 6.8. The vertical and horizontal axes represent the relative energy E_{rel} and the opening angle $\cos\theta_Y$, respectively. The spectra are given in the binning of 0.2 MeV and 0.1. The relative energy was reconstructed from the momentum vectors of ^{9}Li heavy fragment and the decay neutron as described in Sec. 5.9. The resolution of the relative energy was 0.3 MeV at the relative energy of 1 MeV (Sec. 5.9). The resolution of the cosine of the opening angle was 0.3 (FWHM) at the relative energy of 1 MeV (Sec. 5.12). The experimental acceptance was corrected for (Sec. 5.11). The spectra were fitted by the Legendre functions. The derivation of the fitting function is given in Appendix A.

A slight enhancement of the yield is seen at $E_{\text{rel}} \sim 5.5$ MeV in Fig. 6.8. This locus corresponds to the d-wave resonance reported in Sec. 6.1.3.

The averaged opening angle distribution is shown in the bottom panel of Fig. 6.8. The averaged expectation value of the opening angle in momentum space was obtained as $\langle\theta_Y\rangle = 95 \pm 10$ degrees, by integrating the opening angle θ_Y with respect to the relative energy. The averaged expectation value of the opening angle in position space was calculated as $\langle\theta_Y^x\rangle = 85 \pm 10$ degrees, by using the relation of

$$\langle\theta_Y^x\rangle = 180° - \langle\theta_Y\rangle. \tag{6.8}$$

The definition of the opening angles is given in Sec. 1.2.1 and in Sec. 2.3. A theoretical framework is needed to derive the relation between the opening angles defined in different two coordinates, Y- and V-coordinates. Herein, we derive the relation by employing the very
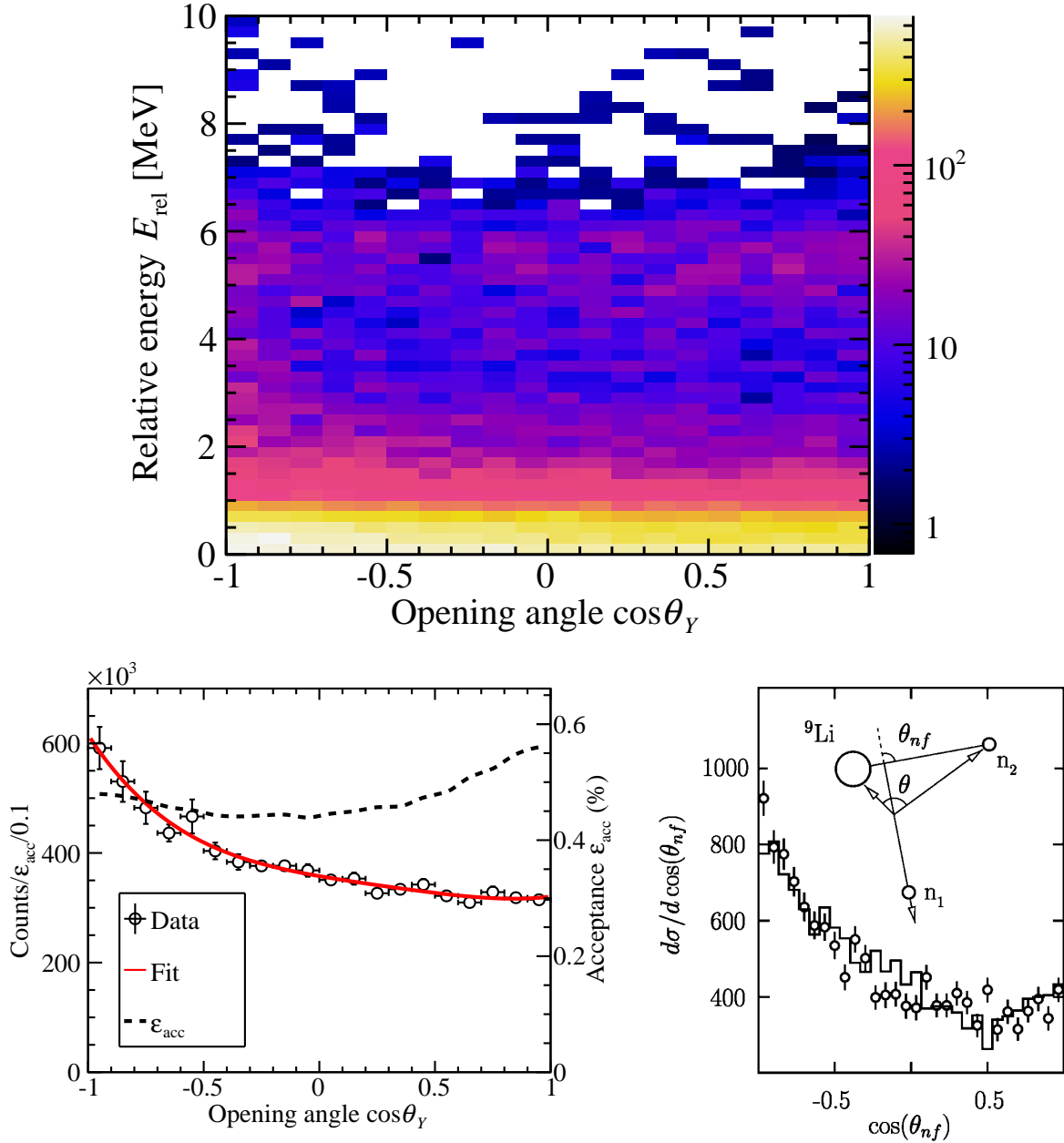
Figure 6.8: (Top) Two-dimensional plot of the yield of the ^{11}Li$(p, pn)^9$Li $+ n$ reaction. The horizontal and the vertical axes represent the opening angle $\cos\theta_Y$ and the relative energy E_{rel}, respectively. (Bottom left) The projection of top panel onto the x axis. The horizontal and the vertical axes show the opening angle and the counts divided by the acceptance factor, respectively. The red solid and black dotted curved lines represent the fitting function and the acceptance factor, respectively. (Bottom right) Integrated opening angle distribution obtained in the previous study. Taken from Ref. [60].

simplified classical picture that the ^{11}Li is composed of three point-like particles: the ^{9}Li core and two neutrons. Then, the relation between two opening angles can be written as

$$\theta_V^x = \tan^{-1}\left(\frac{m_{^9\text{Li}}\sin\theta_Y^x}{m_n + m_{^9\text{Li}}\cos\theta_Y^x}\right), \tag{6.9}$$

where m_n and $m_{^9\text{Li}}$ denote masses of a neutron and a ^{9}Li particle. Owing to this relation, the expectation value of the opening angle in V-coordinates $\langle\theta_V^x\rangle$ can be calculated as $\langle\theta_V^x\rangle = 77$ degrees.

Figure 6.9 shows opening angle distributions for different relative energies. One could clearly see that the opening angle distribution depended on the relative energy. The spectra were fitted with the Legendre functions.

Figure 6.10 shows expectation values of the opening angle in momentum space $\langle\theta_Y(E_{\text{rel}})\rangle$ as a function of the relative energy. Each data point was calculated from the opening angle distribution for the different relative energy (Fig. 6.9). The $\langle\theta_Y\rangle$ value obtained in the previous work [60] was shown as the blue hatched area in Fig. 6.10.

6.3.2 Dineutron correlation in ^{11}Li

In this subsection, the relative energy dependence of the opening angle is discussed for the first time, as an indication of the radial position dependence of the opening angle. Then, the expectation value of the opening angle is compared with those obtained in previous works. The data are summarized in Table 6.7. Finally, the differences of the probes and their possible effect on the result are discussed.

It became apparent that the opening angle of two neutrons depends on the relative energy, as seen in Figs. 6.9 and 6.10. The opening angle in the momentum space $\langle\theta_Y(E_{\text{rel}})\rangle$ was clearly larger than 90 degrees at a small relative energy region ($E_{\text{rel}} < 4$ MeV), indicating the development of the dineutron correlation, while it was almost consistent with 90 degrees at a large relative energy region ($4 < E_{\text{rel}} < 7$ MeV). The relative energy E_{rel} and the relative momentum vector $\boldsymbol{K_Y}$ defined in Eq. (2.5) follow the relation

$$m_{\text{inv}}^2 = (E_{\text{rel}} + m_Y)^2 = |\boldsymbol{K_Y}|^2 - m_Y^2, \tag{6.10}$$

where m_Y represents a reduced mass of ^{9}Li + n system. The small and the large relative momentum K_Y correspond to the surface and the inner part of the nucleus [73], respectively. The E_{rel} value also gives same information on the radial position as the K_Y value. Therefore, this result suggested that the dineutron correlation is much more developed in the surface region. It is qualitatively consistent with the theoretical prediction that the dineutron correlation appears at the surface [5].

In Fig. 6.10, the opening angle in momentum space $\langle\theta_Y(E_{\text{rel}})\rangle$ had the maximal value around
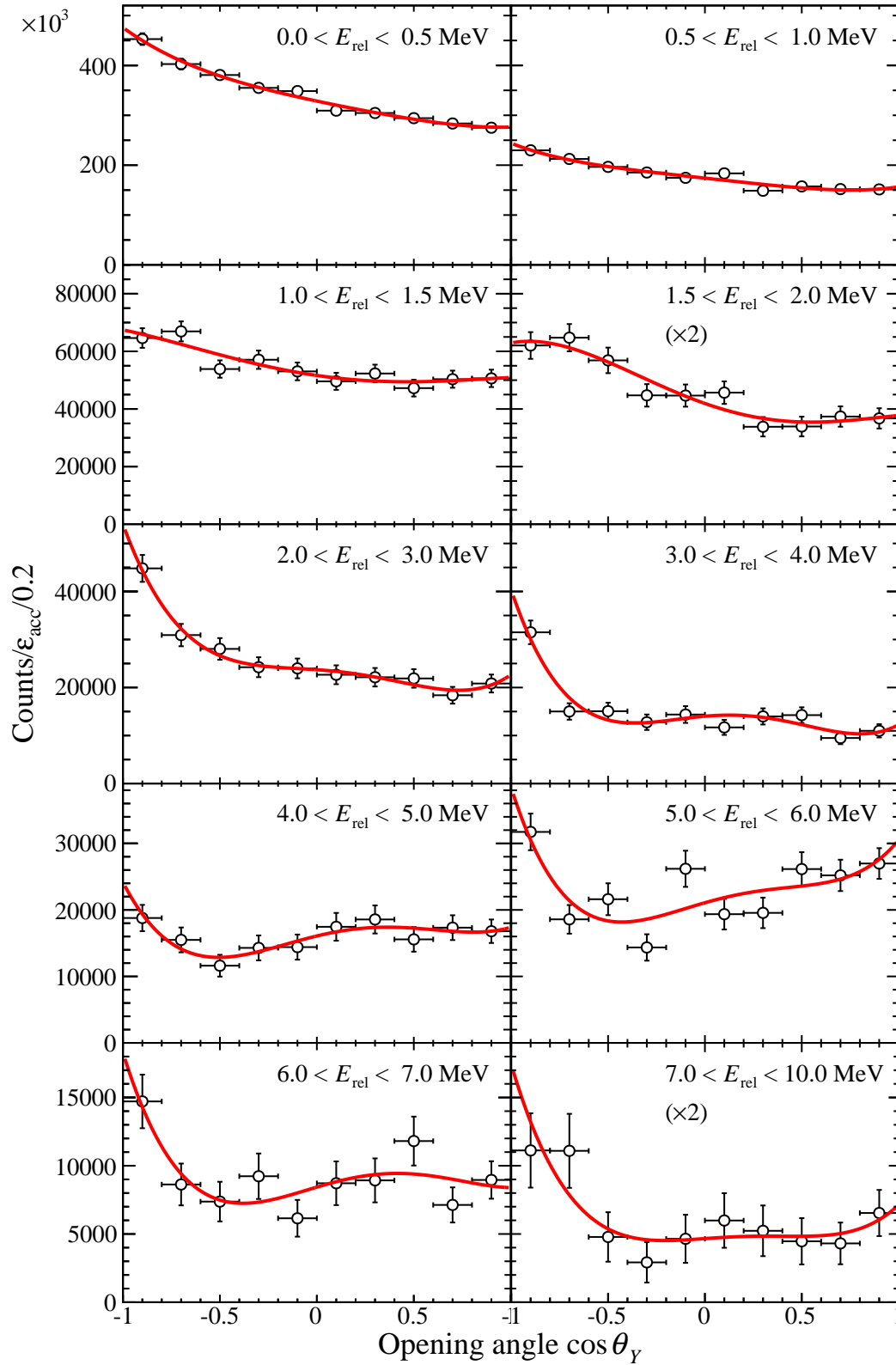
Figure 6.9: Opening angle $\cos\theta_Y$ distribution for each relative energy E_{rel}. The horizontal and the vertical axes show the opening angle and the counts divided by the acceptance factor, respectively. The spectra are fitted with the Legendre functions.
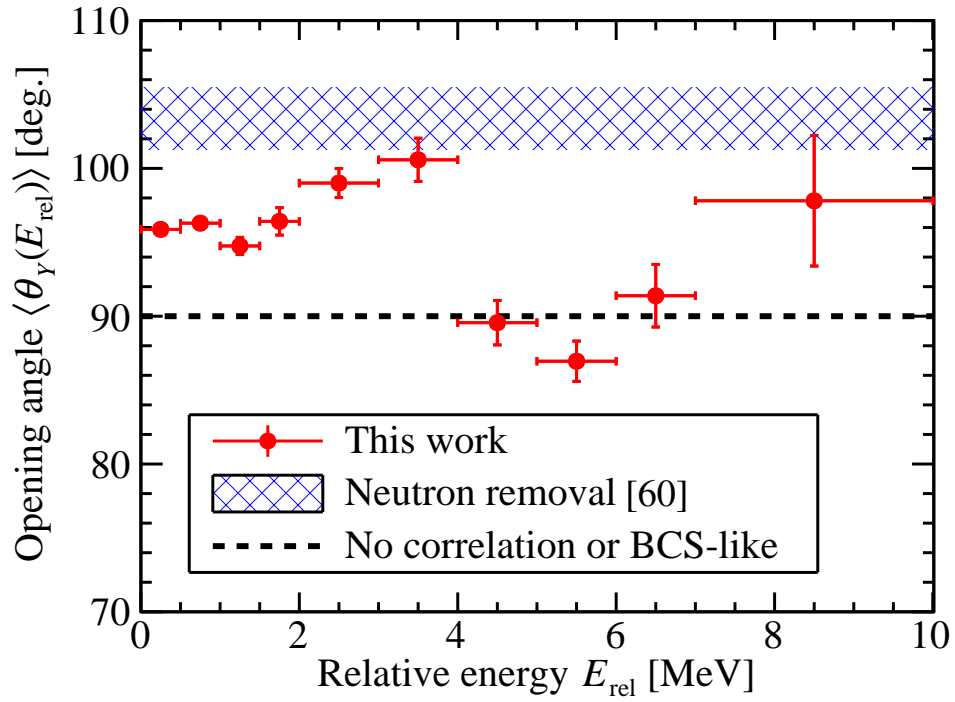
Figure 6.10: Expectation values of the opening angle in momentum space $\langle\theta_Y(E_{rel})\rangle$ as a function of the relative energy E_{rel}. The red closed points show the data obtained in the present study. The vertical error bars represent only statistical uncertainties. The blue hatched area shows the opening angle obtained in the previous study [60]. The black dashed line shows the expected opening angle for two neutrons having the BCS-like correlation or no correlation.

$E_{\rm rel} \sim 3$ MeV. It may be due to the strong admixture of the p and d wave in this region: The admixture of opposite parity configurations is essential to create the spatial localization [24]. The large $\langle \theta_Y(E_{\rm rel}) \rangle$ value in this region agreed with the MDA results that the contributions of the $p_{1/2}$ and $d_{5/2}$ states in this region was almost the same (Sec. 6.2.2). On the other hand, the $\langle \theta_Y(E_{\rm rel}) \rangle$ value around $E_{\rm rel} \sim 5$ MeV was almost consistent with 90 degrees, implying no dineutron correlation. It also agreed with the MDA results that only the $d_{5/2}$ state dominated in this region (Sec. 6.2.2).

The opening angle θ_Y should be associated with the multipole fractions $S_{\ell j}$ as described in Appendix A. In the present study, the $S_{\ell j}$ and the θ_Y values were experimentally determined (Sec. 6.2.2 and Sec. 6.3.1). The results provide an opportunity for further theoretical discussions. It is noteworthy that such a simple expression of Eq. (A.1) holds when the integration is performed for entire region. For the quantitative discussion, the relative energy dependence as well as the experimental sensitivity (Sec. 2.2.4) should be taken into consideration.

The expectation values of the opening angle determined in the present and the previous studies are summarized in Table 6.7. In this study, the averaged expectation value of the opening angle in position space was determined as $\langle \theta_Y^x \rangle = 85 \pm 10$ degrees. By employing the simplified classical picture (Eq. (6.9)), the averaged expectation value of the opening angle in V-coordinates was calculated as $\langle \theta_V^x \rangle = 77$ degrees. The opening angle in V-coordinates $\langle \theta_V^x \rangle$ of smaller than 90 degrees suggests the existence of the dineutron correlation. It agrees with current understanding that the dineutron correlation develops in ^{11}Li. However, the development is weaker than expected from previous studies. It agreed with the weaker admixture of different parity configurations (Sec. 6.2.3).

Table 6.7: Expectation values of the opening angle in the position space. The opening angle is shown in the Y-coordinates or the V-coordinates (Fig. 2.5) depending on the analysis model. The number in a parenthesis is calculated by employing the simplified classical picture.

		Probe/model	$\langle \theta_Y^x \rangle$ [deg.]	$\langle \theta_V^x \rangle$ [deg.]
Exp.	Ref. [40]	Coulomb breakup		48^{+14}_{-18}
	(Sec. 1.2.2)	[40] + core excitation		65 ± 11
Theor.	Ref. [57]	[40] + improved $\langle r_{c,2n} \rangle$		$65.2^{+11.4}_{-13.0}$
Theor.	Ref. [18]	TOSM		65.3
Theor.	Ref. [25]	Compilation	72.2	61.7
Exp.	Ref. [60]	Neutron removal	76.6 ± 2.1	
Exp.	This work	Quasi-free (p, pn)	85 ± 10	(77)

The bottom right panel of Fig. 6.8 shows the integrated opening angle distribution in the previous work using the neutron removal reaction with a carbon target [60]. The opening angle in Jacobi coordinates of $\langle \theta_Y^x \rangle = 180° - \theta_{nf} = 76.6 \pm 2.1$ degrees was obtained by employing Eq. (6.8). Although this value marginally agrees with the opening angle of $\langle \theta_Y^x \rangle = 85 \pm 10$ degrees obtained in the present work within the error bar, the larger opening angle, namely the weaker

dineutron correlation is indicated in the present work. We suppose it is due to the difference of the probe: The neutron removal reaction with the nuclear target is peripheral, while the proton-induced quasi-free (p, pn) reaction is more transparent [73]. By employing the surface probe such as the neutron removal reaction, the signature of the dineutron correlation is expected to be enhanced because the dineutron is considered to be formed at the surface [5]. In the case of the transparent probe such as the (p, pn) reaction, the signature of the dineutron is averaged over the whole nuclear volume, and is weakened.

In the previous study using the Coulomb breakup reaction [40], the expectation value of the opening angle in position space was determined as $\langle \theta_V^x \rangle = 48^{+14}_{-18}$ degrees by employing the the the non-energy-weighted $E1$ cluster sum rule based on the three-body model [12]. By taking into account the 15% reduction of the $E1$ sum rule value due to the ^{9}Li core excitation in the ground state [23], the opening angle was calculated as $\langle \theta_V^x \rangle = 65 \pm 11$ degrees. Ref. [58] showed the similar value of $\langle \theta_V^x \rangle = 65.2^{+11.4}_{-13.0}$ degrees by improving the averaged neutron-neutron distance and by taking into consideration the effect of the Pauli forbidden transitions. The opening angle of $\langle \theta_V^x \rangle = 77$ degrees obtained in the present work is larger than these values. However, we cannot discuss the $\langle \theta_V^x \rangle$ values quantitatively at this moment. As mentioned in Sec. 1.2.2, the theoretical interpretation on the $B(E1)$ measurement might have not been finalized. In addition, the very simplified picture was employed in the present study to calculate the opening angle of $\langle \theta_V^x \rangle = 77$ degrees. For the quantitative discussion, a theoretical model is needed to convert the θ_Y distribution to the $\langle \theta_V^x \rangle$ value.

In the Ref. [25], the ^{11}Li structure was investigated by fitting the model wave function to reproduce available experimental data including the carbon-induced neutron removal experiment [60, 61]. They reconstructed the wave function of the ground-state ^{11}Li and obtained the opening angle in two different coordinates: $\langle \theta_Y^x \rangle = 72.7$ degrees and $\langle \theta_V^x \rangle = 62.2$ degrees. Although the systematic uncertainty is not given, the opening angle seems smaller than that obtained in the present study. We speculate it is because the model wave function was determined so as to reproduce the data of Refs. [60, 61], where the strength of the dineutron correlation in ^{11}Li might have been overestimated.

Chapter 7

Conclusion

Neutron-neutron correlation in light neutron-rich Borromean nuclei has attracted much attention. These nuclei are weakly bound and have a surface made of neutrons. In such a weakly-bound system, a hypothetical bound state of two neutrons, *dineutron*, may exist near the surface. It has long been presumed that the neutron-neutron correlation caused by the dineutron (dineutron correlation) is a key ingredient to understand the binding mechanism as well as the exotic structures of these nuclei.

In the present work, the neutron momentum distribution in ^{11}Li was determined by employing the quasi-free (p, pn) reaction at 246 MeV/nucleon followed by the neutron emission. The effect of the final-state interactions (FSIs), which distorts the momentum distribution, was minimized owing to the reaction mechanism. We employed a new method of kinematically complete measurement, which enabled us to extract the ground-state neutron-neutron correlation in ^{11}Li through the momentum measurement of the neutron as well as to investigate the structure of the ^{9}Li + n subsystem through the invariant mass spectroscopy.

The experiment was performed at the Radioactive Isotope Beam Factory (RIBF) in RIKEN. The MINOS device was used so as to achieve high luminosity without losing the resolution. After an occurrence of the ^{11}Li(p, pn) reaction in the MINOS target, the scattered recoil proton and knocked-out neutron were respectively detected by the RPD and the WINDS, both constructed for this study, so as to reconstruct the neutron momentum distribution. The reaction residue, the heavy fragment ^{9}Li and the decay neutron were analyzed by the SAMURAI spectrometer and the NEBULA for the invariant mass spectroscopy. Gamma rays emitted from ^{9}Li were detected by the DALI2 for tagging the core excitation.

The spectroscopy of the reaction residue ^{10}Li provided strong constraints on the interaction between a neutron and a ^{9}Li nucleus, which is essential to describe ^{11}Li. The existence of the s-wave virtual state and of the p-wave resonance state was confirmed in the invariant mass spectrum of the ^{10}Li, and their resonance parameters were determined. Moreover, the d-wave resonance state was newly found at $E_r = 5.52 \pm 0.04$ MeV with a decay width of $\Gamma = 0.72 \pm 0.10$ MeV. This new resonance state has not been reproduced by available theoretical models.

The one-neutron ground-state momentum distribution gave the information of the spatial distribution of the valence neutron. The multipole decomposition analysis (MDA) was performed on the internal momentum of the knocked-out neutron k_Y. The fraction of each multipole up to d-wave was obtained as $35 \pm 4\%$, $59 \pm 1\%$, and $6 \pm 4\%$ for the two-neutron configurations $(s_{1/2})^2$, $(p_{1/2})^2$, and $(d_{5/2})^2$ or $(d_{3/2})^2$, respectively. The fraction of the s-wave is small compared to the previous works. This indicates the dineutron correlation in ^{11}Li can be weaker than previously reported.

The spatial distribution of two valence neutrons in ^{11}Li was studied by using the relative energy as a measure of the radial position. The relative energy dependence of the opening angle distribution of two neutrons was measured for the first time. The result suggested that the dineutron correlation developed in the surface region. The averaged expectation value of the opening angle between the two neutrons was determined as $\langle \theta_Y^x \rangle = 85 \pm 10$ degrees. The larger opening angle as compared with the previous work implies the weaker dineutron correlation in ^{11}Li than expected from the previous works.

For further study, the extraction of core excited components will be performed through the ^{11}Li$(p, pn)^{10}$Li$^* \rightarrow {}^8$Li $+ 2n$ and ^{7}Li $+ 3n$ channels in the present data, with theoretical help of handling the FSIs. As a naive extension of this method, one can apply this technique to other Borromean nuclei for the study of the neutron-neutron correlation. Moreover, it is also possible to study the other correlation such as the proton-proton correlation by employing another kinds of knockout reactions. The reaction model we employed for this study can be calibrated precisely, by conducting the ^{6}He(p, pn) and the ^{6}He$(p, p\alpha)$ measurements.

Appendix A

Legendre expansion of the opening angle distribution

The opening angle distribution is expanded [151] by using the Legendre function $P_\lambda(x)$ as

$$\frac{\mathrm{d}\sigma}{\mathrm{d}\cos\theta_Y} = \sum_\lambda P_\lambda(\cos\theta_Y)$$
$$\times \sum_{\ell j \ell' j'} S_{\ell j} S_{\ell' j'} \mathrm{e}^{-2\mathrm{i}(\phi_{\ell j} - \phi_{\ell' j'})} C_\lambda(\ell, j, \ell', j'), \tag{A.1}$$

$$C_\lambda(\ell, j, \ell', j') = \frac{1}{2} \sum_L (-1)^{2\ell + 2\ell' + j + j' + L + 1} (2\ell + 1)(2\ell' + 1)$$
$$\times \sqrt{(2j + 1)(2j' + 1)(2L + 1)} \, \langle \ell\, 0\, \ell'\, 0 | \lambda\, 0 \rangle^2$$
$$\times \begin{Bmatrix} \ell & \ell & L \\ \frac{1}{2} & \frac{1}{2} & j \end{Bmatrix} \begin{Bmatrix} \ell' & \ell' & L \\ \frac{1}{2} & \frac{1}{2} & j' \end{Bmatrix} \begin{Bmatrix} \ell & \ell' & \lambda \\ \ell' & \ell & L \end{Bmatrix}, \tag{A.2}$$

where $\langle \ell\, 0\, \ell'\, 0 | \lambda\, 0 \rangle$ and $\begin{Bmatrix} j_1 & j_2 & j_3 \\ j_4 & j_5 & j_6 \end{Bmatrix}$ denote the Clebsch-Gordan coefficient and Wigner's 6-j symbol. Although the quantum number of the generalized angular momentum λ runs in an infinite range, finite coefficients $C_\lambda(\ell, j, \ell', j')$ have non-zero values when the finite numbers of the neutron angular momentum ℓ, ℓ' are considered. Coefficients with finite values in the case up to the d-wave components ($\ell, \ell' \leq 2$) are taken into account, are summarized in Appendix B.

We here consider the two-neutron wave function in jj-coupling scheme as

$$\Phi(nn) = \sum_{\ell j} \phi_\ell(r_1)\phi_\ell(r_2) \left[[Y_\ell(\hat{r}_1), \chi_{1/2}]_j, [Y_\ell(\hat{r}_2), \chi_{1/2}]_j \right]_{00}, \tag{A.3}$$

where it is assumed that the neutron pair couples to $J^\pi = 0^+$.

Using the wave function given in Eq. (A.3), the opening angle distribution is calculated as

$$\langle \Phi(nn)| \delta(\hat{r}_1 \cdot \hat{r}_2 - \cos\theta_Y) |\Phi(nn)\rangle$$
$$= \sum_{\ell\ell'jj'} \int \int dr_1 dr_2 \, \phi_\ell^*(r_1)\phi_\ell^*(r_2)\phi_{\ell'}(r_1)\phi_{\ell'}(r_2)$$
$$\times \left\langle \left[[Y_\ell(\hat{r}_1), \chi_{1/2}]_j, [Y_\ell(\hat{r}_2), \chi_{1/2}]_j \right]_{00} \middle| \delta(\hat{r}_1 \cdot \hat{r}_2 - \cos\theta_Y) \right.$$
$$\times \left. \middle| \left[[Y_{\ell'}(\hat{r}_1), \chi_{1/2}]_{j'}, [Y_{\ell'}(\hat{r}_2), \chi_{1/2}]_{j'} \right]_{00} \right\rangle. \tag{A.4}$$

The angular and spin part is evaluated as

$$\left\langle \left[[Y_\ell(\hat{r}_1), \chi_{1/2}]_j, [Y_\ell(\hat{r}_2), \chi_{1/2}]_j \right]_{00} \middle| \delta(\hat{r}_1 \cdot \hat{r}_2 - \cos\theta_Y) \right.$$
$$\times \left. \middle| \left[[Y_{\ell'}(\hat{r}_1), \chi_{1/2}]_{j'}, [Y_{\ell'}(\hat{r}_2), \chi_{1/2}]_{j'} \right]_{00} \right\rangle$$
$$= 8\pi^2 \sin\theta_Y \sum_{LSL'S'} (2j+1)(2j'+1)\sqrt{(2L+1)(2S+1)(2L'+1)(2S'+1)}$$
$$\times \begin{Bmatrix} \ell & \ell & L \\ \frac{1}{2} & \frac{1}{2} & S \\ j & j & 0 \end{Bmatrix} \begin{Bmatrix} \ell' & \ell' & L' \\ \frac{1}{2} & \frac{1}{2} & S' \\ j' & j' & 0 \end{Bmatrix} \left\langle \left[[Y_\ell(\hat{r}_1), Y_\ell(\hat{r}_2)]_L, [\chi_{1/2}, \chi_{1/2}]_S \right]_{00} \right|$$
$$\times \delta(\hat{r}_1 \cdot \hat{r}_2 - \cos\theta_Y) \left| \left[[Y_{\ell'}(\hat{r}_1), Y_{\ell'}(\hat{r}_2)]_{L'}, [\chi_{1/2}, \chi_{1/2}]_{S'} \right]_{00} \right\rangle$$
$$= 8\pi^2 \sin\theta_Y \sum_{LSL'S'} (2j+1)(2j'+1)\sqrt{(2L+1)(2S+1)(2L'+1)(2S'+1)}$$
$$\times \frac{(-1)^{\ell+\frac{1}{2}+j+L}}{\sqrt{(2j+1)(2L+1)}} \begin{Bmatrix} \ell & \ell & L \\ \frac{1}{2} & \frac{1}{2} & j \end{Bmatrix} \frac{(-1)^{\ell'+\frac{1}{2}+j'+L'}}{\sqrt{(2j'+1)(2L'+1)}} \begin{Bmatrix} \ell' & \ell' & L' \\ \frac{1}{2} & \frac{1}{2} & j' \end{Bmatrix}$$
$$\times \delta_{LS}\delta_{L'S'}\delta_{LL'}\delta_{SS'}$$
$$\times \sum_{M^L} \frac{1}{2L+1} [Y_\ell(\hat{r}_1), Y_\ell(\hat{r}_2)]^*_{LM^L} [Y_{\ell'}(\hat{r}_1), Y_{\ell'}(\hat{r}_2)]_{LM^L}$$
$$= 8\pi^2 \sin\theta_Y \sum_L (-1)^{\ell+\ell'+j+j'+1}\sqrt{(2j+1)(2j'+1)(2L+1)}$$
$$\times \begin{Bmatrix} \ell & \ell & L \\ \frac{1}{2} & \frac{1}{2} & j \end{Bmatrix} \begin{Bmatrix} \ell' & \ell' & L \\ \frac{1}{2} & \frac{1}{2} & j' \end{Bmatrix}$$
$$\times \sum_{M^L} \frac{1}{2L+1} (-1)^{M^L-L} [Y_\ell(\hat{r}_1), Y_\ell(\hat{r}_2)]_{L-M^L} [Y_{\ell'}(\hat{r}_1), Y_{\ell'}(\hat{r}_2)]_{LM^L}$$

$$= 8\pi^2 \sin\theta_Y \sum_L (-1)^{\ell+\ell'+j+j'+1} \sqrt{(2j+1)(2j'+1)(2L+1)}$$

$$\times \begin{Bmatrix} \ell & \ell & L \\ \frac{1}{2} & \frac{1}{2} & j \end{Bmatrix} \begin{Bmatrix} \ell' & \ell' & L \\ \frac{1}{2} & \frac{1}{2} & j' \end{Bmatrix}$$

$$\times \sum_{M^L} \sum_\Lambda \sum_{\lambda\lambda'} \frac{1}{2L+1} (-1)^{M^L-L} \langle L - M^L\, L\, M^L | \Lambda\, 0 \rangle$$

$$\times \frac{(2\ell+1)(2\ell'+1)(2L+1)}{4\pi}$$

$$\times \langle \ell\, 0\, \ell'\, 0 | \lambda\, 0 \rangle \langle \ell\, 0\, \ell'\, 0 | \lambda'\, 0 \rangle \begin{Bmatrix} \ell & \ell' & \lambda \\ \ell & \ell' & \lambda' \\ L & L & \Lambda \end{Bmatrix} [Y_\lambda(\hat{\bm{r}_1}), Y_{\lambda'}(\hat{\bm{r}_2})]_{\Lambda 0}$$

$$= 2\pi \sin\theta_Y \sum_L (-1)^{\ell+\ell'+j+j'+1} \sqrt{(2j+1)(2j'+1)(2L+1)}$$

$$\times \begin{Bmatrix} \ell & \ell & L \\ \frac{1}{2} & \frac{1}{2} & j \end{Bmatrix} \begin{Bmatrix} \ell' & \ell' & L \\ \frac{1}{2} & \frac{1}{2} & j' \end{Bmatrix} \sum_\Lambda \sum_{\lambda\lambda'} (2\ell+1)(2\ell'+1)\sqrt{2L+1}\,\delta_{\Lambda 0}$$

$$\times \langle \ell\, 0\, \ell'\, 0 | \lambda\, 0 \rangle \langle \ell\, 0\, \ell'\, 0 | \lambda'\, 0 \rangle \begin{Bmatrix} \ell & \ell' & \lambda \\ \ell & \ell' & \lambda' \\ L & L & \Lambda \end{Bmatrix} [Y_\lambda(\hat{\bm{r}_1}), Y_{\lambda'}(\hat{\bm{r}_2})]_{\Lambda 0}$$

$$= 2\pi \sin\theta_Y \sum_L (-1)^{\ell+\ell'+j+j'+1} \sqrt{(2j+1)(2j'+1)(2L+1)}$$

$$\times \begin{Bmatrix} \ell & \ell & L \\ \frac{1}{2} & \frac{1}{2} & j \end{Bmatrix} \begin{Bmatrix} \ell' & \ell' & L \\ \frac{1}{2} & \frac{1}{2} & j' \end{Bmatrix} \sum_\lambda (2\ell+1)(2\ell'+1)\sqrt{2L+1}$$

$$\times \langle \ell\, 0\, \ell'\, 0 | \lambda\, 0 \rangle \langle \ell\, 0\, \ell'\, 0 | \lambda\, 0 \rangle \begin{Bmatrix} \ell & \ell' & \lambda \\ \ell & \ell' & \lambda \\ L & L & 0 \end{Bmatrix} [Y_\lambda(\hat{\bm{r}_1}), Y_\lambda(\hat{\bm{r}_2})]_{00}$$

$$= 2\pi \sin\theta_Y \sum_L (-1)^{\ell+\ell'+j+j'+1} \sqrt{(2j+1)(2j'+1)(2L+1)}$$

$$\times \begin{Bmatrix} \ell & \ell & L \\ \frac{1}{2} & \frac{1}{2} & j \end{Bmatrix} \begin{Bmatrix} \ell' & \ell' & L \\ \frac{1}{2} & \frac{1}{2} & j' \end{Bmatrix} \sum_\lambda (2\ell+1)(2\ell'+1)\sqrt{2L+1}$$

$$\times \langle \ell\, 0\, \ell'\, 0 | \lambda\, 0 \rangle \langle \ell\, 0\, \ell'\, 0 | \lambda\, 0 \rangle \frac{(-1)^{\ell+\ell'+\lambda+L}}{\sqrt{(2L+1)(2\lambda+1)}} \begin{Bmatrix} \ell & \ell' & \lambda \\ \ell' & \ell & L \end{Bmatrix}$$

$$\times [Y_\lambda(\hat{\bm{r}_1}), Y_\lambda(\hat{\bm{r}_2})]_{00}$$

$$= 2\pi \sin\theta_Y \sum_L (-1)^{\ell+\ell'+j+j'+1} \sqrt{(2j+1)(2j'+1)(2L+1)}$$

$$\times \begin{Bmatrix} \ell & \ell & L \\ \frac{1}{2} & \frac{1}{2} & j \end{Bmatrix} \begin{Bmatrix} \ell' & \ell' & L \\ \frac{1}{2} & \frac{1}{2} & j' \end{Bmatrix} \sum_\lambda (-1)^{\ell+\ell'+\lambda+L} \frac{(2\ell+1)(2\ell'+1)}{\sqrt{2\lambda+1}}$$

$$\times \langle \ell\, 0\, \ell'\, 0 | \lambda\, 0 \rangle \langle \ell\, 0\, \ell'\, 0 | \lambda\, 0 \rangle \begin{Bmatrix} \ell & \ell' & \lambda \\ \ell' & \ell & L \end{Bmatrix} \frac{(-1)^\lambda}{\sqrt{2\lambda+1}} \cdot \frac{2\lambda+1}{4\pi} P_\lambda(\cos\theta_Y)$$

$$= 2\pi \sin \theta_Y \sum_L (-1)^{\ell+\ell'+j+j'+1} \sqrt{(2j+1)(2j'+1)(2L+1)}$$

$$\times \begin{Bmatrix} \ell & \ell & L \\ \frac{1}{2} & \frac{1}{2} & j \end{Bmatrix} \begin{Bmatrix} \ell' & \ell' & L \\ \frac{1}{2} & \frac{1}{2} & j' \end{Bmatrix} \sum_\lambda (-1)^{\ell+\ell'+L}(2\ell+1)(2\ell'+1)$$

$$\times \langle \ell\, 0\, \ell'\, 0 | \lambda\, 0 \rangle \langle \ell\, 0\, \ell'\, 0 | \lambda\, 0 \rangle \begin{Bmatrix} \ell & \ell' & \lambda \\ \ell' & \ell & L \end{Bmatrix} P_\lambda(\cos \theta_Y). \tag{A.5}$$

Appendix B

Coefficient C_λ for $\ell \leq 2$

The coefficient C_λ defined in Eq. (A.2) is calculated under the constraint of $\ell, \ell' \leq 2$, and summarized in Table B.1.

Table B.1: Coefficient $C_\lambda(\ell, j, \ell', j')$ up to $\ell, \ell' = 2$. The rows and the columns represent (ℓ, j) and (ℓ', j'), respectively. Only the finite values are presented.

$\lambda = 0$	$s_{1/2}$	$p_{1/2}$	$p_{3/2}$	$d_{3/2}$	$d_{5/2}$
$s_{1/2}$	0.5000				
$p_{1/2}$		0.3591	0.0996		
$p_{3/2}$		0.0996	0.4296		
$d_{3/2}$				0.3732	0.1035
$d_{5/2}$				0.1035	0.4155

$\lambda = 1$	$s_{1/2}$	$p_{1/2}$	$p_{3/2}$	$d_{3/2}$	$d_{5/2}$
$s_{1/2}$		-0.5000	-0.7071		
$p_{1/2}$	-0.5000			-0.5278	-0.1464
$p_{3/2}$	-0.7071			-0.2268	-0.6313
$d_{3/2}$		-0.5278	-0.2268		
$d_{5/2}$		-0.1464	-0.6313		

$\lambda = 2$	$s_{1/2}$	$p_{1/2}$	$p_{3/2}$	$d_{3/2}$	$d_{5/2}$
$s_{1/2}$				0.7071	0.8660
$p_{1/2}$		0.1409	0.6075		
$p_{3/2}$		0.6075	0.5704		
$d_{3/2}$	0.7071			0.4094	0.2489
$d_{5/2}$	0.8660			0.2489	0.5111

$\lambda = 3$	$s_{1/2}$	$p_{1/2}$	$p_{3/2}$	$d_{3/2}$	$d_{5/2}$
$s_{1/2}$					
$p_{1/2}$				-0.1793	-0.7196
$p_{3/2}$				-0.7732	-0.5934
$d_{3/2}$		-0.1793	-0.7732		
$d_{5/2}$		-0.7196	-0.5934		

$\lambda = 4$	$s_{1/2}$	$p_{1/2}$	$p_{3/2}$	$d_{3/2}$	$d_{5/2}$
$s_{1/2}$					
$p_{1/2}$					
$p_{3/2}$					
$d_{3/2}$				0.2174	0.8723
$d_{5/2}$				0.8723	0.5735

Bibliography

[1] J. Bardeen, L. N. Cooper, and J. R. Schrieffer, Phys. Rev. **108**, 1175 (1957).

[2] L. N. Cooper, R. L. Mills, and A. M. Sessler, Phys. Rev. **114**, 1377 (1959).

[3] A. J. Moerdijk, et al., Phys. Rev. Lett. **72**, 40 (1994).

[4] A. Bohr, B. R. Mottelson, and D. Pines, Phys. Rev. **110**, 936 (1958).

[5] A. B. Migdal, Soviet J. of Nucl. Phys. **16**, 238 (1973).

[6] T. Oishi, K. Hagino, and H. Sagawa, Phys. Rev. C **82**, 024315 (2010).

[7] M. Matsuo, K. Mizuyama, and Y. Serizawa, Phys. Rev. C **71**, 064326 (2005).

[8] N. Pillet, N. Sandulescu, and P. Schuck, Phys. Rev. C **76**, 024310 (2007).

[9] M. Matsuo, Phys. Rev. C **73**, 044309 (2006).

[10] M. V. Zhukov, et al., Phys. Rep. **231**, 151 (1993).

[11] M. V. Zhukov, et al., Nucl. Phys. **539**, 177 (1992).

[12] G. F. Bertsch and H. Esbensen, Ann. Phys. (NY) **209**, 327 (1991).

[13] F. Barranco, et al., Eur. Phys. J. A **11**, 385 (2001).

[14] S. Aoyama, et al., Prog. Theor. Phys. **93**, 99 (1995).

[15] K. Hagino, et al., Phys. Rev. Lett. **99**, 022506 (2007).

[16] S. Funada, H. Kameyama, and Y. Sakuragi, Nucl. Phys. **575**, 93 (1994).

[17] K. Hagino and H. Sagawa, Phys. Rev. C **72**, 044321 (2005).

[18] T. Myo, et al., Prog. Theor. Phys. **119**, 561 (2008).

[19] A. Csótó, Phys. Rev. C **49**, 3035 (1994).

[20] Y. Suzuki, Nucl. Phys. **528**, 395 (1991).

[21] T. Myo, et al., Phys. Rev. C **63**, 054313 (2001).

[22] Y. Kikuchi, et al., Phys. Rev. C **81**, 044308 (2010).

[23] Y. Kikuchi, et al., Phys. Rev. C **87**, 034606 (2013).

[24] F. Catara, et al., Phys. Rev. C **29**, 1091 (1984).

[25] N. B. Shulgina, B. Jonson, and M. V. Zhukov, Nucl. Phys. **825**, 175 (2009).

[26] *Evaluated Nuclear Structure Data File (ENSDF) database* (2016), `http://www.nndc.bnl.gov/`.

[27] G. D. Alkhazov, et al., Phys. Rev. Lett. **78**, 2313 (1997).

[28] J. S. Al-Khalili and J. A. Tostevin, Phys. Rev. Lett. **76**, 3903 (1996).

[29] T. Moriguchi, et al., Nucl. Phys. **929**, 83 (2014).

[30] T. Suzuki, et al., Nucl. Phys. **658**, 313 (1999).

[31] Y. Togano, et al., Phys. Lett. B **761**, 412 (2016).

[32] G. Ewald, et al., Phys. Rev. Lett. **93**, 113002 (2004).

[33] R. Sánchez, et al., Phys. Rev. Lett. **96**, 033002 (2006).

[34] E. W. Otten, *Treatise on Heavy Ion Science: Volume 8: Nuclei Far From Stability* (Springer US, Boston, MA, 1989), chap. Nuclear Radii and Moments of Unstable Isotopes, pp. 517–638.

[35] H.-J. Kluge and W. Nörtershäuser, Spectrochim. Acta B **58**, 1031 (2003).

[36] I. Tanihata, et al., Phys. Rev. Lett. **55**, 2676 (1985).

[37] I. Tanihata, et al., Phys. Lett. B **206**, 592 (1988).

[38] H. Esbensen and G. F. Bertsch, Nucl. Phys. **542**, 310 (1992).

[39] A. Bonaccorso and N. V. Mau, Nucl. Phys. **615**, 245 (1997).

[40] T. Nakamura, et al., Phys. Rev. Lett. **96**, 252502 (2006).

[41] K. Ieki, et al., Phys. Rev. Lett. **70**, 730 (1993).

[42] T. Aumann, et al., Phys. Rev. C **59**, 1252 (1999).

[43] L. V. Chulkov, et al., Nucl. Phys. **759**, 23 (2005).

[44] T. Kobayashi, et al., Phys. Lett. B **232**, 51 (1989).

[45] T. Nakamura, et al., Phys. Lett. B **331**, 296 (1994).

[46] T. Nakamura, et al., Phys. Rev. Lett. **83**, 1112 (1999).

[47] U. D. Pramanik, et al., Phys. Lett. B **551**, 63 (2003).

[48] R. Palit, et al. (LAND/FRS Collaboration), Phys. Rev. C **68**, 034318 (2003).

[49] N. Fukuda, et al., Phys. Rev. C **70**, 054606 (2004).

[50] D. Sackett, et al., Phys. Rev. C **48**, 118 (1993).

[51] S. Shimoura, et al., Phys. Lett. B **348**, 29 (1995).

[52] M. Zinser, et al., Nucl. Phys. **619**, 151 (1997).

[53] J. Wang, et al., Phys. Rev. C **65**, 034306 (2002).

[54] M. Labiche, et al., Phys. Rev. Lett. **86**, 600 (2001).

[55] C. A. Bertulani and M. S. Hussein, Phys. Rev. C **76**, 051602 (2007).

[56] F. M. Marqués, et al., Phys. Lett. B **476**, 219 (2000).

[57] K. Hagino and H. Sagawa, Phys. Rev. C **76**, 047302 (2007).

[58] K. Hagino and H. Sagawa, Few-Body Syst. **57**, 185 (2016).

[59] H. Esbensen, et al., Phys. Rev. C **76**, 024302 (2007).

[60] H. Simon, et al., Phys. Rev. Lett. **83**, 496 (1999).

[61] H. Simon, et al., Nucl. Phys. **791**, 267 (2007).

[62] Yu. Aksyutina, et al., Phys. Lett. B **666**, 430 (2008).

[63] Yu. Aksyutina, Ph.D. thesis, Johann Wolfgang Goethe-Universität in Frankfurt am Main (2009).

[64] Yu. Aksyutina, et al., Phys. Lett. B **718**, 1309 (2013).

[65] K. Hagino and H. Sagawa, in private communication.

[66] G. Potel, et al., Phys. Rev. Lett. **105**, 172502 (2010).

[67] Y. Kubota and A. Corsi, Proposal for Nuclear Physics Experiment at RI Beam Factory, NP1312-SAMURAI18R1 (2013).

[68] I. Sick and P. deWitt Huberts, Comments Nucl. Part. Phys. **20**, 177 (1991).

[69] G. Jacob and Th. A. J. Maris, Rev. Mod. Phys. **38**, 121 (1966).

[70] G. Jacob and Th. A. J. Maris, Rev. Mod. Phys. **45**, 6 (1973).

[71] R. Serber, Phys. Rev. **72**, 1114 (1947).

[72] T. Noro, in *ECT* workshop* (2008).

[73] Y. Kikuchi, et al., Prog. Theor. Exp. Phys. **2016**, 103D03 (2016).

[74] A. Gade, et al., Phys. Rev. C **77**, 044306 (2008).

[75] N. Austern, M. Yahiro, and M. Kawai, Phys. Rev. Lett. **63**, 2649 (1989).

[76] N. Austern, M. Kawai, and M. Yahiro, Phys. Rev. C **53**, 314 (1996).

[77] D. Baye, P. Capel, and G. Goldstein, Phys. Rev. Lett. **95**, 082502 (2005).

[78] G. Goldstein, D. Baye, and P. Capel, Phys. Rev. C **73**, 024602 (2006).

[79] L. D. Faddeev, Sov. Phys. JETP **12**, 1014 (1961).

[80] E. O. Alt, P. Grassberger, and W. Sandhas, Nucl. Phys. B **2**, 167 (1967).

[81] R. J. Glauber, *Lectures in Theoretical Physics* (Interscience, New York, 1959).

[82] M. Yahiro, et al., Prog. Theor. Phys. **120**, 767 (2008).

[83] M. Yahiro, K. Ogata, and K. Minomo, Prog. Theor. Phys. **126**, 167 (2011).

[84] K. Ogata, K. Yoshida, and K. Minomo, Phys. Rev. C **92**, 034616 (2015).

[85] K. Ogata, in *13th RIBF Discussion* (2015).

[86] K. Ogata, et al., Phys. Rev. C **73**, 024605 (2006).

[87] D. Betounes, *Differential Equations: Theory and Applications* (Springer, 2001).

[88] Y. Yano, Nucl. Inst. & Meth. **B 261**, 1009 (2007).

[89] H. Okuno, N. Fukunishi, and O. Kamigaito, Prog. Theor. Exp. Phys. **2012**, 03C002 (2012).

[90] T. Nakagawa, et al., Nucl. Inst. & Meth. **B 226**, 392 (2004).

[91] T. Kubo, et al., IEEE Trans. Appl. Supercond. **17**, 1069 (2007).

[92] K. Kusaka, et al., IEEE Trans. Appl. Supercond. **14**, 310 (2004).

[93] H. Kumagai, et al., Nucl. Inst. & Meth. **A 470**, 562 (2001).

[94] H. Kumagai, et al., Nucl. Inst. & Meth. **B 317**, 717 (2013).

[95] O. B. Tarasov and D. Bazin, Nucl. Inst. & Meth. **B 266**, 4657 (2008).

[96] K. Sümmerer and B. Blank, Phys. Rev. C **61**, 034607 (2000).

[97] M. Berz, K. Makino, and W. Wan, *An Introduction to Beam Physics* (CRC Press, 2014).

[98] *Photogrammetry : Restoration Institute : Clemson University : South Carolina* (2016), `http://www.clemson.edu/restoration/wlcc/equipment_services/equipment/photogrammetry.html`.

[99] *V-STARS S — Geodetic Systems, Inc.* (2014), `http://www.geodetic.com/products/systems/v-stars-s.aspx`.

[100] T. Kobayashi, et al., Nucl. Inst. & Meth. **B 317**, 294 (2013).

[101] H. Sato, et al., IEEE Trans. Appl. Supercond. **23**, 4500308 (2013).

[102] Y. Shimizu, et al., Nucl. Inst. & Meth. **B 317**, 739 (2013).

[103] A. Obertelli and T. Uesaka, Eur. Phys. J. A **47**, 105 (2011).

[104] A. Obertelli, et al., Eur. Phys. J. A **50**, 8 (2014).

[105] Y. Giomataris, et al., Nucl. Inst. & Meth. **A 376**, 29 (1996).

[106] I. Giomataris, et al., Nucl. Inst. & Meth. **A 560**, 405 (2006).

[107] C. Santamaria, et al., JPS Conf. Proc. **6**, 030130 (2015).

[108] N. Abgrall, et al., Nucl. Inst. & Meth. **A 637**, 25 (2011).

[109] P. Baron, et al., IEEE Trans. Nucl. Sci. **55**, 1744 (2008).

[110] S. Anvar, et al., in *Nuclear Science Symposium and Medical Imaging Conference (NSS/MIC), 2011 IEEE* (2011), pp. 745–749.

[111] F. Château and S. Anvar, in *Real-Time Conference, 2007 15th IEEE-NPSS* (2007), pp. 1–6.

[112] Y. Kubota and M. Sasano, RIKEN Accel. Prog. Rep. **47**, 177 (2014).

[113] J. Yasuda, et al., Nucl. Inst. & Meth. **B 376**, 393 (2016).

[114] K. Yako, et al., CNS Ann. Rep. **CNS-REP-90**, 22 (2013).

[115] S. Noji, et al., Nucl. Inst. & Meth. **A 578**, 267 (2007).

[116] S. Takeuchi, et al., Nucl. Inst. & Meth. **A 763**, 596 (2014).

[117] S. Agostinelli, et al., Nucl. Inst. & Meth. **A 506**, 250 (2003).

[118] J. Allison, et al., IEEE Trans. Nucl. Sci. **53**, 270 (2006).

[119] Y. Kondo, et al., RIKEN Accel. Prog. Rep. **44**, 150 (2011).

[120] T. Nakamura and Y. Kondo, Nucl. Inst. & Meth. **B 376**, 156 (2016).

[121] R. Tanaka, Master's thesis, Tokyo Institute of Technology (2012).

[122] H. Baba, et al., Nucl. Inst. & Meth. **A 616**, 65 (2010).

[123] H. Baba, et al., in *Real Time Conference (RT), 2014 19th IEEE-NPSS* (2014), pp. 1–5.

[124] H. Baba, *RIBF data format (RIDF) nov. 12, 2010 version 1.5* (2010), `https://ribf.riken.jp/RIBFDAQ/index.php?plugin=attach&refer=DAQ%2FManual%2FDataformat&openfile=dataformat_101112e.pdf`.

[125] H. Baba, et al., RIKEN Accel. Prog. Rep. **46**, 213 (2013).

[126] H. Baba, et al., RIKEN Accel. Prog. Rep. **47**, 235 (2014).

[127] *Mod. V1290-VX1290 A/N, 32/16 Ch. Multihit TDC*, Rev. 15 ed. (2012).

[128] S. Koyama, H. Otsu, and for SAMURAI08 collaboration, RIKEN Accel. Prog. Rep. **48**, 46 (2015).

[129] P. V. C. Hough, *Methods and means for recognizing complex patterns* (1962), U.S. Patent 3.069.654.

[130] R. O. Duda and P. E. Hart, Commun. ACM **15**, 11 (1972).

[131] D. H. Ballard, Pattern Recogn. **13**, 111 (1981).

[132] C. Santamaria, Ph.D. thesis, Université Paris-Sud XI (2015).

[133] T. J. Gooding and H. G. Pugh, Nucl. Inst. & Meth. **7**, 189 (1960).

[134] W. R. Leo, *Techniques for Nuclear and Particle Physics Experiments: A How-to Approach* (Springer, 1994).

[135] H. Takeda and K. Yoshida, *BigRIPS Optics Standard mode* (2012), `http://ribf.riken.jp/BigRIPSInfo/optics/fig/matrix_1st_7Tm.txt`.

[136] P. Doornenbal, Prog. Theor. Exp. Phys. **2012** (2012).

[137] H. Sato, *SAMURAI Magnet and Detectors* (2015), `http://ribf.riken.jp/SAMURAI/index.php?Magnet`.

[138] Y. Kikuchi, in private communication.

[139] G. F. Bertsch, K. Hencken, and H. Esbensen, Phys. Rev. C **57**, 1366 (1998).

[140] H. B. Jeppesen, et al., Phys. Lett. B **642**, 449 (2006).

[141] T. Kobayashi, et al., Nucl. Phys. **616**, 223 (1997).

[142] M. G. Gornov, et al., Bull. Russ. Acad. Sci., Phys. Ser. **62**, 1781 (1998).

[143] H. G. Bohlen, et al., Z. Phys. A-Hadron. Nucl. **344**, 381 (1993).

[144] H. G. Bohlen, et al., Prog. Part. Nucl. Phys. **42**, 17 (1999).

[145] K. Ikeda, et al., *Clusters in Nuclei: Volume 1* (Springer Berlin Heidelberg, Berlin, Heidelberg, 2010), chap. Di-Neutron Clustering and Deuteron-like Tensor Correlation in Nuclear Structure Focusing on ^{11}Li, pp. 165–221.

[146] K. Katō, T. Yamada, and K. Ikeda, Prog. Theor. Phys. **101**, 119 (1999).

[147] T. Myo, et al., Prog. Theor. Phys. **117**, 257 (2007).

[148] T. Myo, et al., Phys. Rev. C **76**, 024305 (2007).

[149] T. Noro, in *ECT* workshop* (2010).

[150] H. T. Fortune, Phys. Rev. C **91**, 017303 (2015).

[151] Y. Kikuchi, in private communication.

Acknowledgment

First of all, I would like to express my largest gratitude to my supervisor Dr. T. Uesaka for providing me the precious chance to study the nuclear physics with many outstanding researchers. He showed me his philosophy of physics and experiments during my 5-years course in the graduate school to be an eligible researcher. His unperturbed calm encouraged me a lot to try a challenging theme.

I would like to express my special appreciation to Dr. M. Sasano. His continuous advice enriched my understanding of physics. He showed what is researcher through his attitude to everything; he always started to consider from basic principles to find rational judgments without being disturbed by non-scientific matters such as a historical background. He also patiently taught me how to manage the large collaboration and to maximize the output. Moreover, he devoted time to give me suggestions on the English writing.

I would like to thank to Prof. K. Yako, Prof. H. Yamaguchi, and Prof. E. Ideguchi for agreeing to become my supervisors after the transfer of Prof. T. Uesaka from The University of Tokyo to RIKEN Nishina Center. They were always cooperative and spent a lot of time for giving me precious suggestions.

I also appreciate for Dr. S. Ota for giving me priceless suggestions and instructions. His advice was always sufficiently pragmatic to guide me forward. He taught me how to manage an experiment mainly through the design and the construction of the data acquisition system; one cannot design even a trigger logic circuit if one does not fully understand physics of interest or the mechanism of detectors.

I would like to thank to Prof. K. Ogata for providing fruitful discussion to trigger this study as well as to realize the present experiment. I also would like to thank to Dr. Y. Kikuchi. His theoretical support is definitely needed to design the present experiment. He provided not only theoretical calculation but also the precious suggestions for the interpretation of the result.

I would like to thank to Dr. A. Obertelli and Dr. A. Corsi for giving me a chance to realize the present study through the MINOS project at RIKEN. They kindly helped me to polish up my proposal as well as to refine my talk for the Program Advisory Committee Meeting for Nuclear-Physics Experiments at RI Beam Factory.

I am extremely grateful to all the collaborators of the NP1312-SAMURAI18R1 experiment. This study was carried out as an international collaboration of 16 institutes. I acknowledge that